Modeling and TCOs Engineering for Thin-Film Photovoltaic Technologies

Federica Saitta

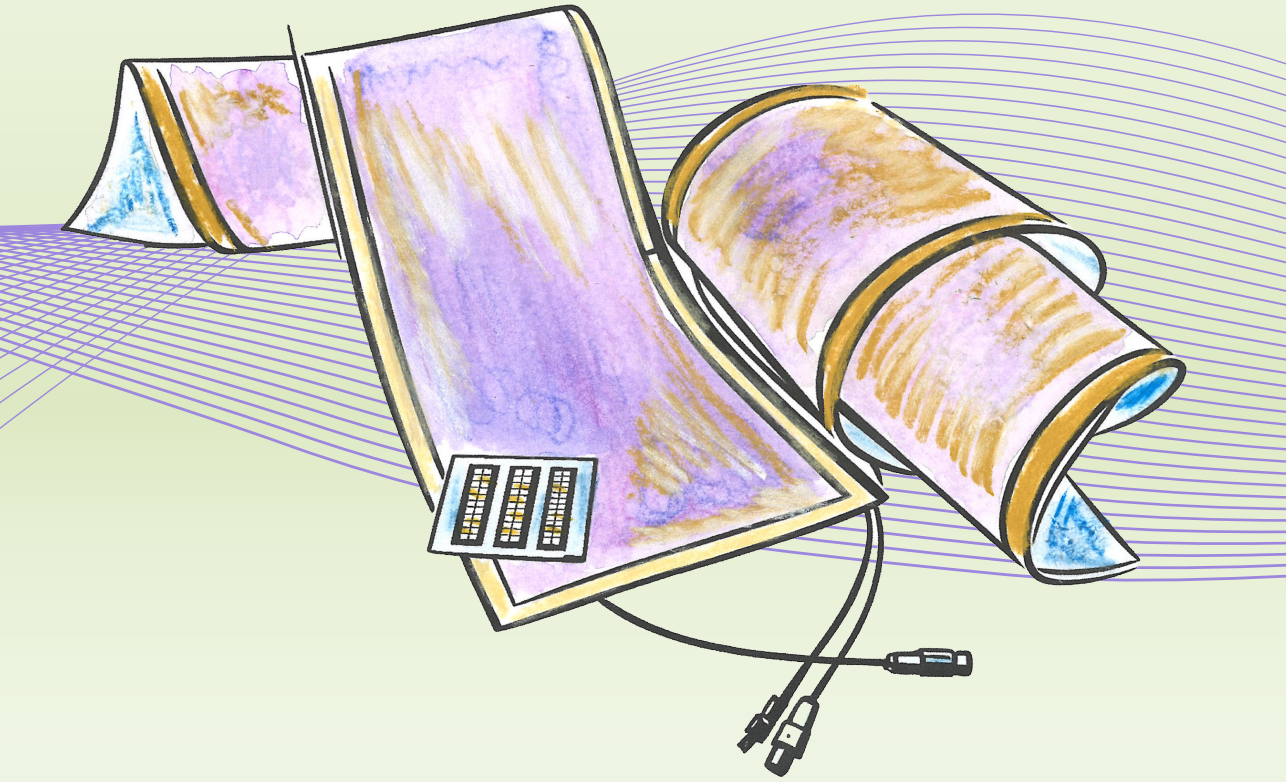

Modeling and TCOs Engineering for Thin-Film Photovoltaic Technologies

Federica SAITTA

Modeling and TCOs Engineering for Thin-Film Photovoltaic Technologies

Dissertation

for the purpose of obtaining the degree of doctor
at Delft Univerity of Technology,
by the authority of the Rector Magnificus, Prof. dr. ir. H. Bijl,
Chair of the Board for Doctorates
to be defended publicly on
Friday, 29 May 2026 at 12:30

by

Federica SAITTA

This dissertation has been approved by the promotor and the copromotor.

Composition of the doctoral committee:

Rector Magnificus	chairperson
Prof. dr. ir. A. H. M. Smets	Delft University of Technology, promotor
Dr. ir. R. Santbergen	Delft University of Technology, copromotor

Independent members:

Prof. dr. A. W. Weeber	Delft University of Technology
Prof. dr. L. J. A. Koster	University of Groningen, the Netherlands
Prof. dr. J. Krč	University of Ljubljana, Slovenia
Prof. dr. M. Morales-Masis	University of Twente, the Netherlands
Prof. dr. R. Schlatmann	Helmholtz Zentrum Berlin, Germany
Prof. dr. ir. O. Isabella	Delft University of Technology, reserve member

ISBN 978-94-6518-311-4

An electronic version of this dissertation is available at
http://repository.tudelft.nl/.

Printed by: Ridderprint

Cover design by: Giorgia Brugnoli, Cecilia Edvige De Conti

Life is and will ever remain an equation incapable of solution,
but it contains certain known factors.

Nikola Tesla

CONTENTS

SUMMARY

Thin-film silicon photovoltaics are among the most mature photovoltaic technologies, with well-established material physics, reliable device performance, and a long history of industrial deployment. Although their efficiency limits large-scale power generation, thin-film silicon remains a powerful platform for optical and electrical device design. Its compatibility with substrate texturing, advanced light management, and superstrate fabrication enables multiscale interfaces, novel transparent electrodes, and high temperature processing for improved material quality. These features make it a robust foundation for emerging lightweight and flexible photovoltaic concepts, including perovskite-based devices.

This thesis advances superstrate thin-film photovoltaics across three interconnected areas: transparent conductive oxide development, optoelectrical device modeling, and the design of emerging perovskite architectures. It begins with the engineering of transparent conductive oxides, a critical component of high performance superstrate solar cells, where performance is governed by trade-offs between transparency, conductivity, material abundance, and scalability.

Chapter 2 investigates bilayer transparent conductive oxides deposited by magnetron sputtering on glass. By separating optical transparency and electrical conductivity into complementary layers and exploiting the natural texture of polycrystalline zinc oxide, the bilayer design overcomes the limitations of single-layer electrodes. The study provides an understanding of charge transport, optical scattering, and interface morphology, and establishes a general framework for high performance front electrodes.

Chapter 3 focuses on sustainable, earth-abundant alternatives based on tin oxide. By controlling oxygen and hydrogen incorporation during room temperature sputtering, combined with fluorine doping and post-deposition annealing, the chapter clarifies how stoichiometry, defect chemistry, and dopant activation govern carrier density and mobility. These results define processing routes for high performance indium-free transparent conductive oxides compatible with temperature-sensitive devices.

The optimized electrodes developed in Chapter 2 and Chapter 3, together with textured glass substrates engineered within our research group, provide the experimental foundation for the device-level modeling that follows. Their measured optical and electrical properties are directly implemented in the simulation framework, ensuring predictive and physically grounded analysis.

Chapter 4 establishes an experimentally validated optical modeling approach for predicting broadband absorption and reflection losses in multiscale-textured thin-film silicon solar cells. By integrating realistic interface morphologies with measured optical constants, the model enables unified prediction of optical behavior. Applications to both commercial Asahi textured glass and engineered honeycomb microtextures yield design rules transferable across thin-film technologies.

Chapter 5 extends this framework by coupling optical and electrical simulations and validating the approach using devices fabricated on glass and flexible aluminum foil carriers. The framework is subsequently applied to single-junction and tandem perovskite architectures on flexible substrates. The analysis identifies the hole transport layer as a key parameter governing energy-level alignment, carrier selectivity, and interfacial losses, thereby defining critical design strategies for high efficiency flexible perovskite photovoltaics compatible with roll-to-roll manufacturing.

Together, these studies establish an integrated framework linking transparent conductive oxide engineering, optoelectrical modeling, and device architecture design. They demonstrate how the superstrate configuration enables high temperature and high quality materials processing, and advanced light management within scalable thin-film photovoltaic platforms. Thin-film silicon devices emerge as versatile experimental and modeling test platform for next generation thin-film technologies. Overall, this work outlines a pathway toward scalable, high efficiency, and mechanically flexible photovoltaic technologies extending beyond conventional wafer-based systems.

PREFACE

Research is rarely a straight path. Mine has oscillated between models and experiments, between moments of apparent certainty and humbleness of failure. I have found out that what does not work can be as revealing as what does, and that trust in science comes as much from doubt as from proof.

I have been guided with care by great supervisors, and in turn I have learned to guide people. I have come to see that guidance is less about removing obstacles and more about creating space for others to navigate them: a lesson in patience and in faith.

The world beyond work also leaves its marks. Rules and freedoms often collide in paradoxical ways, reminding us that progress is measured not only in results, but in the courage to confront contradictions. And perhaps, as in life, the ride is worth taking only when it rises and falls, when it challenges us.

This dissertation is therefore not only a work of research, but also a record of a journey of questioning, guiding, struggling, and daring.

A stream of consciousness
on my work and propositions

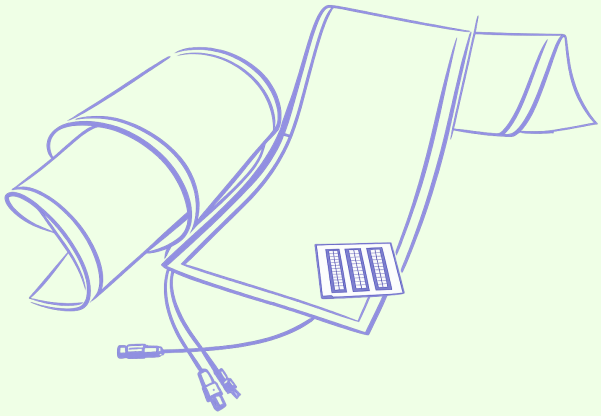

1

INTRODUCTION

1

1.1. Why (still) doing thin-film silicon?

Thin-film silicon (TF-Si) photovoltaics have accompanied the evolution of solar technology for more than four decades. At first sight, continued research in TF-Si technology may appear counterintuitive in a landscape increasingly shaped by high efficiency crystalline silicon (c-Si) and the rapid rise of perovskite based devices. This leads to the central question motivating this thesis: *"Why should we still study and develop thin-film silicon today?"*

The answer lies in the distinctive role that TF-Si occupies at the intersection of materials science, optical engineering, and device architecture. Its ultra-thin absorber layers, engineered interfaces, and compatibility with large area manufacturing create a design space that neither wafer based photovoltaics nor emerging perovskites can replicate. Therefore, this technology serves as a scientifically instructive and enabling platform for advancing photovoltaic design, a role that can be understood through interconnected aspects outlined in the following.

The thin absorber layers, typically ranging from hundreds of nanometers to a few micrometers, as exemplified by hydrogenated amorphous silicon (a-Si:H) and hydrogenated nanocrystalline silicon (nc-Si:H), enable bandgap tuning, compositional grading, exploration of spectral utilization limits, and multi-junction stacking without incurring prohibitive transport losses [1]. The TF-Si technology also provides a controlled environment for developing and validating light trapping strategies, substrate texturing, diffractive optics, and engineered back reflectors for the advancement of light management concepts [2].

For example, superimposed sacrificial texturing and engineered hexagonal microtextures on glass substrates, developed in our group, demonstrate how multiscale morphologies can enhance optical path length, reduce reflection, and redistribute light across the visible and near-infrared (NIR) range of the solar spectrum in solar devices [3, 4].

While related light management approaches are also implemented in c-Si technologies using industrially established random pyramid texturing [5, 6], as well as advanced methods such as reactive ion etching (RIE) [7], TF-Si provides a complementary platform for studying the interplay between optical design and device performance. Consequently, these design principles and physical insights can be extended to organic photovoltaics such as perovskites, and emerging tandem concepts.

Furthermore, TF-Si serves as a effective platform for analyzing performance limits in ultra-thin photovoltaic devices. Key loss mechanisms, including defect creation kinetics associated with the Staebler–Wronski effect, bottlenecks at tunnel recombination junctions, optical losses arising from sub-gap absorption in defective or doped layers, and trade-offs between optical scattering and recombination, have been systematically investigated in thin-film silicon devices [8, 9]. While many of these physical processes are also well understood in c-Si technologies, TF-Si enables their investigation in thickness regimes and device architectures that are directly relevant to the broader thin-film photovoltaic field.

At the manufacturing level, its compatibility with large area, low temperature, roll-to-roll (R2R) processing enables flexible and lightweight photovoltaic modules. While other TF technologies, such as copper indium gallium selenide (CIGS) and cadmium telluride (CdTe), have demonstrated higher efficiencies and industrial scalability, all thin-film approaches share key advantages including low material consumption, reduced thermal budgets, and compatibility with a wide range of substrates [10].

By comparison, flexible c-Si technologies have recently emerged through approaches based on substrate thinning and polymer-based encapsulation, enabling lightweight and mechanically compliant designs while preserving the high efficiency and stability of mainstream c-Si technology. However, flexibility remains limited compared to TF photovoltaics due to the intrinsic brittleness and thickness constraints of silicon wafers. Additionally, most implementations rely on adapted module architectures rather than intrinsically flexible materials. As a result, flexible c-Si currently occupies an intermediate position between conventional rigid wafer-based technologies and intrinsically flexible thin-film solar cells [11, 12].

In practice, the industrial potential of thin-film silicon has already been demonstrated by United Solar Ovonic [13], whose stainless steel and high temperature polymer substrates enabled lightweight photovoltaic modules for curved surfaces, rooftop applications, and building integrated photovoltaics (BIPV) [14].

More recent progress by the Dutch company LiftPV, formerly HyET Solar, has advanced R2R TF-Si by targeting applications that require extreme weight reduction, mechanical resilience, and scalable continuous manufacturing [15]. In this context, temporary metal carrier foils have been introduced to decouple high temperature processing from the final flexible substrate. This temporary superstrate concept also presents a promising processing route for perovskite photovoltaics, creating opportunities to integrate high quality processed materials into fully flexible device architectures.

From an environmental perspective, TF-Si belongs to a broader class of photovoltaic technologies that require less material and lower manufacturing energy than mainstream c-Si. Life cycle assessment studies report lower cumulative energy demand and global warming potential for TF technologies, although their lower efficiencies can result in less favorable energy payback times. Among commercially established options, a-Si:H is identified as one of the more favorable technologies in terms of energy demand and greenhouse gas emissions, while CdTe and CIGS also perform well but raise concerns related to material criticality and toxicity [16–18].

In addition, TF-Si is compatible with high throughput R2R processing, enabling resource-efficient large area manufacturing. It also exhibits stabilized performance over operational lifetimes comparable to conventional modules, allowing competitive environmental performance per unit of electricity generated. Thin-film silicon therefore represents a relevant compromise between environmental performance, material availability, and compatibility with lightweight, flexible and cost effective photovoltaic applications [13, 19].

1.2. The aim and the proposed route

Thin-film silicon based solar cells fabricated on glass have reached stabilized efficiencies of around 10% for single-junction a-Si:H, 12% for a-Si:H/nc-Si:H tandems, and up to 14% for triple-junction devices at laboratory scale, typically demonstrated on cell areas of the order of 1 cm^2 [20–22].

Amorphous silicon is a semiconductor characterized by a mobility gap of approximately 1.6–1.8 eV and a high density of localized states within the bandgap. Its optical absorption coefficient is significantly higher than that of crystalline silicon, enabling efficient light absorption in sub-micrometer thicknesses [23].

However, charge transport is limited by low carrier mobility and defect-mediated recombination, making device performance highly sensitive to optical management and interface engineering. Performance improvements have been achieved through increased architectural complexity, progressing from single- to multi-junction designs. This evolution is illustrated schematically in Figure 1.1.

Despite these advances, the achievable efficiency of thin-film silicon remains lower than that of competing photovoltaic technologies, particularly crystalline silicon and perovskite-based devices. This limitation does not diminish the relevance of thin-film silicon. Instead, it highlights its role as a versatile platform for exploring advanced device architectures, light management strategies, and interface engineering in ultra-thin photovoltaic systems.

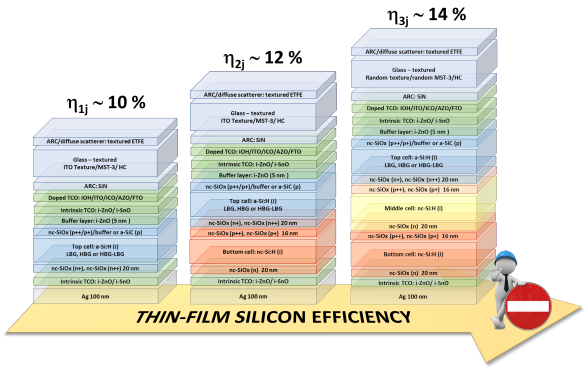

Figure 1.1: Schematic illustration of TF-Si solar cell architectures, highlighting the evolution from single- to multi-junction configurations and the associated efficiency improvements.

The aim of this work is to explore and assess transparent conductive oxide (TCO) materials for superstrate thin-film photovoltaic devices, exploiting the design freedom offered by the superstrate configuration to investigate front electrode concepts beyond conventional indium based solutions.

Building on this, a physically grounded optoelectrical modeling framework is developed and validated, establishing a direct link between material properties, optical design, and electrical performance in thin-film devices. This framework enables the systematic evaluation of TCO design choices, supports device optimization in TF-Si, and provides a foundation for extending these design principles to broader photovoltaic architectures, including perovskites.

Transparent conductive oxides are typically degenerately doped wide bandgap semiconductors, combining high optical transparency (bandgap > 3 eV) with sufficient electrical conductivity through high carrier densities (10^{19}–10^{21} cm^{-3}). Their optoelectrical performance is governed by the interplay between carrier density and mobility: increasing carrier concentration improves conductivity but enhances free carrier absorption in the NIR, while high mobility reduces resistive losses without compromising transparency [24].

The superstrate configuration offers significantly greater freedom in front electrode design than substrate-based device architectures. In superstrate devices, the TCO governs both optical in-coupling and lateral charge transport, directly influencing device efficiency. As a result, the front electrode must simultaneously satisfy optical transparency, electrical conductivity, and compatibility with the processing constraints of the device architecture.

The competing requirements associated with TCO selection are illustrated in Figure 1.2, highlighting the interdependence among optical transparency, electrical conductivity, material abundance, and compatibility with flexible device architectures. Indium-based TCOs, such as indium tin oxide (ITO), represent the state-of-the-art, combining high carrier mobility with carrier densities on the order of 10^{20}–10^{21} cm^{-3}, enabling low resistivity and high transparency across the visible spectrum.

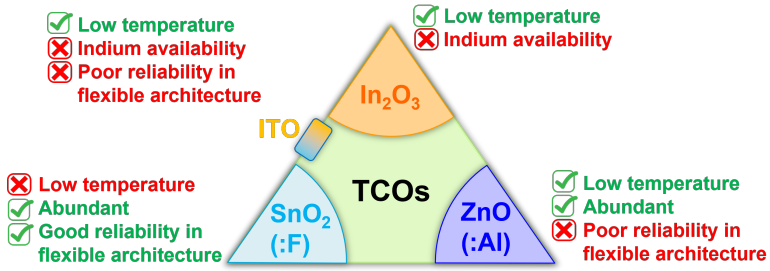

Figure 1.2: Schematic overview of transparent conductive oxide (TCO) materials based on metal oxides derived from tin dioxide (SnO_2), indium oxide (In_2O_3), and zinc oxide (ZnO), illustrating the trade-offs among low temperature processability, material abundance, and reliability in flexible device architectures.

In established photovoltaic technologies, such as silicon hetero-junction (SHJ) solar cells, ITO films deposited at low temperatures (< 200 °C) typically exhibit electron mobilities in the range of 30–40 cm^2/Vs, illustrating the level of performance achievable under industrially relevant processing conditions [25].

These materials rely on scarce indium resources and exhibit limited mechanical robustness under bending. Earth-abundant alternatives based on zinc oxide (ZnO) and tin dioxide (SnO_2) therefore offer advantages in material availability and, in some cases, improved optical transparency due to lower free carrier absorption. However, their electrical performance is typically limited by lower mobility (below 10 cm^2/Vs) or requires careful control of defect chemistry and doping [26, 27].

In addition, high quality crystalline films often necessitate elevated deposition or post-deposition annealing temperatures, which exceed the thermal limits of common polymer substrates, such as polyethylene terephthalate (PET) or polyethylene naphthalate (PEN) [28].

Superstrate fabrication strategies based on temporary carriers provide a route to decouple front electrode processing from the constraints of the final device substrate, enabling high temperature deposition of high performance TCOs prior to transfer onto flexible supports.

Within this context, the temporary metal foil superstrate configuration represents an effective fabrication route. The photovoltaic device stack is deposited onto a removable aluminum carrier that tolerates processing temperatures not compatible with conventional polymer substrates such as PET/ITO or PEN/ITO.

Fluorine-doped tin oxide (FTO) is fabricated via atmospheric-pressure chemical vapor deposition (APCVD) at around 500 °C, yielding dense, low resistivity, high mobility transparent conductive oxides typically achievable only on rigid glass.

After lamination, the aluminum carrier is removed and the photovoltaic stack is transferred onto a wide range of permanent and flexible substrates, thereby combining high performance front electrodes with R2R manufacturability [29]. While the aluminum foil approach is well established for TF-Si technology, its applicability to other photovoltaics, such as perovskite, has not yet been explored. A schematic overview of this superstrate roll-to-roll process is shown in Figure 1.3.

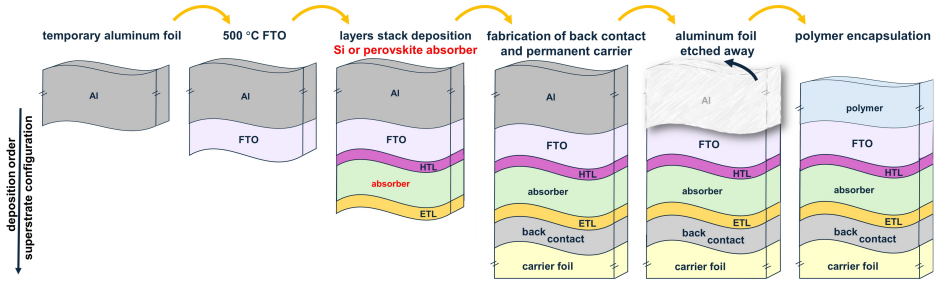

Figure 1.3: Roll-to-roll (R2R) superstrate processing route for flexible thin-film solar cells. The device stack is deposited on a temporary aluminum foil enabling high temperature processing, transferred to a permanent carrier, and encapsulated within flexible polymer layers after removal of the temporary superstrate.

Addressing the trade-offs between optical transparency, electrical conductivity, material sustainability, and process compatibility, while expanding the TCO design space beyond conventional single-layer front electrodes in solar devices, constitutes a first central objective of this thesis.
A second objective is the development of a physically grounded optoelectrical modeling framework to evaluate device architectures across different material systems and to assess the performance potential of next generation thin-film solar cells compatible with high temperature superstrate processing.

1.3. Research questions

The understanding of thin-film silicon photovoltaics is used here as a platform to develop transferable materials, device architectures, and optoelectrical modeling strategies for future TF technologies compatible with scalable manufacturing concepts. This work therefore addresses the following research questions:

1. How can transparent conductive oxide architectures be engineered to decouple optical transparency and electrical conductivity, and which physical mechanisms govern the optoelectrical performance of such electrodes in TF solar cells?

2. What relationships link processing conditions to structural, chemical, and optoelectrical properties in indium-free SnO_2-based transparent conductive oxides deposited under low thermal budget constraints, and how can these relationships be exploited for scalable photovoltaic applications?

3. To what extent can light propagation, absorption, and angular redistribution in multiscale textured thin-film solar cells be predicted using experimentally grounded optical models, and how does their predictive accuracy compare to that of electromagnetic approaches?

4. How can optoelectrical modeling frameworks validated on TF-Si devices be extended to flexible perovskite solar cell devices fabricated in superstrate configurations, and which physical mechanisms limit their performance under high temperature processing conditions?

1.4. Outline

The chapters progress from materials engineering and characterization to experimentally grounded device-level simulations, and finally to the design of flexible photovoltaic architectures compatible with scalable manufacturing. Background theory, state-of-the-art context, and experimental methodologies are introduced within the corresponding chapters, with additional details provided in the appendices where needed.

Chapter 2 explores bilayer transparent conductive oxides as a route to decouple transparency and conductivity in the front electrode. By optimizing complementary sputtered layers and analyzing free-carrier transport and scattering mechanisms, it shows that bilayer designs can outperform their individual components. The chapter further establishes a general framework for engineering high performance front electrodes.

Chapter 3 extends this approach to indium-free tin oxide based materials, motivated by the need for sustainable and earth-abundant alternatives. Controlled incorporation of oxygen, hydrogen, and fluorine during room-temperature deposition and post-annealing is used to tune material properties. The chapter clarifies how stoichiometry and defect chemistry govern mobility and carrier density in SnO_2-based films, thereby outlining processing pathways toward high quality indium-free TCOs compatible with high and low thermal-budget fabrication.

The insights from Chapter 2 and Chapter 3, together with advances in substrate development within our research group, provide the experimental basis for the device-level modeling presented in Chapter 4 and Chapter 5. The experimentally characterized optical and electrical material properties are directly implemented in the simulations, ensuring realistic and physically grounded device analysis.

Chapter 4 introduces an experimentally validated optical modeling framework for predicting broadband absorption and reflection losses in multiscale textured TF-Si devices. The approach combines accurate optical constants with realistic interface morphologies and rigorous light-propagation models, providing a transferable method for other TF photovoltaic technologies.

Finally, Chapter 5 combines optical and electrical modeling to validate TF-Si devices on both glass and flexible substrates, and extends the analysis to perovskite single-junction and tandem architectures. Particular attention is given to the role of the hole-transport layer in band alignment and carrier selectivity. The simulations identify performance limits and outline design strategies for high-efficiency flexible perovskite photovoltaics compatible with large-scale R2R processing.

1

1.5. Main contributions to the PV field

The main contributions of this research are summarized below.

- **Decoupled transparent conductive oxide architectures for thin-film photovoltaics.** Bilayer transparent conductive oxide concepts are developed to decouple optical transparency and electrical conductivity, enabling independent optimization of front electrode properties for thin-film architectures.
- **Indium-free SnO_2-based transparent conductive oxides for scalable applications.** Indium-free SnO_2-based transparent conductive oxides compatible with low thermal budget processing are optimized, linking processing conditions and material structure to optoelectrical properties and resulting front electrode performance.
- **Experimentally grounded optoelectrical modeling of thin-film solar cells.** An optoelectrical modeling is established in which experimentally measured optical and electrical material properties are directly implemented, enabling physically consistent, computationally efficient analysis of thin-film silicon devices with complex and multiscale textured architectures.
- **Extension of thin-film silicon design principles to flexible perovskite photovoltaics.** The validated optoelectrical modeling framework is extended from thin-film silicon to perovskite single-junction and tandem architectures, identifying viable device configurations and design strategies for flexible perovskite solar cells compatible with large scale, high temperature, roll-to-roll superstrate processing.

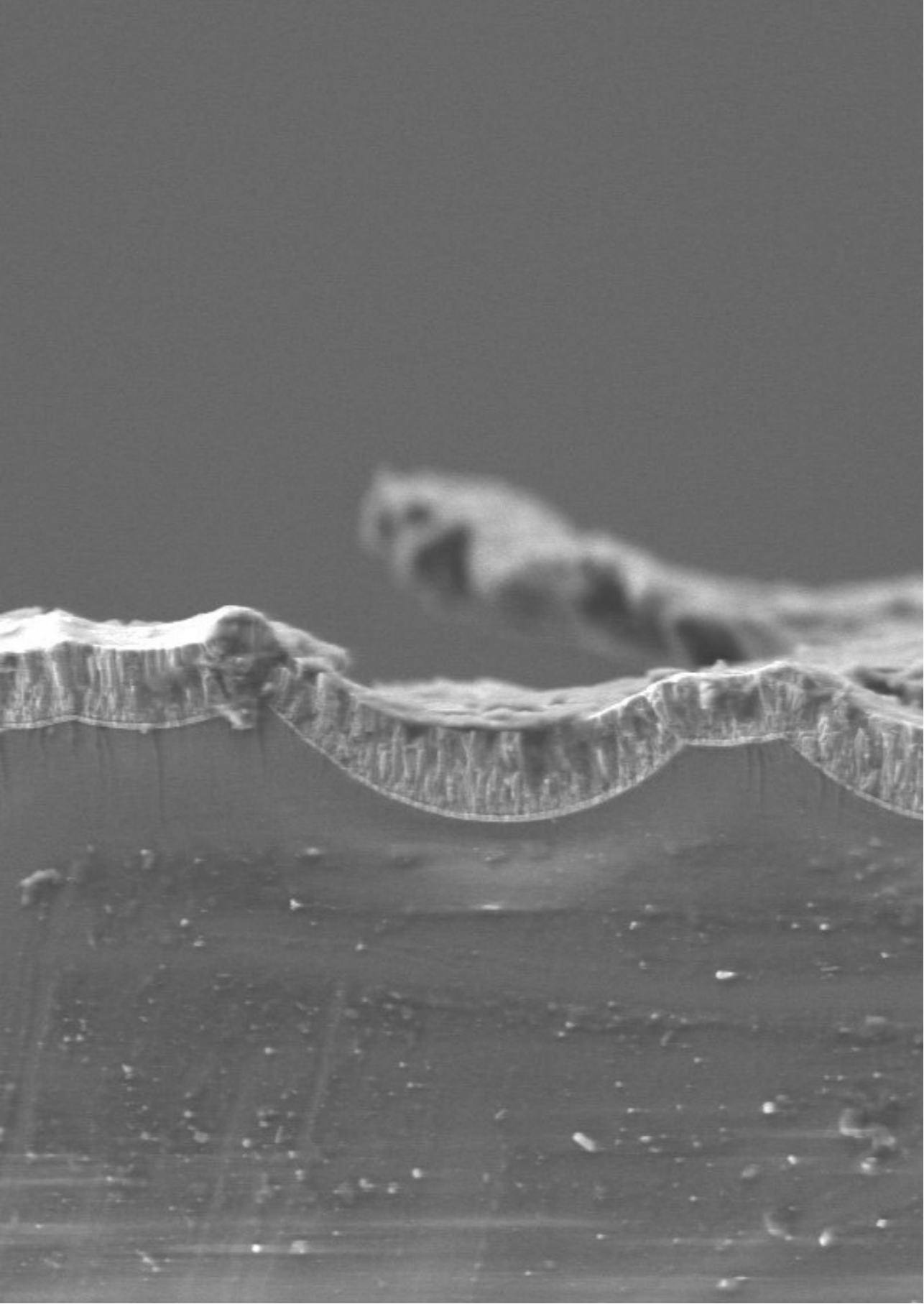

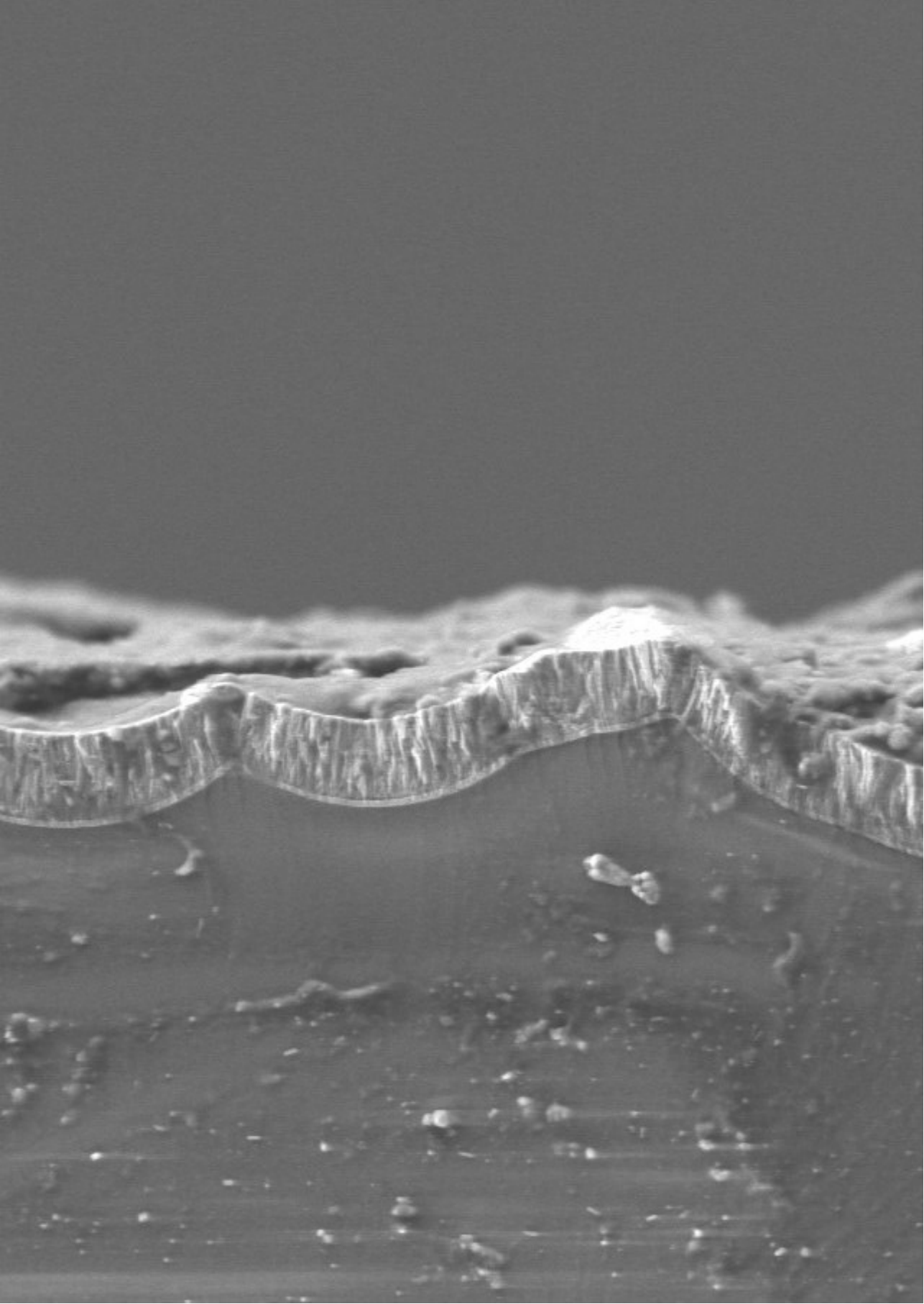

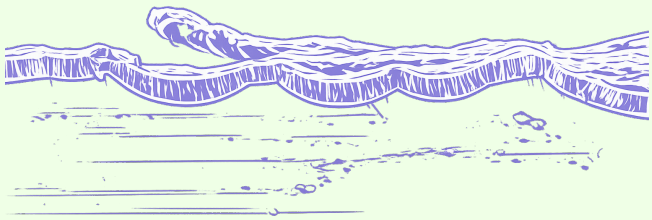

2

DECOUPLING OPTICAL AND ELECTRICAL PROPERTIES IN TCOs

This chapter is based on the following publication:

Saitta, F., Kalpoe, P., Ahluwalia, V., Padmakumar, G., Perez-Rodriguez, P., Limodio, G., Santbergen, R., & Smets, A. H. M. *De-coupling of optical and electrical properties in front TCO using the bilayer concept for thin film solar cells.* Solar Energy Materials and Solar Cells, 290, 113723 (2025), https://doi.org/10.1016/j.solmat.2025.113723.

2.1. Introduction

Transparent conductive oxide (TCO) materials are widely employed as front contact electrodes in thin-film (TF) solar cells [30, 31]. Among the various TCO materials, metal oxides have attracted particular attention due to their favorable optoelectrical properties [32–35]. These properties are governed by the oxidation state of the metal constituent, as well as by the type and concentration of impurities incorporated into the films [36–38].

In_2O_3-based TCOs, such as indium tin oxide (ITO), are widely used as front electrodes in solar cells due to their trade-off between high electrical conductivity and good transparency in the visible light spectrum [39, 40]. However, the simultaneous optimization of both transparency and conductivity in a single TCO layer is inherently constrained by a compromise [24]. Increasing the carrier concentration improves conductivity but reduces transparency in the near infrared (NIR) region due to free carrier absorption (FCA) [37, 41].

The concept of using bilayer TCO structures to overcome the inherent trade-off between transparency and conductivity in single-layer TCOs has been investigated in previous studies [42]. For example, Lee et al. demonstrated that a double-layer transparent conductive oxide structure composed of ITO and niobium-doped titanium dioxide (TNO) effectively acts as an anti-reflection coating, significantly reducing front surface reflectance while ensuring adequate lateral conductivity in silicon solar cells [43].

Furthermore, indium tin oxide/aluminum-doped zinc oxide (AZO) bilayer TCO films have emerged as a highly effective front-electrode architecture for thin-film silicon solar cells. Several studies have shown that such bilayers exhibit superior structural and morphological properties, along with enhanced optoelectrical characteristics, surpassing those of single-layer TCO films [44–46].

Similarly, Tan et al. demonstrated that a bilayer of hydrogenated indium oxide (IO:H) and low-pressure chemical vapor deposition (LPCVD) ZnO in modulated surface textured (MST) electrodes significantly enhances the performance of multijunction TF-Si solar cells. This bilayer effectively minimizes parasitic absorption and ensures efficient light management, resulting in higher initial and stabilized efficiency of solar cells compared to single-layer TCOs [47].

Previous studies have predominantly focused on material selection and performance metrics of TCOs used as front contacts. However, the underlying mechanisms enabling the decoupling of optical and electrical functionalities in bilayer TCO structures remain insufficiently understood. The novelty of this work lies in its fundamental analysis of the free charge carrier transport mechanisms governing bilayer TCO behavior, providing a deeper understanding of their enhanced optoelectrical properties.

The investigation is therefore directed towards the designing and optimization of a two film-stack front contact for thin-film solar cells, employing the sputtering technique as the fabrication method. In addition to its compatibility with high-quality TCO deposition, sputtering is a relatively low-cost and scalable process, making it attractive for industrial applications [30]. In this bilayer design, one TCO is chosen primarily for its high transparency, while the second selected TCO is intended to provide high conductivity (Section 2.3.1). Various TCO metal oxides are analyzed to identify the most suitable candidates, considering the intricate interplay between their optical and electrical properties [48, 49].

By refining the bilayer design (Section 2.3.4) and optimizing the properties of each TCO layer (Section 2.3.2 and 2.3.3), significant enhancements in both optical and electrical performance are achieved (Section 2.3.4.2). Based on the laws of multilayer optics and conductivity, one might expect the bilayer's overall transparency and conductivity to merely reflect the average of its constituent layers. However, the optimized design surpasses these expectations, delivering superior values in both metrics. While this study employs particular TCO materials, the understanding of the working principles behind the TCO bilayer structure (Section 2.3.4.3) is broadly applicable. It not only facilitates significant improvements in the performance and efficiency of TF solar cells (Section 2.3.5) [47, 50] but also offers the way for innovative front-contact designs in a broader range of solar cell technologies [51], potentially using more cost-effective TCO alternatives.

2.2. Experimental procedure

This section outlines the methodologies used for the fabrication, characterization, and evaluation of TCO films and solar cells. Section 2.2.1 details the deposition process of various TCO materials and the post-deposition annealing (PDA) treatment. Section 2.2.2 describes the optical, electrical, and structural characterization techniques employed to assess the properties of the fabricated TCOs. Section 2.2.3 and Section 2.2.4 discuss the key optical and electrical performance metrics relevant to front-contact applications in solar cells. Finally, Section 2.2.5 presents the fabrication and characterization of hydrogenated nanocrystalline silicon (nc-Si:H) solar cells incorporating the developed bilayer TCO front contact.

2.2.1. TCO fabrication and post-deposition annealing

The TCO films are grown on corning glass substrates by using Radio Frequency (RF, 13.56 MHz) magnetron sputtering technique. The geometrical size of the substrate is 10 cm × 2.5 cm × 0.7 mm. Prior to sputtering, each glass substrate is cleaned in acetone and isopropyl alcohol ultrasonic baths for 10 min respectively. Four different types of transparent conductive materials are subjected to investigation. They are hydrogen-doped indium oxide (IO:H), tin-doped indium oxide (ITO), aluminum-doped zinc oxide (AZO) and non-intentionally doped zinc oxide (ZnO).

These films are fabricated in a multi-chamber sputtering tool. Deposition time, power, and temperature are adjusted to investigate various sputtering conditions. In the case of IO:H, the introduction of hydrogen is achieved by varying the partial pressure of water (H_2O) vapor. Table 2.1 presents the power density (P) and substrate temperature (T) window ranges for each investigated TCO.

Table 2.1: Range of power density [W/cm^2] and substrate temperature [°C] windows, varied as deposition parameters for the investigated TCOs.

Material	P_{min} [W/cm^2]	P_{max} [W/cm^2]	T_{min} [°C]	T_{max} [°C]
ITO	1.35	3.00	25	156
IO:H	1.05	1.80	25	107
ZnO	1.00	4.00	95	217
AZO	1.00	4.00	95	217

The deposited TCO samples are subjected to post-deposition annealing (PDA) under controlled temperature and time conditions. Annealing in ambient atmosphere is performed using a conventional furnace, while annealing under vacuum is carried out using a halogen lamp–heated rapid thermal annealer (RTA). The RTA supports various gas environments, including argon (Ar) and forming gas (N_2/10% H_2). Vacuum annealing is conducted both with and without H_2 gas flow.

2.2.2. TCO characterization

Optically, the transmittance (T) and reflectance (R) spectra are measured by a spectrophotometric PerkinElmer Lambda 1050 system, and the absorbance (A) is derived by applying the law of energy conservation ($1 = A + R + T$) for light interaction with materials.
The spectroscopic ellipsometry (SE) M-2000DI system (J.A. Woollam Co., Inc.) is used to determine the bulk thickness (t), refractive index (n), extinction coefficient (k) and optical bandgap (E_g) from the Tauc plot according to the SE-fitted absorption coefficient (α) curve. In SE analysis, the dielectric function of the TCO sample is considered homogeneous in depth and modeled by combining two oscillator theories: Cody–Lorentz and Drude.
Furthermore, the TCO thickness is also determined by a Steag ETA-Optik mini-RT setup. In mini-RT measurements, R and T curves are measured and processed through the Scout software to estimate the sample thickness.
Electrically, the TCO is characterized by the resistivity (ρ), the sheet resistance (R_{sheet}), the carrier density (N) and the mobility (μ). The ρ is determined using the HMS-5000 Hall effect measurement system by applying the van der Pauw method, and N and μ are then derived from the Hall effect at room temperature. The magnetic flux density is set at 0.55 T, the input current at 10 mA and the sample thickness is determined in advance via the Steag ETA-Optik mini-RT setup. The probes are arranged in a square configuration, approximately 1 cm apart, ensuring consistent spacing for accurate measurements. The R_{sheet} is measured using the four-point probe (4PP) method with the AIT CMT-SR2000N system, where four equidistantly positioned contacts are linearly arranged.
In addition to the optoelectrical measurements, material characterization is conducted on the TCO samples to gain a more comprehensive understanding of their properties.
The crystalline nature of the films is analyzed using X-ray diffraction (XRD). The XRD spectra are obtained with a Bruker D8 Advance diffractometer in Bragg–Brentano geometry, and Cu Kα radiation (wavelength 1.5406 Å) is employed from the X-ray tube with a standard focus. The morphological images of the samples are captured using a Hitachi Regulus 8230 field-emission scanning electron microscope (SEM). The Bruker atomic force microscopy (AFM) setup is used for high-resolution imaging and analysis of the surface topography. The image processing and data analysis are performed using the Gwyddion software.

2.2.3. Optical metrics

In a solar cell, the TCO-based front contact contributes to parasitic absorption above the optical bandgap in the ultraviolet (UV) region, and in the near infrared (NIR) region of the solar spectrum due to free carrier absorption (FCA).
A broader transparency window can be achieved through two primary approaches. Firstly, selecting a TCO material with a larger optical energy bandgap can extend the material's capability for optical transparency across a wider wavelength range in the UV region [52].

Secondly, an extended transparency window can also be attained through the Moss–Burstein shift, which occurs when a high carrier concentration fills the lower-energy states in the conduction band, effectively increasing the apparent bandgap of the TCO material [53].
In the NIR wavelength region (above 700 nm), the TCO optical absorption is influenced by intra-band transitions occurring within the conduction band [54]. The modeling of the FCA is often carried out using the Drude oscillator. According to this theory, the absorption coefficient α_{FCA} is calculated as [54, 55]:

$$\alpha_{FCA} = \frac{\lambda^2 e^3 N_e}{4\pi^2 \epsilon_0 c^3 n (m_e^*)^2 \mu_{opt}} \tag{2.1}$$

where λ is the wavelength of the incident light, e is the elementary charge, N_e is the electron carrier concentration for n-type doped TCOs, ε_0 is the vacuum permittivity, c is the speed of light in vacuum, n is the TCO refractive index at the corresponding wavelength, m_e^* is the effective electron mass, and μ_{opt} is the optical mobility.
As shown in Equation 2.1, α_{FCA} is directly proportional to N_e and an increase in carrier concentration enhances the probability of photon–carrier interaction [56]. This increase results in a greater FCA effect. In the case of a TCO front contact, minimizing N_e reduces unwanted absorption of NIR light and ensures material transparency in this spectral range.

2.2.4. Electrical metrics

A device-relevant parameter used for assessing the TCO electrical properties is the sheet resistance. The R_{sheet} is a crucial metric that provides insights into the electrical conductivity (σ), and it is calculated as [36]:

$$R_{sheet} = \frac{1}{\sigma t} = \frac{1}{e N_e \mu t} \tag{2.2}$$

where t is the thickness of the TCO material and μ is the electron mobility when an n-type doped TCO film is considered.
For the optimization of the front contact, low R_{sheet} is crucial to minimize electrical losses toward metal electrodes. The TCO conductivity can be enhanced either by increasing the carrier density (N_e) or by improving the carrier mobility (μ). However, increasing carrier density through doping can lead to higher free carrier absorption (see Equation 2.1) and reduced relaxation times due to dopant-induced scattering, both of which degrade the material's optical and electrical performance.
This demonstrates that achieving optimal performance in a TCO front contact is challenging due to the complex interplay between electrical and optical properties. High carrier mobility and a moderate level of carrier concentration are essential for simultaneously achieving low sheet resistance and good transparency.

2.2.5. Solar cell fabrication and characterization

Hydrogenated nanocrystalline silicon (nc-Si:H) single-junction solar cells ($4 \times 4\,mm^2$) are fabricated to evaluate the performance effects of the developed bilayer front contact design, which decouples the optical and electrical properties. Three different front electrodes are sputtered on micro-textured glass substrates with morphology features in the order of 1–3 µm, commonly used to achieve efficient light trapping in state-of-the-art devices [57]. The front contacts include 150 nm of ITO, 150 nm of IO:H as a monolayer, and a bilayer design with 150 nm of IO:H and 1 µm of ZnO. The choice of a 150 nm thickness is particularly critical, as it ensures full coverage and prevents any part of the craters on the textured glass from being left uncovered.

Additionally, an intermediate ambient PDA treatment is applied to the front contact during the solar cell fabrication. The ITO or IO:H monolayers are annealed for 20 min, while the IO:H/ZnO bilayer is annealed for 2 h and 20 min.

Superstrate-type p-i-n nc-Si:H solar cells are deposited using plasma-enhanced chemical vapor deposition (PECVD) and have a configuration consisting of 16 nm p-SiO_x:H / 2.6 µm i-nc-Si:H / 20 nm n-SiO_x:H. A 10 nm ZnO buffer layer is included between the front contact and the p-i-n structure. The metal back contact is thermally evaporated, comprising 300 nm Ag / 30 nm Cr / 800 nm Al. A schematic representation of the solar cell architecture is provided in Figure 2.1 for reference.

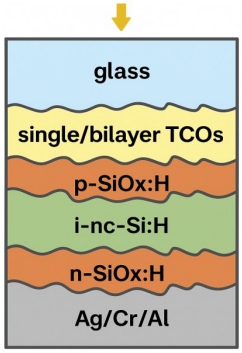

Figure 2.1: Cross-sectional schematic of the nc-Si:H p–i–n solar cell structure for each front contact configuration: ITO, IO:H, and IO:H/ZnO bilayer (layer thicknesses not to scale).

The solar cell performance is evaluated by measuring the current–voltage (J-V) characteristics under an AM 1.5G solar simulator (100 mW/cm^2) at 25 °C. The open-circuit voltage (V_{oc}), fill factor (FF), power conversion efficiency (η), series resistance (R_s) and shunt resistance (R_{sh}) are also recorded.

The external quantum efficiency (EQE) measurements are performed using a monochromatic light setup, from which the short-circuit current density ($J_{sc,EQE}$) is determined. The total absorptance ($1 - R$) is derived from the reflectance measured with the spectrophotometric system.

2.3. Results and discussion

This section focuses on the characterization of both single-layer and bilayer TCOs deposited on glass, with particular attention to their optical and electrical properties, as detailed in Sections 2.3.1 to 2.3.4.

The bilayer is constructed using two types of sputtered TCOs available in the lab: one with the highest lateral conductivity (IO:H) and another with the highest optical transmittance in the NIR region (ZnO), as described in Section 2.3.1. The electrical and optical properties of the individual layers are optimized in Section 2.3.2 and Section 2.3.3. Section 2.3.4 presents the processing and optimization of the IO:H/ZnO bilayer. In Section 2.3.4.2, it is shown that the bilayer charge carrier density and mobility outperform the simple superposition of the properties of the two single layers. Section 2.3.4.3 explains the physical mechanism underlying the decoupling of electrical and optical properties in the bilayer structure. Finally, Section 2.3.5 demonstrates the integration of the bilayer into a hydrogenated nanocrystalline silicon (nc-Si:H) solar cell and compares its performance to devices using single-layer TCOs.

2.3.1. TCO selection for bilayer design

To identify the most suitable TCO candidates, one offering the highest lateral conductivity and the other the highest transmittance in the NIR region, a comparative analysis is conducted based on the absorption coefficient at 1100 nm and the resistivity. The wavelength of 1100 nm is used because it falls within the NIR range and is commonly adopted in optical and photovoltaic research contexts to evaluate the performance of materials in the NIR spectrum.

In Figure 2.2, the optoelectrical properties of each material exhibit scattered data points due to the changes made in deposition parameters space.

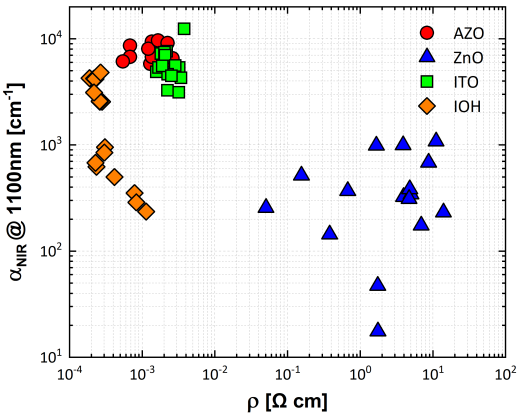

Figure 2.2: Absorption coefficient at $\lambda = 1100\,\text{nm}$ ($\alpha_{\text{NIR@1100 nm}}$) versus resistivity ($\rho$) of processed TCOs: hydrogen-doped indium oxide (IO:H), tin-doped indium oxide (ITO), aluminum-doped zinc oxide (AZO) and zinc oxide (ZnO).

Among the investigated TCOs, AZO and ITO are highly absorptive in the NIR region. The absorption coefficient values are all above $3.0 \times 10^{3}\,\text{cm}^{-1}$ in this spectral range, whereas the minimum resistivity reached is $5.0 \times 10^{-3}\,\Omega\,\text{cm}$. IO:H samples reveal the lowest resistivity values, ranging between 9.0×10^{-3} and $7.0 \times 10^{-3}\,\Omega\,\text{cm}$. The IO:H material shows a broader

distribution of α_{NIR} values between 2.0×10^2 and $5.0 \times 10^3\,cm^{-1}$. These findings align with previous studies on hydrogenated indium oxide films, which report comparable resistivity values and near-infrared absorption characteristics under similar sputtering conditions [58, 59].

Despite the widely varying characteristics of ZnO, Figure 2.2 highlights the poor conductivity of this undoped material together with its high transparency in the NIR region. ZnO emerges as the most suitable TCO due to its low FCA losses, while IO:H consistently achieves the highest conductivity values among all the examined TCOs. Hence, the undoped zinc oxide and the hydrogenated indium oxide materials are selected for the bilayer design.

2.3.2. IO:H optimization

Once the IO:H material is selected as the optimal choice for the first layer deposited in the bilayer structure, the deposition conditions are fine-tuned within a narrow power density range of 1.3–1.8 W/cm^2. The impact of ambient PDA on α_{NIR}, μ and N is investigated. The deposition temperature, H_2O partial pressure and thickness are set at 25 °C, 3.0×10^{-5} mbar and 190 nm, respectively. The deposited samples subsequently undergo annealing in ambient conditions at temperatures of 130, 180, 200 and 250 °C for 20 min.

Figure 2.3 shows that increasing the annealing temperature (T_a) decreases N and therefore α_{NIR}, while simultaneously enhancing μ.

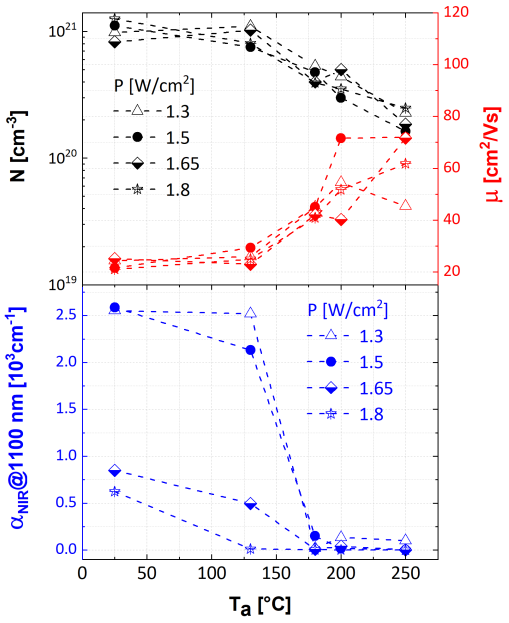

Figure 2.3: Processed IO:H samples at different power densities (P): mobility (μ) and carrier concentration (N) versus annealing temperature (T_a) (top plot); absorption coefficient at $\lambda = 1100$ nm ($\alpha_{NIR@1100\,nm}$) versus annealing temperature (T_a) (bottom plot).

A plateau occurs at 200 °C, representing the optimized PDA temperature for IO:H, in line with other studies on the impact of PDA treatment on the optoelectrical properties of IO:H [60, 61]. The power density is chosen to be 1.5 W/cm^2 on account of the best optoelectrical outcome seen in Figure 2.3

To gain a more comprehensive insight into the improvement of optoelectrical properties in IO:H, the XRD characterization is conducted on a sample deposited under optimized deposition parameters before and after the annealing process.

In Figure 2.4, the IO:H sample appears in an amorphous phase in its as-deposited condition. After ambient PDA, the film exhibits prominent XRD peaks at 2θ = 24.9°, 35.6°, 41.4°, and 59.9°, corresponding to the (211), (222), (400), and (440) planes of polycrystalline In_2O_3 with a cubic bixbyite structure. In particular, the dominance of the peak at 35.6° indicates a preference for the (222) orientation, consistent with previous findings [60, 62].

The enhanced optoelectrical properties of IO:H films can accordingly be attributed to a phase shift in the atomic structure, transitioning from an amorphous phase to a polycrystalline phase.

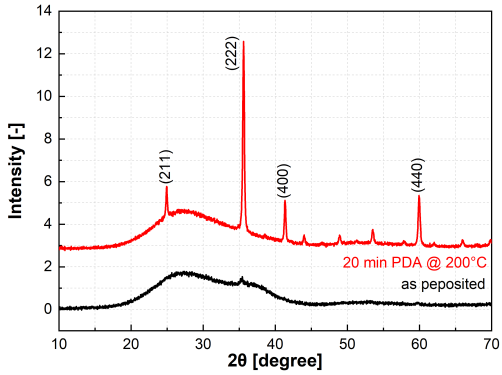

Figure 2.4: XRD results for the IO:H sample under optimized sputtering parameters: in the as-deposited state, and after 20 min ambient PDA at 200 °C.

Additionally, various annealing techniques are examined to optimize the optical transparency of IO:H mono-film on glass, with the sample thicknesses detailed in Table 2.2. Each annealing process is conducted for 20 min at a temperature of 200 °C on IO:H samples deposited using the optimized power density at room temperature, with an H_2O partial pressure of 3.0×10^{-5} mbar.

Table 2.2: Hall mobility [cm^2/Vs], carrier concentration [10^{20} cm^{-3}], sheet resistance [Ω/sq], mini-RT thickness [nm], resistivity calculated from Hall measurements and from four-point probe (4PP) sheet resistance for IO:H films in the as-deposited condition and under different annealing treatments at 200 °C for 20 min.

Sample	μ [cm^2/Vs]	N [10^{20} cm^{-3}]	R_{sheet} [Ω/sq]	t [nm]	ρ_{Hall} [10^{-4} Ω × cm]	ρ_{4PP} [10^{-4} Ω × cm]
as-dep.	26.13	5.17	35.81	128.80	4.62	4.61
ambient an.	66.65	1.94	26.66	140.00	4.82	3.73
vacuum an.	67.28	2.92	20.15	139.90	3.18	2.82
H_2-an.	47.09	3.54	27.22	119.80	3.75	3.26

Table 2.2 shows the electrical properties of IO:H samples in the as-deposited condition and under PDA treatments. Both ambient and vacuum annealing exhibit the most significant improvements in electrical properties, with vacuum annealing achieving the highest mobility (67.28 cm^2/Vs), while ambient annealing results in the lowest carrier concentration ($1.94 \times 10^{20}\,cm^{-3}$). As illustrated in Figure 2.5, the ambient and vacuum annealing techniques yield consistent results and prove to be the most effective methods for enhancing T in the NIR region. Overall, ambient annealing provides the most balanced improvement in optoelectrical properties, effectively enhancing both transparency and electrical conductivity.

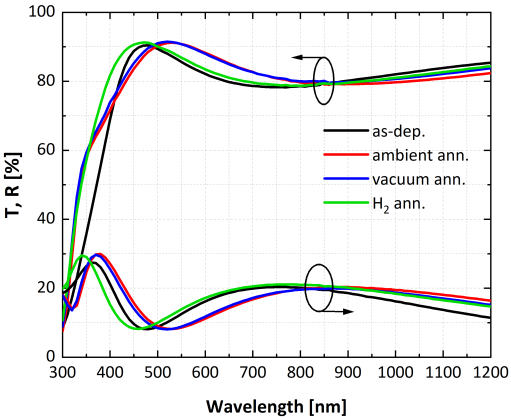

Figure 2.5: Reflectance (R) and transmittance (T) of IO:H samples in the as-deposited state and after ambient, vacuum and H_2 annealing treatments. IO:H thicknesses are reported in Table 2.2.

As detailed in the study by C. Han et al. [63], these improvements can be attributed to the reduction in Urbach energy (E_U), which indicates the width of the tail of localized defect states in the band gap in low-crystalline, disordered or amorphous materials [64]. Lower E_U values lead to enhanced transparency and reduced reflectance, as well as better electrical properties due to decreased charge carrier scattering and fewer charge traps. Conversely, H_2 annealing might result in higher E_U values, implying increased band tail states and promoted atomic structural disorder, thus resulting in less improved material quality during the annealing process [65].

2.3.3. ZnO optimization

As illustrated in Figure 2.2, the intrinsic zinc oxide samples exhibit the lowest parasitic absorption in the near-infrared region of the solar spectrum, but they are highly resistive TCOs. Therefore, the optimization of the ZnO monolayers is primarily focused on the optical function within the bilayer structure. Unlike the approach taken with IO:H, the PDA treatment on ZnO does not induce significant changes in its polycrystalline nature or optoelectrical properties, making it not worth reporting.

Instead, Figure 2.6 presents the refractive index (n) and extinction coefficient (k) behaviors of ZnO mono-film samples deposited on glass at different power densities [2.0 3.0 4.0 W/cm^2] at a set substrate temperature of 95 °C. It is worth noting that depositing ZnO at temperatures higher than the optimized IO:H annealing temperature (T_a) could inadvertently affect the IO:H optoelectrical properties, considering the application of ZnO on top of IO:H in a bilayer configuration.
The sample deposited at 2.0 W/cm^2 displays the widest transparency window, as indicated by the extinction coefficient trend, and an increased energy bandgap (E_g = 3.07 eV). Lower deposition power enables more controlled and gradual growth of ZnO films, reducing the likelihood of defects such as vacancies and interstitials that scatter light. With fewer defects and impurities, the ZnO film exhibits higher optical transparency [66, 67]. Additionally, higher power results in increased energy associated with ion bombardment, which can detrimentally affect the surface morphology of ZnO and the underlying IO:H layer [68].

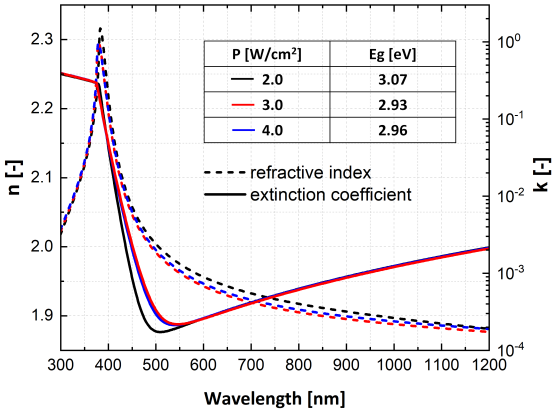

Figure 2.6: Refractive index (n) and extinction coefficient (k) behaviors of ZnO samples by varying power density (P) at a constant substrate temperature of 95 °C. Energy bandgap (E_g) of sputtered films is listed in the table.

2.3.4. Bilayer optimization

After optimizing the individual properties of both the IO:H and ZnO layers, these materials are combined into a bilayer structure to serve as the front contact in solar cells. This combination takes advantage of the high transparency and optimized electrical properties of each layer. Specifically, the bilayer is developed by first depositing the IO:H layer on glass for its excellent lateral conductivity, followed by the deposition of the ZnO layer on top to provide superior transparency and transverse conductivity.
To enhance the bilayer design, a series of annealing times is conducted on three samples. The PDA treatment is performed in ambient atmosphere at a fixed temperature of 200 °C, after the complete deposition of both the IO:H and ZnO layers. This process follows the previously optimized sputtering parameters for the IO:H and ZnO layers.
The thicknesses of the IO:H and ZnO layers for each bilayer are summarized in Table 2.3. Different ZnO thicknesses are chosen to investigate the potential influence of the formation of columnar ZnO crystallites and their subsequent impact on optoelectrical properties.

Table 2.3: IO:H and ZnO layer thicknesses [nm] in bilayer structures for the PDA time optimization.

Bilayer ID	IO:H thickness [nm]	ZnO thickness [nm]
I	113	655
II	113	587
III	113	519

Figure 2.7 illustrates how the gradual increase in annealing time results in stabilized values for both μ and N. In Bilayer III, the mobility reaches its peak with a value of 120 cm^2/Vs, and the corresponding carrier density is 1.97×10^{19} cm^{-3}. It is worth noting that Hall measurements probe effective transport parameters of the bilayer system. Despite the higher carrier concentration of IO:H, the extracted carrier density remains in the ZnO range and does not directly reflect the individual layers. In contrast, the mobility follows IO:H, suggesting that charge transport is dominated by the high-mobility layer.

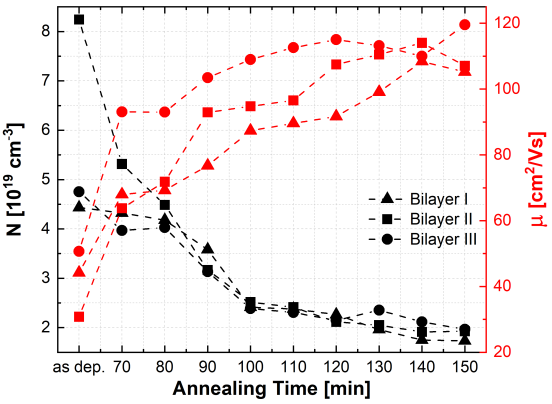

Figure 2.7: Carrier concentration (N) and mobility (μ) of bilayers as a function of annealing time. PDA is performed in ambient at 200 °C.

Furthermore, the absorptance profile of Bilayer III is examined in its as-deposited condition and after 2 h and 30 min of ambient annealing at 200 °C. Figure 2.8 demonstrates the positive influence of PDA on the reduction of parasitic absorptions in both the band-to-band and the NIR regions of the solar spectrum. Wavelengths above 1000 nm show a visible FCA reduction after the PDA treatment in agreement with the carrier density trend from Figure 2.7.
Despite the excellent optical improvements and the high mobility achieved after an annealing time of 150 min, the optimized PDA time for bilayer samples is selected to be 140 min. This choice is grounded in consistent experimental findings showing that the best optoelectrical trade-off is systematically achieved after 2 h and 20 min of PDA treatment.

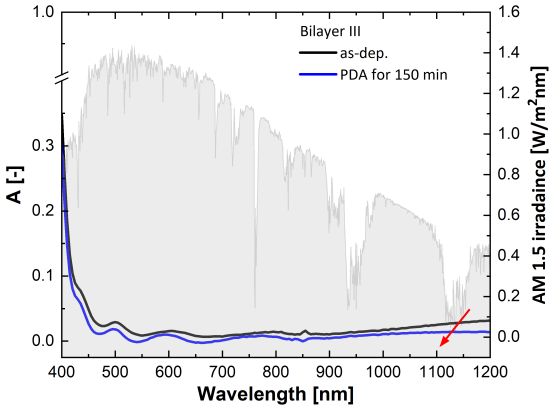

Figure 2.8: Absorptance (A) as a function of wavelength for Bilayer III (thicknesses reported in Table 2.3). The black trend represents the as-deposited condition, while the blue profile shows 150 min of ambient annealing at 200 °C.

2.3.4.1 Material properties

Scanning electron microscopy (SEM) and atomic force microscopy (AFM) are employed as techniques for the material characterization of the bilayer structure. They provide insights into the surface characteristics and support the optimization of the bilayer fabrication process.
The SEM cross section and top view images are taken to investigate the structural growth of the bilayer. IO:H exhibits a uniformly sputtered deposition on flat glass, reaching an approximate thickness of 70 nm, with crystal grains significantly smaller than those of ZnO. Above the IO:H layer, a progressive increase in grain size is observed with the growth of ZnO thickness, reaching 1.5 µm. This development results in the formation of larger grains on top of smaller ZnO grains (Figure 2.9a and Figure 2.9b).
Figure 2.9c and Figure 2.9d demonstrate how the evolution of ZnO grains contributes to a surface with nano-featured characteristics in the bilayer design. In particular, Figure 2.9d highlights the presence of filaments within a single ZnO grain, indicating the preferred growth orientation of the material.
Figure 2.10 presents both top and three-dimensional (3D) AFM views of two representative bilayer samples. Figure 2.10a and Figure 2.10b differ in the ZnO thickness, while the IO:H thickness remains approximately 100 nm in both cases. Figure 2.10a features a deposition of 500 nm of ZnO, whereas Figure 2.10b exhibits a thicker layer with 1 µm of ZnO. These images offer a visual representation of morphological variations, showing that larger grains can form as the ZnO thickness increases.

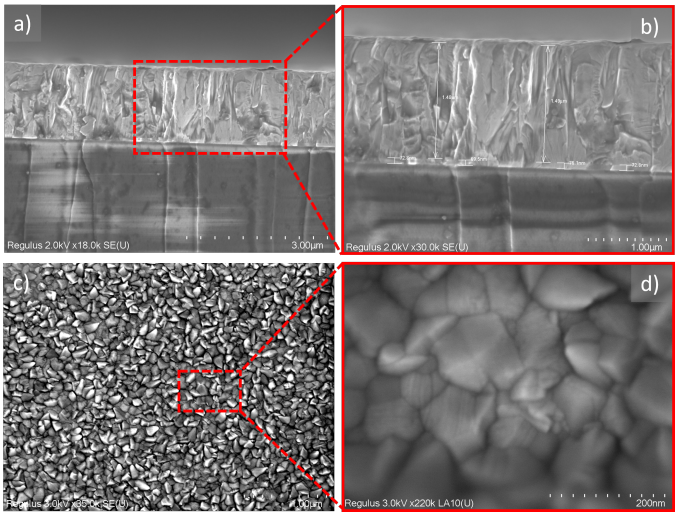

Figure 2.9: SEM cross section images (a and b) and top view images (c and d). Cross section images reveal a bilayer with 70 nm IO:H and 1.5 µm ZnO. The top view images highlight sharp nano features from ZnO.

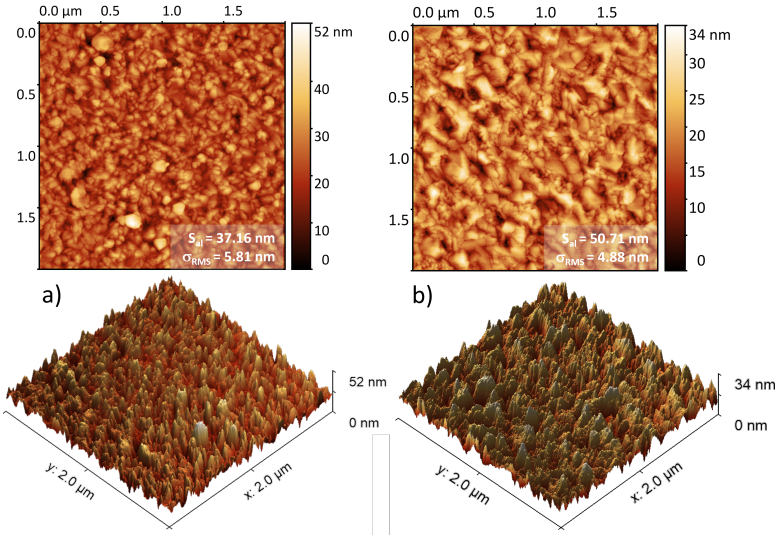

Figure 2.10: AFM top and 3D views of bilayers. (a) Bilayer with 100 nm of hydrogenated indium oxide (IO:H) and 500 nm of zinc oxide (ZnO), while (b) shows a bilayer with 100 nm of IO:H and a thicker layer of 1 µm ZnO.

Furthermore, X-ray diffraction (XRD) is utilized to probe the crystalline structure and phase composition of the transparent conductive bilayer. In this study, both IO:H and ZnO films incorporated within the bilayer design are deposited using the previously optimized sputtering parameters. The bilayer is examined under two conditions: as-deposited and following 140 min of ambient PDA treatment at 200 °C.

As depicted in Figure 2.11, notable alterations are observed in the intensity of the IO:H crystalline peaks, indicating a transition from an amorphous to a more crystalline phase. Moreover, a slight enhancement of the dominant orientation (002) of ZnO is apparent, indicating that the ZnO layer maintains its polycrystalline nature regardless of annealing. This orientation is commonly reported for ZnO films grown on various substrates, including glass [69, 70].

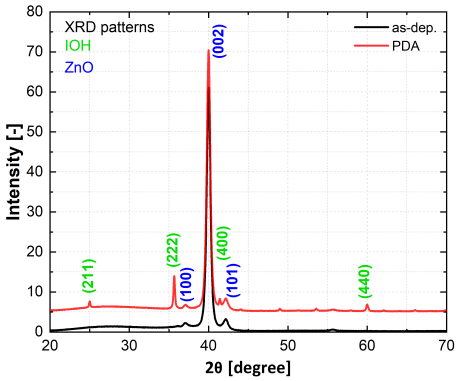

Figure 2.11: XRD results for the bilayer sample under optimized sputtering parameters, in the as-deposited state and after 2 h 20 min ambient PDA at 200 °C. Crystalline phases of IO:H and ZnO are highlighted in red and blue, respectively. Preferred orientations: (222) for IO:H and (002) for ZnO.

2.3.4.2 Scattering mechanisms

Figure 2.12 displays the Hall measurements conducted on various as-deposited and annealed IO:H and ZnO monolayers, as well as on bilayer structures incorporating IO:H and ZnO. The Hall mobility and carrier concentration measured in the bilayers represent effective values of the combined layers. These metrics are critical for assessing the performance of TCOs as front contacts in solar cells. High mobility ensures efficient lateral transport of charge carriers, reducing resistive losses, while an optimal carrier concentration balances electrical conductivity and optical transparency. The plot also illustrates the relevant scattering mechanisms limiting the Hall mobility at varying carrier concentrations.

The ZnO monolayers are deposited by varying power density and temperature settings ranging from 2.0 to 4.0 W/cm^2 and from 95 to 217 °C, respectively. All other sputtering parameters remain constant, consistent with previous sections of this study. The investigation into the influence of deposition power and temperature on mobility and carrier density yields scattered results, and there does not appear to be a clear trend indicating whether annealing improves the performance.

The challenge in probing zinc oxide as an undoped material lies in the difficulty of laterally extracting free carriers from the material. This limitation suggests that low mobility values are predominantly influenced by the presence of grain boundaries.

For IO:H, the values are illustrated based on power density variation while maintaining all other sputtering settings consistent with the analysis detailed above (refer to Figure 2.3). It is evident that the PDA treatment positively affects both mobility and carrier concentration across all IO:H samples. The findings suggest that ionized impurity scattering emerges as the predominant mechanism limiting free carrier transport. Additionally, a mobility of 71.57 cm^2/Vs is obtained at a carrier concentration of approximately 10^{20} cm^{-3} in IO:H.

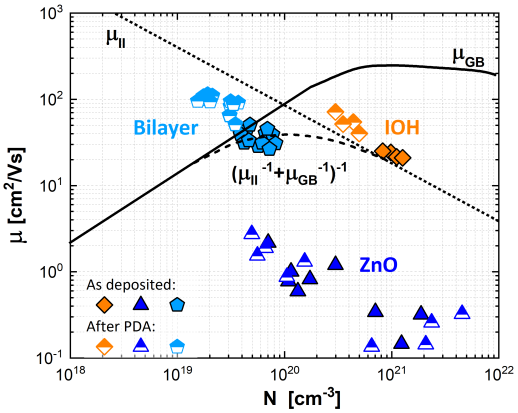

Figure 2.12: Measured Hall mobility (μ) versus carrier concentration (N) of undoped ZnO, IO:H monolayers, and IO:H/ZnO bilayers. The upper dotted line represents the ionized impurity (II) scattering limit using the Brooks–Herring–Dingle theory, accounting for non-parabolicity of the TCO conduction band. The full line shows the grain-boundary scattering mechanism for doped and undoped ZnO films. The dashed trend combines grain-boundary-limited transport with ionized impurity scattering [52, 71].

Bilayer samples are fabricated using the previously optimized settings. The thickness of IO:H is varied, while the desired thickness of ZnO is maintained at approximately 600 nm in each bilayer. For each thickness configuration, three samples are fabricated, and their mobility and carrier concentration values are presented in Figure 2.12. Table 2.4 showcases the best outcome in terms of electrical properties for each bilayer thickness configuration following PDA treatment. Additionally, the values of μ and N are also reported in the as-deposited condition to highlight the beneficial impact of ambient annealing on the samples.

Table 2.4: Hall mobility [cm^2/Vs], carrier concentration [cm^{-3}], mini-RT thickness [nm] for bilayers in as-deposited condition and after PDA treatment at 200 °C for 2 h 20 min.

$t_{IO:H}$ [nm] in bilayer	as-deposited		PDA	
	μ [cm^2/Vs]	N [10^{19} cm^{-3}]	μ [cm^2/Vs]	N [10^{19} cm^{-3}]
144	39.01	7.71	94.80	3.14
113	30.80	8.24	114.0	1.91
81	39.45	3.88	99.70	1.65
70	33.35	4.64	87.40	3.34

Figure 2.12 underlines that the mobility of as-deposited bilayers is capped by grain-boundary scattering and ionized-impurity limits ($\mu_{tot}^{-1} = \mu_{GB}^{-1} + \mu_{II}^{-1}$) [72]. In contrast, annealed bilayers exhibit a consistent trend wherein the grain-boundary scattering mechanism no longer limits mobility [73–75]. Consequently, the bilayers are nearing the ionized-impurity limit, demonstrating higher mobility values at lower carrier concentrations of approximately 10^{19} cm^{-3}. Further discussion of the optoelectrical and material properties of the TCOs, together with additional analysis relevant to the bilayer design, is provided in Appendix A.

2.3.4.3 Bilayer geometry interpretation

This section aims to explain the charge transport mechanism responsible for the enhanced optoelectrical performance observed in the IO:H/ZnO bilayer structure. The correlation between IO:H crystallization and the improvement in bilayer properties suggests that the post-deposition annealing treatment plays a crucial role in optimizing charge transport. As shown in Figure 2.11 and Figure2.12, the transition from an amorphous to a crystalline phase in IO:H, along with improved ZnO orientation, contributes to mobility enhancement.

The mobility of free charge carriers in ZnO is inherently limited by two dominant scattering mechanisms: the ionized impurity scattering (within a single grain) and the grain boundary scattering (in a polycrystalline structure) [76–78].

In a single large ZnO grain, mobility is primarily limited by ionized impurity scattering, caused by Coulomb interactions between free electrons and ionized dopants [79]. This scattering disrupts carrier motion and sets an intrinsic upper bound on mobility. The corresponding limit is described by the Brooks-Herring-Dingle model as depicted in Figure 2.12. With increased carrier density, enhanced Coulombic scattering reduces the carrier mean free path, thereby decreasing mobility [52].

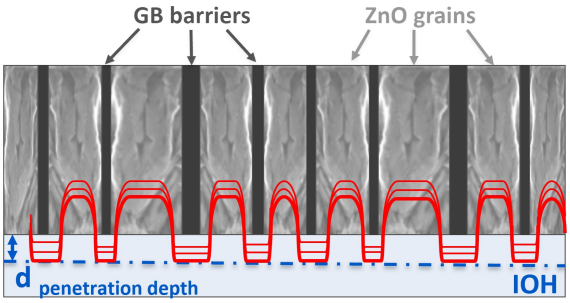

Figure 2.13: Simplified sketch illustrating the bilayer geometry and the role of the interface between IO:H and ZnO layers in facilitating free carrier transport. Undoped ZnO grains and grain boundary (GB) barriers are depicted in light and dark grey respectively. Free charge carrier transport bypassing the grain boundaries is shown in red, while the penetration depth of this transport mechanism within the IO:H layer is in blue.

In a polycrystalline ZnO film, grain boundaries further restrict mobility. Charge carriers must overcome potential barriers at grain interfaces generated by trapped states. The models of Seto and Baccarani et al. yield an effective mobility μ_{eff}, dominated by thermionic emission across grain barriers [80]:

$$\mu_{eff} = \mu_0 \exp\left(\frac{-\phi_b}{k_B T}\right) \tag{2.3}$$

where Φ_b is the barrier height at the grain boundary, T is the sample temperature, k_B the Boltzmann constant, and μ_0 the intra-grain mobility [81, 82].

The presence of grain boundaries therefore forces the free charge carriers to undergo thermionic emission or tunneling, significantly restricting lateral transport. Consequently, the charge transport in ZnO-dominated bilayers is largely transverse, as lateral mobility is constrained by grain boundary effects.

As shown in Figure 2.12, the Hall mobility in the bilayer structure is significantly higher than in a single-layer IO:H. It suggests that lateral conduction occurs preferentially at the IO:H/ZnO interface rather than within the bulk IO:H layer. This effect is directly correlated with the PDA treatment, which facilitates the crystallization of IO:H, leading to the formation of a more conductive interfacial pathway.

The band alignment between IO:H and ZnO may induce charge redistribution, forming an accumulation layer at the interface. This generates an internal electric field that enhances lateral carrier transport, reducing scattering and improving mobility [83, 84]. The effect follows a parallel-transport model in which the interface conductivity $\sigma_{interface}$ contributes significantly to the total bilayer conductivity $\sigma_{bilayer} = \sigma_{IO:H} + \sigma_{interface}$ [85].

It implies that free carrier lateral transport occurs within a certain penetration depth in the IO:H material, defined as the portion of the IO:H thickness near the interface with ZnO that allows free charge carriers to circumvent the ZnO grains. The interpretation of the free charge carrier transport in the bilayer geometry is visually explained in Figure 2.13 through ma simplified sketch..

An IO:H thickness of 70 nm may not be sufficient for bypass transport, as supported by the data in Table 2.4. Conversely, thicker IO:H material may lead to a situation where the transport of some carriers occurs within the bulk of the IO:H material rather than exclusively at the interface, resulting in a decrease in mobility and an increase in carrier density. This leads to the conclusion that bypassing free carrier transport is favorable when the thickness of the conductive layer in the bilayer structure falls within the range of the penetration depth of free electrons, which is approximately between 80 and 110 nm.

Furthermore, the effective carrier density of the bilayer ($N_{bilayer}$), measured via Hall effect, can be approximated as:

$$N_{bilayer} \approx \frac{d_{IOH,\ pen.\ depth}}{d_{IOH,\ pen.\ depth} + d_{ZnO}} N_{IOH} \tag{2.4}$$

In Equation 2.4, $d_{IO:H,pen.depth}$ refers to the portion of the IO:H thickness near the interface with ZnO through which free charge carriers bypass the ZnO grains, d_{ZnO} is the thickness of ZnO layer, and $N_{IO:H}$ is the carrier density in the IO:H layer. Notably, the experimental findings in Figure 2.12 align well with the theoretical prediction. The Hall carrier concentration in the bilayer is reduced by approximately one order of magnitude ($\sim 10^{19}\,cm^{-3}$) compared to the single-layer IO:H structure. This agreement further reinforces the validity of the proposed transport mechanism and the role of interface-driven charge conduction in the bilayer system.

2.3.5. Series resistance analysis in nc-Si:H solar cells

To evaluate both the optical and electrical properties of the bilayer concept, it is integrated as the front contact in nc-Si:H solar cells. For comparison, identical solar cells are processed with single-layer ITO or IO:H as the front contact. It is important to note that while the performance of these solar cells demonstrates the impact of the front contact layers, it does not reach record levels.

Figure 2.14 presents J-V characteristics of 0.16 cm^2 nc-Si:H solar cells, comparing the three different front contact designs under investigation. The corresponding measured electrical parameters are summarized in Table 2.5. For further details regarding the solar cell fabrication process and structural configuration, refer to Section 2.2.5.

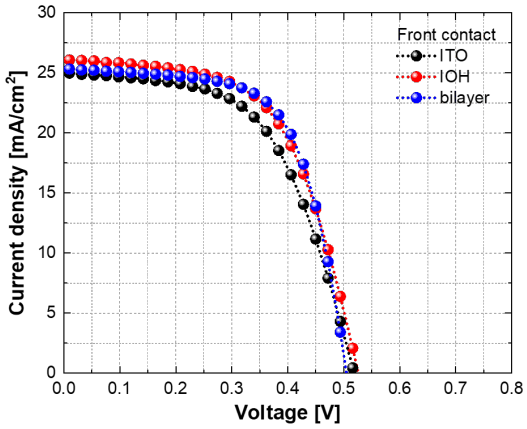

Figure 2.14: Current density-voltage (J-V) characteristics of the best nc-Si:H solar cell for each front contact configuration (ITO, IO:H, and IO:H/ZnO bilayer).

The IO:H front contact results in a slight increase in V_{oc} and a notable enhancement in J_{sc} compared to the ITO reference. In addition, an improvement in fill factor is observed, leading to an overall increase in device efficiency. This can be attributed to the enhanced optoelectrical properties of the optimized IO:H layer, as described in Section 2.3.2, which improves charge carrier collection and contact selectivity.

For the ITO monolayer, the material is selected based on the best optoelectrical trade-off observed in Figure 2.2, where the absorption coefficient versus resistivity of ITO is studied. This optimized ITO is then used as the front contact for comparison with the IO:H and bilayer structures.

Table 2.5: External electrical parameters of the best nc-Si:H solar cell for each front contact configuration (ITO, IO:H, and IO:H/ZnO bilayer). The reported short circuit current density [mA/cm^2] is based on the EQE measurements. The series resistance (R_s) and the shunt resistance (R_{sh}) are extracted from the slopes of the J-V curves near open-circuit and short-circuit conditions, respectively.

TCO	V_{oc} [V]	$J_{sc,EQE}$ [mA/cm^2]	FF [%]	η [%]	R_s [$\Omega\,cm^2$]	R_{sh} [$\Omega\,cm^2$]
ITO	0.52	23.56	56.27	6.89	23.99	1965.00
IO:H	0.53	25.22	58.25	7.79	23.65	2051.28
bilayer	0.51	23.85	64.56	7.85	9.81	2481.95

The improved fill factor and overall efficiency of the cell with the bilayer are linked to a reduction in series resistance and a slight increase in shunt resistance. The IO:H and ZnO bilayer appears to lower series resistance in solar cells by combining the high conductivity and excellent interface properties of both materials. The bilayer structure, being thicker than the IO:H or ITO single-layer front contacts, introduces an interplay between its optimized optoelectrical properties and thickness. Consequently, the thicker bilayer configuration is expected to contribute to a reduction in series resistance. This demonstrates that a bilayer configuration can decouple the optical and electrical properties of a single TCO front contact while preserving or even improving the performance of a solar cell.
Figure 2.15 shows the EQE and reflection losses of the best-performing solar cells with different front contacts. The bilayer structure exhibits reduced EQE at short wavelengths, attributed to increased parasitic absorption in the ZnO layer, which has a lower bandgap than IO:H and ITO (see Appendix A). As a result, the EQE-derived current density is higher for the IO:H front contact than for the IO:H/ZnO bilayer.

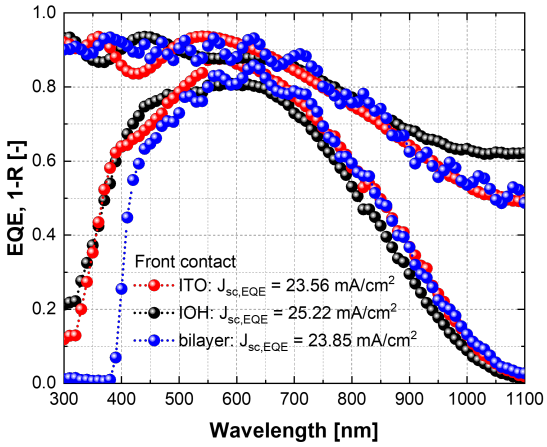

Figure 2.15: External quantum efficiency (EQE) curves of the best nc-Si:H solar cell for each front contact configuration (ITO, IO:H, and IO:H/ZnO bilayer). The plot also includes the 1-R curves, representing the front reflection losses.

Furthermore, the EQE profiles of solar cells with IO:H and the bilayer are comparable in the NIR region, with both outperforming the ITO configuration. Despite the high energy bandgap of ITO, its performance in the NIR region is limited by significantly higher free carrier absorption.
The reflection losses, as observed in the 1-R curves, reveal distinct interference patterns for the various front contact configurations. The blue trend, corresponding to the solar cell with the thick bilayer as the front contact, exhibits clear interference effects across the wavelength range due to its increased thickness. In contrast, the red and black trends, representing the thinner IO:H and ITO front contacts, show pronounced interference primarily at shorter wavelengths. Notably, the IO:H fringe limits the blue response of the IO:H-based cell. Optimizing the interaction between the TCO layers and the textured substrate could further reduce these optical interference effects.

2.4. Conclusions

This study demonstrates the significant advancements achieved by employing a bilayer front contact design in thin-film Si-based solar cells, specifically utilizing hydrogenated indium oxide (IO:H) and non-intentionally doped zinc oxide (ZnO). Through meticulous optimization of deposition parameters and post-deposition annealing (PDA) conditions, this study effectively enhances the optoelectrical performance of transparent conductive oxides (TCOs).

The resulting bilayer structure, featuring IO:H for its exceptional conductivity and ZnO for its minimal parasitic absorption in the near-infrared region, delivers superior optoelectrical properties, achieving a mobility of 120 cm^2/Vs and a carrier density of 1.97×10^{19} cm^{-3}. Incorporating this bilayer structure as the front electrode in hydrogenated nanocrystalline silicon (nc-Si:H) solar cells demonstrates its practical effectiveness.

The differences compared to other front contact designs are relatively modest, and no record-breaking efficiencies are achieved. However, the true value of the bilayer approach lies in the enhanced design flexibility it offers. Rather than relying on a single TCO to simultaneously balance high conductivity and optical transparency, the bilayer configuration enables the decoupling of these optoelectrical properties between two TCO layers. Each TCO is optimized for a specific function: one for high conductivity (e.g., IO:H) and one for minimal free carrier absorption (e.g., ZnO).

Moreover, the interaction at the interface between the two layers offers distinct advantages for optimizing solar cell performance beyond what could be achieved by simply averaging the properties of the individual layers. Notable effects, such as improved lateral carrier transport and reduced recombination at the interface, can significantly contribute to the overall performance.

Future work should focus on optimizing the thickness of the conductive and transparent layers in the bilayer structure, as well as carefully controlling the annealing process to enhance crystallization. These refinements could further improve optoelectrical performance and lead to greater efficiency gains. Additionally, exploring indium-free TCO alternatives for the bilayer concept offers a promising path to reduce reliance on the scarce indium material. Using more abundant materials could enhance the scalability of the bilayer approach in solar cell technologies.

To conclude, the bilayer approach opens new possibilities for designing TCOs in thin-film solar cells, providing a flexible and potentially more effective pathway to improving the performance of solar cell technologies.

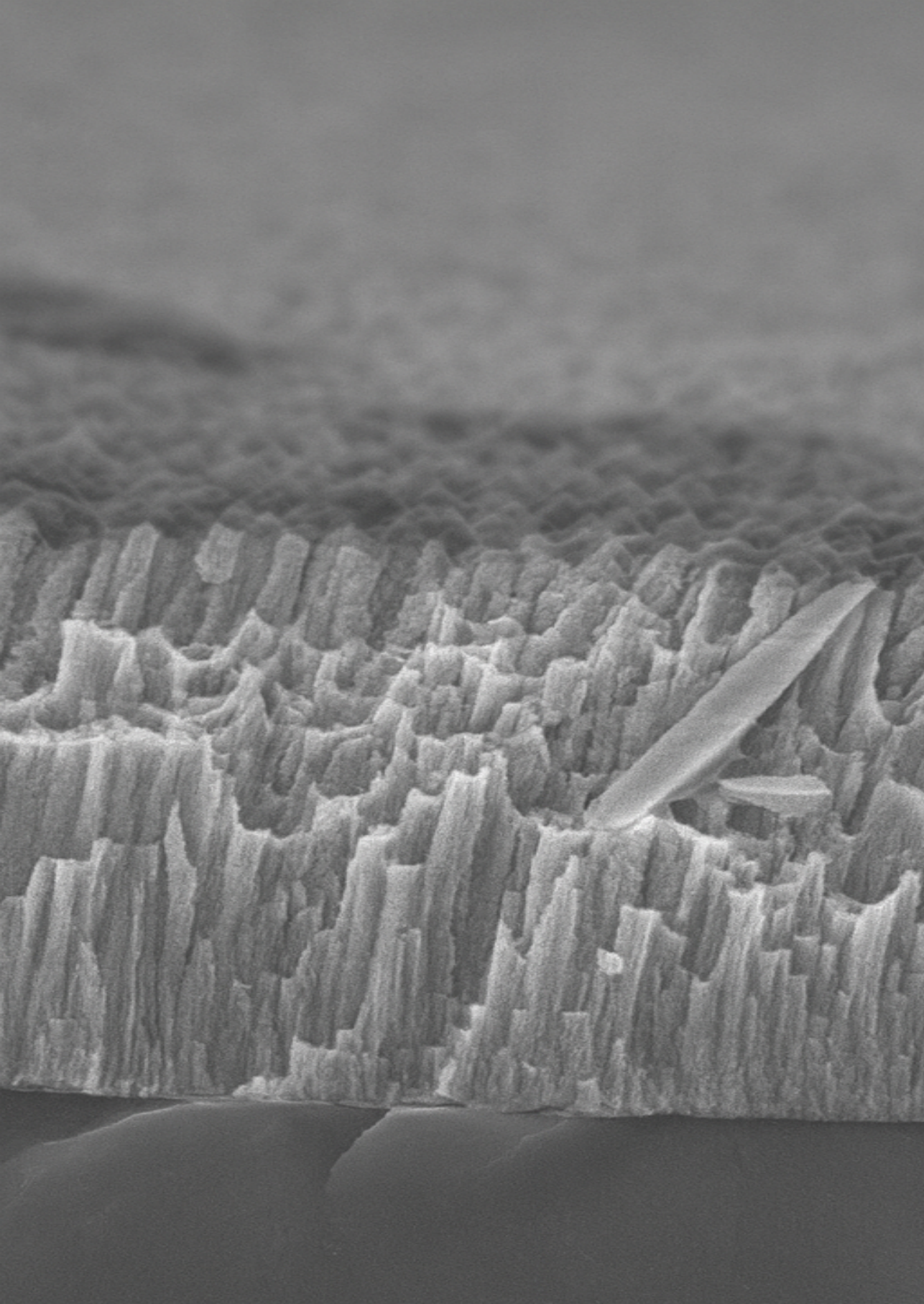

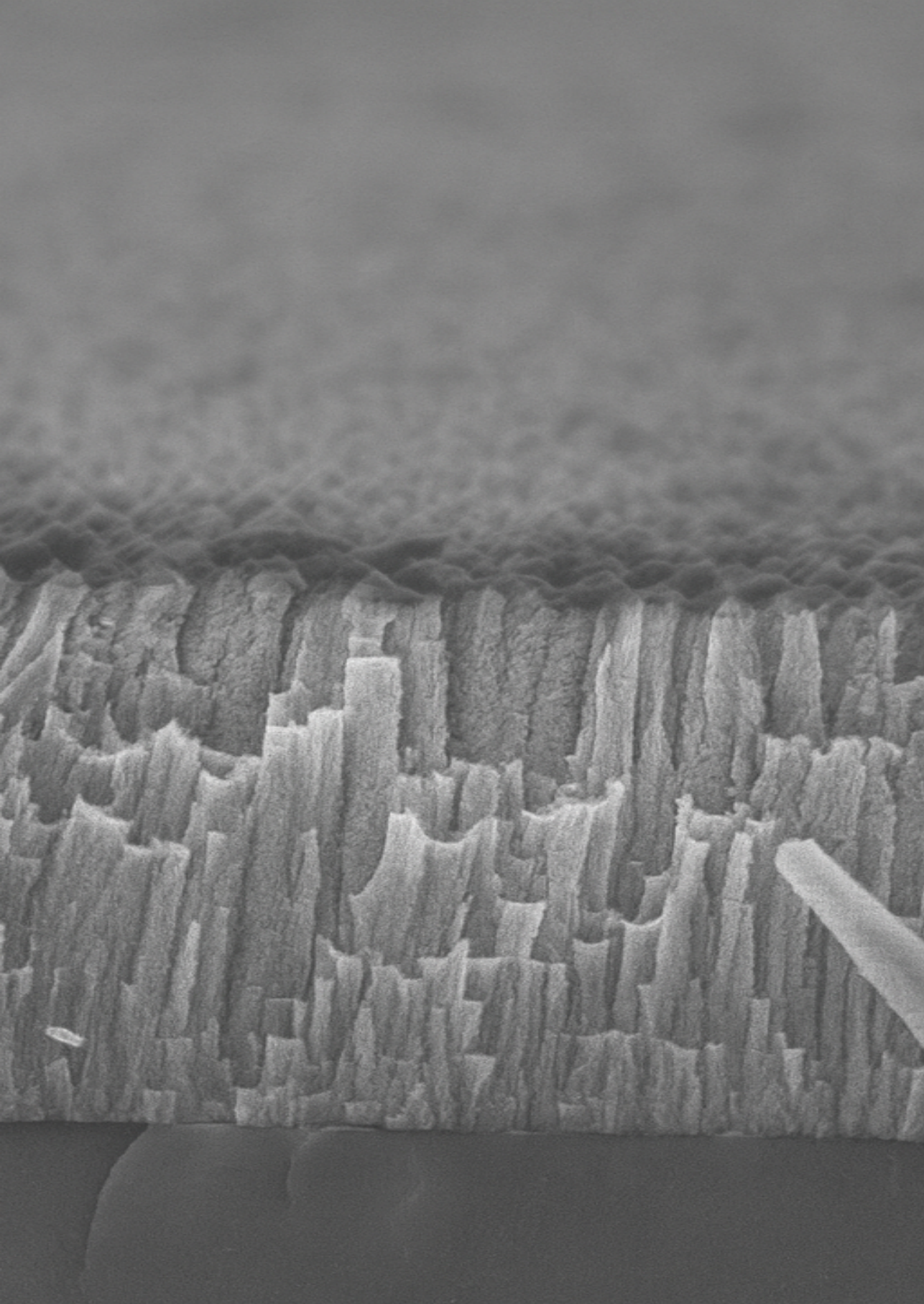

3

INDIUM-FREE TCO ALTERNATIVES

This chapter is based on the following publication:

Saitta, F., Padmakumar, G., Perez-Rodriguez, P., Wilson, A., Gonugunta, P., Anusuyadevi, P. R., Santbergen, R., & Smets, A. H. M. *Room-Temperature Sputtered SnO_2-Based Thin Films as Earth-Abundant Transparent Conductive Oxides for Photovoltaic Applications*. ACS Applied Electronic Materials, 7(20), 9489–9504 (2025), https://doi.org/10.1021/acsaelm.5c01650.

3.1. Introduction

Transparent conducting oxides (TCOs) are critical components in modern optoelectronic devices due to their unique combination of high optical transmittance and electrical conductivity. Indium tin oxide (ITO) remains the benchmark due to its optimal trade-off between optical and electrical performance. However, its reliance on scarce and costly indium, along with sustainability concerns, motivates the search for earth-abundant, indium-free alternatives [86]. Among these, tin-based compounds such as undoped tin dioxide (SnO_2) and fluorine-doped tin oxide (SnO_2:F or FTO) have attracted growing interest as promising candidates to replace ITO in these technologies [26, 27].

Fluorine-doped tin oxide is widely employed in industry when deposited at elevated temperatures (~ 500 °C), typically via atmospheric pressure chemical vapor deposition (APCVD), as exemplified by commercially available Asahi glass substrates [87]. This choice is primarily driven by the excellent crystallinity and superior carrier transport properties of FTO, which are crucial for photovoltaic and other optoelectronic applications [88, 89]. However, such high temperature processes are incompatible with many emerging applications that require temperature-sensitive substrates, such as flexible photovoltaics (e.g., on PEN or PET), tandem solar cells, and roll-to-roll and printing-based manufacturing [90, 91].

Room temperature (RT) sputtering offers a low thermal budget route to TCOs with large-area uniformity and scalability. RT sputtered SnO_2 has been employed as an electron transport layer (ETL) in perovskite solar cells, delivering efficiencies above 17% with extended operational lifetimes and compatibility with flexible substrates [92, 93]. This approach also enables sequential layer-by-layer processing, essential for tandem architectures where sub-cells are fabricated under strict thermal constraints [94]. Moreover, amorphous SnO_2 deposited at RT has improved electrical contact properties in indium-free silicon heterojunction (SHJ) solar cells without sacrificing efficiency [95, 96].

Although RT deposition of SnO_2 films offers significant advantages for flexible and temperature-sensitive device integration, it typically results in films with limited crystallinity, incomplete dopant activation, and suboptimal electrical performance. Therefore, the post-deposition annealing (PDA) treatments at moderate temperatures have proven effective in improving the structural and electronic properties of RT- deposited films without exceeding the thermal budgets of sensitive substrates or adjacent layers [97–99]. Furthermore, annealing in reducing atmospheres can further optimize carrier transport and electrical performance of SnO_2 thin films [100].

While achieving high optoelectrical performance in RT- deposited SnO_2 and FTO remains challenging, the potential of sputtering gas composition to tailor these properties has not been sufficiently explored for photovoltaic applications. In particular, the combined effects of oxygen, critical for stoichiometry and bandgap control, and hydrogen, known to influence carrier concentration, defect chemistry, and passivation, have not been systematically studied in SnO_2-based films under RT sputtering conditions [101–104].

To address this gap in understanding, this study investigates the effect of varying oxygen and hydrogen gas ratios during sputtering on the optoelectrical properties of RT-deposited SnO_2-based films. A post-deposition thermal treatment at 400 °C in nitrogen is applied to assess whether optimized gas-phase deposition conditions can reproduce, in part or in full, the optoelectrical improvements typically obtained through annealing.

This investigation therefore focuses on key optoelectrical metrics relevant to the integration of TCOs in photovoltaic devices, specifically as front electrodes or electron transport layers, including optical transmittance, bandgap energy, carrier density, mobility, and sheet resistance. By correlating these properties with compositional and structural analyses, this work evaluates whether optimized RT-deposited films can approach the performance of their commercial high temperature SnO_2-based counterparts, offering a pathway toward scalable, cost-effective, and thermally compatible solutions for next generation photovoltaic technologies.

3.2. Experimental procedure

This section describes the preparation and characterization of FTO and SnO_2 thin films. Section Section 3.2.1 details the deposition parameters and gas environments used during the RF magnetron sputtering of the films. Section 3.2.2 explains the post-deposition annealing process. Section 3.2.3 presents the optical and electrical characterization methods, and Section 3.2.4 focuses on structural and compositional material analyses.

3.2.1. Film deposition

Fluorine-doped tin oxide (FTO) and undoped tin oxide (SnO_2) thin films are deposited onto Corning Eagle 2000 glass substrates using the radio frequency (RF, 13.56 MHz) magnetron sputtering technique. The substrates, which have dimensions of 10 cm × 2.5 cm × 0.7 mm, are subjected to ultrasonic cleaning in acetone and isopropyl alcohol for 10 min each to remove contaminants before deposition.

Ceramic targets supplied by Process Materials Inc. are utilized in the deposition process, including a SnO_2 target of 99.99% purity for SnO_2 films and a target of 98 wt% SnO_2 with 2 wt% SnF_2, also at 99.99% purity, for FTO films. The sputtering process occurs at room temperature, with a substrate temperature of approximately 19 °C, in a high-vacuum chamber with a base pressure of 1×10^{-6} mbar. Prior to deposition, a 5 min presputtering step is performed to clean the target surface.

Two distinct batches of experiments are conducted to investigate the effect of reactive gas composition on film properties. In the first batch, the oxygen-to-argon (O_2/Ar) ratio is varied from 0% to 0.4% for FTO films and from 0% to 1% for SnO_2 films, with 0% O_2/Ar corresponding to sputtering in a pure argon atmosphere. In the second batch, the O_2/Ar ratio is fixed at 1% for both materials, while the hydrogen-to-argon (H_2/Ar) ratio is varied from 0% to 0.6%. Here, 0% H_2/Ar refers to the baseline oxygen condition (1% O_2/Ar) with no hydrogen added.

All films are deposited at a constant working pressure of 6×10^{-3} mbar. The total gas flow rate remains constant at 50 sccm, using pure argon along with controlled mixtures of oxygen (up to 1% O_2 in Ar) and hydrogen (up to 0.6% H_2 in Ar). All films are deposited at a rate of 0.04 nm/s using an RF power density at 0.8 W/cm^2.

3.2.2. Post-deposition annealing

Following deposition, the films undergo post-deposition annealing to assess its effect on their optoelectrical properties. Annealing is carried out at 400 °C for 20 min in a pure nitrogen (N_2) atmosphere using a Solaris rapid thermal processing (RTP) system, which provides rapid heating and cooling with precise temperature control and a heating rate of 10 °C/s.

3.2.3. Optical and electrical characterization

The transmittance (T) and reflectance (R) spectra of the deposited films are measured using a PerkinElmer Lambda 1050 spectrophotometer. The characterization is conducted over the spectral range of 300–1200 nm, covering the relevant portion of the solar spectrum where efficient light transmission is essential for FTO and SnO_2 in their role as front electrodes in solar cell applications.

The optical bandgap energy (E_g) is extracted using the Tauc plot method [105]. The absorption coefficient (α) is first calculated from transmittance and reflectance data using the following relation, where t is the film thickness:

$$\alpha(\lambda) = \frac{1}{t} \ln\left(\frac{100 - R_{\%}(\lambda)}{T_{\%}(\lambda)}\right) \tag{3.1}$$

For direct bandgap materials such as SnO_2 and FTO, the optical bandgap (E_g) is determined by plotting $(\alpha h\nu)^2$ against photon energy ($h\nu$), following:

$$(\alpha h\nu)^2 = A(h\nu - E_g) \tag{3.2}$$

where A is a proportionality constant and $h\nu$ represents the photon energy. The bandgap value is determined by extending the linear portion of the curve to the energy axis, corresponding to zero absorption. Additional details are provided in Appendix B.

To complement the bandgap analysis and gain insight into defect-related states, the absorption edge is further examined using the Urbach rule. In this model, the absorption coefficient follows an exponential dependence on photon energy in the sub-bandgap region:

$$\alpha(h\nu) = \alpha_0 \exp(h\nu / E_U) \tag{3.3}$$

where α_0 is a constant and E_U is the Urbach energy [106]. This parameter quantifies the width of the exponential tail, which reflects structural disorder and the presence of localized states within the bandgap [107, 108]. Values of E_U are obtained from the slope of $\ln(\alpha)$ versus photon energy in the low-energy region. Further details are provided in Appendix B.

The film thickness is determined using a Steag ETA-Optik mini-RT setup. In mini-RT measurements, R and T spectra are recorded and processed through Scout software to estimate the sample thickness.

The sheet resistance (R_{sheet}) is measured using the four-point probe (4PP) method with an AIT CMT-SR2000N measurement system. In this configuration, four equidistant probes are arranged in a linear geometry to ensure consistent and accurate readings.

The resistivity (ρ) is measured using an HMS-5000 Hall Effect measurement system via the van der Pauw method. The carrier density (N) and mobility (μ) are derived from Hall effect measurements at room temperature. The magnetic flux density is set to 0.55 T, and the input current is 10 mA. The probes are arranged in a square configuration with approximately 1 cm spacing, ensuring uniform geometry for accurate measurements. The sample thickness is determined beforehand using the mini-RT setup.

3.2.3.1 Hall effect measurement

Hall effect measurements on SnO_2-based materials, including fluorine-doped tin oxide (FTO), present inherent challenges, particularly when evaluating intrinsic or near-intrinsic films. In undoped SnO_2,the conduction arises primarily from thermally excited carriers or native defects, leading to mixed conduction [109, 110]. In this regime, both electrons and holes contribute to transport, and the Hall coefficient R_H is governed by their respective concentrations and mobilities [111]:

$$R_H = \frac{p\,\mu_h^2 - n\,\mu_e^2}{q\,(n\mu_e + p\mu_h)^2} \tag{3.4}$$

where p and μ_h are the hole concentration and mobility, n and μ_e are the electron concentration and mobility, q is the elementary charge.
The equation can be simplified for intrinsic materials ($n \approx p$) as:

$$R_H = \frac{\mu_h^2 - \mu_e^2}{q\,n(\mu_e + \mu_h)^2} \tag{3.5}$$

This highlights that the sign and magnitude of the Hall coefficient reflect not just carrier type but also relative mobilities. It means that intrinsic SnO_2-based films can appear as n-type due to the higher mobility of electrons or as p-type due to the higher mobility of holes.
Note the excitation current is set to 10 mA in this study. Although lower excitation currents (< 1 mA) are commonly used for high resistivity materials to limit Joule heating, a higher current is employed in this study to improve the signal-to-noise ratio and enable the reliable detection of Hall voltages. To ensure comparability across all samples, the measurement configuration, including current, magnetic field strength, and contact geometry, is kept constant. This consistency is critical when evaluating carrier concentration and mobility across SnO_2-based and other transparent conducting oxide films.
Each Hall measurement is repeated five times, and the reported carrier concentrations and mobilities represent average values. The standard deviation from these repetitions is reported as the measurement uncertainty. In this study, both positive and negative Hall coefficients are observed across different samples. However, for each individual sample, the sign of the Hall voltage remained consistent across all five measurements (see Appendix B).

3.2.3.2 Optoelectrical metrics

The optoelectrical characterization of SnO_2-based films is guided by their intended function as either front electrodes or electron transport layers in solar cell applications [112, 113]. The selected metrics provide a comprehensive understanding of the trade-offs between optical transparency and electrical conductivity.
For front-contact applications, high optical transmittance across the solar spectrum is essential to maximize photon flux reaching the active layer of solar devices. Minimal reflectance and a wide bandgap help suppress parasitic absorption in the ultraviolet (UV) and visible region, particularly in the blue portion of the spectrum where band-to-band absorption may occur. However, according to the Drude model increased carrier concentration enhances free carrier absorption (FCA) in the near-infrared (NIR) region, which can degrade optical transparency in

this range [114]. Therefore, while a certain level of doping is necessary to improve conductivity, excessive carrier density leads to undesirable absorption losses.
Electrically, the TCO must exhibit low sheet resistance to enable efficient lateral charge transport toward metal contacts when functioning as a front electrode or from the perovskite absorber to the electrode when serving as an ETL. Achieving high Hall mobility is also crucial: it facilitates effective carrier transport and mitigates FCA by reducing carrier scattering.

3.2.4. Structural and compositional characterization

To support and explain trends observed in the optoelectrical properties of the SnO_2-based films, a comprehensive material characterization is conducted, focusing on the bulk composition, crystallinity, and surface chemistry.
Energy dispersive X-ray spectroscopy (EDX) is employed to confirm the presence and relative atomic percentages of Sn, O, and F in the bulk of the films. The measurements are carried out on samples deposited on (100)-oriented silicon wafers to minimize substrate interference, using a Nova NanoSEM 650 instrument equipped with an integrated EDX detector operating at 15 kV. Quantification is performed using the eZAF Smart Quant algorithm, and the atomic percentages along with relative uncertainties are reported in in Appendix B.
X-ray photoelectron spectroscopy (XPS) is performed to analyze the surface chemistry and oxidation states of the constituent elements. Measurements are carried out using a PHI 5400 ESCA system (Physical Electronics, Inc.) equipped with a non monochromatic Al Kα X-ray source ($h\nu$ = 1486.7 eV), operating at 200 W with an accelerating voltage of 13.5 kV. The takeoff angle is fixed at 45° for both survey and high-resolution scans. Each measurement covers a circular analysis area that is 0.4 mm in diameter with an effective sampling depth of approximately 3–5 nm. All XPS spectral processing is performed using MultiPak version 8.0 (Physical Electronics, Inc.). A Shirley-type background subtraction is applied to curve fitting. For the analysis of high-resolution XPS data, the charge neutralization is performed by referencing the C–C peak of the C 1s spectrum at 284.4 eV prior to curve fitting. The extended data of XPS analysis are provided in Appendix B.
The crystalline structure of the films is analyzed using X-ray diffraction (XRD). Diffraction patterns are acquired with a Bruker D8 Advance diffractometer configured in Bragg–Brentano geometry, using Cu Kα radiation (λ = 1.5406 Å). The X-ray tube operates with a standard focus, providing sufficient intensity for high-resolution phase identification.
The surface and cross-sectional morphologies of the films are investigated using field-emission scanning electron microscopy (FE-SEM). A Hitachi Regulus 8230 system is used to obtain high resolution images and evaluate surface texture, film growth, and structure. SEM images are included in Appendix B.

3.3. Results and discussion

The study first examines the optoelectronic properties of FTO and SnO_2 films. The effects of varying the O_2/Ar and H_2/Ar ratios are analyzed in Section 3.3.1.1 and Section 3.3.1.2, respectively. In Section 3.3.2, the material properties are studied through energy dispersive X-ray spectroscopy (EDX), X-ray photoelectron spectroscopy (XPS), and X-ray diffraction (XRD). The role of post-deposition annealing (PDA) is also evaluated, and all measurements are performed on approximately 200 nm thick films.

3.3.1. Optoelectrical properties

3.3.1.1 Oxygen series

To assess the impact of oxygen on the optoelectrical properties of FTO and SnO_2 films, the sheet resistance is used as a key metric due to its direct relation to electrical conductivity in transparent electrodes. In photovoltaic devices, the sheet resistance of the TCO contributes to the series resistance (R_s), affecting lateral charge transport. A high R_{sheet} leads to resistive losses during current extraction, reducing the fill factor and overall power output. Therefore, minimizing R_{sheet} is essential for efficient charge collection.

Figure 3.1 shows the sheet resistance trends of both FTO and SnO_2 films as a function of increasing O_2/Ar ratio in the sputtering atmosphere. For the 0% O_2/Ar condition, the films are deposited in a pure argon environment, serving as the baseline reference.

In FTO (Figure 3.1a), the sheet resistance follows a U-shaped trend, reaching its minimum value of 468 Ω/sq at 0.3% O_2/Ar, before increasing sharply at an O_2/Ar ratio ≥ 0.4%. Oxygen levels between 0.4% and 1% O_2/Ar result in R_{sheet} values exceeding 10^7 Ω/sq, which are far above the threshold relevant for low thermal budget solar cell applications. These conditions are therefore excluded from the investigation.

For the SnO_2 films (Figure 3.1b), the O_2/Ar ratio is extended to 1%, corresponding to the upper limit of the sputtering system. The R_{sheet} exhibits an exponential-like increase with increasing oxygen content, indicating a continuous degradation in electrical conductivity across the investigated range. The minimum R_{sheet} value of 610 Ω/sq is achieved at 1% O_2/Ar after thermal treatment.

Overall, the post-deposition annealing induces a consistent downward shift in sheet resistance toward approximately 10^3 Ω/sq for both materials, even when the oxygen content initially causes a significant reduction in conductivity.

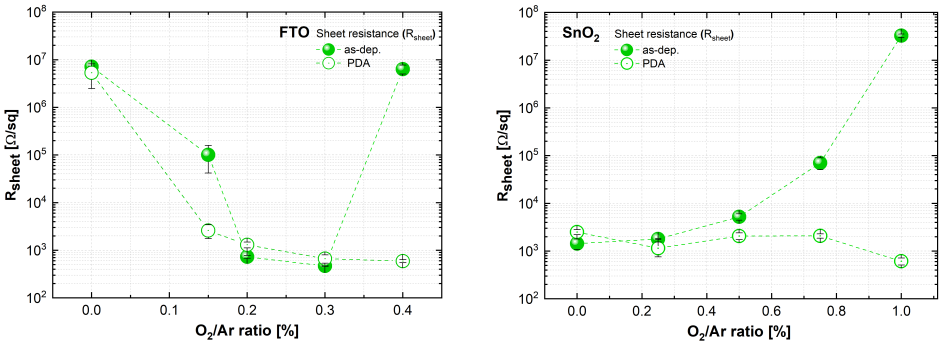

a) b)

Figure 3.1: Sheet resistance trends of (a) FTO and (b) SnO_2 films (~ 200 nm thick) as a function of O_2/Ar ratio.

Figure 3.2 illustrates the evolution of μ and N in the FTO and SnO_2 films as a function of the O_2/Ar ratio under both as-deposited and PDA conditions. A general trend is observed where increasing oxygen content in the sputtering atmosphere leads to higher mobility and lower carrier density in both as-deposited and PDA states.
In the FTO films (Figure 3.2a and Figure 3.2c), the highest mobility (13.73 $cm^2/V\,s$) and lowest carrier density (2.25×10^{19} cm^{-3}) are achieved at 0.4% O_2/Ar in the as-deposited films. In comparison, the SnO_2 films (Figure 3.2b and Figure 3.2d) exhibit slightly better values, with the highest mobility (15.34 $cm^2/V\,s$) and lowest carrier density (1.10×10^{19} cm^{-3}) obtained at 1% O_2/Ar.
Hall measurements revealed both positive and negative Hall coefficients in the FTO and SnO_2 films, suggesting apparent ambipolar behavior. As Hall analysis in mixed-conduction systems is inherently ambiguous, the conduction type cannot be determined conclusively. The discussion therefore focuses on relative trends rather than absolute values. Further details on the measurement procedure are provided in Section 3.2.3.1. Discussion of the ambipolar behavior is given in Section 3.3.1.3, and complete N values are listed in Appendix B.

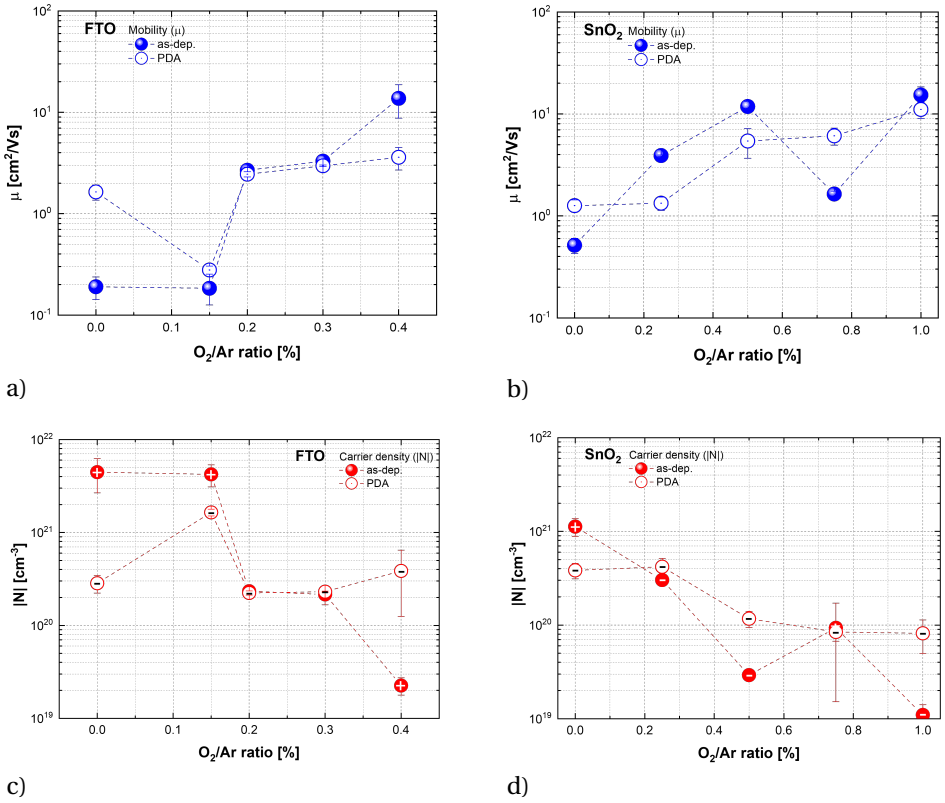

Figure 3.2: Carrier mobility (μ) and density (N) of (a, c) FTO and (b, d) SnO_2 films (~ 200 nm thick) as a function of the O_2/Ar ratio in as-deposited (as-dep.) and post-deposition annealed (PDA) conditions. The carrier density sign is reported on the red dots.

Despite the high Hall mobility and low carrier concentration at 0.4% O_2/Ar, the four-point probe measured sheet resistance is comparatively high. This difference arises because Hall and four-point probe measurements independently assess the carrier transport and overall resistance, respectively. Thus, favorable Hall parameters do not always correspond to low sheet resistance, highlighting the need to report both for a complete electrical characterization [115–117].

The values reported here are in good agreement with those of previous studies on TCO films deposited at or near room temperature. Banyamin et al. [118] reported mobility values around 15 cm^2/ V s for FTO films deposited via low temperature sputtering (~ 170 °C). Similarly, Kam et al. [119] demonstrated that SnO_2 films deposited at room temperature by RF sputtering can achieve μ and N values that make them suitable for use as electron transport layers in optoelectronic devices.

Furthermore, the optical bandgap of the FTO and SnO_2 films is analyzed as a function of oxygen content and post-deposition annealing in Figure 3.3. The E_g values are determined from Tauc plots and details are provided in Appendix B.

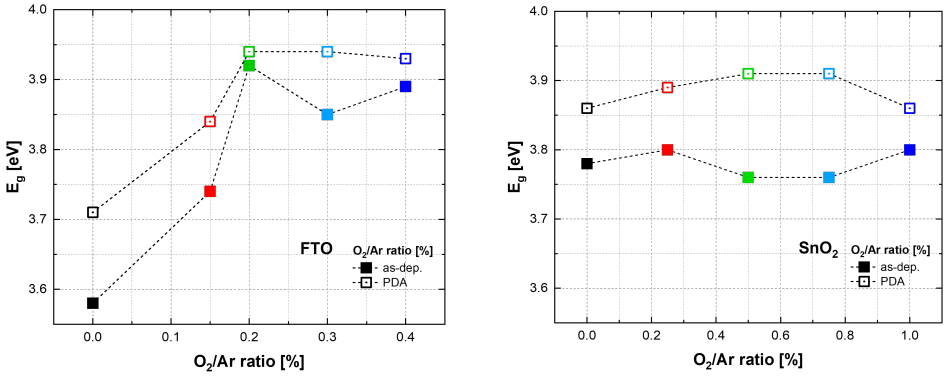

Figure 3.3: Optical bandgap (E_g) of (a) FTO and (b) SnO_2 films (~ 200 nm thick) as a function of the O_2/Ar ratio in as-deposited (as-dep.) and post-deposition annealed (PDA) conditions.

In the FTO films (Figure 3.3a), the optical bandgap generally exhibits an increasing trend with increasing O_2/Ar ratio in the sputtering atmosphere. The highest values are observed at 0.2% O_2/Ar, reaching 3.92 eV in the as-deposited condition and 3.95 eV after PDA. This behavior is consistent with previous reports, where oxygen incorporation during RT sputtering is found to enhance transparency and shift the absorption edge toward higher photon energies [120].

The SnO_2 films (Figure 3.3b) exhibit a more stable bandgap across O_2/Ar ratios. The as-deposited films show a nearly constant bandgap in the range of 3.76–3.80 eV. After the PDA treatment, the greatest E_g shifts are observed at 0.5% and 0.75% O_2/Ar, with values rising from 3.76 to 3.91 eV. These results are comparable to literature reports of RT sputtered or annealed SnO_2 thin films, where bandgaps in the range of ~ 3.7–4.0 eV are commonly observed [93, 121].

In transparent conductive oxides, bandgap widening can result from two opposing effects. The Burstein–Moss shift causes an apparent increase in E_g as conduction band states are

filled by free carriers, while bandgap renormalization leads to a slight narrowing due to carrier interactions [53]. However, the Hall measurements of FTO and SnO_2 (Figure 3.2) generally show a decreasing carrier density with an increasing O_2/Ar ratio. Therefore, the observed bandgap changes are more likely attributed to reduced defect density and improved structural ordering, rather than band-filling effects.

Figure 3.4 presents the transmittance and reflectance spectra of the samples exhibiting the lowest band-to-band absorption, with films deposited in pure argon being used as the reference. For clarity, only FTO films deposited with 0% and 0.2% O_2/Ar (Figure 3.4a) and SnO_2 films deposited with 0% and 0.5% O_2/Ar (Figure 3.4b) are presented. Full T and R spectra for all investigated O_2/Ar ratios are available in Appendix B.

The introduction of oxygen into the sputtering gas results in a marked improvement in transmittance, as indicated by the red arrow pointing from the pure argon condition toward increasing O_2 content in the gas phase. This enhancement is attributed to reduced sub-bandgap absorption, which shifts the absorption edge toward the ultraviolet region [118]. In contrast, the film sputtered in pure argon exhibits a brownish appearance, consistent with an optical cutoff near 300 nm and more absorptive films.

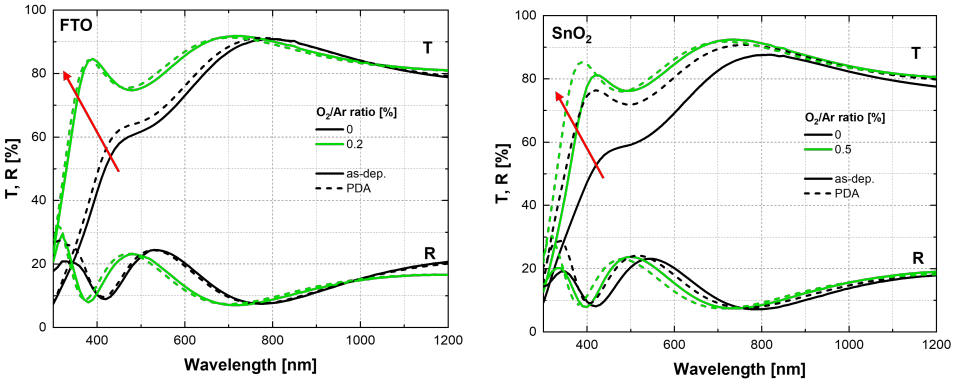

a) b)

Figure 3.4: Transmittance (T) and reflectance (R) spectra of (a) FTO and (b) SnO_2 films (~ 200 nm thick) in as-deposited (as-dep.) and post-deposition annealed (PDA) states. The films are sputtered in oxygen-deficient and oxygen-containing atmospheres.

The fringe shifts in the reflectance spectra of Figure 3.4a and Figure 3.4b likely result from small variations in film thickness rather than changes in the refractive index or density, caused by slight deviations in the deposition rate or uniformity. Although the average reflectance of standalone SnO_2/glass samples remains below 20%, this does not represent device-level behavior. For example, in solar devices in the superstrate configuration, where light enters through the glass substrate before reaching the absorber, reflectance losses are strongly reduced by light management strategies such as antireflective coatings or textured interfaces [122].

For the FTO films (Figure 3.4a), PDA induces only minor changes in both transmittance and reflectance. Meanwhile, the SnO_2 films (Figure 3.4b) show a more pronounced improvement in transmittance after thermal treatment regardless of the presence of oxygen during deposition.

3.3.1.2 Hydrogen series

The hydrogen study is performed at a fixed O_2/Ar ratio of 1%. This approach ensures a consistent and direct comparison between FTO and SnO_2 films, allowing the influence of hydrogen to be isolated from that of oxygen. By maintaining a constant oxygen background, we can more reliably attribute changes in optical and electrical behavior to hydrogen introduced into the sputtering atmosphere. Lower oxygen conditions combined with hydrogen could not be electrically characterized due to sheet resistance values exceeding the measurable range, making 1% O_2/Ar the lowest viable condition for meaningful optoelectrical analysis.

The optical analysis is focused on the evolution of the optical bandgap, as shown in Figure 3.5. The E_g values are extracted using Tauc plots, as described in Section 3.2.3, with additional details on the calculation provided in Appendix B. The as-deposited FTO films exhibit a narrow bandgap range between 3.87 and 3.91 eV, with PDA inducing only minor changes (Figure 3.5a). For SnO_2, the optical bandgap widens with increasing H_2/Ar ratio, reaching 3.88 eV at 0.4% H_2/Ar in the as-deposited state (Figure 3.5b). Following thermal treatment, the FTO bandgap undergoes a slight widening, peaking at 3.92 eV for 0.2% H_2/Ar. The observed E_g values in hydrogen-containing atmosphere are consistent with previous reports on FTO and SnO_2 films sputtered at room temperature or under low-range thermal conditions (150 °C) [120, 123].

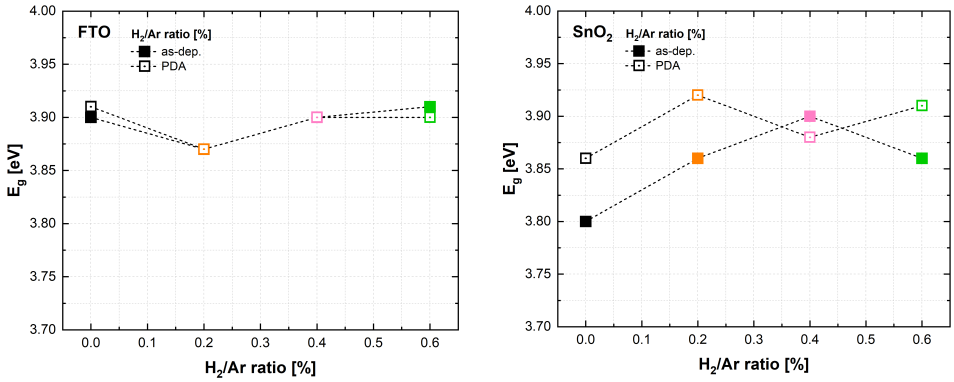

a) b)

Figure 3.5: Optical bandgap (E_g) of (a) FTO and (b) SnO_2 films (~ 200 nm thick) as a function of the H_2/Ar ratio in as-deposited (as-dep.) and post-deposition annealed (PDA) states. The oxygen content is fixed at 1% O_2/Ar.

Figure 3.6 presents the transmittance and reflectance spectra for both materials under 0% and 0.4% H_2/Ar conditions. The T and R spectra for other H_2/Ar ratios are provided in Appendix B. In Figure 3.6a, hydrogen introduction during sputtering leads to a slight decrease in transmittance and a corresponding increase in reflectance, particularly between 400 and 600 nm. The post-deposition annealing induces no significant changes in either trend, indicating a limited optical response to hydrogen in FTO films. This behavior is consistent with previous findings, which show that hydrogen addition to an O_2/Ar sputtering atmosphere does not significantly alter the bandgap energy or optical transparency [124].

In Figure 3.6b, the transmittance increases from 0% to 0.4% H_2/Ar, as indicated by the blue arrow. Notably, none of the SnO_2 films deposited in the O_2/Ar atmospheres achieve transmittance values as high as those observed for the 0.4% H_2/Ar sample, which reach an average of

approximately 87% across the visible range of the solar spectrum (400–800 nm). However, at higher hydrogen content (0.6% H_2/Ar), a pronounced reduction in transmittance is observed, as shown in Appendix B.

Furthermore, hydrogen-containing atmosphere has been reported to influence localized defect states within the bandgap, affecting sub-bandgap absorption [124]. To probe these states, the absorption behavior of FTO and SnO_2 films is analyzed using the Urbach rule (see Appendix B).

For FTO, the Urbach energy slightly decreases from 350 meV (0% H_2/Ar) to 345 meV (0.4% H_2/Ar) in the as-deposited state. After annealing, the values converge to 342 meV for both conditions, indicating a limited influence of hydrogen on sub-bandgap tail states.

For SnO_2, the Urbach energy decreases from 407 meV (0% H_2/Ar) to 363 meV (0.4% H_2/Ar) in the as-deposited state. After PDA, it further decreases to 337 meV for the hydrogen-free sample, while remaining at 363 meV for the hydrogenated film. This suggests that hydrogen reduces structural disorder during deposition, while limiting further relaxation during thermal treatment.

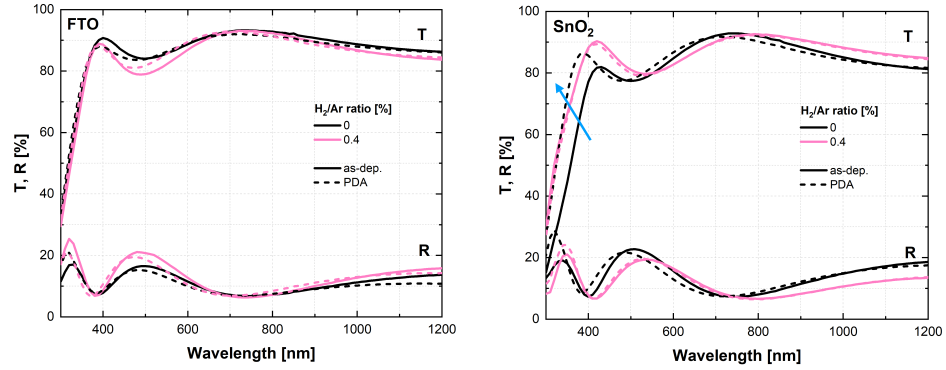

Figure 3.6: Transmittance (T) and reflectance (R) spectra of (a) FTO and (b) SnO_2 films (~ 200 nm thick) deposited with 0% and 0.4% H_2/Ar in as-deposited (as-dep.) and post-deposition annealed (PDA) states. The oxygen content is fixed at 1% O_2/Ar.

Following the analysis of optical properties, the electrical behavior of the films is examined. Figure 3.7 presents the corresponding sheet resistance of FTO and SnO_2. For the as-deposited FTO films (Figure 3.7a), introducing hydrogen into the sputtering atmosphere leads to a reduction in R_{sheet}. After PDA, all samples converge to approximately 1×10^3 Ω/sq. Compared to the pure oxygen series, where the lowest R_{sheet} (468 Ω/sq) is achieved at 0.3% O_2/Ar (Figure 3.1a), the addition of hydrogen does not result in further improvement.

For the SnO_2 films (Figure 3.7b), the sheet resistance decreases with increasing H_2/Ar ratio in the as-deposited state. After annealing, a pronounced reduction is observed for the hydrogen-free sample, indicating that thermal treatment is more effective in improving conductivity in the absence of hydrogen.

The sheet resistance behavior can be interpreted in relation to structural disorder, as quantified by the Urbach energy extracted from the optical analysis. For FTO, a slight decrease in E_U with increasing hydrogen content is observed in the as-deposited state, accompanied by a

reduction in R_{sheet}. After PDA, both 0% and 0.4% H_2/Ar samples exhibit similar E_U values, together with stabilized sheet resistance around 1×10^3 Ω/sq.
For the SnO_2 films, the 0.4% H_2/Ar sample shows lower Urbach energy and sheet resistance than the hydrogen-free sample. After annealing, E_U and R_{sheet} remain nearly unchanged for the hydrogenated sample, while both decrease for the 0% H_2/Ar case.
While these findings suggests a link between reduced disorder and improved conductivity, the limited variation in E_U indicates that additional factors likely govern the electrical behavior [125]. If minimizing sheet resistance is therefore the primary objective, optimized hydrogen content during deposition may eliminate the need for post-deposition annealing, offering an alternative method for the fabrication of TCO layers in solar cell devices.

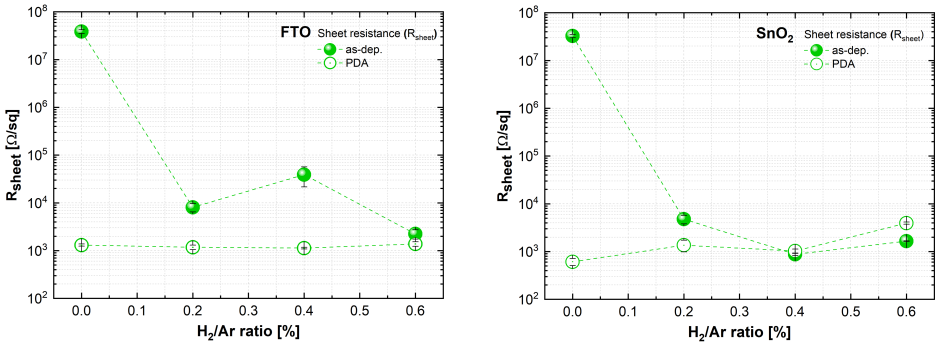

a) b)

Figure 3.7: Sheet resistance (R_{sheet}) of (a) FTO and (b) SnO_2 films (~ 200 nm thick) as a function of the H_2/Ar ratio in as-deposited (as-dep.) and post-deposition annealed (PDA) conditions. The oxygen content is fixed at 1% O_2/Ar.

Figure 3.8 illustrates the evolution of μ and N in the FTO and SnO_2 films as a function of the H_2/Ar ratio under both as-deposited and PDA conditions. The carrier density values obtained from Hall effect measurements reveal both n-type (negative sign) and p-type (positive sign) conduction across FTO and SnO_2 films. A more detailed discussion of this ambipolar behavior is provided in Section 3.3.1.3, while the Hall measurement procedure is described in Section 3.2.3.1. Further details on the carrier density are given in Appendix B.
In the FTO samples (Figure 3.8a, Figure 3.8c), the highest mobility of 15.33 cm^2/Vs is observed at 0.4% H_2/Ar after PDA, exceeding the peak value achieved in the oxygen series (13.73 cm^2/Vs). The carrier density remains higher in hydrogen-containing atmospheres under both as-deposited and annealed conditions compared to the 1% O_2/Ar reference, which reaches 2.5×10^{19} cm^{-3} in the as-deposited state.
In Figure 3.8b and Figure 3.8d, both the mobility and carrier density values of the SnO_2 films exhibit noticeable fluctuations in the as-deposited state, indicating that hydrogen does not induce a systematic trend in charge transport properties prior to annealing. After PDA, μ and N values stabilize, with mobility peaking at 16.14 cm^2/Vs at 0.4% H_2/Ar and carrier density converging around 3×10^{19} cm^{-3} across all hydrogen-containing conditions.

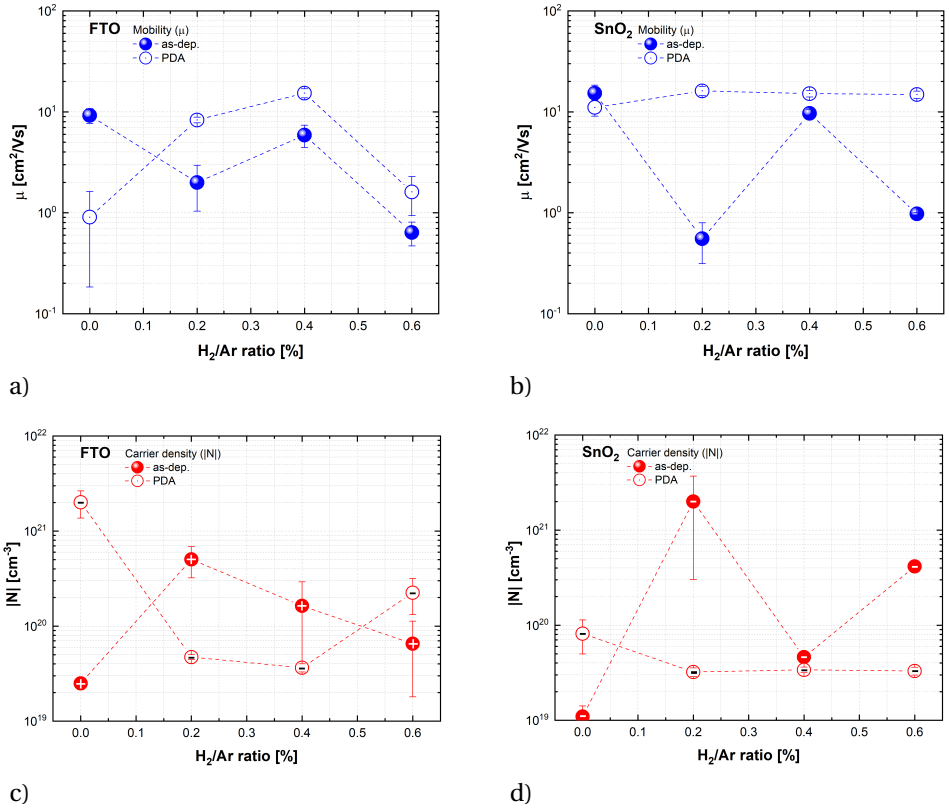

Figure 3.8: Carrier mobility (μ) and density (N) of (a, c) FTO and (b, d) SnO_2 films (~ 200 nm thick) as a function of the H_2/Ar ratio in as-deposited (as-dep.) and post-deposition annealed (PDA) conditions. The oxygen content is fixed at 1% O_2/Ar. The carrier density sign is reported on the red dots.

3.3.1.3 n-type and p-type conductivity

Both Figure 3.2 (Section 3.3.1.1) and Figure 3.8 (Section 3.3.1.2) show apparent n-type and p-type conduction in as-deposited SnO_2 and FTO films, indicating ambipolar transport and complex underlying defect chemistry. The consistent Hall coefficient sign across repeated measurements of individual samples confirms the reproducibility of the dominant carrier type, while variations between samples highlight the sensitivity to processing conditions. The corresponding average carrier densities and carrier types are reported in Appendix B.

This apparent ambipolarity is attributed to the coexistence of donor- and acceptor-like defects combined with structural disorder, which shifts the Fermi level between electron- and hole-dominated regimes. In addition, simultaneous electron and hole transport cannot be excluded; the Hall coefficient therefore reflects a mobility-weighted balance rather than a single carrier type [126–128].

Post-deposition annealing in nitrogen drives all films toward stable n-type behavior, indicating that reducing conditions promote donor-like defects while suppressing compensating states, thereby shifting the Fermi level toward the conduction band.

Previous studies on SnO_x films have shown that small changes in sputtering conditions can induce transitions between p- and n-type conduction by modulating oxygen vacancies and tin interstitials. Oxygen-deficient conditions favor donor-like defects and n-type conduction, whereas more oxygen-rich conditions suppress these donors and can promote acceptor-like states, enabling p-type behavior [129].
The observed conduction behavior is consistent with the defect-state model proposed by Henkel et al. [130], which attributes such phenomena to polaronic states, charge-transfer processes, and excitonic defect configurations. Although a detailed transport mechanism analysis is beyond the scope of this study, the findings underscore the critical role of gas-phase composition during deposition and annealing in shaping the optoelectrical properties and carrier dynamics of SnO_2-based films.

3.3.1.4 TCOs overview

Figure 3.9 provides a comparative overview of transparent conducting oxides, highlighting the relationship between the carrier mobility and carrier density. All samples, both from this work and literature, are characterized using the Hall measurement setup described in Section 3.2.3. The data set includes FTO and SnO_2 films developed in this study, as well as indium tin oxide (ITO), hydrogenated indium oxide (IO:H), aluminum-doped zinc oxide (AZO), and undoped ZnO from Chapter 2.
Two industry benchmarks are also included: commercially available Asahi FTO glass (1.1 mm thick) and FTO deposited via atmospheric pressure chemical vapor deposition (APCVD) at 500 °C [131], produced in collaboration with the industrial partner of this work. These samples represent the upper performance limits achievable with high temperature processing.
The plot maps the distribution of TCOs in relation to the two main scattering mechanisms that limit their performance: grain boundary scattering, which dominates at lower carrier densities, and ionized impurity scattering, which becomes significant at higher concentration [52, 73, 121].

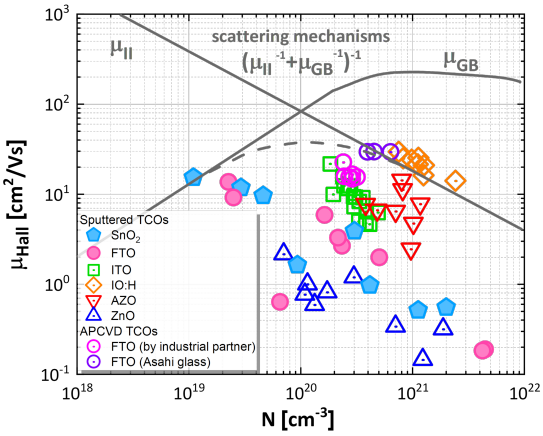

Figure 3.9: Carrier mobility (μ) versus carrier density (N) plot for FTO and undoped SnO_2 deposited by room temperature sputtering in this study, commercial FTO-coated Asahi glass and FTO deposited by atmospheric pressure chemical vapor deposition (APCVD) at 500 °C. Comparative data for ITO, IO:H, AZO, and undoped ZnO are also reported. Gray lines indicate ionized impurity and grain boundary scattering mechanisms.

The SnO_2 and FTO films fabricated in this work exhibit carrier densities ranging from 10^{19} to over 10^{21} cm^{-3}, with mobilities in the range of 10–15 cm^2/Vs. At lower carrier densities, the mobility of FTO is comparable to that of undoped SnO_2. However, the lack of significant thermal activation at room temperature limits dopant activation and crystalline ordering, thereby constraining further mobility improvement.
The relatively low carrier density of these films limits free carrier absorption in the near-infrared, which is beneficial for front electrode applications in solar cells. However, an effective front electrode must also promote light scattering to enhance the optical path length in the solar device. SEM images in Appendix B show smooth and compact surfaces, which favor charge transport but do not support efficient light scattering.
APCVD-grown FTO exhibits a favorable combination of a ~10^{20} cm^{-3} carrier density and higher mobility, attributed to improved crystallinity and dopant activation enabled by high temperature processing (see Appendix B). The Asahi FTO reference shows an even higher carrier density, with mobility comparable to IO:H.
Although the FTO and SnO_2 films developed here do not match the performance of high temperature benchmarks, they demonstrate that room temperature sputtered TCOs can achieve a balanced optoelectrical performance without thermal processing. However, this approach involves trade-offs in crystallinity and dopant activation, which must be carefully considered when developing low temperature, scalable deposition strategies for photovoltaic applications.

3.3.2. Material properties

Reference samples are deposited in four distinct sputtering atmospheres for each material and summarized in Table 3.1. These representative conditions are chosen to explore the relationship between gas-induced compositional and structural changes and the resulting optoelectrical behavior, discussed in Section 3.3.1.1 and Section 3.3.1.2.

Table 3.1: Overview of sputtering gas compositions used for FTO and SnO_2 material characterization. The condition labeled as 0% O_2/Ar and 0% H_2/Ar corresponds to sputtering in a pure argon atmosphere.

FTO		SnO_2	
O_2/Ar [%]	H_2/Ar [%]	O_2/Ar [%]	H_2/Ar [%]
0	0	0	0
0.4	0	0.5	0
1	0	1	0.1
1	0.4	1	0.4

3.3.2.1 Energy dispersive X-ray spectroscopy analysis

Energy dispersive X-ray spectroscopy (EDX) is employed to qualitatively and semi-quantitatively assess the bulk elemental composition of the deposited FTO and SnO_2 films. Although XPS is later used to probe surface chemistry and oxidation states, EDX complements this by offering information from the bulk region of the films. To minimize interference from parasitic oxygen signals originating from glass substrates, EDX measurements are conducted on samples deposited onto (100)-oriented silicon wafers. This approach ensures a more accurate detection of oxygen and other film-specific elements. Quantitative atomic percentages and measurement uncertainties are provided in Appendix B.

Figure 3.10 shows the EDX spectra of FTO and SnO_2 films deposited in selected sputtering atmospheres. The elemental peaks corresponding to tin (Sn), oxygen (O), and fluorine (F) are clearly detected, consistent with the intended film compositions. A silicon (Si) peak (~1.74 keV) from the silicon substrate is omitted from the displayed spectra for clarity. All spectra are normalized to the O Kα peak (~0.52 keV). Measurements are performed at a 15 kV accelerating voltage.
In both material sets, Sn is consistently observed through its characteristic Nα (~0.39 keV), Mα (~3.44 keV), Mβ (~3.67 keV), and Lα (~3.90 keV) peaks [132]. A weak F Kα peak (~0.68 keV) is identified in the FTO samples. A C Kα peak (~0.28 keV) is also detected and is likely due to surface contamination.

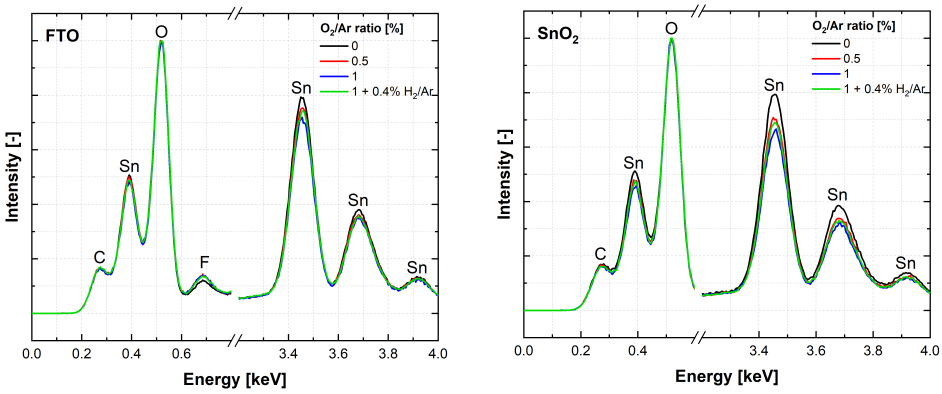

a) b)

Figure 3.10: Normalized EDX spectra of (a) FTO and (b) SnO_2 thin films deposited in four distinct sputtering gas atmospheres. Spectra are normalized to the O Kα peak (~0.52 keV). The Sn, O, F, and C peaks are shown and labeled in the spectra.

In FTO (Figure 3.10a), Sn peak intensities are slightly lower for oxygen- and hydrogen-containing atmospheres compared to pure Ar, suggesting a shift toward a more oxidized composition. A modest increase in the fluorine signal is observed under oxygen-rich conditions, potentially indicating improved fluorine incorporation. However, based on EDX results and the comparable optoelectrical behavior between FTO and undoped SnO_2 (Section 3.3.1.1 and Section 3.3.1.2), fluorine appears to exert limited electronic influence, likely due to the amorphous structure of the films (Section 3.3.2.3) and the low temperature deposition environment [118, 133, 134].
In SnO_2 films (Figure 3.10b), Sn peak intensities decrease as the O_2/Ar ratio increases, consistent with increased oxygen uptake. The sample deposited with both O_2 and H_2 shows a slightly elevated Sn signal compared to the O_2-only sample. The presence of hydrogen may reduce the extent of oxygen incorporation, possibly by inducing a mild reducing environment during deposition or promoting the formation of oxygen vacancies [135].

3.3.2.2 X-ray photoelectron spectroscopy analysis

X-ray photoelectron spectroscopy (XPS) is performed to analyze the chemical composition and Sn oxidation states in FTO and SnO_2 films under the selected O_2/Ar and H_2/Ar sputtering conditions reported in Table 3.1 [136]. The high-resolution Sn $3d_{5/2}$ spectra (Figure 3.11 and Figure 3.12) show three components assigned to Sn^0 (484.5 eV), Sn^{2+} (486.0 eV), and Sn^{4+} (486.7 eV), in agreement with literature values [129, 137]. The full XPS survey spectra, quantified Sn^0, Sn^{2+}, and Sn^{4+} contents from the high-resolution data, and atomic percentages of all detected elements are provided in Appendix B.

In Figure 3.11, the Sn $3d_{5/2}$ spectra of FTO films deposited in pure Ar or O_2-containing atmospheres are dominated by the Sn^{4+} component, indicating a predominantly stoichiometric SnO_2 surface. In contrast, the 0.4% H_2/Ar sample shows a shift toward lower binding energies, with a dominant contribution from sub-oxidized Sn^{2+} species, consistent with the reducing nature of the sputtering atmosphere.

After annealing, the Sn $3d_{5/2}$ spectra remain largely unchanged for the O_2/Ar samples, suggesting a stable surface chemical environment. However, for the 0.4% H_2/Ar sample, PDA leads to a further increase in Sn^{2+} content, with the Sn^{4+} fraction decreasing from 24% to 15% and Sn^{2+} increasing from 62% to 70%. This trend indicates that hydrogen-rich conditions favor sub-stoichiometric tin states. The observed reduction is consistent with reports linking increased Sn^{2+} content to oxygen vacancies in tin oxide systems [137, 138].

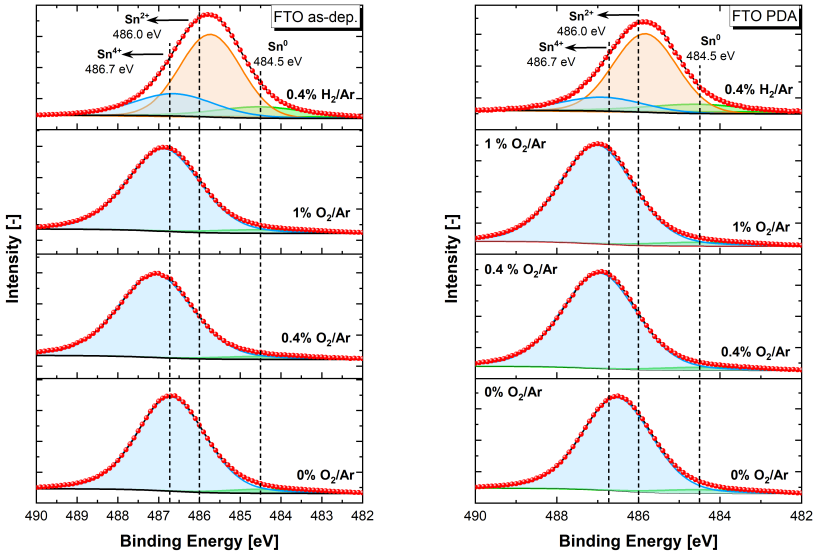

a) b)

Figure 3.11: Sn $3d_{5/2}$ XPS spectra of FTO films with varying gas ratios: (a) as-deposited (as-dep.) and (b) post-deposition annealed (PDA). The 0.4% H_2/Ar sample is deposited at a fixed 1% O_2/Ar ratio.

The XPS results provide insight into the optoelectrical behavior of the FTO films. While increasing O_2/Ar ratios lead to enhanced optical transmittance and bandgap widening (Figure 3.3a and Figure 3.4a), they are also accompanied by a significant rise in sheet resistance (Figure 3.1a). However, these trends cannot be directly linked to changes in Sn oxidation states, as the Sn^{4+} phase remains predominant across all O_2-containing conditions.
In contrast, the enhanced electrical conductivity observed in films sputtered with hydrogen (Figure 3.7a) may be associated with the presence of Sn^{2+} species, suggesting a correlation with oxygen vacancy formation under reducing conditions. The additional decrease in sheet resistance following PDA further coincides with an increased Sn^{2+} contribution, as revealed by XPS.
Figure 3.12 presents the high-resolution Sn $3d_{5/2}$ spectra for SnO_2 films deposited under varied gas ratios. Across all conditions, the spectra exhibit a symmetric peak centered near 486.6 eV, characteristic of fully oxidized Sn^{4+} in stoichiometric SnO_2 [134]. The PDA treatment induces no significant shift in the Sn $3d_{5/2}$ binding energies, reflecting the chemical robustness of the SnO_2 matrix across the investigated conditions. The relative contents of Sn^0, Sn^{2+}, and Sn^{4+} remain largely unchanged before and after annealing, as detailed in Appendix B.

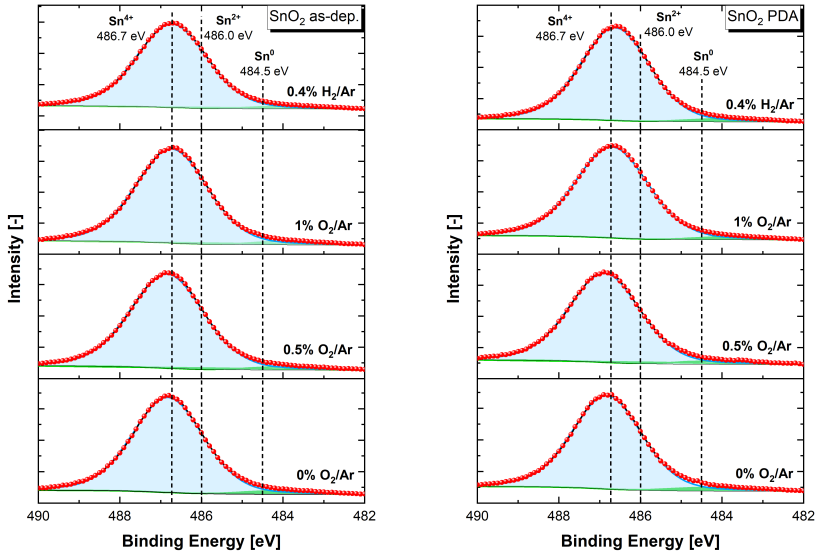

a) b)

Figure 3.12: Sn $3d_{5/2}$ XPS spectra of SnO_2 films with varying gas ratios: (a) as-deposited (as-dep.) and (b) post-deposition annealed (PDA). The 0.4% H_2/Ar sample is deposited at a fixed 1% O_2/Ar ratio.

In Section 3.3.1.1, the optoelectrical trends indicate that increasing the O_2/Ar ratio enhances optical transmittance (Figure 3.4b) but raises sheet resistance (Figure 3.1b) in the as-deposited SnO_2 films. The post-deposition annealing further enhances transparency and stabilizes conductivity across all gas compositions. However, these trends do not directly correlate with the XPS results, which show minimal shifts in the Sn 3d5/2 binding energy and negligible changes in the relative Sn^0, Sn^{2+}, and Sn^{4+} contributions.

This discrepancy likely arises from the surface sensitivity of XPS, which probes only the top ~ 5 nm of the film and may not reflect bulk chemical variations. In contrast, the EDX analysis in Figure 3.10b captures the overall film stoichiometry and indicates compositional changes not resolved by XPS.
In Section 3.3.1.2, introducing hydrogen into an oxygen-rich sputtering atmosphere increases transparency (Figure 3.5b and Figure 3.6b) and reduces sheet resistance (Figure 3.7b), despite no detectable change in the Sn oxidation state. After annealing, carrier mobility and density converge across all H_2/Ar conditions. These results suggest that hydrogen enhances optoelectrical performance through defect passivation and structural reordering, without significantly altering the oxidation state, as supported by XPS analysis [139–141].

3.3.2.3 X-ray diffraction analysis

X-ray diffraction (XRD) is used to assess the structural properties of selected FTO (Figure 3.13) and SnO_2 (Figure 3.14) samples deposited at room temperature and annealed at 400 °C for 20 min in a pure nitrogen (N_2) atmosphere. This post-deposition annealing step is intended to promote crystallization in an oxygen-deficient atmosphere [142]. Due to the limited film thickness (~ 200 nm), a high background from the amorphous glass substrate is present in the raw patterns. To enhance peak visibility, all spectra have been background-subtracted.
In FTO films deposited in pure Ar (Figure 3.13a), no crystalline peaks are observed after PDA, indicating an amorphous structure. In contrast, oxygen-containing atmospheres yield weak diffraction peaks after annealing, corresponding to the (110), (101), and (211) planes of rutile SnO_2. These features indicate limited crystallization without preferred orientation, consistent with randomly oriented nanocrystalline domains [118].

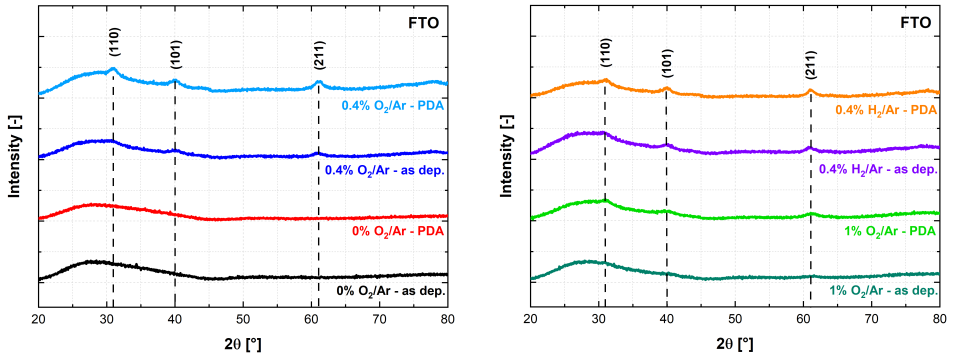

Figure 3.13: XRD patterns of representative FTO films deposited in (a) pure Ar (0% O_2/Ar) and 0.4% O_2/Ar and (b) 1% O_2/Ar and 1% O_2/Ar with 0.4% H_2/Ar, shown for both as-deposited (as-dep.) and post-deposition annealed (PDA) conditions.

In Figure 3.13b, the addition of hydrogen to a 1% O_2/Ar atmosphere slightly enhances crystallization, as reflected by sharper diffraction peaks. However, the PDA treatment induces only minor additional changes, suggesting that hydrogen primarily affects early-stage nucleation rather than promoting significant grain growth during annealing [143]. In highly disordered or amorphous structures, the lack of well-defined substitutional sites may hinder the incorpo-

ration of F^- ions, confining them to less favorable or interstitial positions [144, 145]. These results therefore suggest that the reduction in sheet resistance after PDA (Figure 3.1a and Figure 3.7a) in oxygen-containing atmospheres, including hydrogen-containing conditions, is associated with the onset of crystallization and increased structural ordering during the amorphous-to-crystalline transition.

The XRD patterns of SnO_2 films (Figure 3.14) show weak crystallization with no preferred orientation under all tested conditions, consistent with previous reports [146, 147]. Post-deposition annealing in nitrogen induces slight structural ordering, although the films remain largely amorphous. Notably, the sample deposited with 1% O_2/Ar and 0.4% H_2/Ar (Figure 3.14b) exhibits slightly sharper diffraction peaks than the oxygen-only counterpart. As observed for FTO, the reduction in sheet resistance after PDA (Figure 3.1b and Figure 3.7b) is likely associated with the onset of crystallization detected by XRD.

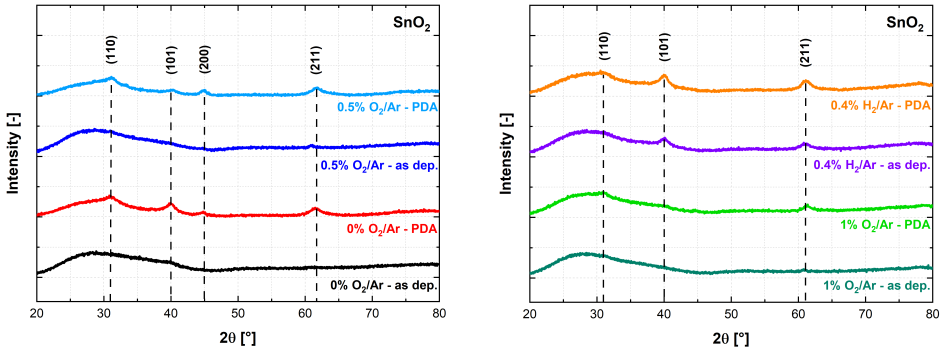

a) b)

Figure 3.14: XRD patterns of representative SnO_2 films deposited in (a) pure Ar (0% O_2/Ar) and 0.5% O_2/Ar and (b) 1% O_2/Ar and 1% O_2/Ar with 0.4% H_2/Ar, shown for both as-deposited (as-dep.) and post-deposition annealed (PDA) conditions.

The average grain size and full width at half maximum (FWHM) of the (101) and (211) diffraction peaks are analyzed, with FWHM values corrected for instrumental broadening. Grain sizes are estimated using the Debye–Scherrer equation:

$$D_{hkl} = \frac{0.9\lambda}{\beta \cos\theta} \tag{3.6}$$

where D_{hkl} is the crystallite size, λ is the wavelength of Cu Kα radiation ($\lambda = 0.15406$ nm), β is the FWHM value in radians, and θ is the Bragg diffraction angle [148]. The resulting grain sizes range from 6.8 to 9 nm for FTO films and from 6.5 to 7.5 nm for SnO_2 films.

While fluorine incorporation at elevated temperatures (e.g., ≥ 400 °C) is known to promote crystallite growth [149], the small grain sizes and weak diffraction peaks observed here suggest that, under room temperature sputtering conditions, fluorine primarily promotes nucleation rather than grain growth. The crystallite sizes remain in the nanometer range, indicating that the available thermal energy is insufficient to drive significant structural coarsening.

3.4. Conclusions

This study systematically investigates the impact of reactive sputtering gas composition on the optoelectrical, structural, and surface chemical properties of room-temperature (RT) sputtered fluorine-doped tin oxide (FTO) and undoped tin dioxide (SnO_2) thin films. By correlating optical transmittance, charge transport, sheet resistance, and spectroscopic data, key processing–property relationships are identified to guide the design of these transparent conducting oxides (TCOs) for photovoltaic applications. The results demonstrate competitive optoelectrical performance compared to typical RT-sputtered SnO_2-based films, highlighting that careful control of the sputtering gas composition enables effective tuning of film properties.

First, oxygen incorporation in the sputtering atmosphere governs the balance between optical transparency and electrical conductivity. In FTO, 0.3–0.4% O_2/Ar ratios yield the lowest sheet resistance (468 Ω/sq) and highest carrier mobility (13.7 cm^2/Vs) while maintaining a wide optical bandgap (E_g > 3.9 eV). In undoped SnO_2, sheet resistance increases monotonically with oxygen content. However, the optimum condition occurs at 1% O_2/Ar, where mobility peaks (15.3 cm^2/Vs) with moderate carrier density (~ 10^{19} cm^{-3}).

Second, introducing hydrogen into an oxygen-rich atmosphere (1% O_2/Ar) significantly influences the optoelectrical response of undoped SnO_2 films. Hydrogen addition enhances transparency and reduces sheet resistance in the as-deposited state. XPS analysis shows no change in the dominant Sn^{4+} oxidation state, suggesting that hydrogen acts primarily through defect passivation and structural modification rather than chemical reduction. After post-deposition annealing (PDA) at 400 °C in an N_2 atmosphere, both hydrogenated and non-hydrogenated samples exhibit converging mobilities and carrier densities. In FTO films, hydrogen has a subtle effect on optical properties, while conductivity stabilizes at ~10^3 Ω/sq after PDA.

Although RT-sputtered FTO and SnO_2 films do not yet match the optoelectrical performance of high-temperature deposition methods, precise control of the sputtering gas composition enables a tunable balance between transparency and conductivity. This provides a thermally compatible, scalable, and cost-effective approach for fabricating transparent conductive electrodes and charge transport layers, particularly for thermally sensitive technologies such as polymer-based and next generation solar cells.

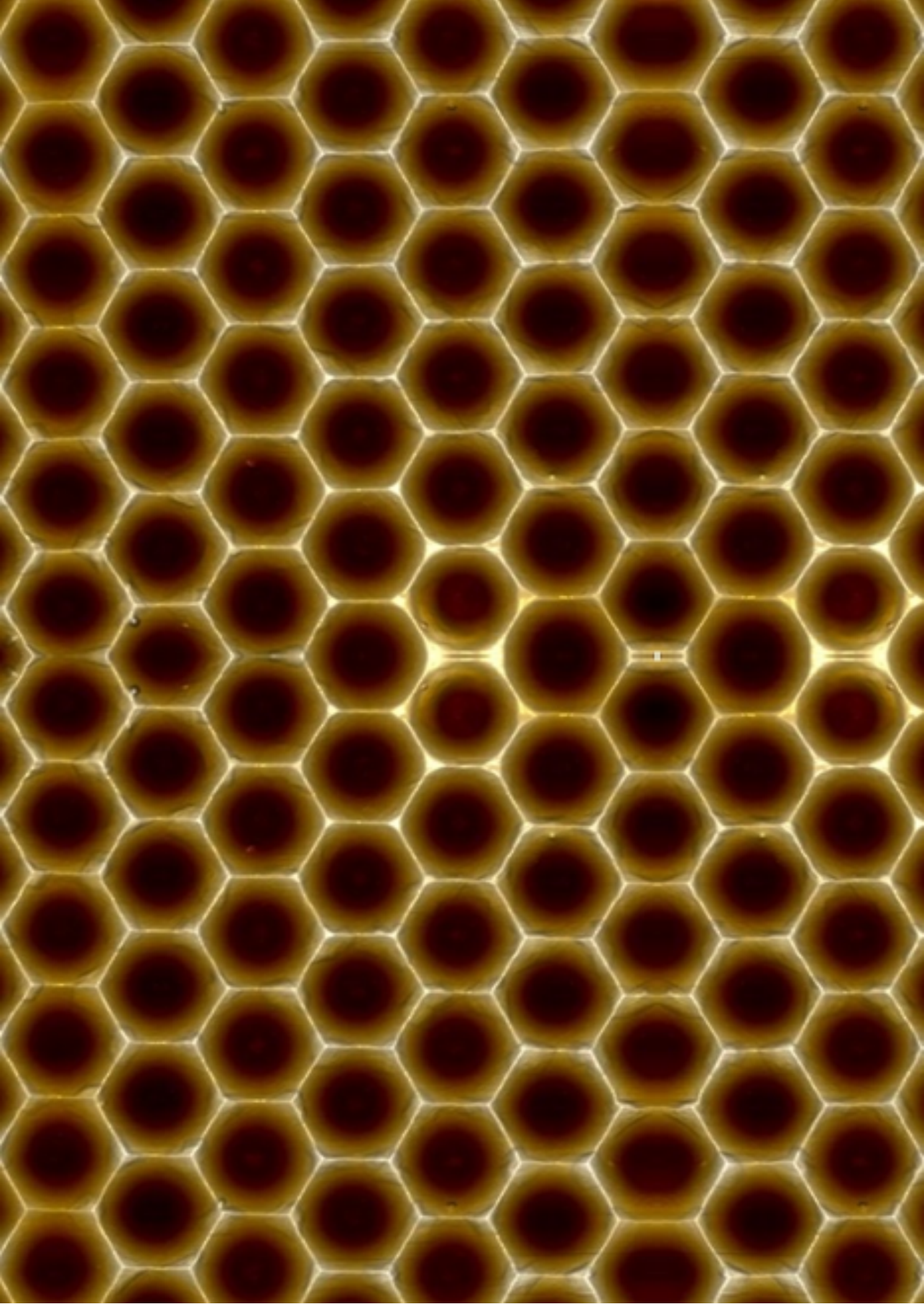

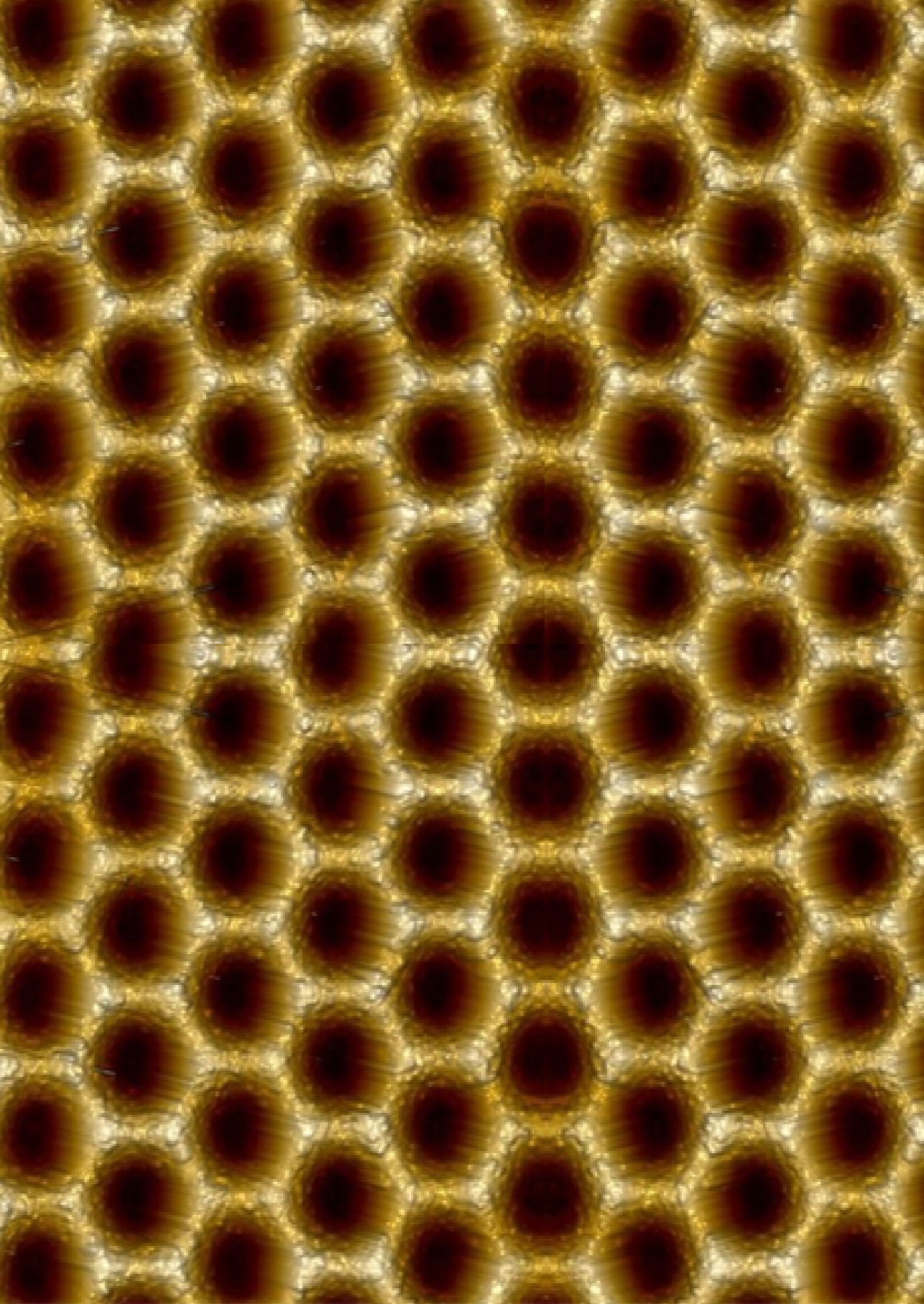

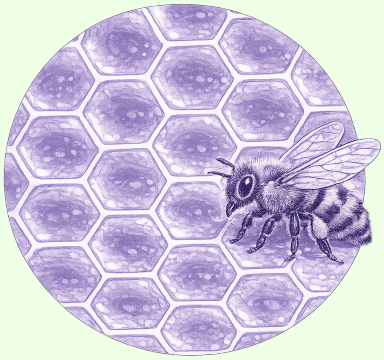

4

OPTICAL MODELING OF MULTISCALE TEXTURED TF-Si SOLAR CELLS

This chapter is based on the following publication:

Saitta, F., Padmakumar, G., Perez-Rodriguez, P., Procel Moya, P., Santbergen, R., & Smets, A. H. M. *Time-Efficient, Accurate, and Experimentally Grounded Optical Modeling of Multiscale-Textured Thin-Film Solar Cells.* Global Challenges, e00448 (2025), https://doi.org/10.1002/gch2.202500448.

4.1. Introduction

Thin-film (TF) Si-based solar cells remain attractive for cost-effective, lightweight, and scalable photovoltaic technologies [1, 150]. Although amorphous silicon exhibits strong absorption at short wavelengths due to its direct-like bandgap, its wider bandgap compared to crystalline silicon limits near-infrared absorption and constrains device efficiency [151]. Effective light-management strategies are therefore essential to minimize reflection losses and maximize photon absorption in both single and multijunction TF architectures [152, 153].

Previous studies have explored a range of textured substrates to enhance light management in thin-film silicon solar cells, including modulated surface textured (MST) electrodes [47], random and periodic Si textures [154], Asahi glass [155], and flexible laminates [156]. High efficiencies have also been achieved using advanced textures such as honeycomb patterns on crystalline Si wafers [157, 158]. However, despite these developments, predictive optical modeling of such complex architectures remains limited.

In particular, a unified optical model that captures both external quantum efficiency (EQE) and front reflection losses (1 – R) in realistic multiscale device structures is still lacking [159, 160]. Most prior studies treat these quantities separately or rely on simplified geometries, leading to discrepancies between simulations and actual device architectures [161, 162].

In this work, these metrics are integrated within a single experimentally validated optical model, enabling a consistent and quantitative assessment of optical response and loss mechanisms in textured TF-Si solar cells. Achieving this requires addressing two key challenges. First, accurate modeling depends on reliable optical constants, refractive index (n) and extinction coefficient (k), for all constituent materials. Second, realistic representation of interface texturing is essential, as it governs light scattering, trapping, and interference within the multilayer stack [163].

To address these challenges, two optical modeling approaches are investigated: rigorous coupled-wave analysis (RCWA) [164] and ray optics [165]. The comparison is carried out using two textured glasses: the widely used but less optically characterized Asahi VU-type glass with random nanostructures [166], serving as the substrate for a single-junction hydrogenated amorphous silicon (a-Si:H) solar cell, and a novel micro-periodic honeycomb-textured glass developed in-house [4], used as the substrate for a single-junction hydrogenated nanocrystalline silicon (nc-Si:H) solar cell.

The RCWA model provides a full-wave solution capable of capturing complex interference and scattering effects by solving Maxwell's equations, and is therefore expected to deliver high accuracy for fine-scale textures. However, its application to complex, non-periodic, or conformal structures is computationally demanding and requires extensive optimization [167, 168]. In contrast, the ray tracing optical model offers significantly reduced computational effort but is often considered less reliable for nanoscale features [169].

In this study, RCWA and ray optics are compared on experimentally fabricated a-Si:H and nc-Si:H single-junction devices on commercial and in-house textured substrates, and extended to an a-Si:H/nc-Si:H tandem architecture. By combining realistic interface morphologies, measured optical constants, and validation against EQE and reflection data, the model reproduces absorption and reflection in multiscale textured TF-Si devices with high accuracy and computational efficiency. Beyond the specific cases investigated, this framework enables predictive optical modeling of next generation textured photovoltaics.

4.2. Optical modeling framework

The optical response of the solar cell structures is simulated using the GenPro4 solver [170], which employs the net-radiation method with angular intensity distributions of reflection and transmission as input. This approach captures multiple reflections, transmissions, and scattering events, enabling realistic modeling of multilayer stacks with textured interfaces.

In GenPro4, each material within the solar cell stack is classified as either a layer or a coating, depending on how interference is expected to influence light propagation. This distinction is based on the optical thickness of the film relative to the coherence length of sunlight and on the optical contrast between adjacent layers. The coherence length defines the distance over which the phase of the electromagnetic wave remains correlated.

When this correlation is maintained, typically in thin or weakly absorbing films, reflected and transmitted waves can interfere, and the film is considered optically coherent. Such layers are modeled as coatings, where light propagation is treated in terms of field amplitudes including both magnitude and phase.

When the optical thickness is sufficiently large or absorption is strong, the phase correlation between multiple reflections is lost and interference effects average out. These layers are considered optically incoherent and are modeled as layers, where only light intensities are summed. This hybrid formalism enables GenPro4 to describe both coherent and incoherent optical behavior within the same simulation framework [171].

Another key input to GenPro4 is the complex refractive index of each material, defined by its refractive index (n) and extinction coefficient (k). These wavelength-dependent optical constants determine the reflectance (R), transmittance (T), and absorptance (A) within the stack. The implied photocurrent density J_{ph} is calculated from the absorptance spectrum according to Equation 4.1 [172]:

$$J_{ph} = -e \int_{\lambda_1}^{\lambda_2} A(\lambda)\, \Phi_{AM1.5G}(\lambda)\, d\lambda \tag{4.1}$$

where $A(\lambda)$ is the absorptance in the photoactive layer, $\Phi_{AM1.5G}(\lambda)$ (photons $cm^{-2}\, s^{-1}\, nm^{-1}$) is the AM1.5G spectral photon flux density, and e is the elementary charge. The integration limits λ_1 and λ_2 correspond to the lower and upper bounds of the spectral range, respectively, with λ_2 typically set by the optical bandgap of the absorber material.

The standard GenPro4 solver models light interaction with textured surfaces using two complementary approaches: ray optics and wave optics. The wave-optics formalism is based on the scalar scattering theory developed by K. Jäger, which performs well for small-scale textures such as Asahi U-type glass but loses accuracy for larger or more complex morphologies [173]. Full-wave Maxwell solvers can rigorously model light scattering but are computationally demanding and generally constrained to periodic boundary conditions, restricting simulations to small unit cells that may not represent the complexity of random thin-film morphologies. The rigorous coupled-wave analysis offers a practical alternative, enabling accurate treatment of non-periodic and sub-wavelength textures at reduced computational cost. In this work, RCWA is integrated into GenPro4 as an alternative Maxwell solver.

For the validation study, ray optics and RCWA are applied independently within GenPro4, and their predictions are directly compared with the measured optical response of the fabricated solar cells. This strategy makes it possible to evaluate which model best reproduces the experimental EQE and reflection spectra while quantifying the trade-off between computational efficiency and predictive accuracy.
The deviation between simulated and experimental spectra is quantified by calculating the root mean squared error (RMSE), expressed in percentage form as in Equation 4.2 [174]:

$$\mathrm{RMSE}(\%) = 100 \sqrt{\frac{1}{N} \sum_{i=1}^{N} [X_{\mathrm{model}}(\lambda_i) - X_{\mathrm{meas}}(\lambda_i)]^2} \tag{4.2}$$

where $X_{\mathrm{model}}(\lambda_i)$ and $X_{\mathrm{meas}}(\lambda_i)$ denote the simulated and experimental values at wavelength λ_i, and N is the number of spectral points. X_{model} represents either the simulated absorptance or the simulated total front reflection losses, while X_{meas} corresponds to the external quantum efficiency or the measured total front reflection losses, respectively. When simulated and experimental spectra are sampled on different wavelength grids, the simulated data are linearly interpolated onto the experimental grid prior to error evaluation.

4.2.1. Rigorous coupled-wave analysis (RCWA)

In RCWA, the structure is discretized into thin layers along the propagation direction (z-axis), while arbitrary variations are retained in the transverse (x–y) plane. Maxwell's equations are solved in the Fourier domain using a semi-analytical approach: analytically along the z-axis and numerically in the x and y directions.
In principle, an infinite number of Fourier harmonics is required to fully describe arbitrary geometries. In practice, the expansion is truncated, and its accuracy depends on the number of retained modes. A convergence analysis shows that 17 Fourier modes are sufficient to obtain stable reflectance and absorption spectra for the investigated TF-Si structures, with higher orders providing only marginal improvements at significantly increased computational cost. The optimal number of modes is case-dependent and influenced by factors such as texture height, feature geometry, and refractive index contrast.
In addition to harmonic truncation, the spatial discretization must be sufficiently fine to resolve the electric field distribution $\vec{E}$ in the x, y, and z directions. As with the number of Fourier modes, the grid resolution requires balancing accuracy and computational cost, since finer discretization improves field representation but increases simulation time.
The RCWA simulations are executed on a workstation equipped with an AMD EPYC 7552 48-core processor and 1024 GB RAM. A complete wavelength sweep for each solar cell configuration requires approximately one week of computation time.

4.2.1.1 Tukey window function

Since RCWA relies on periodic boundary conditions, accurate modeling of experimentally measured morphologies requires preprocessing of atomic force microscopy (AFM) height maps. While the ray tracing model uses the AFM matrix directly, RCWA needs smoothed input to suppress edge artifacts at the unit cell boundaries.

To address this, the AFM height matrices are processed using a two-dimensional (2D) Tukey window function [172]. The window gradually tapers height values at the edges of the domain, reducing discontinuities while preserving central features of the measured profile. The smoothing is controlled by an overall lateral rescale factor r = 0.2, which provides sufficient tapering at the edges without significant loss of morphological detail. In this case, the central 64% of the AFM map remains completely unchanged, while the surrounding 36% is gradually suppressed, ensuring that the core morphology is preserved while unit cell discontinuities are minimized. Smaller values of r leave sharp edges, whereas larger values overly suppress the central topography.

Geometrically, the smoothed morphology resembles a frustum of a square pyramid with isosceles trapezoidal lateral faces, as illustrated in Figure 4.1.

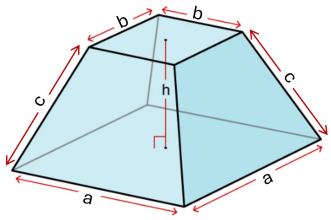

Figure 4.1: Geometric representation of the three-dimensional (3D) Tukey window function used to smooth AFM height maps prior to RCWA simulations. Parameters are the base length a, the top length b, the frustum height h and the lateral face length c.

The frustum height is set to h = 1, the side length of the base equals the AFM pixel dimension a, and the top face length is b = (1 − r) a. The lateral face length c is calculated in Equation 4.3:

$$c = \sqrt{h^2 + \left(\frac{r\,a}{2}\right)^2} \tag{4.3}$$

4.3. Simulation input

This section outlines the model inputs required to predict the optical performance of TF-Si solar cells. Emphasis is placed on the accurate representation of textured interfaces and material optical properties, both of which are critical for obtaining realistic results with ray optics and RCWA. Section 4.3.1 details the morphological characterization of the textured glass substrates. Section 4.3.2 and Section 4.3.3 describe the device architectures, layer stacks and optical constants of the a-Si:H and nc-Si:H single-junction solar cells, respectively. The optical constants are subsequently used as inputs for a-Si:H/nc-Si:H tandem solar cell simulations. Finally, Section 4.3.4 summarizes the key differences between the two optical models in tabular form.

4.3.1. Textured glass substrates

A widely used substrate for TF Si-based solar devices is the commercial SnO_2:F (FTO)-coated glass from Asahi Glass Company [175, 176]. The earlier Asahi U-type glass featured random pyramidal facets with moderate slopes, designed to enhance light scattering while minimizing potential electrical losses [177]. The shift from U-type to the current VU-type substrates was motivated by the need to enhance long-wavelength light scattering (600–1000 nm), which is crucial for improving performance in multijunction solar cells [178, 179]. The main morphological differences between Asahi U- and VU-type glass are described in Section 4.3.2.1.

While the U-type has been extensively characterized, detailed optical data on VU-type glass remain limited. The increasing use of VU-type substrates in high-performance TF Si devices, including this work, underscores the importance of accurate optical and morphological characterization for reliable modeling and device design.

Figure 4.2 shows the AFM characterization of the Asahi VU-type glass surface. The morphology exhibits a complex random nanoscale texture with peak-to-valley heights of approximately 0.31 µm over a 5 µm × 5 µm area, with a root mean square roughness (σ_{RMS}) of 45 nm.

Random textures such as those of Asahi glass scatter light diffusely without selectivity, which limits their ability to redirect light into oblique guided paths or to efficiently scatter light at longer wavelengths. This reduces their effectiveness in devices such as nc-Si:H solar cells, where absorption extends beyond 1 µm. In contrast, engineered periodic textures enable controlled light scattering, diffraction, and guided-mode coupling, improving absorption across a broader spectral range.

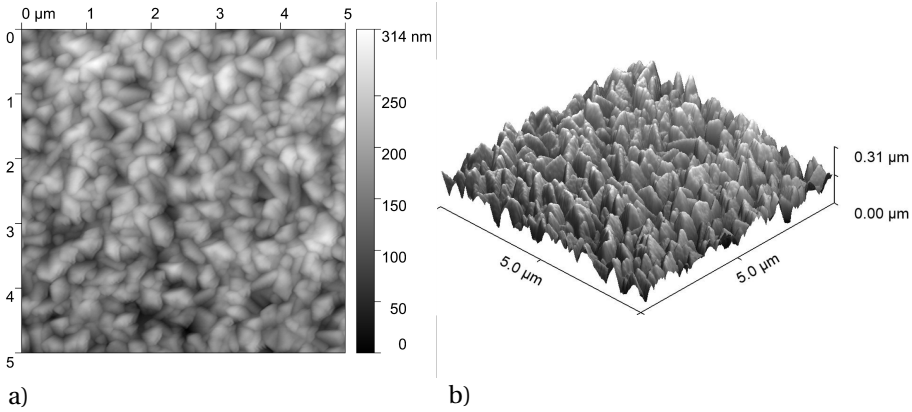

Figure 4.2: AFM images of the Asahi VU-type glass substrate: (a) 2D top-view and (b) 3D morphology. The random texture exhibits a root mean square roughness σ_{RMS} = 45 nm over a 5 µm × 5 µm area.

Figure 4.3 displays the AFM characterization of the in-house fabricated honeycomb-textured glass substrate. The morphology exhibits a highly uniform and periodic microstructure with a lateral period of approximately 5 µm and a feature height of about 1 µm, corresponding to an RMS roughness of σ_{RMS} = 262 nm.

The well-defined geometry promotes efficient angular redistribution of incident light, increasing the optical path length within the absorber and thereby enhancing light trapping in nc-Si:H devices with thicknesses of approximately 3 µm, where improved long-wavelength absorption is required.

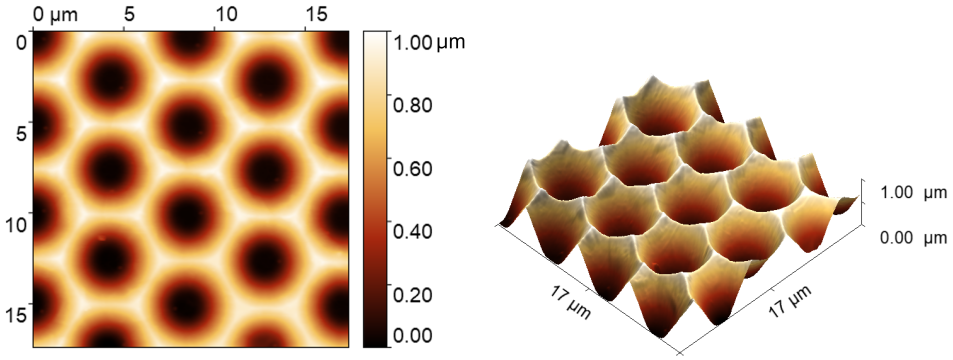

a) b)

Figure 4.3: AFM images of the honeycomb-textured glass substrate: (a) 2D top-view and (b) 3D morphology. The periodic structure exhibits a root mean square roughness σ_{RMS} = 262 nm over a 17 µm × 17 µm area.

4.3.2. a-Si:H solar cell on Asahi VU-type substrate

On the Asahi VU-type substrate, a p-i-n a-Si:H single-junction solar cell is fabricated in a superstrate configuration. This architecture exploits the enhanced light scattering of VU-type glass to improve optical confinement and device performance. The solar cell structure is illustrated in Figure 4.4 (not to scale).

The device is deposited on a 1.1 mm Asahi VU-type glass coated with a 700 nm SnO_2:F layer, which functions as the transparent front electrode. The intrinsic a-Si:H absorber layer is 300 nm thick, with p-type and n-type regions of 10 to 20 nanometers located at the front and rear, respectively. Both the p-type and n-type layers are composed of nanocrystalline silicon oxide (nc-SiO_x). A 10 nm thick aluminum-doped zinc oxide (AZO) buffer layer is inserted between the substrate and the p-type layer.

In addition, a thin 3 nm intrinsic a-SiO_x layer is inserted between the p-type nc-SiO_x and the intrinsic absorber. This interfacial layer improves the p/i interface quality by promoting favorable nucleation of the intrinsic layer and reducing interface-related recombination. It has also been reported to limit boron cross-contamination from the doped layer, contributing to improved device performance [180].

The rear contact is modeled as a 300 nm silver layer acting as a back reflector. Although the experimental stack includes Ag/Cr/Al, the contributions of chromium and aluminum are neglected due to their negligible impact on the optical response.

All subsequent layers conform to the textured substrate, such that each interface inherits the underlying morphology, with progressive smoothing as the film thickness increases. To account for this in the optical model, two sample structures are fabricated and characterized, terminated at the p-type and n-type interfaces, respectively. Accordingly, the AZO/nc-SiO_x (p) and nc-SiO_x (n) layers define the first and second optical interfaces.

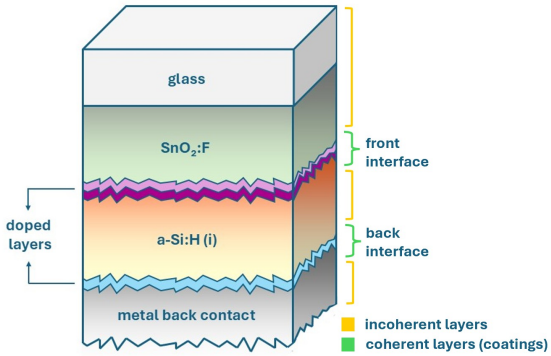

Figure 4.4: Schematic cross-section of the a-Si:H single-junction solar cell on Asahi VU-type glass (not to scale). Layers sequence: Asahi VU-type glass (1.1 mm) with SnO_2:F (700 nm) / AZO (10 nm) / p-type nc-SiO_x (10 nm) / a-SiO_x (3 nm) / a-Si:H (300 nm) / n-type nc-SiO_x (20 nm) / Ag back reflector (300 nm).

The AFM scans of 20 µm × 20 µm areas (Figure 4.5) show that deposition of AZO and nc-SiO_x (p) reduces the surface roughness of the original VU-type substrate (σ_{RMS} = 45 nm, Figure 4.2) to 32 nm. With deposition of the a-Si:H absorber, the roughness decreases further to 23 nm, accompanied by a noticeable increase in lateral feature size (Figure 4.5b). The AFM-derived height maps of these two interfaces are directly implemented in the ray tracing simulations.

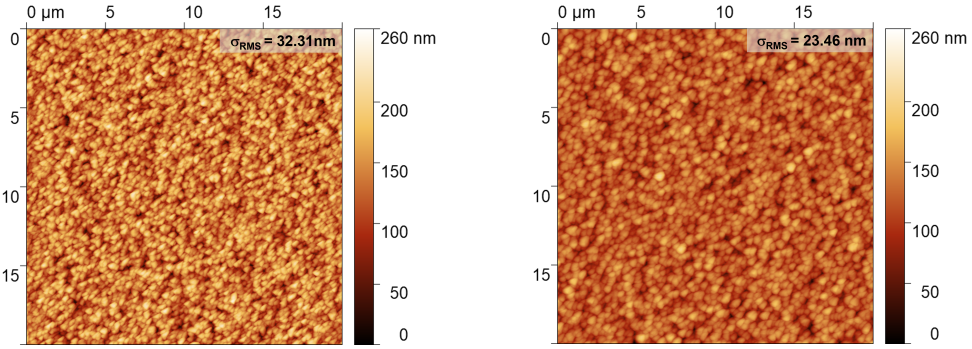

a) b)

Figure 4.5: AFM top-view images of the textured interfaces in the a-Si:H single-junction solar cell on Asahi VU-type glass. (a) Surface after deposition of p-type nc-SiO_x layer. (b) Surface after subsequent deposition of the intrinsic a-Si:H absorber.

Additional steps are necessary to handle the Asahi VU-type texture when the optical performance is simulated with the RCWA solver. The AFM maps are first downscaled from 20 µm × 20 µm to 2 µm × 2 µm sections (Figure 4.6a and Figure 4.6c), retaining key morphological features while ensuring computational feasibility. A three-dimensional (3D) Tukey window function (see Section 4.2.1.1) is then applied to suppress edge discontinuities and enable periodic boundary conditions.

The preprocessed height maps are shown in Figure 4.6b and Figure 4.6d are used as RCWA inputs, ensuring numerical stability while preserving the essential characteristics of the experimental textures. The resulting height matrices are discretized on 1001 × 1001 grids to resolve fine surface features. This resolution ensures sufficient refinement in the x, y, and z directions to numerical compatibility with the spatial resolution of the $\vec{E}$ distribution.

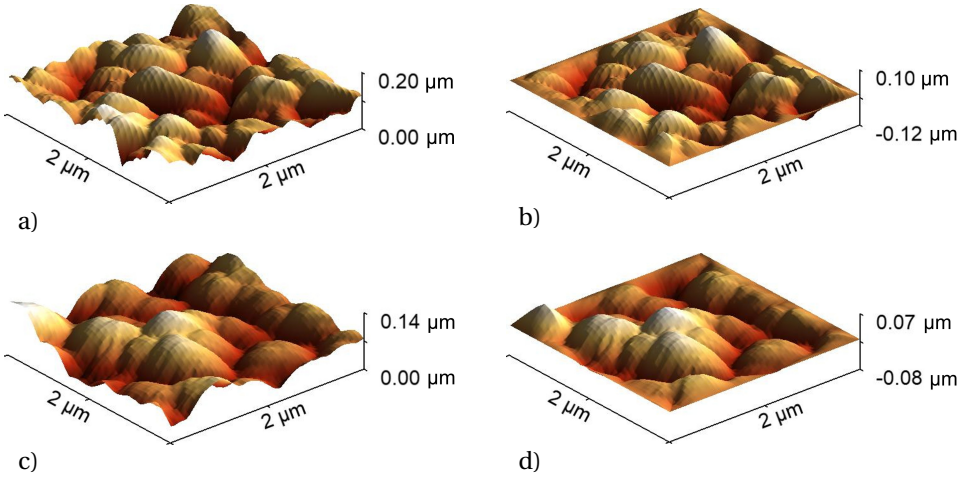

Figure 4.6: Preprocessing of AFM-derived surface morphologies for RCWA simulations of the a-Si:H solar cell on Asahi VU-type glass. (a, c) Downscaled 2 µm × 2 µm AFM maps of the interfaces. (b, d) Corresponding morphologies after application of the 3D Tukey window function.

4.3.2.1 Optical constants

The refractive index and extinction coefficient of all layers in the device stack are key inputs for reliable optical modeling, regardless of the chosen optical solver. The FTO-coated Asahi VU-type glass, serving as the textured front contact, plays a critical role in light coupling and scattering. Its optical properties depend on deposition method, thickness, and surface morphology [118, 145, 181]. Wavelength-resolved n and k data are required to quantify reflection losses, parasitic absorption, and overall device performance.

Figure 4.7 compares the complex refractive index of FTO on U-type and VU-type substrates. The U-type results from Sap et al. [182], obtained by fitting reflectance and transmittance spectra with SCOUT software [183], serve as a reference. This work extends the characterization to VU-type substrate using variable-angle spectroscopic ellipsometry (SE). The measured amplitude ratio (Ψ) and phase difference (Δ) spectra are fitted in CompleteEASE software [184]. A multilayer optical model is constructed, consisting of a surface SnO_2 thin film for roughness-induced modifications, a conductive FTO bulk layer described by Drude–Lorentz oscillators, and a depth-dependent conductivity gradient for vertical inhomogeneity in the film.

While the real part (n) remains comparable for the U- and VU-type substrates in the UV–visible range, the extinction coefficient (k) of the VU-type increases toward the near-infrared. Because the absorption coefficient is given by $\alpha = 4\pi k/\lambda$, this rise in k directly translates into stronger absorption at long-wavelengths [185].

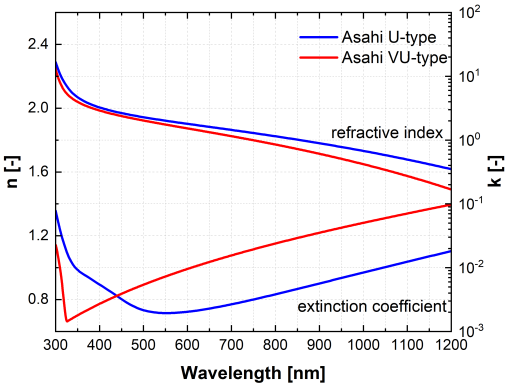

Figure 4.7: Refractive index (n) and extinction coefficient (k) spectra of FTO-coated Asahi U-type and VU-type glass substrates. The VU-type data are obtained in this work from ellipsometry fitting, while the U-type reference data are taken from [182].

In transparent conducting oxides, such near-infrared absorption originates from free-carrier absorption (FCA), where conduction-band electrons absorb low-energy photons through intra-band (Drude-type) transitions. The strength of this process increases with carrier density and decreases with carrier mobility, producing a characteristic long-wavelength tail in k(λ) [186]. The enhanced k in the NIR region observed for the VU-type FTO is attributed to its higher FCA, whereas the differences in bandgap energy, film thickness, and surface roughness reported in Table 4.1 primarily affect visible-range transmission and scattering. These results therefore highlight the importance of direct, substrate-specific optical characterization.

Table 4.1: Optical and morphological parameters of FTO-coated Asahi U-type and VU-type glass substrates. The VU-type results are obtained in this work: bandgap energy and layer thickness from SE fitting, and RMS roughness from AFM measurements. The U-type reference data are taken from [182].

FTO-Asahi	U-type	VU-type
Bandgap energy [eV]	4.26	4.05
Layer thickness [nm]	833.4	667.8
RMS roughness [nm]	39.88	45.49

The complete n and k spectra for all layers in the a-Si:H solar cell are shown in Figure 4.8. For Ag and the glass substrate (excluding the FTO coating), previously measured SE data are used [187, 188]. The glass exhibits a constant n of approximately 1.5 with negligible absorption. Silver exhibits a refractive index well below 1 and an extinction coefficient above 2 across most of the spectrum, consistent with strong metallic absorption and reflectivity [189].
All remaining materials are deposited and characterized in-house. Their optical constants are extracted from SE measurements using a Cody–Lorentz model to describe inter-band transitions, accounting for the presence of band tail states in disordered materials. An additional Drude term is included for layers exhibiting free-carrier absorption in the near-infrared region.

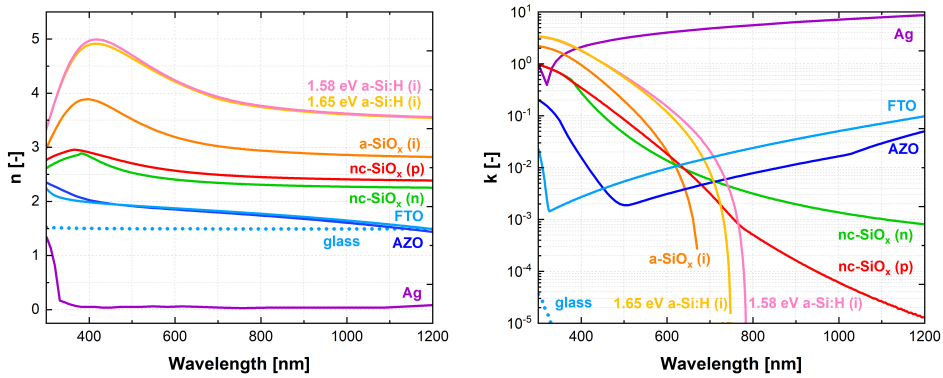

a) b)

Figure 4.8: Optical constants of the a-Si:H single-junction solar cell on Asahi VU-type glass: (a) refractive index (n) and (b) extinction coefficient (k) of all layers, including glass, FTO, AZO, intrinsic a-SiO_x, p- and n-type nc-SiO_x, and Ag. The a-Si:H films with optical bandgaps of 1.58 eV and 1.65 eV are compared.

To improve the short-circuit current density (J_{sc}) of the solar cell, a narrow-bandgap a-Si:H material is employed. This material is deposited by plasma-enhanced chemical vapor deposition (PECVD) under process conditions optimized to lower the bandgap [190, 191]. The resulting film exhibits an optical bandgap of 1.58 eV. Its refractive index peaks near 5.0 at 400 nm and decreases to approximately 3.5 in the near-infrared. For comparison, Figure 4.8 also shows the optical behavior of a wider-bandgap a-Si:H material (1.65 eV). The measured data are consistent with previously reported values [192, 193].

Compared with FTO, AZO exhibits a more gradual decrease of the extinction coefficient from the UV to the visible region, while FTO shows a sharper reduction followed by a renewed increase at longer wavelengths due to free carrier absorption. Overall, both materials remain highly transparent in the visible range, whereas their near infrared response is governed by Drude type losses [194]. The refractive index of both TCOs remains comparable across the spectrum despite the differences in absorption behavior.

The intrinsic a-SiO_x buffer layer shows a refractive index that peaks at 3.6 around 400 nm and decreases to a stable value of 2.8 in the near-infrared. The extinction coefficient cuts off at 670–680 nm, corresponding to an optical bandgap of approximately 1.84 eV. These findings are consistent with previous reports [195].

The n-type and p-type nc-SiO_x layers exhibit peak refractive indices of approximately 2.8 and 3.0, respectively. Both show moderate absorption in the blue spectral region and negligible extinction beyond 700 nm, reflecting the combined effects of nano-crystallinity and oxygen incorporation [192, 196, 197].

4.3.3. nc-Si:H solar cell on honeycomb substrate

On the honeycomb-textured glass substrate, a p-i-n nc-Si:H single-junction solar cell is fabricated in a superstrate configuration. This architecture exploits the engineered periodic honeycomb pattern to enhance long-wavelength scattering and improve optical confinement in the absorber layer. The device structure is shown in Figure 4.9a, with layer thicknesses not drawn to scale.

The solar cell comprises a 135 nm hydrogenated indium oxide (IO:H) front contact, a 5 nm ZnO buffer layer, and nanocrystalline p- and n-type SiO_x layers with thicknesses of 10 nm and 20 nm, respectively. A 3.2 µm intrinsic nc-Si:H layer serves as the absorber, while the back reflector consists of a 60 nm ZnO layer and a 300 nm Ag contact. As noted in Section 4.3.2, the back contact is optically simplified for modeling purposes.

A key feature of this architecture is the conformal replication of the honeycomb geometry throughout the entire stack. This is confirmed by cross-sectional SEM imaging (Figure 4.9b), which shows that the texture is faithfully preserved across all deposited layers. From the same SEM, the honeycomb period, depth, and individual layer thicknesses are determined, confirming both structural integrity and fabrication accuracy.

The apparent gap visible between the back contact and the underlying deposition stack arises from mechanical damage introduced during sample cleaving for cross-sectional imaging and is not present in the actual device.

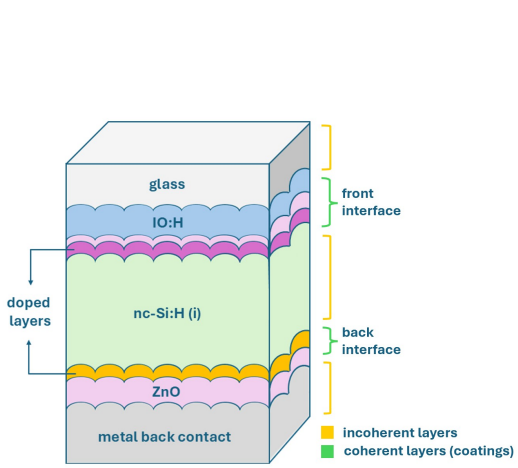

a)

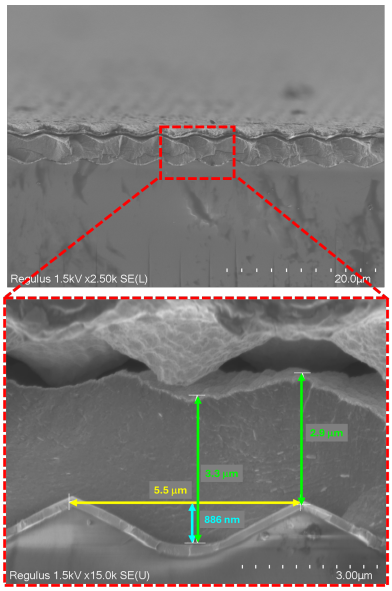

b)

Figure 4.9: Structure of the nc-Si:H single-junction solar cell on honeycomb-textured glass. (a) Schematic cross-section of the device stack (not to scale). Layers sequence: glass (0.7 mm) / IOH (135 nm) / ZnO (5 nm) / p-type nc-SiO_x (10 nm) / a-SiO_x (3 nm) / nc-Si:H (3.2 µm) / n-type nc-SiO_x (20 nm) / ZnO (60 nm) / Ag (300 nm). (b) Cross-sectional SEM images showing conformal replication of the honeycomb texture throughout the solar cell. The SEM magnified view highlights the honeycomb texture period and depth, and the nc-Si:H thickness distribution.

Optically, two textured interfaces are defined in the model, where the optical solvers (ray tracing or RCWA) are applied to resolve the angular intensity distribution of scattered light. These correspond to the front and rear sides of the intrinsic nc-Si:H absorber, where texturing governs light coupling and redistribution within the device. The first interface, at the front of the absorber, comprises the IO:H, ZnO, and p-type nc-SiO_x layers, located between the glass substrate and the nc-Si:H layer. Both the glass and nc-Si:H are modeled as incoherent layers. This textured interface follows the honeycomb geometry shown in Figure 4.3.
The second interface, at the rear of the absorber, includes the n-type nc-SiO_x and ZnO layers at the nc-Si:H/Ag boundary. The AFM scans of the absorber surface (Figure 4.10) reveal that the honeycomb texture is preserved after nc-Si:H deposition. Fine scale nanofeatures developed during nc-Si:H growth, without significantly affecting the overall macro-scale texture. The σ_{RMS} remains approximately 262 nm, indicating that the macro-scale roughness profile is maintained. In contrast, VU-type substrate exhibits a reduction in σ_{RMS} after depositing layers (see Section 4.3.2).

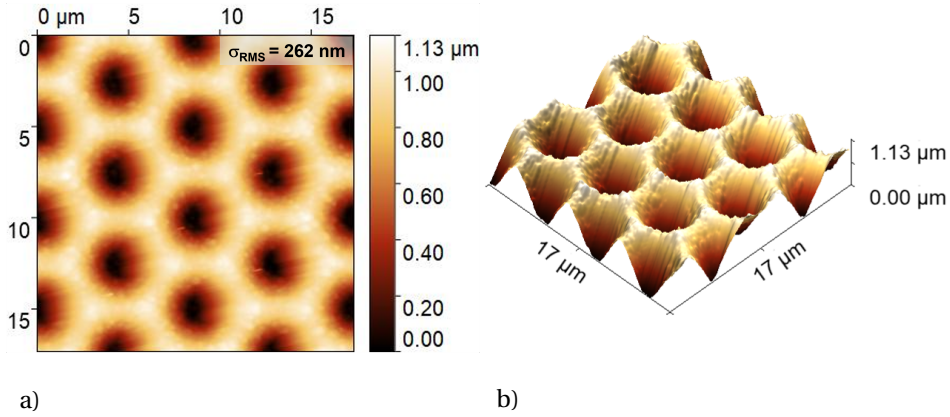

Figure 4.10: AFM images of the honeycomb-textured glass substrate: (a) 2D top-view and (b) 3D morphology. The periodic structure exhibits a root mean square roughness σ_{RMS} = 262 nm over a 17 µm × 17 µm area.

As with the Asahi VU-type texture (Section 4.3.2), implementing the honeycomb texturing in the RCWA model requires defining a finite, periodic unit cell compatible with the boundary conditions. In this case, the full geometry of a single honeycomb unit can be effectively captured within a 6 µm × 6 µm section, which sufficiently represents the periodicity and structural features of the texture.
To enforce RCWA boundary conditions, the unit cell edges are gradually tapered to zero height, avoiding abrupt discontinuities and ensuring numerical stability during Fourier decomposition. The resulting height matrices are discretized on 1001 × 1001 grids to resolve surface features. This resolution ensures sufficient refinement in the x, y, and z directions to numerical compatibility with the spatial resolution of the $\vec{E}$ distribution.

Figure 4.11a shows a 6 µm × 6 µm honeycomb unit cell extracted from the AFM morphology of the front interface (Figure 4.3), and shows the corresponding unit cell of the rear interface (Figure 4.10). Figure 4.11b and Figure 4.11d display the same structures after application of the 3D Tukey window function. This preprocessing step enables accurate representation of the honeycomb morphology in RCWA while maintaining computational feasibility and minimizing boundary artifacts.

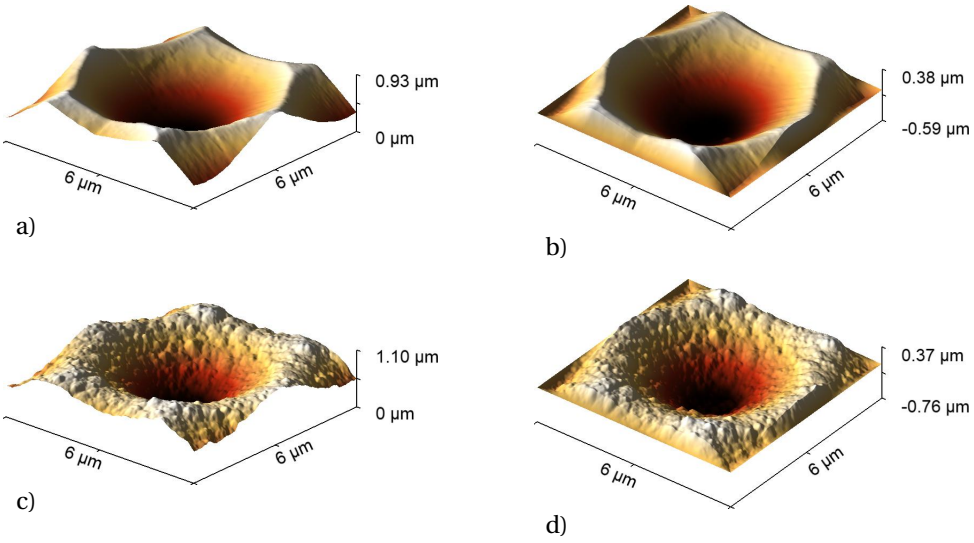

Figure 4.11: Preprocessing of AFM-derived honeycomb morphologies for RCWA simulations. (a) 6 µm × 6 µm unit cell of the front interface and (b) same unit cell after application of the 3D Tukey window function. (c) 6 µm × 6 µm unit cell of the rear interface and (d) same unit cell after Tukey window preprocessing.

4.3.3.1 Optical constants

The optical constants of the TCO layers at the front electrode and of the intrinsic nc-Si:H absorber are shown in Figure 4.12. The optical properties of the remaining layers in the device, the glass substrate, the p-type and n-type SiO_x layers, and the Ag back contact, are provided in Figure 4.8 and discussed in Section 4.3.2.1.

Figure 4.12a presents the refractive index and extinction coefficient spectra of the optimized TCO stack, consisting of hydrogenated indium oxide (IO:H) and zinc oxide (ZnO). The optical constants are obtained from spectroscopic ellipsometry and fitted using combined Cody–Lorentz and Drude models, capturing refractive index dispersion, ultraviolet absorption, and free-carrier absorption in the near-infrared. The layers are deposited under optimized conditions to balance optical transparency and electrical conductivity, ensuring high transmission while maintaining sufficient carrier transport, as discussed in Chapter 2.

Optically, IO:H exhibits a peak refractive index of 2.4 at 320 nm, while ZnO peaks at 2.3 near 380 nm. The optical bandgaps are approximately 3.7 eV for IO:H and 3.0 eV for ZnO. IO:H exhibits stronger near-infrared FCA absorption, whereas ZnO shows lower absorption. Controlling FCA absorption in IO:H is therefore essential to minimize parasitic losses and sustain high photocurrent generation in devices with absorption extending beyond 1 µm.

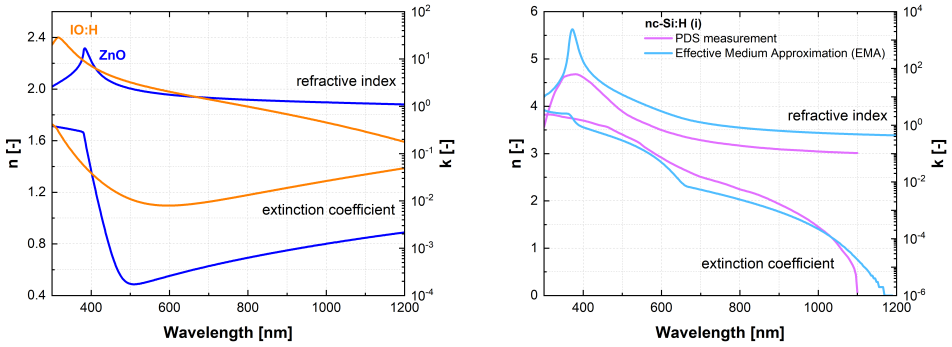

Figure 4.12: Refractive index (n) and extinction coefficient (k) spectra of: (a) IO:H and ZnO; (b) nc-Si:H, with optical constants obtained from PDS ([162]) and EMA fitting of SE data (this work).

Reliable optical constants of nc-Si:H are essential for realistic device simulation but remain challenging to obtain due to its heterogeneous microstructure. Figure 4.12b compares the refractive index and extinction coefficient spectra obtained by photothermal deflection spectroscopy (PDS) [198] and by effective medium approximation (EMA) [199–201].

In the PDS method, parasitic contributions such as defect-related absorption are subtracted from the raw data to approximate a more representative extinction coefficient [162]. Additional corrections account for interference effects arising from inhomogeneity along the growth direction.

In this work, the optical constants are obtained from spectroscopic ellipsometry measurements of a 250 nm nc-Si:H film deposited on Corning glass. The dielectric function is modeled using a Bruggeman EMA, treating the film as a mixture of crystalline and amorphous silicon phases. The optical constants of the constituent materials are taken from the J.A. Woollam and Palik datasets [184, 202].

Within the Bruggeman formalism, the effective dielectric function is determined self-consistently, from which the refractive index and extinction coefficient are obtained, inherently satisfying the Kramers–Kronig relations. The approach assumes bulk-like polarizability of the constituent phases and structural homogeneity on the wavelength scale, conditions that are fulfilled for the optimized material studied here.

Previous studies indicate that a crystalline volume fraction of 60–65% yields optimal solar cell performance, which is consistently achieved in this work through precise control of plasma conditions during growth [203].

The EMA approach yields smooth spectral behavior and avoids artifacts commonly associated with PDS. The extracted optical constants exhibit an optical bandgap close to 1.12 eV and accurately describe the dielectric response of the material, providing a reliable basis for optical modeling of nc-Si:H solar cells.

4.3.4. Optical solvers overview

Table 4.2 summarizes the key differences between RCWA and ray optics solvers. RCWA requires periodic boundary conditions; thus, measured textures are downscaled and tapered at the unit cell edges using a Tukey window to enforce continuity. Ray optics does not impose such constraints and can directly incorporate the measured morphology.
In single-junction architectures, the absorber layer is treated incoherently. The thin layers between the glass substrate and the absorber define the front interface, while those between the absorber and the metallic back contact define the back interface of the optical design.
At each defined interface, the corresponding AFM morphology is either preserved or reshaped depending on the solver requirements. Both methods rely on experimentally determined optical constants of the device materials.
The most pronounced difference lies in computational demand: RCWA typically requires about one week for device-scale runs, whereas ray optics simulation completes within 30 minutes. Further details on computation time and resolution are provided in Section 4.4.1 and Section 4.4.2 for the a-Si:H and nc-Si:H single-junction devices, respectively.

Table 4.2: RCWA and ray optics solver comparison for optical performance prediction in TF-Si solar cells.

Aspect	RCWA	Ray optics
Boundary conditions	Texture approximation required	Not applicable
Texture	Downscaled AFM maps + Tukey window (tapered edges)	AFM maps
Coherent layers	Front and back interfaces	Front and back interfaces
Optical constants	Experimentally characterized	Experimentally characterized
Computation time	~ 1 week	< 30 min

4.4. Single-junction solar cells validation

This section presents the simulated optical performance of TF-Si single-junction solar cells. Predictions from ray optics and rigorous coupled-wave analysis are compared with experimental measurements of external quantum efficiency (EQE) and total front reflection losses (1–R) from in-house fabricated devices. Section 4.4.1 focuses on the a-Si:H solar cell on random nano-textured Asahi VU-type glass, while Section 4.4.2 examines the nc-Si:H device on periodic honeycomb-textured glass.

4.4.1. a-Si:H solar cell optical performance

Figure 4.13 shows a comparison between simulated and measured optical response for the a-Si:H single-junction solar cell on random nano-textured Asahi VU-type glass. The results include predictions from ray optics and RCWA applied to the device structure described in Section 4.3.2. A wavelength step of 10 nm is used in both models to ensure consistency.
The RCWA simulations are performed with convergence-optimized settings: 125 sublayers, a 25-point spatial grid in all directions, and 17 Fourier modes, sufficient for accurate thin-film solar cell modeling [204, 205]. The presented results require approximately one week of computation with RCWA and 30 minutes with ray optics.

The ray optics model shows close agreement with experiment: the simulated a-Si:H absorptance matches the measured EQE, and 1–R reproduces the reflection losses across the full spectral range. In contrast, RCWA shows deviations, particularly in the near-infrared, where absorption is underestimated and reflection losses are overestimated.
The dip between 300–350 nm in the measured 1–R likely arises from additional scattering in the TCO, which is not captured by either model. Oscillations in the 550–800 nm range are attributed to thin-film interference within the multilayer stack and are only partially reproduced due to the different treatments of coherence and interface morphology.

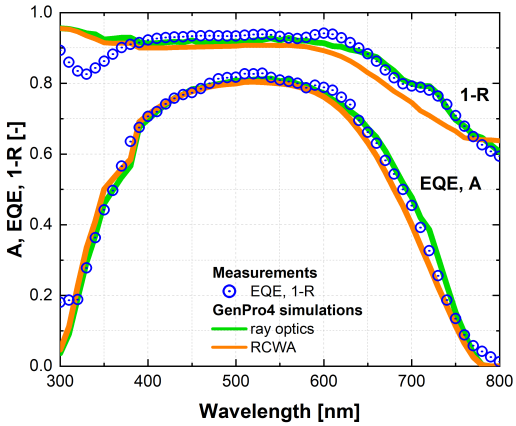

Figure 4.13: Optical performance of the a-Si:H single-junction solar cell on Asahi VU-type glass. Blue dots represent measured external quantum efficiency (EQE) and total reflection losses (1-R). Green lines show simulated absorptance (A) in the a-Si:H absorber and 1-R obtained with the ray optics, while orange lines show the corresponding results from RCWA model.

Table 4.3 summarizes the short-circuit current density from EQE and the implied photocurrent density predicted by the models. Assuming every absorbed photon in the a-Si:H absorber contributes to charge collection (i.e., negligible electrical losses), the J_{sc} extracted from EQE agrees closely with the J_{ph} from the ray optics model, indicating its predictive accuracy. The photocurrent estimated by the RCWA model is noticeably lower than the measured J_{sc}, reflecting limitations of this approach under the current simulation conditions.

Table 4.3: EQE short-circuit current density ($J_{sc,\,EQE}$), ray optics and RCWA implied photocurrent density (J_{ph}) for the a-Si:H solar cell on Asahi VU-type glass. The measurement uncertainty in $J_{sc,EQE}$ is quantified using the root-mean-square error, yielding RMS ≈ 0.7 % (absolute).

Method	J_{ph} or $J_{sc,\,EQE}$ [mA/cm^2]
RCWA	15.62
Ray optics	16.08
EQE measurement	16.01

A key limitation arises from the Asahi VU-type substrate morphology: its non-periodic nanofeatures are not fully compatible with the inherently periodic RCWA framework, which can lead to inaccuracies in scattering and angular redistribution. Despite its theoretical rigor, RCWA is therefore less suited for this case, whereas the simpler and faster ray optics model provides a more reliable description of the optical behavior of the a-Si:H solar cell.
Over the spectral range of 300–800 nm, the root mean squared error (Equation 4.2 in Section 4.2) amounts to 3.6% for the ray optics and 3.3% for RCWA when comparing simulated absorptance with measured EQE. These values confirm that both models reproduce EQE with good accuracy, with RCWA performing slightly better on average.
For 1–R, the deviations are 3.7% for ray optics and 4.7% for RCWA, consistent with the trends in Figure 4.13, where the ray optics model better captures the experimental reflectance across the spectrum. Together with the J_{sc} analysis in Table 4.3, these results show that both approaches are quantitatively reliable, while the ray optics model achieves comparable or better agreement with experiment and offers substantially higher computational efficiency for the a-Si:H solar cell on random nano-textured glass.

4.4.1.1 Scattering matrices

Figure 4.14 shows the angular scattering matrices calculated at different interfaces of the a-Si:H solar cell using ray optics and RCWA. In GenPro4, scattering matrices describe the probability of light being reflected or transmitted between angular intervals on both sides of an interface [170]. Each matrix is represented as a 2D map, with columns corresponding to incoming angles and rows to outgoing angles, spanning ± 90° relative to the surface normal. Further details are provided in Appendix C.
At the flat air/glass interface (Figure 4.14a), reflection is purely specular and transmission follows Snell's law due to the refractive index contrast. Figure 4.14b and Figure 4.14c show the scattering matrices of the FTO-coated Asahi glass/a-Si:H interface calculated by ray optics and RCWA, respectively. Figure 4.14d and Figure 4.14e present the corresponding results for the absorber/back-contact interface.
Ray optics (Figure 4.14b and Figure 4.14d) produces broad angular redistribution, with significant scattering into oblique angles, consistent with the diffuse nature of the random VU-type texture. In contrast, RCWA (Figure 4.14c and Figure 4.14e) concentrates energy in the specular direction and a limited number of diffraction orders, reflecting the periodic assumptions and finite harmonic truncation inherent to the method.
These differences directly affect absorption and photocurrent generation. By capturing diffuse angular redistribution, ray optics reproduces the light-trapping behavior of the Asahi VU-type glass and agrees well with experimental trends. RCWA, by underestimating diffuse scattering, does not fully capture long-wavelength light confinement in this device architecture.

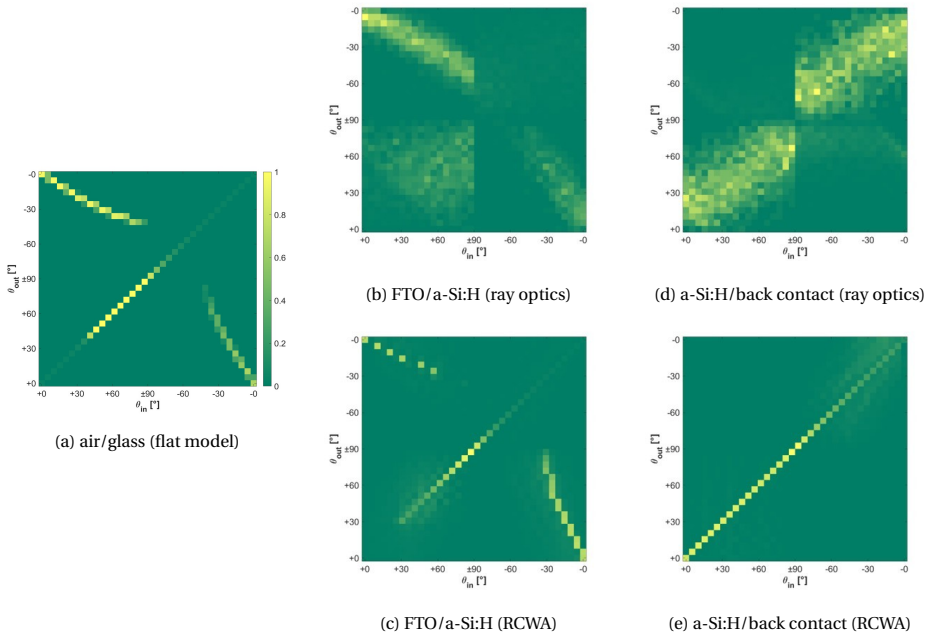

Figure 4.14: Angular scattering matrices of the a-Si:H solar cell on Asahi VU-type glass: (a) flat air/glass interface; (b, c) glass–absorber and absorber/back-contact interfaces from ray optics; (d, e) corresponding RCWA results. The matrices are shown as 2D maps with incident (ϑ_{in}) and scattered (ϑ_{out}) angles over ± 90° (calculated for λ = 800 nm).

4.4.2. nc-Si:H solar cell optical performance

Figure 4.15 shows a comparison between simulated and measured optical response for the nc-Si:H single-junction solar cell on periodic honeycomb-textured glass. The RCWA simulations are performed with convergence-optimized settings: 100 sublayers, a spatial resolution of 50 nm in the x–y plane and 10 nm along z, and 17 Fourier modes.

A spectral interval of 100 nm is used to limit computation time. The RCWA spectra are then interpolated using a shape-preserving cubic scheme to match the 20 nm resolution of the ray optics model and measurements, without introducing artificial oscillations. In contrast, the ray optics simulations are completed within approximately 30 minutes.

The ray optics model shows very good agreement with experiment, reproducing both the absorptance in the nc-Si:H layer and the 1-R losses across the full spectral range. In contrast, RCWA systematically underestimates absorption and overestimates reflection, with the largest deviations observed between 800 and 1100 nm. Moreover, RCWA does not capture the interference feature between 400 and 500 nm, which originates from the TCO front contact.

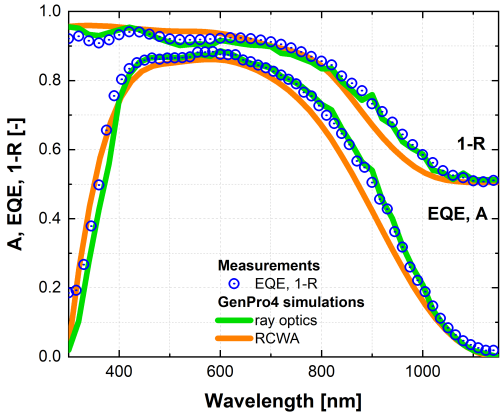

Figure 4.15: Optical performance of the nc-Si:H single-junction solar cell on honeycomb-textured glass. Blue dots represent measured external quantum efficiency (EQE) and total front reflection losses (1-R). Green lines show simulated absorptance (A) in the nc-Si:H absorber and 1-R obtained with the ray optics, while orange lines show the corresponding results from RCWA model.

Table 4.4 summarizes the J_{sc} extracted from EQE and the J_{ph} predicted by the two models, under the assumption that each absorbed photon generates a collected carrier. The J_{sc} obtained from EQE shows excellent agreement with J_{ph} from the ray optics model, confirming its high predictive accuracy. The RCWA model yields a significantly lower photocurrent, reflecting its limited ability to describe light trapping and scattering in this architecture under the chosen input settings.

Table 4.4: EQE short-circuit current density ($J_{sc,\,EQE}$), ray optics and RCWA implied photocurrent density (J_{ph}) for the nc-Si:H solar cell honeycomb-textured glass. The measurement uncertainty in $J_{sc,EQE}$ is quantified using the root-mean-square error, yielding RMS ≈ 0.7 % (absolute).

Method	J_{ph} or $J_{sc,\,EQE}$ [mA/cm^2]
RCWA	27.90
Ray optics	28.90
EQE measurement	28.90

Over the 300–1150 nm range, the absorptance predicted by the ray optics model deviates on average by 4.0% from the measured EQE, whereas RCWA shows a larger deviation of 5.2%. For the 1-R losses, the ray optics model again provides the closer match, with an average deviation of 1.7%, compared to 3.2% for RCWA. These larger deviations observed for RCWA should not be interpreted as fundamental shortcomings of the method, but rather as a consequence of the limited parameter optimization carried out in this study. With further refinement of the numerical settings and improved preprocessing of the input textures, the accuracy of RCWA could be enhanced.
Nevertheless, for the present case, the ray optics model offers a more accurate, reliable, and markedly faster description of the optical performance of the nc-Si:H solar cell on periodic honeycomb-textured glass.

4.4.2.1 Scattering matrices

Figure 4.16 compares the angular scattering matrices calculated at different interfaces of the nc-Si:H single-junction solar cell using ray optics and RCWA.

At the glass/nc-Si:H interface (Figure 4.16b), ray optics predicts pronounced angular redistribution, with a significant fraction of the light scattered into oblique angles. This spread is broader than in the Asahi VU-type case (Figure 4.14), reflecting the larger feature size and aspect ratio of the honeycomb texture. In contrast, the corresponding RCWA result (Figure 4.16c) is confined to a limited set of discrete diffraction orders, with only modest angular broadening, indicating that angular redistribution remains governed by diffraction and interference.

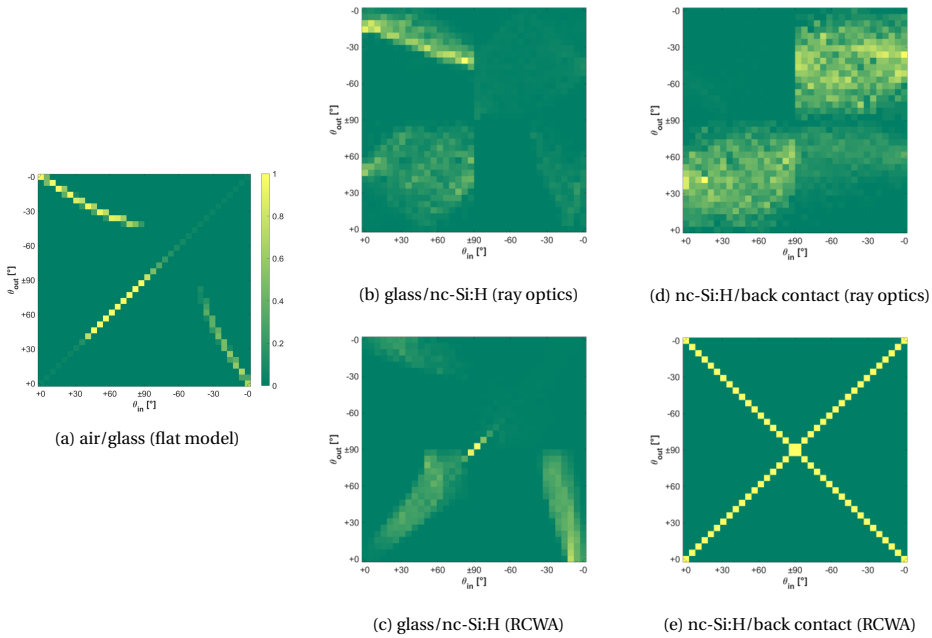

Figure 4.16: Angular scattering matrices of the nc-Si:H solar cell on honeycomb-textured glass: (a) flat air/glass interface; (b, c) glass–absorber and absorber/back-contact interfaces from ray optics; (d, e) corresponding RCWA results. The matrices are shown as 2D maps with incident (ϑ_{in}) and scattered (ϑ_{out}) angles over ± 90° (calculated for λ = 1100 nm).

At the nc-Si:H/back-contact interface, ray optics (Figure 4.16d) predicts strong redistribution toward high propagation angles, promoting internal reflection and increasing the optical path length. The RCWA matrix (Figure 4.16e) instead exhibits highly symmetric, localized features forming a cross-like pattern, suggesting preferential coupling into specific diffraction orders. However, this behavior should be interpreted with caution. Since each incident-angle column is expected to satisfy energy conservation after normalization, the presence of simultaneously intense symmetric branches may indicate artifacts related to normalization, angular mapping, or binning, rather than a purely physical scattering response.

4.5. Tandem solar cell validation

The optical modeling is first validated on two single-junction devices: an a-Si:H solar cell on a randomly nano-textured Asahi VU-type substrate (Section 4.4.1) and an nc-Si:H solar cell on a periodically micro-textured honeycomb substrate (Section 4.4.2). Two complementary solvers are employed: a simplified refractive-regime approach based on ray tracing, and a full wave-optical method based on RCWA.

While RCWA, grounded in rigorous electromagnetic theory, encounters challenges when handling experimentally realistic input textures and requires substantially higher computational effort, the ray optics model, when supplied with accurate optical constants and realistic interface morphologies, successfully reproduces both absorptance and total front reflection losses. These findings establish ray tracing as a robust and computationally efficient predictive tool for TF-Si devices.

Building on this validation, the investigation is extended to an a-Si:H/nc-Si:H tandem solar cell fabricated on honeycomb-textured glass. Tandem configurations leverage the complementary absorption ranges of the wide-bandgap a-Si:H top cell (1.65 eV) and the narrow-bandgap nc-Si:H bottom cell (1.12 eV), enabling improved utilization of the solar spectrum. Accurate prediction of the optical response is particularly critical in this case, as both current matching and light-trapping efficiency determine overall device performance.

Accordingly, ray optics simulations, validated as reliable and computationally efficient, are employed here together with detailed material characterization and morphological inputs (see Section 4.3) to assess the optical behavior of the tandem architecture. In practice, the simulations are performed with a wavelength resolution of 10 nm, keeping the total runtime below 30 minutes.

4.5.1. a-Si:H/nc-Si:H solar cell structure

A schematic representation of the device structure is provided in Figure 4.17. For visual clarity, layer thicknesses are not drawn to scale. The front electrode consists of a 130 nm IO:H layer and a 5 nm ZnO buffer layer. The top cell (ToC) comprises a p–i–n junction with a 20 nm p-type SiO_x layer, a 3 nm intrinsic a-SiO_x buffer, a 300 nm a-Si:H absorber, and a 50 nm n-type SiO_x layer. The bottom cell (BoC) is also a p–i–n junction, incorporating a 3 µm nc-Si:H absorber between 20 nm p-type and 50 nm n-type SiO_x layers. The rear stack consists of an 80 nm ZnO back reflector and a 300 nm Ag back contact. Optical constants for all layers are reported in Figure 4.8 (Section 4.3.2) and Figure 4.12 (Section 4.3.3).

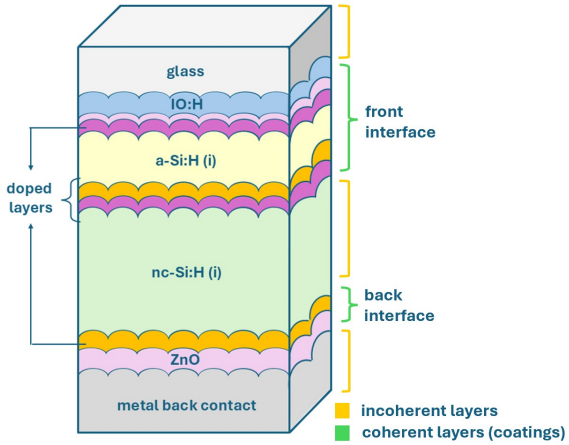

Figure 4.17: Schematic of a-Si:H/nc-Si:H tandem device structure on periodic honeycomb-textured glass (not to scale). Layers sequence: glass (0.7 mm) / IOH (130 nm) / ZnO (5 nm) / p-type nc-SiO_x (20 nm) / a-SiO_x (3 nm) / intrinsic a-Si:H (300 nm) / n-type nc-SiO_x (50 nm) / p-type nc-SiO_x (20 nm) / nc-Si:H (3 µm) / n-type nc-SiO_x (50 nm) / ZnO (80 nm) / Ag (300 nm).

In the optical model, the TCO front contact and the whole a-Si:H top cell are treated coherently as an assumed simplification, since their sub-micrometer thicknesses fall within the coherence length of light and are dominated by interference effects. The thick nc-Si:H absorber in the bottom cell is instead modeled incoherently due to its micrometer-scale thickness and strong internal scattering, which randomize phase and suppress coherent interference.
The front textured interface in the model is defined by all layers between the glass substrate and the intrinsic nc-Si:H absorber. The rear textured interface consists of the n-type SiO_x of the bottom cell together with the ZnO/Ag back reflector. The honeycomb texture is implemented at both interfaces, following the same assumptions used for the nc-Si:H single-junction device (Section 4.4.2), where conformal growth preserves the textured morphology throughout the stack.

4.5.2. a-Si:H/nc-Si:H solar cell optical performance

Figure 4.18 compares the measured 1-R and EQE spectra with the modeled optical response. The agreement is very good across the full spectral range, with both the overall spectral shape and the interference fringes between 550–800 nm accurately reproduced. This demonstrates that the combination of ray optics with coherent treatment of thin layers captures both scattering and interference effects.
For the top cell, the simulated absorptance is slightly lower than the EQE in the 300–450 nm range, suggesting a modest overestimation of parasitic absorption in the supporting layers. The EQE peak is lower than predicted, likely reflecting measurement-related uncertainties.
For the bottom cell, the EQE closely follows the simulated absorptance across the entire spectrum, confirming accurate transmission through the top cell and absorption in the nc-Si:H layer. The comparison of short-circuit current densities with implied photocurrent densities further supports this consistency, indicating that performance is limited by the top cell.

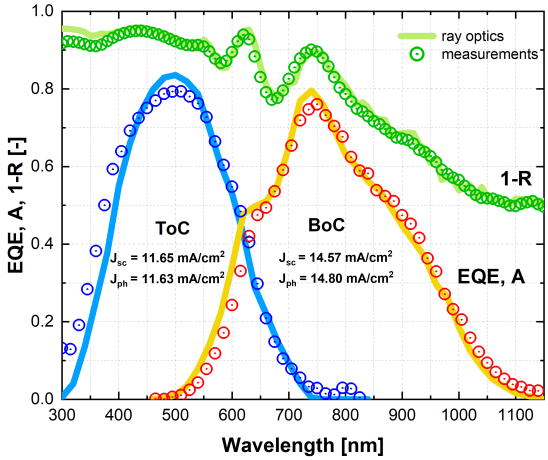

Figure 4.18: Optical performance of the a-Si:H/nc-Si:H tandem solar cell on honeycomb-textured glass: measured external quantum efficiency (EQE) of the a-Si:H top cell (ToC, blue dots) and nc-Si:H bottom cell (BoC, red dots), with corresponding simulated absorptance (A) shown as blue and yellow lines. Total front reflection losses (1–R) are shown as green dots (measured) and a green line (simulated). $J_{sc,\,EQE}$ and J_{ph} predicted by ray optics are reported for both ToC and BoC. The measurement uncertainty in $J_{sc,EQE}$ is quantified using the root-mean-square error, yielding RMS ≈ 0.7 % (absolute).

The quantitative comparison between modeled and measured spectra for the a-Si:H/nc-Si:H tandem solar cell is performed using the RMSE metric defined in Equation 4.2 (Section 4.2). Over the 300–800 nm range, the top cell A deviates on average by 6.1% from the measured EQE, while in the 450–1150 nm range the nc-Si:H bottom cell shows an average deviation of 3.6%. For the total front reflection losses over 300–1150 nm, the deviation between simulation and experiment is 1.7%. These results confirm that the ray optics model, when complemented by coherent treatment of thin layers, accurate optical constants, and realistic interface morphologies provides a reliable, fast and quantitatively accurate description of the optical performance of the tandem device on periodic micro-textured glass.

4.6. Conclusions

Thin-film silicon solar cells are used as a framework to evaluate how accurately the optical response of devices on multiscale textured substrates can be predicted. Two representative architectures are fabricated in-house: an a-Si:H cell on randomly nano-textured Asahi glass and an nc-Si:H cell on a micro-periodic honeycomb-textured substrate. In both cases, the analysis incorporates experimentally derived optical constants and realistic interface morphologies directly into the simulations.

A direct comparison is performed between a simplified ray optics model operating in the refractive regime and rigorous coupled-wave analysis (RCWA). While RCWA captures electromagnetic scattering in detail, its application is constrained by periodic boundary conditions and high computational cost. Ray optics, in contrast, directly accommodates realistic morphologies. When supplied with experimental inputs, it reproduces absorptance and reflection spectra with accuracy comparable to or exceeding that of RCWA, while reducing computation time from approximately one week to less than 30 minutes.

Benchmarking against measured external quantum efficiency (EQE) and front reflection losses (1–R) of single-junction a-Si:H and nc-Si:H devices quantifies the predictive accuracy of both methods using the root-mean-square error (RMSE). Across all cases, the ray optics model achieves deviations comparable to or smaller than RCWA (typically 2–6%), while maintaining substantially higher computational efficiency. Extending the approach to an a-Si:H/nc-Si:H tandem solar cell on honeycomb-textured glass, the simulations reproduce the measured response with deviations within 6%. The predicted photocurrent densities (J_{ph}) and short-circuit currents (J_{sc}) show a current mismatch below 0.2 mA/cm^2, demonstrating the robustness of the approach.

These results show that ray optics, combined with accurate optical constants and realistic morphology, can reliably capture absorption, reflection, and angular scattering in multiscale textured thin-film solar cells. This establishes ray optics as a computationally efficient and predictive tool for thin-film silicon photovoltaics. The methodology is readily transferable to other thin-film technologies, including perovskites, where multiscale light management is central to next generation device design.

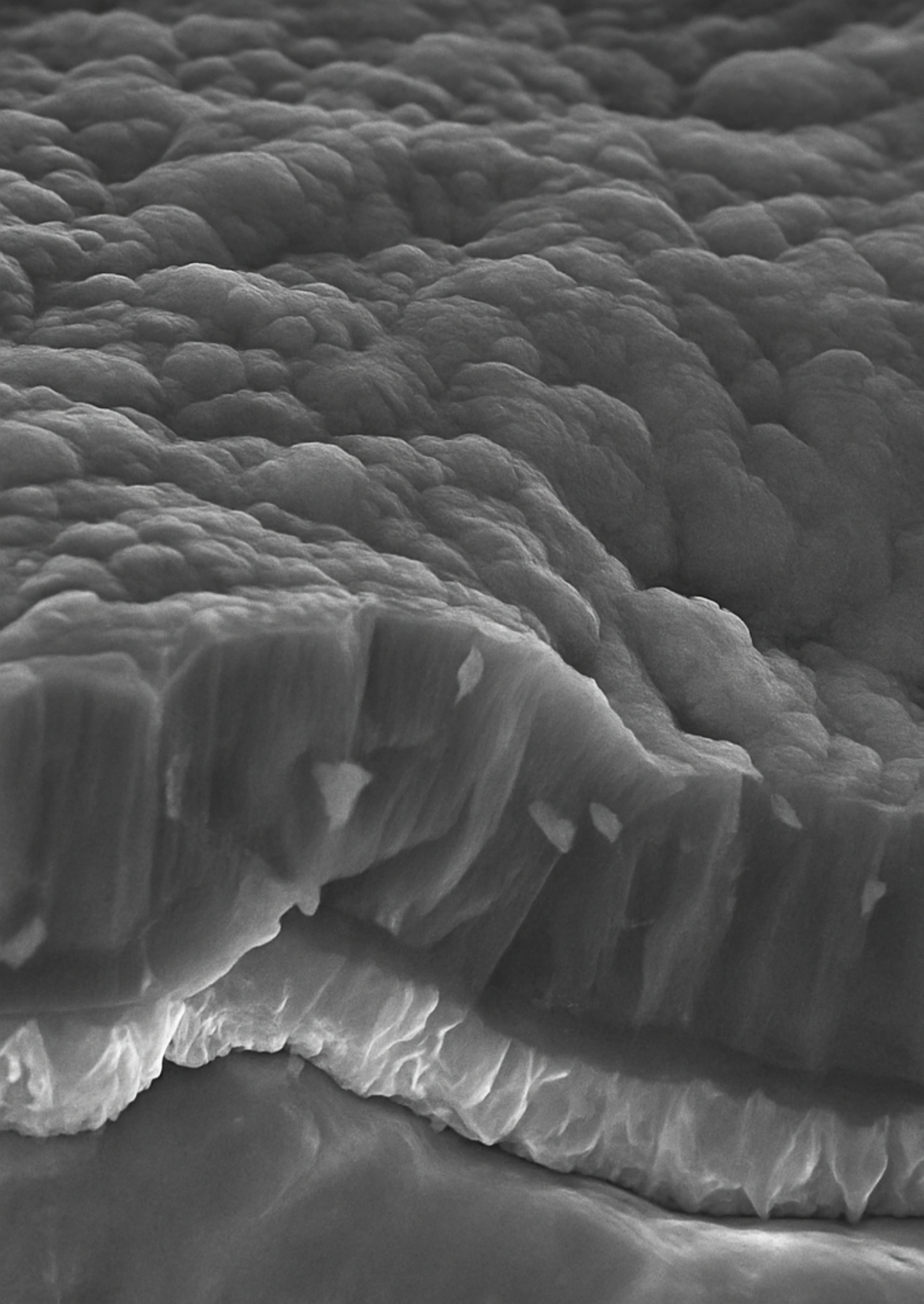

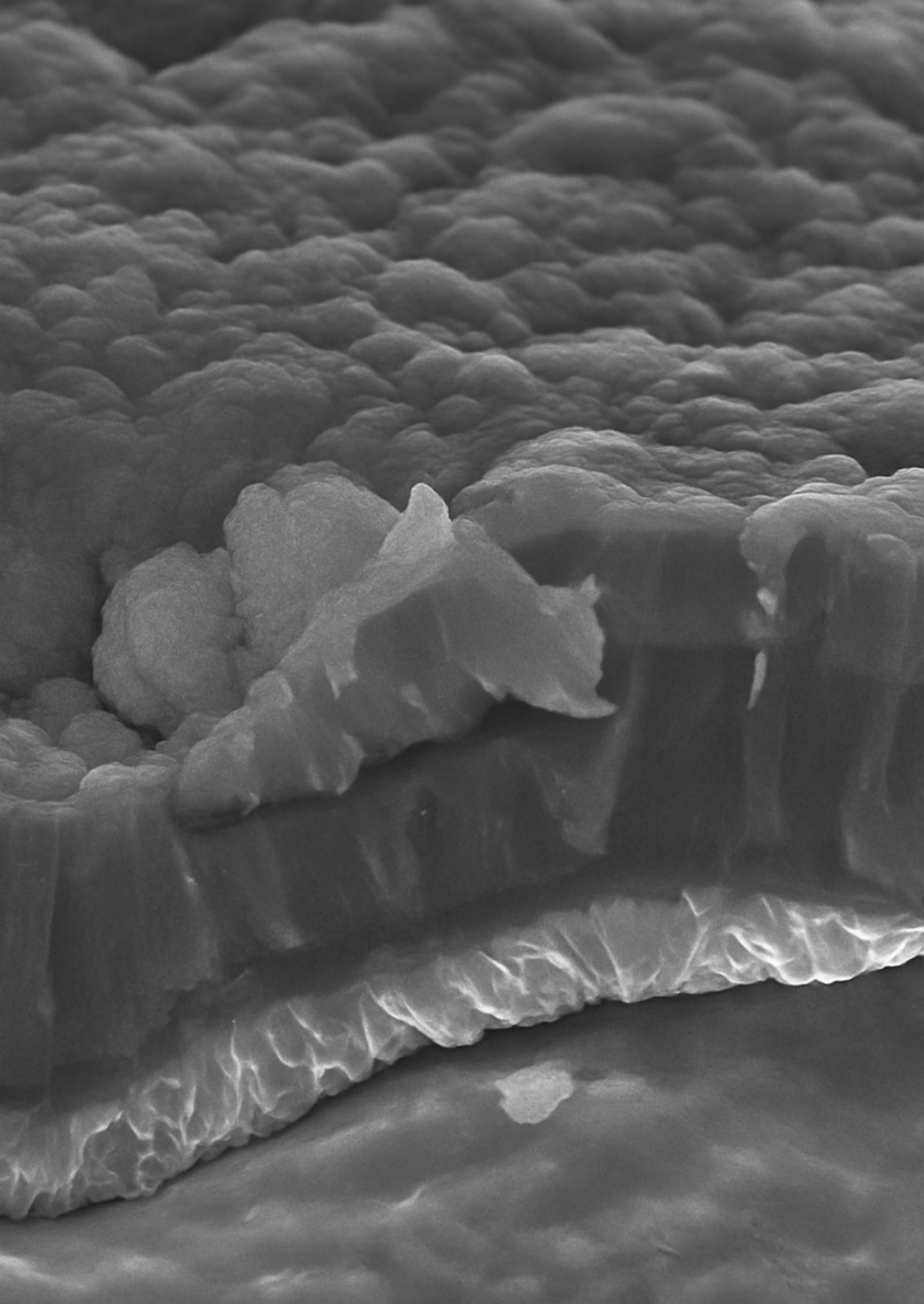

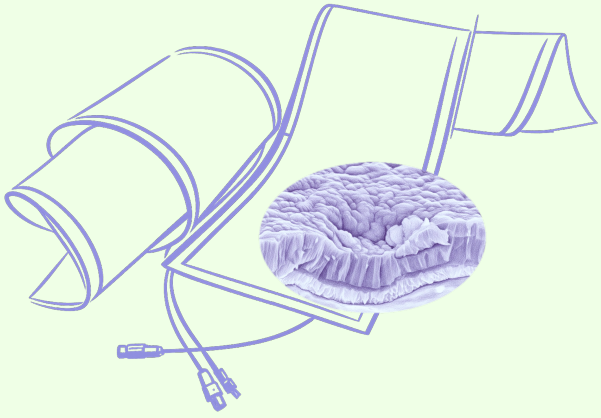

5

OPTOELECTRICAL MODELING OF FLEXIBLE & SCALABLE TF SOLAR CELLS

This chapter is based on the following manuscript under review:

Saitta, F., Huijskes, B., Padmakumar, G., van Silfhout, N., Perez-Rodriguez, P., Procel Moya, P., Santbergen, R., & Smets, A. H. M. *Bridging Flexible Perovskite Photovoltaics with Thin-Film Silicon Manufacturing through High Temperature Superstrate Foils.* EES Solar (2026).

5.1. Introduction

Perovskite solar cells (PSCs) have become one of the most intensively researched thin-film (TF) photovoltaic technologies, driven by their solution processability, tunable bandgaps, and rapid gains in power conversion efficiency (PCE). Single-junction PSCs now exceed 27% efficiency on small area devices (0.1065 cm^2), rivaling crystalline silicon and surpassing other TF technologies [20, 206]. Their low temperature processing and compatibility with diverse substrates further enable lightweight and flexible photovoltaics. However, translating these record efficiencies into scalable, mechanically flexible photovoltaic technologies remains a central challenge.

Flexible perovskite solar cells (f-PSCs) have attracted substantial interest in recent years. For small-area devices (below 1 cm^2), single-junction flexible perovskite solar cells have been reported to exceed 23% efficiency, while flexible all-perovskite tandem devices have approached 26% [207].

Early large-area flexible perovskite modules demonstrated efficiencies of 15.5% over 100 cm^2, 12.9% over 225 cm^2, and 11.8% over 400 cm^2 aperture area [208]. More recently, flexible perovskite modules exceeding 20% efficiency have also been reported [209]. In contrast, rigid glass-based perovskite modules generally continue to exhibit higher efficiencies at large scale, including a 0.73 m^2 module reaching 17.7% [210].

Achieving high PCE on flexible substrates remains challenging for conventional polymer substrates such as polyethylene terephthalate (PET) and polyethylene naphthalate (PEN) coated with indium tin oxide (ITO), due to non-uniform perovskite crystallization, limited thermal tolerance of polymeric substrates, and the intrinsic brittleness of ITO, which is prone to crack formation under mechanical strain, thereby limiting device stability and performance [211–214].

These challenges are further compounded by stringent requirements on charge transport layers (CTLs), which must provide suitable energy-level alignment with adjacent materials to enable selective carrier extraction, exhibit sufficient carrier mobility to suppress recombination losses, maintain high optical transparency, and ensure stability under thermal, chemical, and environmental stress [215, 216]. Additional limitations arise from the low thermal tolerance of polymer substrates, typically below 150 °C, together with their limited resistance to oxygen and moisture ingress [211, 217]. Collectively, these constraints motivate the development of alternative device architectures and processing strategies.

Among scalable manufacturing strategies, roll-to-roll (R2R) processing is widely regarded as one of the most promising industrial routes for flexible photovoltaics [218, 219]. LiftPV (formerly HyET Solar) has developed a distinctive manufacturing technology in which flexible thin-film silicon (TF-Si) solar devices are fabricated in a superstrate configuration on a temporary aluminum (Al) foil capable of withstanding high temperature processing.

In contrast to conventional polymer substrates, the temporary Al foil enables the deposition of transparent conductive oxides (TCOs) and Si-based layers at temperatures up to 500 °C. Following device fabrication, the back contact is sputtered and a permanent polymer carrier foil is laminated onto the stack. The temporary Al foil on the front side is removed by etching, resulting in ultralight flexible devices encapsulated between polymeric layers [15, 29, 220].

Within this process, fluorine-doped tin oxide (FTO) is deposited by atmospheric pressure chemical vapor deposition (APCVD) at 500 °C and employed as a mechanically robust and chemically stable alternative to indium tin oxide (ITO) for the front electrode. Consequently, temporary Al foils coated with FTO provide a promising route to overcome the thermal limitations of polymeric substrates while enabling the integration of high quality TCOs [221, 222].

Although this manufacturing concept is well established in TF-Si photovoltaics, its potential application to PSCs remains largely unexplored [223]. A schematic representation of the LiftPV processing sequence is shown in Figure 5.1, where the main steps of the R2R fabrication line are illustrated from left to right and the device layers are deposited in a superstrate configuration.

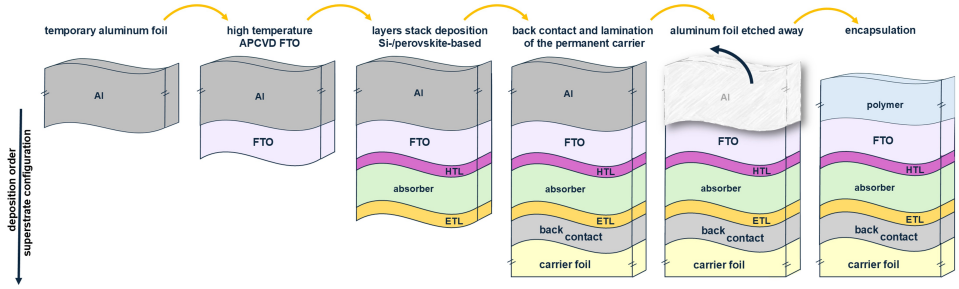

Figure 5.1: Schematic processing sequence of the LiftPV technology: a temporary Al foil is coated with APCVD-grown FTO, followed by deposition of the p–i–n stack, including the hole transport layer (HTL), absorber (Si or perovskite), and electron transport layer (ETL), and a metal back contact. A polymer carrier is laminated, the Al foil is removed by etching, and the device is completed with polymer encapsulation.

In this work, the manufacturing concepts established in TF-Si technologies are extended to flexible perovskite solar cells. Predictive optoelectrical simulations are employed as a design tool to investigate viable device architectures compatible with superstrate foils and to assess their performance potential.

To support this exploration, a validated thin-film silicon modeling framework is extended by combining optical simulations in GenPro4 with two-dimensional TCAD simulations in Synopsys Sentaurus [170, 224]. The approach leverages the well-established device physics of hydrogenated amorphous silicon (a-Si:H) and hydrogenated nanocrystalline silicon (nc-Si:H) technologies as an industrial reference point.

After benchmarking against experimental single- and tandem-junction devices, the framework is applied to conceptual flexible architectures enabled by high temperature superstrate foils. These include (i) a hybrid tandem combining a wide-bandgap a-Si:H top cell with a tin–lead (Sn–Pb) perovskite bottom cell, and (ii) an all-perovskite tandem integrating wide- and narrow-bandgap absorbers.

In the hybrid architecture, the a-Si:H top junction simultaneously functions as a photovoltaic layer and UV–blue spectral filter below 450 nm, potentially mitigating halide migration, interfacial defect formation, and photochemical degradation [225]. Its amorphous silicon robustness also limits oxygen and moisture ingress [226], which is advantageous for flexible devices with less effective encapsulation.

5.2. Methods

5.2.1. Simulation framework

Optical absorption in the simulated devices is evaluated using the GenPro4 optical simulator developed [170]. The model accounts for both coherent and incoherent light propagation, with light scattering described through a ray-tracing approach that captures angular redistribution and geometric light trapping in textured layers. Optical constants, layer thicknesses, and interface morphologies are taken from experimentally validated datasets [227]. Further details are presented in Chapter 4.

The simulation output provides spectrally and spatially resolved absorption profiles $A(x,\lambda)$, from which the local generation rate is derived as showed in Equation 5.1:

$$G(x,\lambda) = \frac{A(x,\lambda)}{\Delta x}\,\Phi_{AM1.5G}(\lambda) \tag{5.1}$$

where Δx is the slice thickness of the discretized simulation grid and $\Phi_{AM1.5G}(\lambda)$ (photon cm^{-2} s^{-1} nm^{-1}) is the AM1.5G spectral photon flux density. This formulation ensures photon conservation, assuming one electron–hole pair per absorbed photon [228].

The depth- and wavelength-resolved generation profiles are imported into Sentaurus TCAD [224]. Sentaurus TCAD performs two-dimensional (2D) drift–diffusion simulations that self consistently solve Poisson's equation and carrier-continuity equations under Fermi–Dirac statistics, enabling rigorous modeling of electrostatics and charge transport.

The framework allows explicit representation of sub-gap defect states, including exponential band tails and Gaussian deep traps, as well as tunneling mechanisms such as trap-assisted (TAT) and band-to-band (BTB) tunneling. Surface recombination velocities (S_n, S_p) describe interfacial losses, while adaptive meshing and numerical stabilization ensure convergence in devices with high defect densities and strong internal fields [229].

Each layer of the simulated device stack is defined by its fundamental electronic parameters: bandgap (E_g), electron affinity (χ), dielectric permittivity (ε), and carrier mobilities (μ_n, μ_p), together with material-specific physical models that describe charge transport and recombination.

For semiconductors such as a-Si:H and nc-Si:H, localized defect distributions are represented by exponential band-tail states near the band edges and Gaussian mid-gap traps, with electron and hole capture cross sections (σ_n, σ_p) governing Shockley–Read–Hall (SRH) recombination dynamics.

For perovskite absorbers, carrier recombination is modeled through an effective bulk lifetime (τ) rather than explicit defect distributions. This approach reflects the relatively delocalized electronic structure of perovskites and the experimentally observed dominance of band-to-band and SRH recombination under operating conditions [230, 231].

Charge transport layers (CTLs) define the energy landscape at the absorber interfaces in p–i–n architectures. The hole transport layer (HTL) selectively conducts holes while blocking electrons, whereas the electron transport layer (ETL) performs the complementary function. Charge transport across these heterointerfaces occurs through thermionic emission or tunneling depending on the barrier height and width determined by the conduction- and valence-band offsets (ΔE_C, ΔE_V) and the local carrier concentration [232, 233].

The TA and B2B tunneling mechanisms are implemented through non-local meshes, while surface-recombination velocities define carrier losses at defective interfaces. This treatment enables accurate modeling of band alignment and defect-assisted recombination at heterojunctions.
Numerical stability is ensured through adaptive meshing with local refinement in regions of strong band bending or high electric fields, combined with quasi-stationary voltage stepping. The EQE spectra are computed by sweeping the probe wavelength under fixed bias, while bias illumination is applied to decouple the contributions of individual sub-cells in tandem configurations.
The combined GenPro4–Sentaurus TCAD framework provides a physically consistent description of optical generation, charge transport, recombination, and interfacial effects in thin-film solar cells, enabling quantitative analysis of single-junction and tandem architectures.
The simulation workflow is summarized in Figure 5.2. Optical absorption profiles calculated in GenPro4 (Chapter 4) are used to derive the generation rate, which is then imported into Sentaurus TCAD for electrical simulation.
The device structure is defined through material parameters including E_g, χ, ε, N, μ, effective tunneling masses of electrons and holes (m_t), and density of states (DOS). These parameters are coupled with the semiconductor transport equations to compute band diagrams, current density–voltage (J–V) characteristics, and external quantum efficiency (EQE) spectra.

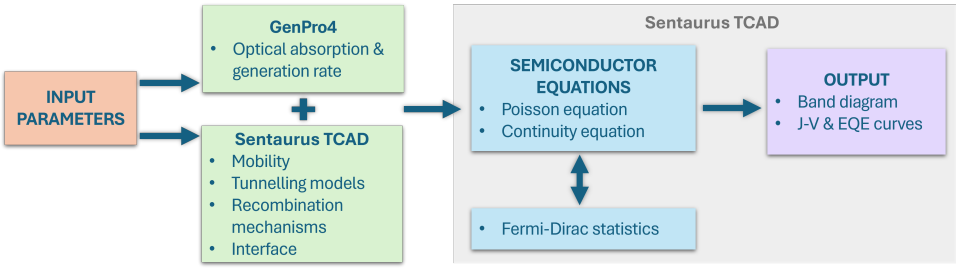

Figure 5.2: Flowchart of the simulation framework coupling GenPro4 and Sentaurus TCAD. Input parameters are processed through physical models and semiconductor equations, yielding band diagrams, current density–voltage (J–V) characteristics, and external quantum efficiency (EQE) spectra.

5.2.2. Modeling approach

A stepwise approach is adopted, starting from single-junction devices and extending to tandem architectures, which are used to validate the framework before application to flexible perovskite solar cells on aluminum foil.
The first stage focuses on single-junction TF-Si devices in a p–i–n configuration on glass, serving as a benchmark to calibrate fundamental transport and recombination parameters in a well-controlled architecture. Simulated and measured J–V characteristics and EQE spectra are matched by adjusting bulk and interfacial SRH trap densities, capture cross sections, mobility models, and contact energetics. This calibration ensures that the simulations accurately reproduce single-junction device behavior before extending the analysis to multijunction configurations.

The second stage applies the calibrated model to a-Si:H/nc-Si:H tandem devices. Simulated and experimental J–V and EQE responses are compared to verify the ability of the GenPro4–Sentaurus TCAD framework to reproduce the behavior of both sub-cells. The tandem configuration is then transferred from glass to an aluminum carrier foil, enabling direct comparison with experimental flexible devices and quantifying the influence of substrate choice on device operation.
The third stage investigates perovskite-based architectures on Al foil. A hybrid tandem combining a 1.65 eV wide-bandgap (WBG) a-Si:H top cell with a 1.23 eV narrow-bandgap (NBG) Sn–Pb perovskite bottom cell is first considered, leveraging complementary spectral absorption between silicon and perovskite absorbers. Building on this concept, the analysis is extended to an all-perovskite tandem consisting of a WBG (1.68 eV) top cell and a Sn–Pb (1.23 eV) bottom cell.
Across all stages, Sentaurus TCAD serves as the central physics-based simulation tool. Continuous validation against experimental J–V and EQE data constrains the parameter space to physically meaningful, literature-consistent values, ensuring that simulated performance improvements arise from device design rather than numerical artifacts. This stepwise progression from simple to complex architectures enables the extraction of quantitative design guidelines for f-PSCs on Al foil.

5.2.3. Device fabrication

A p–i–n a-Si:H single-junction solar cell is fabricated in superstrate configuration on 1.1 mm Asahi VU-type textured glass coated with 700 nm fluorine-doped tin oxide (FTO). A 10 nm Al-doped zinc oxide (AZO) layer is deposited next to protect the underlying FTO from hydrogen induced reduction during the deposition of silicon-based layers. The intrinsic a-Si:H absorber (300 nm) is sandwiched between 13 nm p-type and 20 nm n-type nanocrystalline silicon oxide (nc-SiO_x) layers [234, 235]. On the p-type side, a 3 nm intrinsic a-SiO_x barrier is included to prevent boron cross-contamination [180]. The device is completed with a 300 nm Ag back contact and the schematic cross-section is shown in Figure 5.3a.
A p-i-n nc-Si:H single-junction solar cells is fabricated on in-house developed honeycomb-textured glass substrate, 0.7 mm thick with a hexagonal periodicity of 6 µm [4]. The transparent front electrode consists of 135 nm hydrogenated indium oxide (IO:H) layer with 5 nm ZnO buffer. The p–i–n junction comprises 10 nm p-type nc-SiO_x, 3 nm intrinsic nc-SiO_x buffer, 3.2 µm intrinsic nc-Si:H absorber, and 20 nm n-type nc-SiO_x layer. A 60 nm ZnO layer and 300 nm Ag reflector form the back electrode. A schematic cross-section of the device is shown in Figure 5.3b.

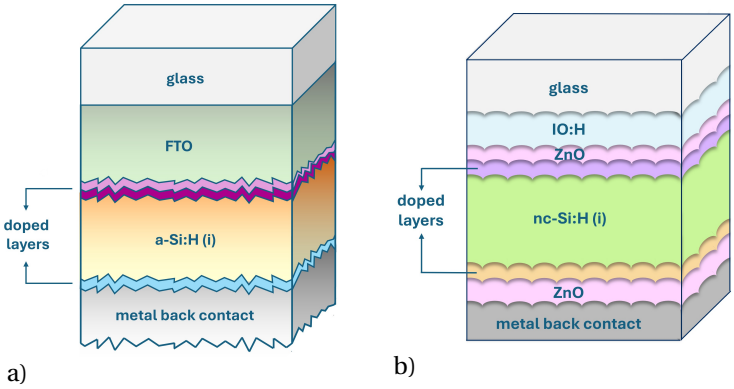

Figure 5.3: TF-Si single-junction solar cells structure (not to scale): (a) 1.1 mm Asahi VU-type glass coated with FTO (700 nm) / AZO (10 nm) / p-type nc-SiO_x (13 nm) / a-SiO_x (3 nm) / a-Si:H (300 nm) / n-type nc-SiO_x (20 nm) / AZO (10 nm) / Ag (300 nm); (b) honeycomb-textured glass (0.7 mm) / IO:H (135 nm) / ZnO (5 nm) / p-type nc-SiO_x (5 nm) / nc-Si:H (3.2 µm) / n-type nc-SiO_x (20 nm) / ZnO layer (20 nm) / Ag (300 nm).

An a-Si:H/nc-Si:H tandem device combining a WBG a-Si:H top cell (1.65 eV) with a NBG nc-Si:H bottom cell (1.12 eV) is first fabricated on honeycomb-textured glass. The transparent front electrode consists of 130 nm IO:H layer and 5 nm ZnO buffer. The top cell follows a p–i–n configuration with 20 nm p-type nc-SiO_x, 3 nm intrinsic a-SiO_x buffer, 300 nm intrinsic a-Si:H absorber, and 50 nm n-type nc-SiO_x. The bottom cell incorporates 3 µm intrinsic nc-Si:H absorber between 20 nm p-type nc-SiO_x and 50 nm n-type nc-SiO_x layers. The rear electrode is formed by 80 nm ZnO and 300 nm Ag. This architecture is illustrated in Figure 5.4a.

A flexible tandem device is fabricated in superstrate configuration on a temporary aluminum foil, where 700 nm FTO followed by 5 nm AZO are deposited on the Al foil. The top cell is then formed, comprising 10 nm p-type nc-SiO_x, a 225 nm intrinsic a-Si:H absorber, and 20 nm n-type nc-SiO_x. The bottom cell is deposited next by sequential deposition of 16 nm p-type nc-SiO_x, 2 µm intrinsic nc-Si:H absorber, and 15 nm n-type nc-SiO_x. The rear electrode consists of 80 nm AZO and 300 nm Al.

The device is then laminated onto a permanent flexible polymer carrier foil. The temporary front aluminum foil is then selectively removed by wet etching, exposing the FTO front electrode while preserving the underlying photovoltaic stack. This release step yields a freestanding flexible tandem device mechanically supported by the polymer carrier and encapsulated by polymeric layers, as previously illustrated in Figure 5.1.The final device layout after removal of the temporary aluminum foil is shown in Figure 5.4b.

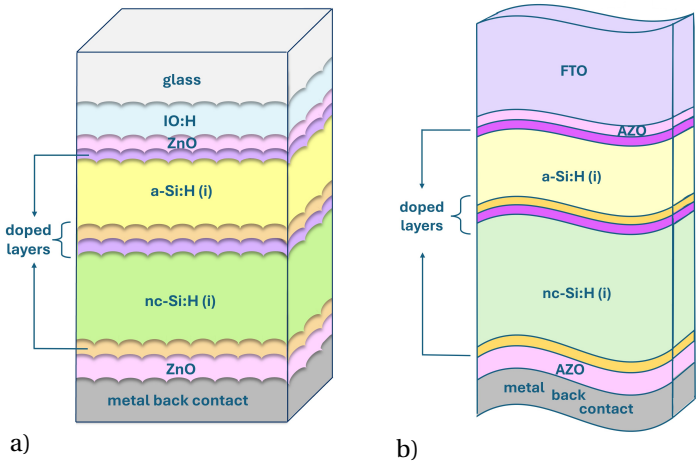

Figure 5.4: a-Si:H/nc-Si:H tandem solar cells structure (not to scale): (a) honeycomb-textured glass (0.7 mm) / IO:H (135 nm)/ ZnO (5 nm) / p-type nc-SiO_x (20 nm) / a-SiO_x (3 nm) / a-Si:H (300 nm) / n-type nc-SiO_x (50 nm) / p-type nc-SiO_x (20 nm) / nc-Si:H (3 µm) / n-type nc-SiO_x (50 nm) / ZnO (80 nm) / Ag (300 nm); (b) FTO (700 nm) / AZO (5 nm) / p-type nc-SiO_x (10 nm) / a-Si:H (225 nm) / n-type nc-SiO_x (20 nm) / p-type nc-SiO_x (16 nm) / nc-Si:H (2 µm) / n-type nc-SiO_x (15 nm) / AZO (80 nm) / Al metal back contact (300 nm).

5.2.4. Device characterization

The devices are characterized through current density–voltage (J–V) measurements and external quantum efficiency (EQE) analysis. J–V curves are measured at 25 °C under simulated AM1.5G illumination (100 mW/cm^2) using a WACOM-class AAA xenon–halogen dual-lamp continuous solar simulator. EQE spectra are recorded with an in-house developed setup based on monochromatic light, operated under short-circuit conditions (0 V).
The short-circuit current density derived from EQE ($J_{sc,EQE}$) is obtained by integrating the measured EQE with the AM1.5G reference spectrum. This procedure prevents over- or underestimation of current that may arise from spectral mismatch between the WACOM solar simulator and the AM1.5G standard. In addition, it eliminates errors associated with the determination of the active area in small-area devices.

5.3. Model validation using TF-Si devices

Before exploring flexible and perovskite-based architectures, the predictive capability of the modeling framework is validated against experimentally realized TF-Si reference devices. Single-junction and tandem a-Si:H/nc-Si:H solar cells are used as benchmark structures to verify the accuracy of the coupled optoelectrical simulations. The calibration focuses on physically meaningful material and defect parameters, whose influence is previously examined through a sensitivity analysis (see Appendix C). This validation establishes a reliable baseline before extending the framework to flexible substrates and emerging perovskite device concepts

5.3.1. Single-junction validation

The a-Si:H single-junction device serves as the first experimental benchmark for validating the optoelectrical simulation framework. The device architecture is described in Section 5.2.3 and shown in Figure 5.3a. The calibrated parameters are all listed in Appendix C.

The p-type front contact consists of a highly doped 3 nm nc-SiO_x (p^+) layer and a 10 nm moderately doped nc-SiO_x (p) layer. This graded configuration follows established TF-Si design principles [236], where the p^+ layer enhances the electric field and hole extraction, while the p-layer reduces the valence-band offset and limits interface recombination. Acceptor concentrations of 1×10^{20} cm^{-3} and 5×10^{19} cm^{-3} are assigned to the p^+ and p layers, respectively, consistent with reported values for nc-SiO_x:H [237, 238].

The electron affinities (χ) of the nc-SiO_x layers are interpolated between nc-Si (4.05 eV) and SiO_2 (0.90 eV) to reflect their mixed-phase nature. For the p-type layer (E_g = 2.84 eV), χ = 3.36–3.39 eV, while for the n-type layer (E_g = 2.42 eV), χ = 3.53–3.56 eV, yielding band offsets consistent with experimental reports [239].

The effective density of states ($N_C = N_V = 1 \times 10^{20}$ cm^{-3}) and bandgap (E_g = 1.63 eV) are tuned to match V_{oc} while remaining consistent with literature [237, 240–242]. The defect-related parameters of the intrinsic absorber are then adjusted to reproduce the measured J_{sc} and V_{oc}. Donor- and acceptor-like band-tail states are characterized by Urbach energies (E_U) of 30 meV and 22 meV, respectively [162]. The corresponding tail-state density (N_{tail}) is set to 2×10^{20} $cm^{-3}eV^{-1}$, while the dangling-bond density (N_{DB}) is fixed at 0.8×10^{16} cm^{-3}. Further details are provided in Appendix C.

In Figure 5.5, the resulting simulated J–V and EQE characteristics exhibit excellent agreement with measurements. In Table 5.1, the validated reference cell reaches an efficiency of 9.81%, placing it close to the state-of-the-art for p–i–n a-Si:H single-junction devices in superstrate configuration. High performance p–i–n a-Si:H cells fabricated on Asahi glass have demonstrated efficiencies of 10.22 % for a device area of 1.04 cm^2 [21].

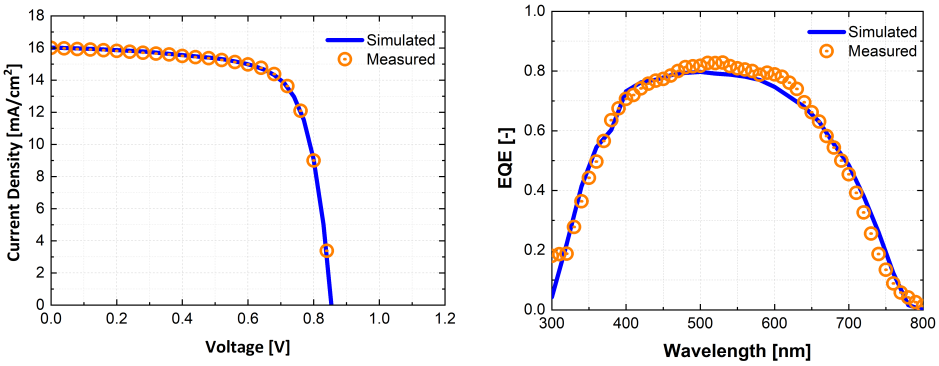

a) b)

Figure 5.5: Calibration of the a-Si:H solar cell. Simulated and measured (a) current density-voltage (J-V) characteristics under AM1.5G illumination; (b) external quantum efficiency (EQE) spectra.

Table 5.1: Simulated and measured performance of the a-Si:H solar cell, including open-circuit voltage (V_{oc}), short-circuit current density ($J_{sc,EQE}$), fill factor (FF), and power conversion efficiency (η_{EQE}). The standard deviation (σ_d) of the performance parameters, evaluated from the five best-performing cells, amounts to $\sigma_d(V_{oc}) \approx 2$ mV and $\sigma_d(FF) \approx 0.5$ %. The measurement uncertainty in $J_{sc,EQE}$ is quantified using the root-mean-square error, yielding RMS ≈ 0.7 % (absolute).

Performance metrics	Simulated	Measured
V_{oc} [V]	0.85	0.86
$J_{sc,EQE}$ [mA/cm^2]	16.02	16.01
FF [%]	71.67	71.67
η_{EQE} [%]	9.81	9.81

The nc-Si:H single-junction device serves as the second experimental reference for validating the simulation framework. Its structure is described in Section 5.2.3 and shown in Figure 5.3b. The calibrated parameters are all listed in Appendix C.

In the model, the intrinsic nc-Si:H absorber is subdivided into three depth-dependent subregions (nc-Si_1, nc-Si_2, nc-Si_3) to reflect the evolution of crystalline fraction and defect density during PECVD growth. Increasing crystallinity generally corresponds to reduced structural disorder, leading to lower Urbach energy and bulk defect density, although grain-boundary defects may still contribute to recombination [198].

From nc-Si_1 to nc-Si_3, the Urbach energy increases from 0.031 to 0.039 eV and the dangling-bond density from 1.0 to 1.5 × 10^{14} cm^{-3}, while the electron and hole mobilities increase from 20 to 30 cm^2/Vs and from 3 to 6 cm^2/Vs, respectively. The bandgap decreases from 1.25 to 1.15 eV.

The p- and n-type nc-SiO_x layers employ the same parameters as in the a-Si:H device, except for the n-layer N_D set to 4 × 10^{19} cm^{-3}, and the χ set to 3.48 eV, producing ΔE_C for electron extraction consistent with experimental values [243].

In Figure 5.6, the resulting simulated J–V and EQE characteristics exhibit excellent agreement with measurements, with deviations of 0.02 mA/cm^2 in J_{sc} and 0.02% in FF and efficiency presented in Table 5.2.

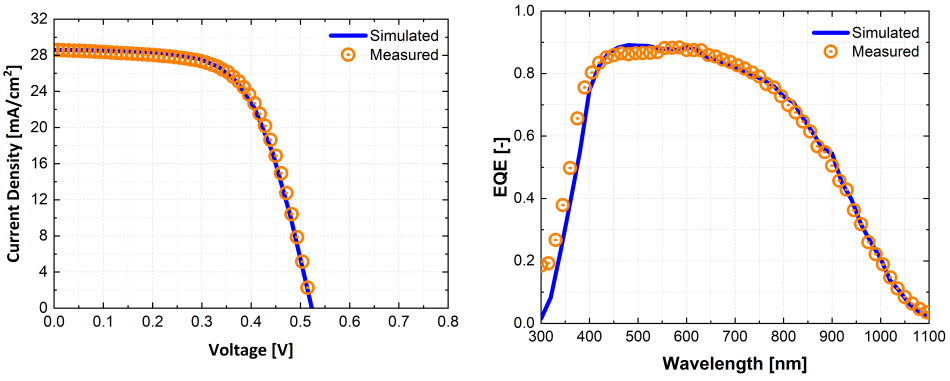

a) b)

Figure 5.6: Calibration of the nc-Si:H solar cell. Simulated and measured (a) current density-voltage (J-V) characteristics under AM1.5G illumination; (b) external quantum efficiency (EQE) spectra.

Table 5.2: Simulated and measured performance of the nc-Si:H single-junction solar cell, including open-circuit voltage (V_{oc}), short-circuit current density ($J_{sc,EQE}$), fill factor (FF), and power conversion efficiency (η_{EQE}). The standard deviation (σ_d) of the performance parameters, evaluated from the five best-performing cells, amounts to $\sigma_d(V_{oc}) \approx 3$ mV and $\sigma_d(FF) \approx 0.7$ %. The measurement uncertainty in $J_{sc,EQE}$ is quantified using the root-mean-square error, yielding RMS ≈ 0.7 % (absolute).

Performance metrics	Simulated	Measured
V_{oc} [V]	0.52	0.52
$J_{sc,EQE}$ [mA/cm^2]	28.59	28.60
FF [%]	62.18	62.20
η_{EQE} [%]	9.32	9.30

5.3.2. Tandem validation

The wide-bandgap a-Si:H and narrow-bandgap nc-Si:H single-junction devices described in Section 5.3.1 are integrated into a monolithic two-terminal tandem architecture. The stack consists of a p–i–n a-Si:H top cell (ToC) electrically coupled to a p–i–n nc-Si:H bottom cell (BoC) through a highly doped tunnel recombination junction.

The material, defect, and transport parameters calibrated for the single-junction devices serve as the baseline for the tandem model (see Appendix C). Since multijunction fabrication can modify interfacial and electronic properties through plasma exposure, interlayer mixing, and defect kinetics [241, 244, 245], only a limited subset of parameters is adjusted, while maintaining consistency with the validated single-junction reference.

5.3.2.1 Energy band diagram

Figure 5.7 shows the equilibrium energy band diagram of the a-Si:H/nc-Si:H tandem solar cell obtained from the self-consistent Poisson solution. The diagram illustrates band alignment and the dominant charge transport mechanisms across the multilayer stack, independent of the substrate.

In the a-Si:H top cell, the carriers transport mechanism at the TCO/p-nc-SiO_x and p-nc-SiO_x/a-Si:H interfaces is governed by a combination of B2B and TA tunneling, accounting for both direct tunneling through narrow barriers and defect-mediated recombination via localized gap states.

The two cells are electrically connected through a highly doped tunnel recombination junction that ensures current continuity with minimal resistive loss. The TRJ is modeled using a non-local B2BT formulation, where tunneling occurs over a finite spatial region defined by the tunneling length and permeation depth. The junction links the n-type a-Si:H layer to the p-type nc-Si:H layer, and the adjacent nc-SiO_x contact layers create strong band bending that promotes efficient tunneling. The graded p-type SiO_x bilayer on the BoC side further enhances tunneling probability while maintaining low contact resistance.

The built-in electric field across the intrinsic layers drives carrier separation, while tunneling and thermionic emission processes ensure efficient recombination at the TRJ and selective carrier extraction at the contacts.

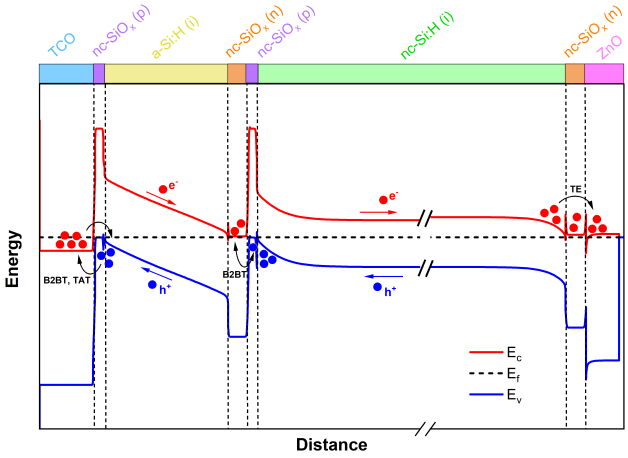

5

Figure 5.7: Energy band diagram of the a-Si:H/nc-Si:H tandem solar cell in the dark at thermal equilibrium. The solid blue line is the top of the valence band (E_V). The solid red line is the bottom of the conduction band (E_C). The black dashed line is the Fermi level (E_F). The arrows represent the transport of free charge carriers. The illustrated transport mechanisms of free charge carriers are trap-assisted tunneling (TAT), band-to-band tunneling (B2BT) and thermionic emission (TE).

5.3.2.2 Tandem performance

The a-Si:H/nc-Si:H tandem solar cell is first validated on micron-scale hexagonal textured glass. The simulated J–V and EQE characteristics, together with the resulting performance metrics, are reported in Figure 5.8 and Table 5.3. The model closely reproduces the experimentally measured J_{sc} ~ 11.7 mA/cm^2 and V_{oc} of 1.35 V, showing that both transport and optical mechanisms are accurately captured. As discussed in Chapter 4, the textured glass enhances light scattering, increases angular redistribution, and extends the optical path length in the nc-Si:H bottom cell, leading to improved current generation.

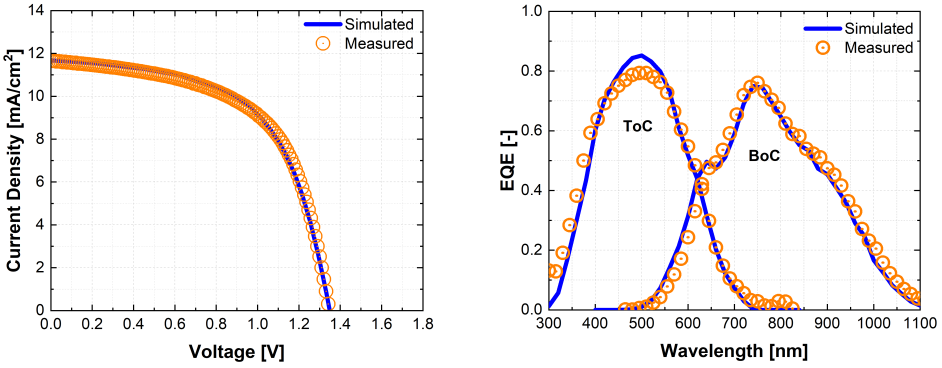

a) b)

Figure 5.8: Calibration of the a-Si:H/nc-Si:H tandem solar cell on glass. Simulated and measured (a) current density-voltage (J-V) characteristics under AM1.5G illumination; (b) external quantum efficiency (EQE) spectra.

Table 5.3: Simulated and measured performance of the a-Si:H/nc-Si:H tandem solar cell on glass substrate, including open-circuit voltage (V_{oc}), total and sub-cells current density (J_{total}, $J_{sc,ToC}$, $J_{sc,BoC}$), fill factor (FF), and power conversion efficiency (η_{EQE}). The standard deviation (σ_d) of the performance parameters, evaluated from the five best-performing cells, amounts to $\sigma_d(V_{oc}) \approx 3$ mV and $\sigma_d(FF) \approx 0.9$ %. The measurement uncertainty in J_{sc} derived from the EQE setup is quantified using the root-mean-square error, yielding $RMS(J_{sc,EQE}) \approx 0.7$ % (absolute).

Performance metrics	Simulated	Measured
V_{oc} [V]	1.35	1.35
$J_{sc,ToC}$ [mA/cm^2]	11.68	11.65
$J_{sc,BoC}$ [mA/cm^2]	14.40	14.57
J_{total} [mA/cm^2]	26.08	26.22
FF [%]	58.22	58.22
η_{EQE} [%]	9.17	9.16

The tandem device is next validated on a flexible architecture (see Figure 5.4b), with further details provided in Section 5.2.3. Compared with the tandem device developed on honeycomb-textured glass, the FTO morphology of the front electrode provides weaker optical confinement, which contributes to a measurable reduction in photocurrent.
The simulated J–V and EQE characteristics together with the performance outcome are reported in Figure 5.9 and Table 5.4. The model remains in close agreement with the experimental data, indicating that the calibrated transport and recombination parameters reliably extend to the flexible platform.

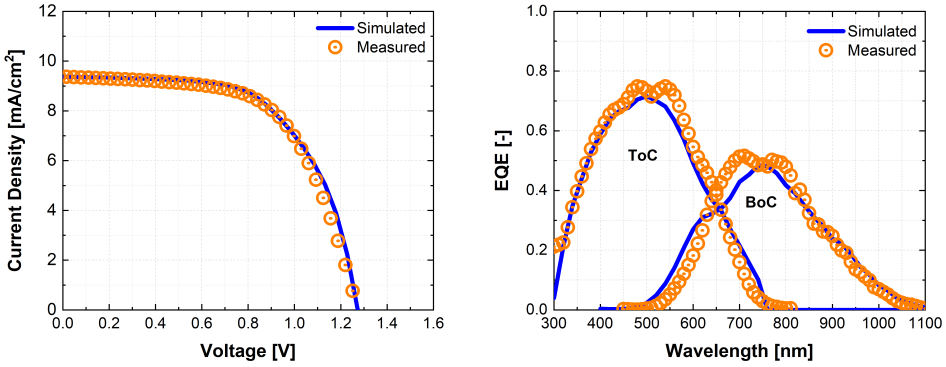

a) b)

Figure 5.9: Calibration of flexible a-Si:H/nc-Si:H tandem solar cell. Simulated and measured (a) current density-voltage (J-V) characteristics under AM1.5G illumination; (b) external quantum efficiency (EQE) spectra.

Table 5.4: Simulated and measured performance of flexible a-Si:H/nc-Si:H tandem solar cell, including open-circuit voltage (V_{oc}), total and sub-cells current density (J_{total}, $J_{sc,ToC}$, $J_{sc,BoC}$), fill factor (FF), and power conversion efficiency (η_{EQE}). The standard deviation (σ_d) of the performance parameters, evaluated from the five best-performing cells, amounts to $\sigma_d(V_{oc}) \approx 3$ mV and $\sigma_d(FF) \approx 0.9$ %. The measurement uncertainty in J_{sc} derived from the EQE setup is quantified using the root-mean-square error, yielding $RMS(J_{sc,EQE}) \approx 0.7$ % (absolute).

Performance metrics	Simulated	Measured
V_{oc} [V]	1.27	1.27
$J_{sc,ToC}$ [mA/cm^2]	11.37	11.70
$J_{sc,BoC}$ [mA/cm^2]	9.37	9.40
J_{total} [mA/cm^2]	20.77	21.10
FF [%]	60.78	60.80
η_{EQE} [%]	7.25	7.26

The fabricated flexible a-Si:H/nc-Si:H tandem exhibits a PCE of ~7 %, lower than the textured-glass reference but representative of devices processed on flexible substrates. This reduction primarily originates from processing constraints associated with the temporary Al carrier foil rather than intrinsic limitations of the tandem architecture.
Benchmark values for mature flexible TF-Si technologies, such as PEN-based tandems reaching 11.2 % initial (9.8 % stabilized) efficiency [246] and roll-to-roll mini-modules on Al substrates achieving 10.3 % [218], highlight the gap between early demonstrations and optimized flexible devices. Within this context, the present results provide a physically grounded modeling framework for designing scalable TF perovskite architectures compatible with high temperature processing on flexible substrates.

5.4. Designing flexible perovskite solar cells

Building on the experimentally validated thin-film modeling framework established in Section 5.3, it is extended to perovskite solar cells on flexible substrates. This approach enables the performance prediction of perovskite device architectures while preserving physical consistency with the calibrated reference devices.

5.4.1. Hole transport layer

In flexible perovskite solar cells, the hole transport layer (HTL) plays a central role in determining device performance and stability. Its electronic structure governs interfacial band alignment and charge selectivity, while its defect landscape controls non-radiative recombination and long-term device resilience [247, 248]. These effects become particularly important on aluminum foil substrates, where the increased thermal tolerance shifts performance limitations from substrate constraints toward interfacial electronic properties. For this reason, the present analysis focuses on HTL engineering as the primary variable for assessing the feasibility of f-PSCs on Al foil.
In the model, the HTL/perovskite interface is defined through the HTL electron affinity, bandgap, and doping density, which together determine the valence and conduction band offsets (ΔE_V, ΔE_C) and the resulting band bending. Interfacial recombination is described through surface recombination velocities (S_n, S_p), which quantify the degree of interface passivation and the associated non-radiative recombination losses.

Five representative HTL materials are investigated to span the relevant design space. Poly(3,4-ethylenedioxythiophene):polystyrene sulfonate (PEDOT:PSS) serves as a highly processable polymeric benchmark, but suffers from hygroscopicity and chemical instability [249]. Poly[bis(4-phenyl)(2,4,6-trimethylphenyl)amine] (PTAA) offers improved stability and hydrophobicity, although its performance depends strongly on doping and surface wetting [250]. The self-assembled monolayer (SAM) 2PACz (2-[9H-carbazol-9-yl]ethylphosphonic acid) enables precise tuning of the work function and effective interfacial passivation [251]. Nickel oxide (NiO_x) represents a leading inorganic HTL, combining chemical robustness with tunable electronic properties, although its transport is often limited by defects and stoichiometry [252]. Finally, nc-SiO_x provides a thermally stable metalloid oxide compatible with scalable deposition processes, and serves as a bridge to thin-film silicon manufacturing concepts [234].

5.4.2. Single-junction perovskite device

The analysis explores a single-junction perovskite solar cell as a test platform for HTL engineering. The device structure is shown in Fig. 5.10. The structural and electronic parameters of the investigated HTLs are summarized in Table 5.5 and taken from literature [253–255]. The remaining material parameters are provided in Appendix C.

The optical front stack consists of an encapsulated multilayer composed of ethylene–tetrafluoroethylene (ETFE) and optical adhesive layers deposited above the transparent electrode. This configuration creates a graded refractive-index transition from air (n = 1.0) to ETFE (n = 1.43), adhesive (n = 1.53), and FTO (n ~ 1.9 in the UV), reducing reflection losses [256, 257].

The absorber is a mixed Sn–Pb metal–halide perovskite (ABX_3 structure, where A = Cs, FA, MA; B = Pb, Sn; X = I). The nominal composition is $Cs_{0.1}FA_{0.6}MA_{0.3}Pb_xSn_{1-x}I_3$. The energy bandgap is 1.23 eV, other material parameters are adopted from literature [258].

Electron extraction is modeled using a fullerene/organic bilayer consisting of [6,6]-phenyl-C61-butyric acid methyl ester (C60) and bathocuproine (BCP). The C_{60} layer acts as the electron transport layer (ETL), while the thin BCP layer introduces a favorable conduction-band offset that suppresses electron backflow and supports high open-circuit voltage.

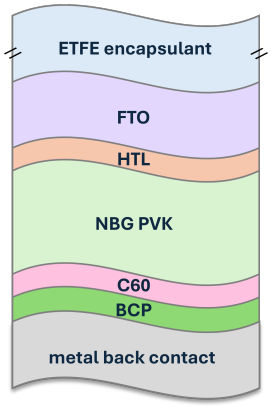

Figure 5.10: Flexible Sn–Pb-based perovskite solar cell (not to scale). Light enters through an adhesive ETFE encapsulant (240 µm), followed by FTO (700 nm) / HTL (variable thickness) / Sn–Pb metal–halide perovskite (900 nm) / C_{60} (25 nm) / BCP (8 nm) / Al metal back contact (300 nm).

Table 5.5: Parameters of the hole transport layers (PEDOT:PSS, PTAA, 2PACz (SAM), NiO_x, nc-SiO_x) used in Sentaurus TCAD model.

Parameter	PEDOT:PSS	PTAA	2PACz (SAM)	NiO_x	nc-SiO_x
Thickness [nm]	20	20	2	20	13
E_g [eV]	1.60	3.30	3.40	3.80	2.84
χ [eV]	3.50	1.80	1.70	1.46	3.37
N_D [cm^{-3}]	1×10^{19}	1×10^{19}	1×10^{20}	1×10^{19}	1×10^{20}
N_C [cm^{-3}]	2.2×10^{18}	2.2×10^{18}	2.0×10^{18}	2.2×10^{18}	1.0×10^{20}
N_V [cm^{-3}]	1.8×10^{19}	1.8×10^{19}	2.0×10^{19}	1.8×10^{19}	1.0×10^{20}
μ_n [cm^2/Vs]	1.8×10^{-3}	4×10^{-5}	1×10^{-3}	1×10^{-3}	10
μ_p [cm^2/Vs]	1.9×10^{-2}	4×10^{-5}	1×10^{-3}	1×10^{-3}	2
S_n/S_p [cm s^{-1}]	100	20	–	100	–

The equilibrium band diagrams obtained for the investigated HTLs are shown in Figure 5.11 (organic contacts) and Figure 5.12 (inorganic contacts).

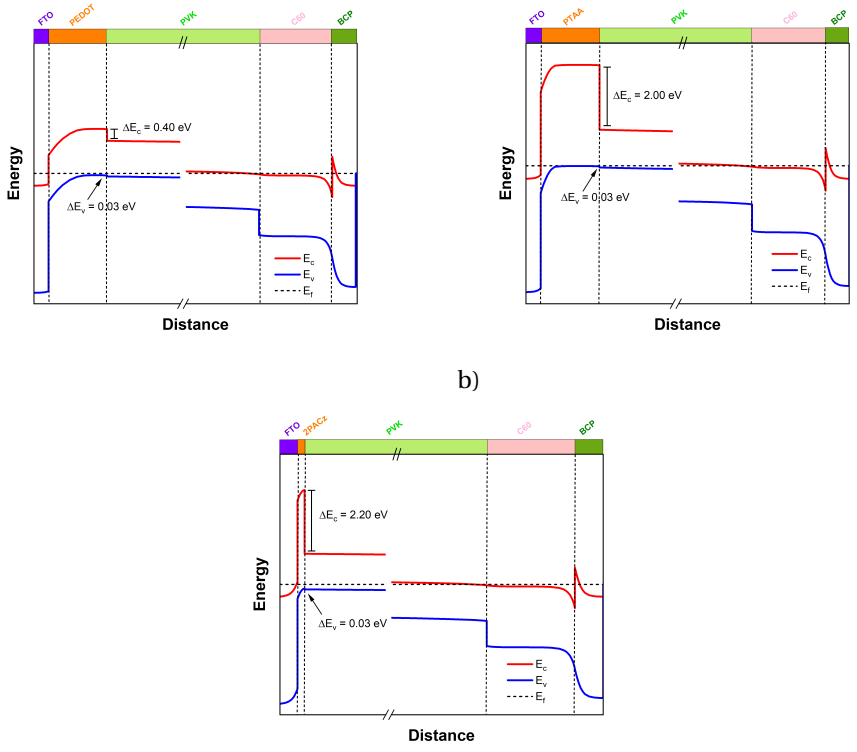

Figure 5.11: Energy band diagrams in the dark at thermal equilibrium for the Sn–Pb perovskite solar cell with (a) PEDOT: PSS, (b) PTAA, and (c) 2PACz as HTL.

Among the organic HTLs, PTAA provides near-ideal alignment with $\Delta E_V = 0.03$ eV and $\Delta E_C = 2.0$ eV, enabling efficient hole extraction and strong electron blocking. PEDOT:PSS exhibits a similar ΔE_V but a smaller ΔE_C (0.4 eV) due to its narrower bandgap, resulting in reduced electron-blocking capability and increased recombination susceptibility.
For 2PACz, an effective acceptor density is introduced to reproduce the dipole-induced interface potential step. The resulting alignment ($\Delta E_V = 0.03$ eV, $\Delta E_C = 2.2$ eV) approaches the ideal selective-contact condition. However, the ultrathin 2 nm SAM layer leads to tunneling-dominated transport, such that electron-blocking effectiveness is limited by thickness rather than energetics, and may benefit from combination with an additional HTL.

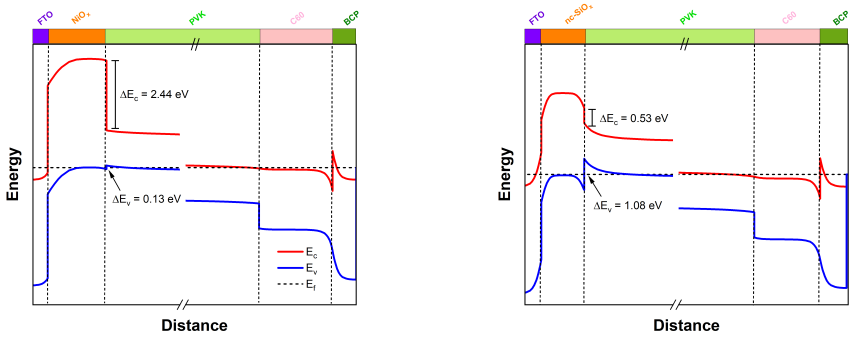

a) b)

Figure 5.12: Energy band diagrams in the dark at thermal equilibrium for the Sn–Pb perovskite solar cell with (a) NiO_x, (b) nc-SiO_x as HTL.

Among the inorganic HTLs, NiO_x forms a small $\Delta E_V = 0.13$ eV and a large $\Delta E_C = 2.44$ eV, providing strong electron blocking with minimal barrier for hole extraction. In contrast, nc-SiO_x induces a large $\Delta E_V = 1.08$ eV and a moderate $\Delta E_C = 0.5$ eV, resulting in a transport regime dominated by barrier-limited conduction and tunneling. NiO_x thus behaves as a conventional selective HTL, whereas nc-SiO_x functions as a tunneling-type contact.

5.4.2.1 Performance prediction

Based on energetic alignment, PEDOT:PSS and NiO_x are selected as representative hole transport layers for full-device simulations. PEDOT:PSS serves as a process-compatible benchmark for low-bandgap perovskites, while NiO_x represents the inorganic counterpart with strong electron-blocking capability and robust electronic properties [259–263]. Limiting the analysis to these two cases ensures physical relevance while maintaining manageable computational cost for drift–diffusion simulations involving tunneling and defect-rich interfaces.
The simulated J–V and EQE characteristics (Figure 5.13) and corresponding performance metrics (Table 5.6) indicate efficiencies above 22% for both HTLs, suggesting that, under the present modeling assumptions, device performance is primarily governed by interfacial energetic alignment. NiO_x yields a slightly higher J_{sc} (32.60 vs 32.13 mA/cm^2), consistent with improved carrier selectivity and reduced interfacial recombination, while V_{oc} (0.85 V) and FF ($\sim$ 81%) remain essentially unchanged.

The EQE spectra overlap across 400–1000 nm, with minor ultraviolet losses for NiO_x due to parasitic absorption. Despite identical density of states and doping, NiO_x improves interfacial transport through its wider bandgap and favorable band alignment, which enhance carrier selectivity and support efficient hole extraction.

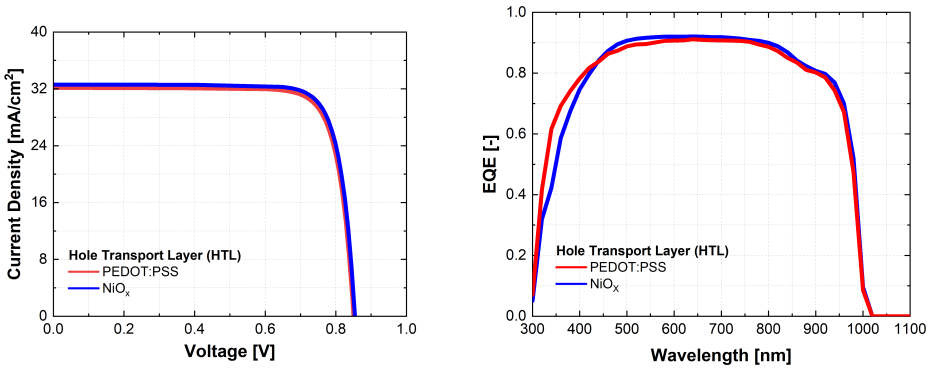

a) b)

Figure 5.13: Simulated (a) current density-voltage (J–V) and (b) external quantum efficiency (EQE) characteristics of flexible Sn–Pb perovskite solar cells employing PEDOT:PSS (red) and NiO_x (blue) as HTL.

Table 5.6: Simulated open-circuit voltage (Voc), short-circuit current density (Jsc), fill factor (FF), and power conversion efficiency (η) for the Sn–Pb perovskite solar cell, using PEDOT:PSS and NiO_x as HTL.

Performance Metrics	HTL – PEDOT:PSS	HTL – NiO_x
V_{oc} [V]	0.85	0.85
J_{sc} [mA/cm^2]	32.13	32.60
FF (%)	81.09	81.30
η (%)	22.15	22.64

These results highlight the potential of NiO_x as an effective HTL. However, this conclusion is currently limited to simulation. Experimentally, flexible Sn–Pb perovskite solar cells on ITO/PET using PEDOT:PSS reach 21.02% [264], while NiO_x-based devices achieve up to 22.68%, albeit with wider-bandgap absorbers [265].

5.4.3. Perovskite-based tandem devices

The analysis is extended to two-terminal multijunction architectures, including a hybrid a-Si:H/perovskite tandem and an all-perovskite tandem, as shown in Figure 5.14. The corresponding material parameters are provided in Appendix C.

For both architectures, two HTL configurations are investigated: (i) an organic configuration, employing PTAA in the top cell (ToC) and PEDOT:PSS in the bottom cell (BoC); and (ii) an inorganic configuration using NiO_x in both sub-cells. The sub-cells are monolithically connected through a 5 nm ITO recombination layer, forming a tunnel recombination junction that links the ETL of the top cell to the HTL of the bottom cell.

The hybrid design integrates a wide-bandgap a-Si:H top cell (E_g = 1.65 eV), adapted from the calibrated a-Si:H/nc-Si:H tandem, with a Sn–Pb perovskite bottom cell (E_g = 1.23 eV). The all-perovskite tandem couples a wide-bandgap ($Cs_{0.15}FA_{0.85}Pb(I_{0.92}Br_{0.08})_3$) top absorber ($E_g$ = 1.68 eV) with the Sn–Pb perovskite bottom absorber (E_g = 1.23 eV) [258].

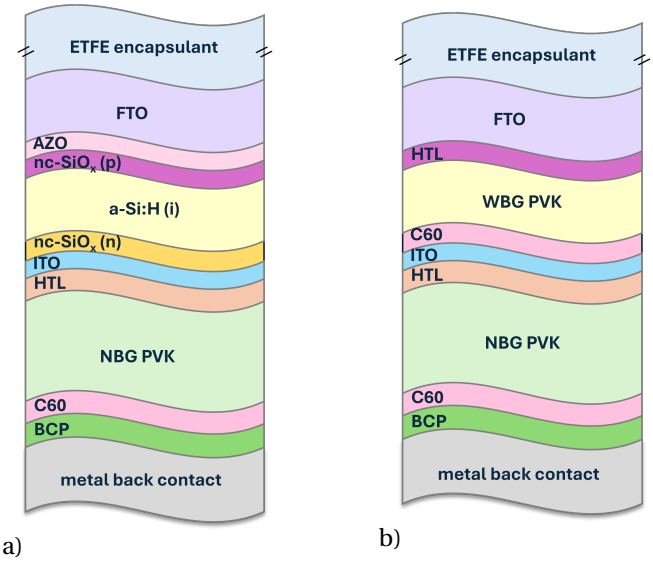

Figure 5.14: Flexible erovskite-based tandem solar cell architectures (not to scale): (a) ETFE encapsulant (190 µm) / FTO (700 nm) / AZO (10 nm) / p-type nc-SiO_X (16 nm) / a-Si:H (280 nm) / n-type nc-SiO_X (50 nm) / ITO (5 nm) / HTL (20 nm) / NBG perovskite (900 nm) / C_{60} (20 nm) / BCP (8 nm) / Al metal back contact (300 nm); (b) ETFE encapsulant (190 µm) / FTO (700 nm) / HTL (20 nm) / WBG perovskite (280 nm) / C_{60} (25 nm) / ITO (5 nm) / HTL (20 nm) / NBG perovskite (900 nm) / C_{60} (20 nm) / BCP (8 nm) / Al metal back contact (300 nm).

For the hybrid tandem, a 10 nm AZO buffer layer is introduced between FTO and the p-type nc-SiO_x to prevent hydrogen-induced reduction of the front TCO during silicon deposition, consistent with the device design described in Section 5.2.3. In particular, exposure to atomic hydrogen during PECVD can reduce SnO_2-based TCOs, degrading their electrical and optical properties. The AZO layer therefore acts as a protective barrier under these conditions.
The AZO layer is not included in the perovskite tandem architecture, as no hydrogen-rich plasma processes are involved, and therefore no such reduction of the front TCO is expected.

5.4.4. Hybrid a-Si:H/perovskite tandem performance prediction

PEDOT:PSS and NiO_x are selected as representative organic and inorganic HTLs to assess their impact on tandem operation. Figure 5.15 presents the equilibrium band diagrams, highlighting the alignment at the tunnel recombination junction and the HTL/perovskite interface.
NiO_x exhibits a substantially larger conduction-band offset (ΔE_C = 2.44 eV) than PEDOT:PSS (0.40 eV), consistent with its wider bandgap and resulting in stronger electron blocking. In contrast, both materials show similarly small valence-band offsets (0.02–0.03 eV).

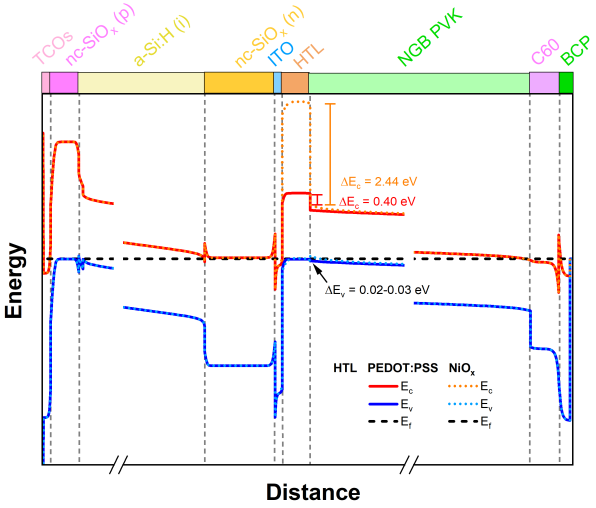

Figure 5.15: Energy band diagrams in the dark at thermal equilibrium of the hybrid a-Si:H/perovskite tandem solar cell using (a) PEDOT:PSS and (b) NiO_x as HTL in the BoC. The diagrams highlight the modeled band offsets at the HTL/perovskite interface for the conduction band (ΔE_C) and valence band (ΔE_V).

The simulated J–V and EQE characteristics are shown in Figure 5.16, with performance metrics summarized in Table 5.7. Both configurations exhibit comparable efficiencies. A shallow EQE dip is observed in the perovskite bottom cell near 800 nm for PEDOT:PSS, shifting to 900 nm for NiO_x. This feature arises from optical contrast introduced by the a-Si:H top cell, positioned between the low-index front TCOs and the tunnel recombination junction [266].

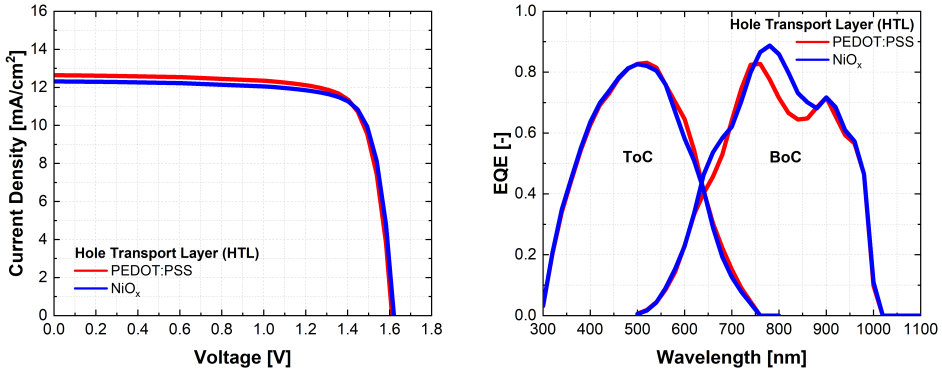

a) b)

Figure 5.16: Simulated (a) current density–voltage (J–V) and (b) external quantum efficiency (EQE) characteristics of the hybrid a-Si:H/perovskite tandem with PEDOT:PSS (red) and NiO_x (blue) as HTL.

Table 5.7: Simulated open-circuit voltage (V_{oc}), total and sub-cells current density (J_{total}, $J_{sc,ToC}$, $J_{sc,BoC}$, BoC), fill factor (FF), and efficiency (η) for the hybrid a-Si:H/perovskite tandem solar cell, using either PEDOT:PSS or NiO_x as HTL in the BoC.

Performance Metrics	PEDOT:PSS	NiO_x
V_{oc} [V]	1.61	1.62
$J_{sc,ToC}$ [mA/cm^2]	12.64	12.31
$J_{sc,BoC}$ [mA/cm^2]	15.61	16.83
J_{total} [mA/cm^2]	28.25	29.14
FF [%]	78.13	79.17
η [%]	15.91	15.80

Although the hybrid architecture exhibits lower efficiency than the single-junction f-PSC (Section 5.4.2.1), it outperforms the TF-Si tandem discussed in Section 5.3.2. The hybrid device therefore serves as an intermediate platform between thin-film silicon and all-perovskite multijunctions, enabling controlled investigation of interfacial energetics, optical coupling, and tunnel recombination..

5

5.4.5. All-perovskite tandem performance prediction

The simulations isolate the influence of HTL on all-perovskite tandem performance by comparing an organic configuration, PTAA in the ToC and PEDOT:PSS in the BoC, with an inorganic alternative using NiO_x in both sub-cells. In Figure 5.17, NiO_x as HTL provides greater electron-blocking barriers in bot top and bottom junctions ($\Delta E_{C,ToC}$ = 2.64 eV, $\Delta E_{C,BoC}$ = 2.44 eV).

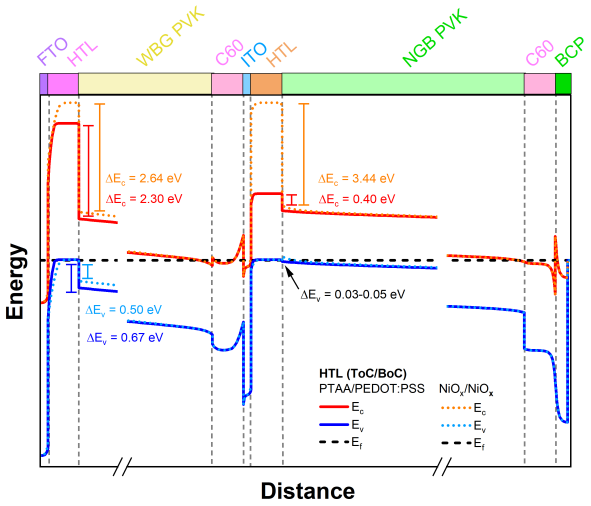

Figure 5.17: Energy band diagrams in the dark at thermal equilibrium of the all-perovskite tandem solar cell for PTAA/PEDOT:PSS and NiO_x/NiO_x as HTLs. The diagrams highlight the modeled band offsets at the HTL/perovskite interfaces for the conduction band (ΔE_C) and valence band (ΔE_V).

The simulated J–V and EQE characteristics in Figure 5.18, together with the performance metrics in Table 5.8, reveal a pronounced HTL-dependent performance difference. The tandem employing inorganic HTLs achieves efficiencies above 29 %, surpassing the organic configuration (η = 26.5 %), consistent with improved carrier selectivity, stronger electron blocking, and enhanced photocurrent extraction (33.4 mA/cm^2).

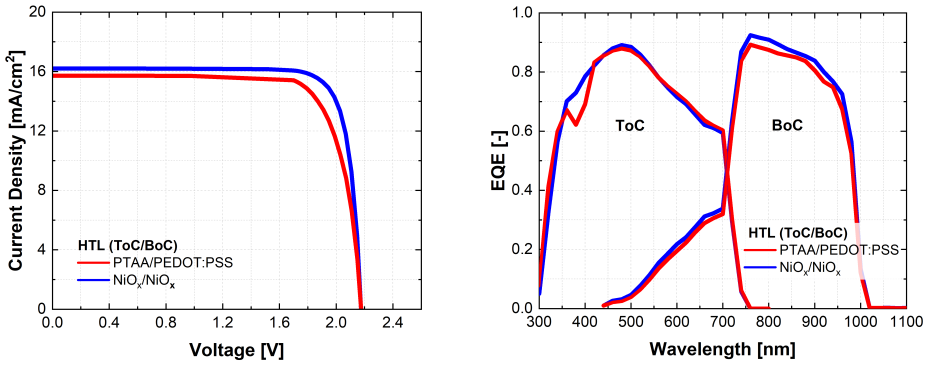

a) b)

Figure 5.18: Simulated (a) current density–voltage (J–V) and (b) external quantum efficiency (EQE) characteristics of the all-perovskite tandem solar cell using PTAA/PEDOT:PSS (red) and NiO_x/NiO_x (blue) as HTLs in the ToC and BoC, respectively.

Table 5.8: Simulated open-circuit voltage (V_{oc}), total and sub-cells current density (J_{total}, $J_{sc,ToC}$, $J_{sc,BoC}$), fill factor (FF), and efficiency (η) for all-perovskite tandem solar cell, using PTAA/PEDOT:PSS and NiO_x/NiO_x as HTLs in the ToC and BoC, respectively.

Performance Metrics	PTAA/PEDOT:PSS	NiO_x/NiO_x
V_{oc} [V]	2.18	2.17
$J_{sc,ToC}$ [mA/cm^2]	15.71	16.21
$J_{sc,BoC}$ [mA/cm^2]	16.51	17.19
J_{total} [mA/cm^2]	32.22	33.4
FF [%]	77.44	82.64
η [%]	26.47	29.13

For comparison, flexible two-terminal all-perovskite tandems on PET/ITO employing solution-processed NiO nanocrystal HTLs have achieved efficiencies of 24.7% (certified 24.4%) and 23.5% for device areas of 0.049 cm^2 and 1.05 cm^2, respectively [267]. More recently, efficiencies up to 27.5% have been reported for 0.049 cm^2 flexible tandem solar cells employing NiO_x and self-assembled monolayer hole-selective contacts in the wide-bandgap top cell [268]. In contrast, rigid glass-based all-perovskite tandems have surpassed 29% efficiency [269, 270]. The simulated performance therefore approaches the current state-of-the-art for rigid all-perovskite tandems, suggesting that high temperature flexible architectures could potentially achieve comparable efficiencies through further optimization of charge transport layers, interface quality, and recombination management.

5.5. Conclusions

This work establishes a physically grounded optoelectrical modeling framework for the predictive design of perovskite photovoltaic devices. Validation against thin-film silicon single-junction and tandem solar cells fabricated on rigid and flexible substrates provides an experimentally anchored basis for extending the analysis to flexible perovskite solar cells on high temperature aluminum foil substrates.

Application of the framework to Sn–Pb metal-halide flexible perovskite devices identifies the hole transport layer (HTL) as a key parameter governing band alignment, interfacial selectivity, and overall device performance. In single-junction devices, simulated efficiencies of 22.1% with PEDOT:PSS and 22.6% with NiO_x demonstrate the advantage of inorganic HTLs, primarily due to their stronger electron-blocking capability. The same trend persists in tandem architectures: hybrid a-Si:H/perovskite tandems achieve efficiencies above 15%, while fully perovskite tandems reach 29.1% with NiO_x/NiO_x HTLs, compared with 26.5% for the PTAA/PEDOT:PSS configuration.

The results establish HTL energetic alignment and carrier selectivity as central design criteria for high performance flexible perovskite photovoltaics. More broadly, the study highlights the potential of high temperature aluminum foil substrates, already established in roll-to-roll thin-film silicon manufacturing, to support scalable fabrication of flexible perovskite devices. The framework presented here therefore provides a predictive tool for guiding device architecture and interface engineering, indicating that monolithic flexible perovskite tandems approaching 30% efficiency may be achievable through further optimization of charge-transport layers and interfacial properties.

Pacific Sun by Dale Chihuly, Chihuly Garden and Glass Museum, Seattle, U.S.

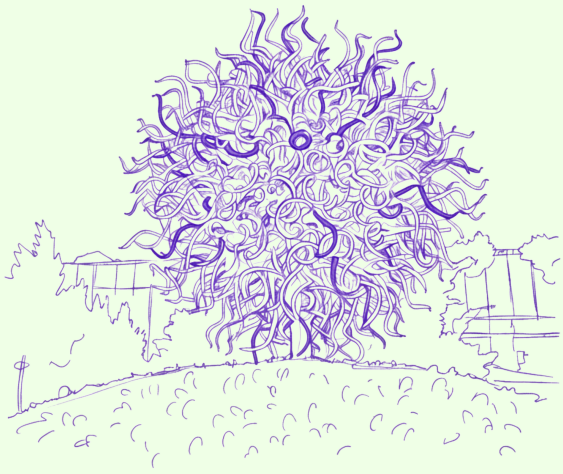

6

CONCLUSIONS & OUTLOOK

The image placed at the opening of this chapter depicts Pacific Sun by Dale Chihuly, installed at the Chihuly Garden and Glass Museum in Seattle, U.S. Chihuly has frequently emphasized his fascination with how light interacts with glass, and the sun motif is one of the forms through which he most explicitly explores this relationship. In his artistic vocabulary, works from the Sun series are conceived as a celebration of glass as a medium of light, rather than merely as a structural or decorative material. This artist-driven emphasis on light–material interaction provides a visual analogy for one of the central themes of this thesis, which focuses on understanding, engineering, and modeling light–matter interactions in complex and multiscale textured thin-film solar cells.

6.1. Conclusions

This thesis employed thin-film silicon (TF-Si) photovoltaics as a mature and experimentally accessible platform to investigate transparent conductive oxides, multiscale light management, and optoelectrical modeling strategies relevant to scalable next-generation thin-film solar cells. The resulting framework was subsequently extended toward flexible perovskite photovoltaic architectures compatible with high temperature superstrate processing. The research questions were addressed as follows.

The *first research question* addressed the engineering of transparent conductive oxide (TCO) architectures capable of decoupling optical transparency and electrical conductivity, together with the physical mechanisms governing their optoelectrical performance in TF-Si devices. Chapter 2 demonstrated that bilayer TCO architectures provide an effective strategy to overcome the intrinsic trade-off between conductivity and optical transparency that limits conventional single layer electrodes.

By combining hydrogenated indium oxide (IO:H) as a highly conductive layer with non-intentionally doped zinc oxide (ZnO) as an optically transparent layer, the bilayer architecture enabled independent optimization of carrier transport and optical losses. The resulting electrodes exhibited carrier mobilities up to 120 cm^2/Vs together with reduced near-infrared parasitic absorption, while remaining fully compatible with thin-film silicon device integration.

The interface between the two TCO layers played an active role in determining charge transport, indicating that interface engineering itself constitutes an important design parameter in advanced front electrode architectures. Although the resulting solar cell efficiency improvements remained moderate, the bilayer concept introduced an additional degree of freedom in front electrode engineering.

Additional investigations demonstrated that the concept was not limited to a specific TCO system. Bilayers based on indium cerium oxide (ICO) and ZnO confirmed the transferability of the approach. Fully indium-free bilayers, such as fluorine-doped tin oxide (FTO) and non-intentionally tin dioxide (SnO_2), showed that good charge transport properties could be achieved while maintaining compatibility with low thermal budget processing and scalable manufacturing.

The *second research question* examined the relationships between deposition conditions and the resulting structural, chemical, and optoelectrical properties of indium-free SnO_2-based thin films processed under low thermal budget constraints.
Chapter 3 established quantitative processing–property relationships for room temperature deposited FTO and SnO_2 thin films through systematic reactive sputtering investigations. Oxygen incorporation into the Ar forming-gas sputtering atmosphere during deposition was identified as the relevant parameter governing the trade-off between optical transparency and electrical conductivity. Optimal optoelectrical performance emerged within a narrow oxygen window range that enhanced carrier mobility while limiting defect-related optical absorption. Hydrogen was found to primarily influence the films through defect passivation and microstructural modification rather than direct chemical reduction, leading to enhanced transparency and reduced sheet resistance in the as-deposited state. Following post-deposition annealing at 400 °C in nitrogen atmosphere, hydrogenated and non-hydrogenated films converged toward similar electronic properties, indicating that annealing-induced crystallization governed long-term charge transport.
Although the absolute performance of room temperature sputtered SnO∗2-based films remained below that of high temperature deposited counterparts, the identified processing–property relationships established a tunable and thermally compatible design space for indium-free TCOs. These results position SnO∗2-based materials as viable candidates for front TCO electrodes and charge-transport layers (CTLs) in future photovoltaic technologies, where thermal budget, mechanical flexibility, and material sustainability are critical constraints.

The *third research question* examined the extent to which light propagation, absorption, and angular redistribution in multiscale textured TF-Si solar cells could be predicted using experimentally grounded optical models with computation times below 30 minutes, and how their predictive accuracy compared with rigorous electromagnetic approaches.
Chapter 4 provided direct experimental validation of ray optics modeling as a quantitatively accurate and computationally efficient tool for predicting both front reflection losses and the optical performance of thin-film photovoltaic devices.
By directly implementing experimentally measured optical constants together with realistic interface morphologies, the ray tracing framework reproduced measured reflection spectra (1-R) and external quantum efficiency (EQE) under the assumption of negligible recombination losses. The deviations between simulation and experiment were comparable to, and in several cases lower than, those obtained using rigorous coupled-wave analysis (RCWA).
While RCWA provides a rigorous electromagnetic description, its applicability is restricted by periodic boundary conditions and high computational cost. In contrast, ray optics accommodates realistic non-periodic morphologies and reduces computation times from approximately one week to less than 30 minutes without sacrificing predictive accuracy when properly parameterized. The resulting framework accurately captured absorption, reflection, and angular redistribution induced by multiscale surface textures.
These results establish experimentally grounded ray tracing as a practical and predictive tool for multiscale optical design in thin-film photovoltaics, while providing a transferable methodology for other thin-film technologies where advanced light management is essential.

The *fourth research question* explored how optoelectrical modeling frameworks validated on TF-Si devices could be extended to flexible perovskite solar cells fabricated in superstrate p-i-n configurations, and which physical mechanisms most strongly limited device performance under high temperature processing routes.
Chapter 5 established an optoelectrical modeling framework enabling physically grounded performance prediction for flexible perovskite solar cells processed using the temporary aluminum foil route. Validation against thin-film silicon single-junction and tandem devices ensured that the framework remained anchored in experimentally characterized photovoltaic devices.
Application of the framework to Sn–Pb metal-halide perovskite architectures identified HTL energetic alignment and carrier selectivity as key factors governing interfacial losses and overall device performance. Across both single-junction and tandem configurations, inorganic NiO_x-based HTLs consistently outperformed organic alternatives by providing stronger electron-blocking barriers and improved carrier selectivity. Simulated efficiencies approaching 30% in monolithic tandem devices therefore demonstrate the potential of high temperature flexible perovskite architectures compatible with scalable thin-film manufacturing concepts.

6.2. Outlook

The results presented in this thesis open several research directions spanning TCOs engineering, multiscale optical modeling, and predictive optoelectrical simulation of next generation thin-film solar cells.

- Future development of bilayer TCOs should focus on improving ultraviolet transparency while preserving high electrical conductivity. Although indium-based bilayers successfully decoupled optical and electrical functionalities, parasitic ultraviolet absorption remains a limitation for front electrode applications. Replacing indium-containing conductive layers with tin-based alternatives may improve short-wavelength transparency while maintaining favorable transport properties.
  In addition, future bilayer architectures could exploit the intrinsic nanoscale surface morphology of SnO_2-based layers to enhance short-wavelength scattering without requiring additional surface texturing. More broadly, reducing front reflection losses will require integrated optimization of thickness, refractive-index grading, and interface morphology, rather than thickness tuning alone.
  From a processing perspective, this thesis relied exclusively on radio-frequency sputtering because of its compatibility with industrial manufacturing. Future work may explore alternative deposition routes to further improve scalability and industrial integration.

- Future investigations of SnO_2-based TCOs should extend defect-engineering strategies beyond room temperature deposition toward processing routes that promote dopant activation, crystallinity, and carrier transport. Under low temperature deposition conditions, fluorine doping remains only partially effective because electrically inactive dopants, defect trapping, and scattering mechanisms fundamentally limit conductivity.

Promising directions include high temperature deposition and post-deposition annealing strategies aimed at improving dopant activation, grain growth, and defect passivation. In this context, high temperature superstrate processing on temporary metal carrier foils offers a viable pathway to combine high quality indium-free TCOs with scalable flexible photovoltaic manufacturing.

- The experimentally validated ray optics framework developed in this work represents an important step toward fast and reliable optical design of multiscale textured thin-film solar cells. Future work should extend the framework to a broader range of thin-film photovoltaic technologies to evaluate its general applicability.
  Further developments are also required to relax some of the assumptions adopted in the present implementation. While interference effects were retained at optically coherent interfaces, the current framework neglects coherent propagation within optically incoherent absorber regions. This approximation may become limiting in thinner or weakly textured absorbers where coherent effects extend over larger fractions of the device.
  Coupled modeling approaches combining ray optics for incoherent regions with interference based electromagnetic descriptions for coherent layers could therefore improve predictive accuracy across a wider range of device architectures. In addition, extending the framework to explicitly account for grain-induced scattering in polycrystalline TCOs would further enhance its physical relevance.
  Future studies should also revisit rigorous electromagnetic approaches such as RCWA within targeted and well-defined applications. Rather than full-device simulations of complex multiscale morphologies, RCWA may be more effectively employed to benchmark specific interface geometries, periodic textures, and sub-wavelength scattering mechanisms. Such coupled strategies could combine the physical rigor of electromagnetic simulations with the speed and flexibility required for realistic device optimization.

- The coupling of advanced optical modeling in GenPro4 with drift–diffusion model in Sentaurus TCAD constitutes a powerful framework for predictive design of next generation thin-film solar cells. Future model developments should extend the physical description beyond effective interface parameters toward explicit treatment of transport and degradation mechanisms relevant to perovskite photovoltaics.
  In particular, incorporation of ion migration, field-dependent recombination, and time-dependent interfacial degradation would allow the framework to capture hysteresis and stability losses that remain critical challenges in perovskite solar cells. Integrating such mechanisms would significantly strengthen the predictive capability of the model and improve its ability to guide experimental device design and materials selection.
  For tandem architectures, future studies should replace the idealized ITO-based recombination junctions employed in this work with physically realistic tunnel recombination junctions including defect-assisted transport and interface recombination. This would enable more accurate prediction of multijunction devices performance.

A

APPENDIX

A

A.1. TCOs optoelectrical properties

The transparent conductive oxides (TCOs) presented in this appendix are selected as representative materials to illustrate general trends in optical constants relevant to thin-film photovoltaic applications. All films are deposited by radio frequency magnetron sputtering (13.56 MHz) under varying processing conditions, including power density (W/cm^2), substrate temperature (°C), chamber pressure (mbar), and argon flow (sccm). Substrates with dimensions of 10 cm × 2.5 cm × 0.7 mm are used. The resulting dataset therefore provides a qualitative comparison of material dependent dispersion behaviour rather than a direct performance benchmark.

Figure A.1a shows the wavelength dependent refractive index (n) and extinction coefficient (k) of indium tin oxide (ITO), hydrogenated indium oxide (IO:H), indium cerium oxide (ICO), aluminum doped zinc oxide (AZO), fluorine doped tin oxide (FTO), and intentionally undoped zinc oxide (ZnO) and tin oxide (SnO_2). Optical constants are extracted by spectroscopic ellipsometry using a Cody-Lorentz model for the ultraviolet visible range and a Drude term to account for free carrier absorption in the near infrared.

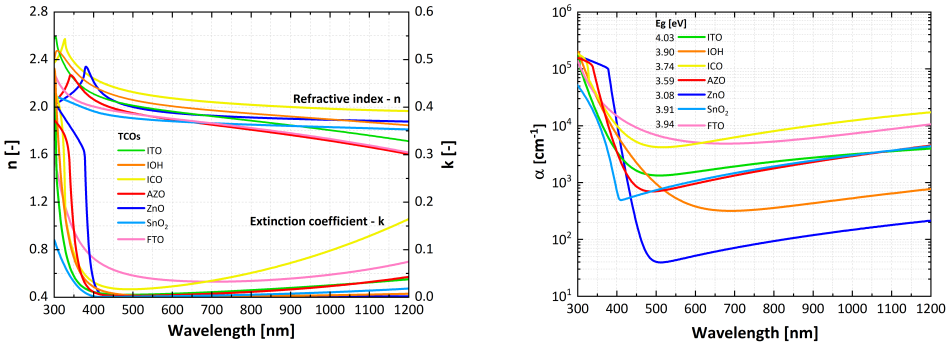

a) b)

Figure A.1: Optical properties of ITO, IO:H, ICO, AZO, ZnO, SnO_2, and FTO): (a) refractive index (n) and extinction coefficient (k); (b) absorption coefficient (α) shown on a logarithmic scale, including extracted optical bandgap (E_g) values.

All materials exhibit a maximum in refractive index in the near-ultraviolet region. In_2O_3-based compounds (ITO, IO:H, ICO) show the highest peak values (approximately 2.4–2.6) between 300 and 350 nm. ZnO and AZO display slightly lower maxima (below 2.4), shifted toward 350–400 nm, consistent with their wider optical bandgap and corresponding shift of inter-band transitions to lower energies. SnO_2 and FTO exhibit maxima below 300 nm, reflecting the higher-energy onset of inter-band transitions in tin-oxide-based systems.

In the near-infrared region, differences in dispersion slope become evident. ITO, FTO, and AZO exhibit a more pronounced decrease in refractive index compared to IO:H, ICO, ZnO, and SnO_2. This behavior is attributed to differences in free-carrier contributions, as described by the Drude response, with higher carrier concentrations leading to stronger dispersion in this spectral range.

The extinction coefficient exhibits a similar distinction. At short wavelengths, the increase in k is associated with inter-band absorption near the optical band edge. Toward longer wavelengths, a characteristic infrared tail emerges due to free-carrier absorption. This Drude contribution depends primarily on carrier concentration and carrier mobility. A pronounced infrared tail is observed for ICO and FTO, while AZO, ITO, and SnO_2 show moderate absorption. ZnO and IO:H exhibit significantly reduced extinction in the near-infrared region.
Figure A.1b presents the absorption coefficient (α) calculated from the extinction coefficient according to $\alpha = 4\pi k/\lambda$. The logarithmic scale allows clear comparison of both the absorption onset and the magnitude of absorption across the spectral range.
ZnO exhibits an optical bandgap of approximately 3.1 eV and shows the sharpest absorption edge and lowest sub-bandgap absorption among the materials considered. Upon aluminum doping, AZO displays an increased bandgap (3.6 eV), consistent with a Burstein–Moss shift induced by increased carrier concentration. The In_2O_3-based materials (ITO, IO:H, ICO) exhibit higher optical bandgaps (3.7–4.0 eV), accompanied by stronger high-energy absorption compared to ZnO. Tin-oxide-based films (SnO_2, FTO) show bandgap values above 3.9 eV, comparable to indium-based TCOs. Differences in absorption magnitude and spectral shape indicate variations in carrier concentration, defect states, and scattering mechanisms associated with the deposition conditions.

Figure A.2 provides an overview of carrier mobility (μ) as a function of carrier density (N) for representative TCO materials. The solid black curves indicate the theoretical mobility limits for ZnO based metal oxides, illustrating the transition between different scattering regimes, with the overall mobility governed by combined contributions according to $(\mu_{II}^{-1} + \mu_{GB}^{-1})^{-1}$, where μ_{II} denotes ionized impurity scattering and μ_{GB} grain boundary scattering.

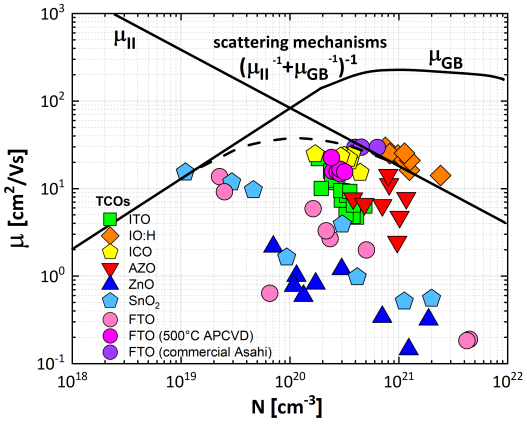

Figure A.2: Carrier mobility (μ) as a function of carrier density (N) for In_2O_3 based materials (ITO, IO:H, ICO), ZnO based films (ZnO, AZO), SnO_2 based films (SnO_2, FTO), and FTO deposited by APCVD in collaboration with the industrial partner as well as commercial FTO-coated Asahi glass. Solid black curves indicate theoretical mobility limits governed by ionized impurity (μ_{II}) and grain boundary (μ_{GB}) scattering contributions for ZnO based metal oxides combined as $(\mu_{II}^{-1} + \mu_{GB}^{-1})^{-1}$.

The ITO data points cluster in the intermediate to high carrier concentration range (10^{20}–10^{21} cm^{-3}), with moderate mobilities, reflecting the typical trade-off between electrical conductivity and ionized impurity scattering in doped In_2O_3-based systems. IO:H exhibits comparatively higher mobility at carrier concentrations around 10^{21} cm^{-3}, indicating reduced ionized impurity scattering, commonly attributed to hydrogen incorporation. Furthermore, ICO samples show mobilities comparable to or slightly exceeding those of ITO at equivalent carrier concentration.

ZnO-based films are located at lower carrier concentrations, with mobility values limited by grain boundary and ionized impurity scattering. Aluminum doping (AZO) shifts the distribution toward higher carrier concentrations, with a corresponding increase in electrical conductivity.

The SnO_2 and FTO films span a broader range of carrier concentrations with moderate to low mobilities. The FTO dataset includes films deposited by atmospheric pressure chemical vapor deposition (APCVD) in collaboration with an industrial partner, as well as commercial FTO-coated Asahi glass. The industrial APCVD FTO exhibits relatively high carrier concentration combined with mobility values comparable to ITO and ICO, positioning it within the conductivity regime relevant for industrial thin-film photovoltaic applications.

A.2. ICO/ZnO bilayer

Figure A.3a compares carrier mobility as a function of carrier concentration for single layer TCOs (ITO, IO:H, ICO) and ICO/ZnO and IO:H/ZnO bilayers, both in the as-deposited state and after post-deposition annealing (PDA) at 200 °C for 2 h 20 min in ambient environment. The as-deposited bilayers exhibit mobilities comparable to single layer TCOs, but at reduced carrier concentrations (10^{19}–10^{20} cm^{-3}). Following PDA, both bilayer configurations show a pronounced increase in mobility, approaching or exceeding 100 cm^2/Vs while maintaining similar carrier concentration levels.

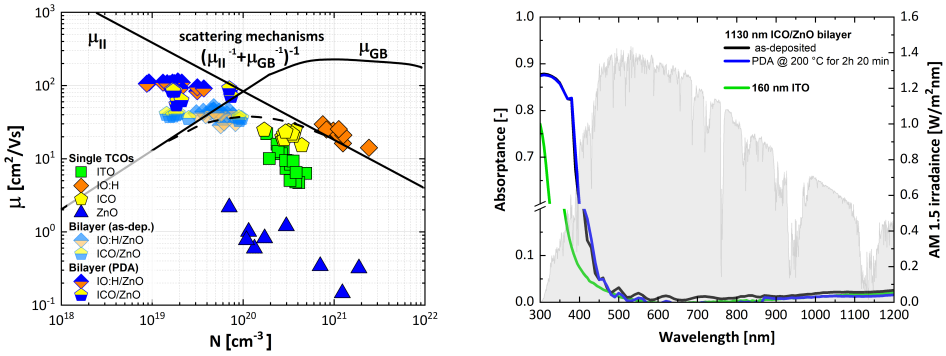

a) b)

Figure A.3: (a) Mobility (μ) versus carrier density (N) for ITO, IO:H, ICO, and ZnO, with bilayer structures IO:H/ZnO (blue/orange) and ICO/ZnO (blue/yellow) shown in as-deposited and PDA treated states. (b) Spectral absorptance (A) of a reference ITO monolayer and an ICO/ZnO bilayer before and after PDA.

Figure A.3b shows the spectral absorptance of a 1.1 µm thick ICO/ZnO bilayer in the as-deposited and post-deposition annealed states, compared to a 160 nm thick ITO reference. The AM 1.5 spectrum is included for contextual reference.
The ICO/ZnO bilayer exhibits increased parasitic absorption over a broader wavelength range in the blue region (300–500 nm) compared to single layer ITO. This is primarily attributed to the bilayer thickness and the absorption contribution of the ZnO layer near its band edge. In contrast, the absorptance in the visible and near-infrared range remains comparable to that of the ITO reference.
Figure A.4 shows the cross sectional SEM image of a representative ICO/ZnO bilayer deposited on glass. The structure consists of a dense and homogeneous 100 nm ICO layer directly on the glass substrate, followed by a 1.7 µm ZnO layer exhibiting pronounced columnar grain growth. The ZnO grains nucleate with small dimensions at the interface and progressively coarsen with increasing thickness, resulting in a textured top surface.

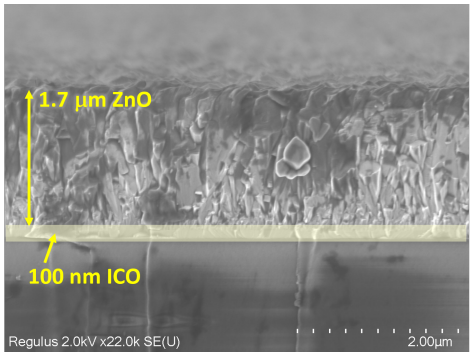

Figure A.4: SEM cross-section image of an ICO/ZnO bilayer on glass 100 nm ICO and 1.7 µm ZnO.

A.3. FTO/SnO_2 bilayer

Figure A.5a compares carrier mobility as a function of carrier density for single layer TCOs (ITO, IO:H, ZnO, SnO_2, FTO) and, IO:H/ZnO and FTO/SnO_2 bilayers in the as-deposited state and after post-deposition annealing (PDA) at 300 °C for 20 min in a controlled nitrogen environment.
The as-deposited FTO/SnO_2 bilayers exhibit mobility values in the intermediate range at carrier concentrations on the order of 10^{19} cm^{-3}. After PDA, mobility increases significantly, reaching up to 97 cm^2/Vs at a carrier density of 3×10^{18} cm^{-3}.
Compared to the IOH/ZnO bilayer, similar mobility values are achieved at even lower carrier density. Notably, the FTO/SnO_2 bilayers follow the same slope trend as the single layer FTO and SnO_2 references in the µ–N representation. This suggests that the dominant scattering mechanisms remain consistent with those governing the individual materials.
Figure A.5b presents the spectral absorptance of a 600 nm thick FTO/SnO_2 bilayer in both as-deposited and post-deposition annealed (PDA) conditions, compared to a 160 nm thick ITO reference. In contrast to the ICO/ZnO case, the absorptance in the blue spectral region is comparable to the ITO reference, consistent with the wide bandgap of both FTO and SnO_2.

Across the visible and near-infrared range, the absorptance remains low, indicating limited free-carrier absorption. Following PDA, the electrical performance is improved and the optical transparency is largely preserved. The FTO/SnO_2 results highlight that the bilayer maintains a favorable balance between electrical conductivity and optical losses.

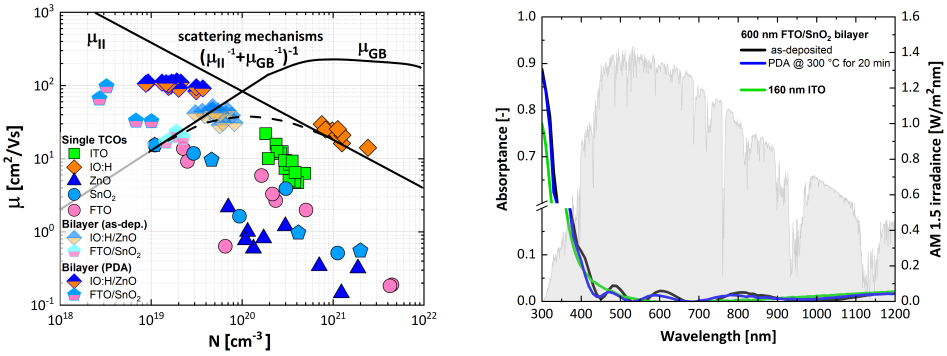

a) b)

Figure A.5: (a) Mobility (μ) versus carrier density (N) for ITO, IO:H, FTO, SnO_2 and ZnO, with bilayer structures IO:H/ZnO (blue/orange) and FTO/SnO_2 (light blue/pink) shown in as-deposited and PDA treated states. (b) Spectral absorptance (A) of a reference ITO monolayer and an FTO/SnO_2 bilayer before and after PDA.

Figure A.6 shows a cross-sectional SEM image of a representative FTO/SnO_2 bilayer deposited on glass. The structure consists of a 100 nm FTO layer followed by a 400 nm SnO_2 film exhibiting columnar growth. The columns maintain nearly constant lateral dimensions throughout the film thickness, showing limited grain coarsening during growth.

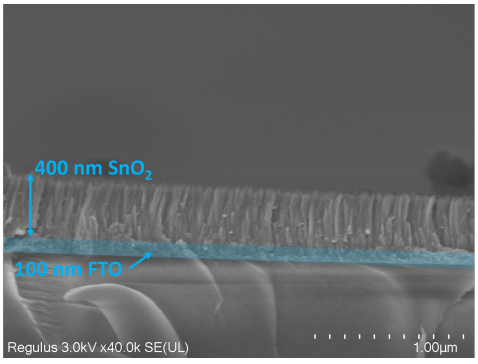

Figure A.6: SEM cross-section image of an FTO/SnO_2 bilayer on glass: 100 nm FTO and 400 nm SnO_2.

A.3.1. SEM images of high temperature FTO

Figure A.7 compares cross-sectional SEM images of commercial FTO-coated Asahi glass and FTO deposited by atmospheric pressure chemical vapor deposition (APCVD) at 500 °C in collaboration with the industrial partner of this work. In both cases, the FTO thickness is approximately 700 nm.

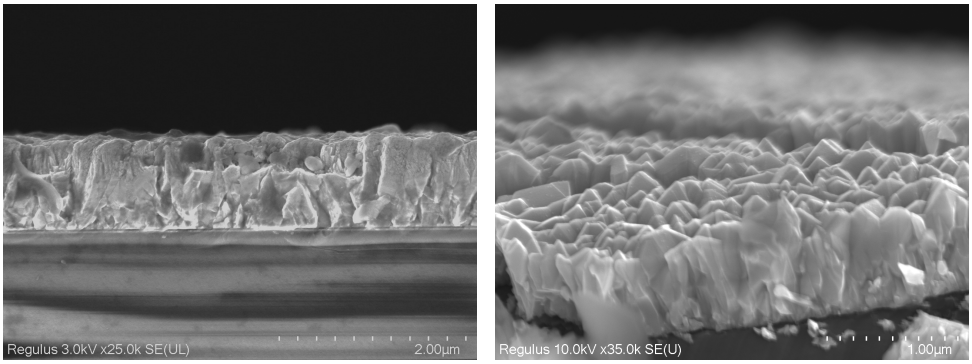

a) b)

Figure A.7: SEM cross-section images of high temperature FTO films (~ 700 nm): (a) commercial FTO-coated Asahi glass, (b) APCVD deposited FTO at 500 °C.

In Figure A.7a, the commercial FTO-coated Asahi glass exhibits a relatively compact columnar morphology, with moderate surface roughness and fairly uniform grain size throughout the film thickness.

In contrast, the APCVD FTO in Figure A.7b shows a clear evolution of the microstructure during growth. A fine-grained nucleation layer forms at the substrate interface, followed by progressive grain coarsening along the thickness direction. As a result, the upper region of the film consists of larger, faceted grains that form sharp, randomly distributed pyramidal features at the surface.

A

A.4. TCOs overview

Table A.1 provides a comparative overview of the key performance metrics relevant for TCO selection and engineering within thin-film photovoltaic architectures. The evaluation is structured around the design objective of developing single layer and bilayer TCOs that simultaneously satisfy optical and electrical requirements for front window, intermediate, and back reflector application in solar devices.

From an optical perspective, the target characteristics include a high optical bandgap (E_g) to preserve the blue spectral response of the device, low parasitic absorption across the visible and near-infrared range (α_{1000nm}), intrinsic or engineered surface texture to promote diffuse scattering, and appropriate refractive index contrast to enable optical grading at adjacent interfaces.

From an electrical perspective, the ideal TCO should exhibit high carrier mobility (μ) together with an optimized carrier concentration (N), enabling high conductivity while limiting free-carrier absorption losses.

Table A.1: Optoelectrical properties of single layer (ITO, IO:H, ICO, AZO, ZnO, FTO, SnO_2) and bilayer (IO:H/ZnO, ICO/ZnO, FTO/SnO2) TCOs. Optical metrics include bandgap energy (E_g) and absorption coefficient at 1000 nm (α1000nm); electrical metrics include carrier concentration (N) and mobility (μ). Surface texture is also indicated.

	High μ	Low N	High E_g	Low $\alpha_{1000\ nm}$	Natural Texture
ITO	✓	✗	✓	✗	✗
IO:H	✓	✗	✓	✓	✗
ICO	✓	✗	✓	✗	✗
AZO	✓	✗	✓	✗	✗
ZnO	✗	✓	✗	✓	✓
FTO	✓	✓	✓	✗	✓
SnO_2	✗	✓	✓	✗	✓
IO:H/ZnO (bilayer)	✓	✓	✗	✓	✓
ICO/ZnO (bilayer)	✓	✓	✗	✓	✓
FTO/SnO_2 (bilayer)	✓	✓	✓	✓	✓

The comparison highlights that individual materials typically excel in specific metrics but rarely satisfy all requirements simultaneously. Indium-based oxides provide favorable electrical transport properties, whereas ZnO- and SnO_2-based materials offer advantages in optical transparency and surface morphology.

Consequently, bilayer configurations emerge as an effective strategy to combine materials with complementary properties. For instance, high-mobility indium-based oxides such as IO:H or ICO can be combined with optically favorable layers such as ZnO, while conductive FTO can be paired with SnO_2 to exploit complementary transparency and morphological characteristics.

B

APPENDIX

B

B.1. Influence of oxygen on optical properties

B.1.1. Extended reflectance and transmittance spectra

The effect of oxygen on the optical behavior of FTO and SnO_2 films is examined through transmittance (T) and reflectance (R) measurements. Figure B.1 displays the full T and R spectra for samples deposited under varying O_2/Ar ratios. To illustrate the trends more comprehensively than in Chapter 3, a broader range of conditions is included. Specifically, FTO films sputtered with 0%, 0.15%, 0.2%, 0.3%, and 0.4% O_2/Ar are shown, along with SnO_2 films deposited at 0%, 0.25%, 0.5%, 0.75%, and 1% O_2/Ar.

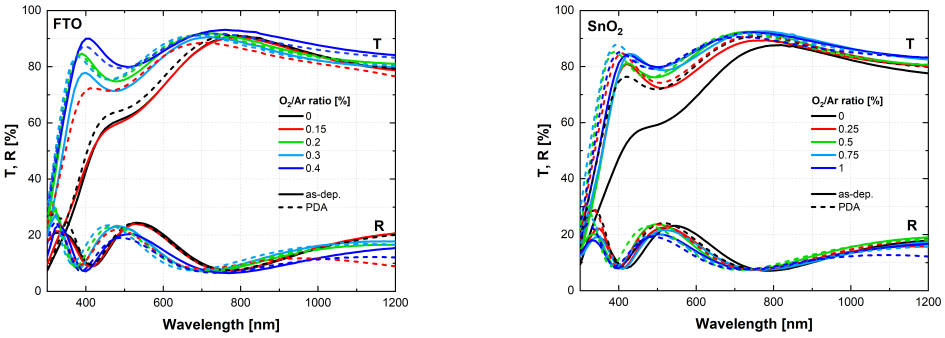

a) b)

Figure B.1: Transmittance (T) and reflectance (R) spectra of (a) FTO and (b) SnO_2 thin films (~ 200 nm thick) deposited under varying O_2/Ar ratios in as-deposited (as-dep.) and post-deposition annealed (PDA) states.

B.1.2. Tauc plot analysis

Figure B.2 shows the complete Tauc plots used to extract E_g values for both FTO and SnO_2 films across the full range of O_2/Ar ratios. The absorption coefficient (α) is derived from transmittance and reflectance spectra, and $(\alpha h\nu)^2$ is plotted versus photon energy ($h\nu$) to estimate the optical bandgap (E_g), assuming a direct bandgap transition.

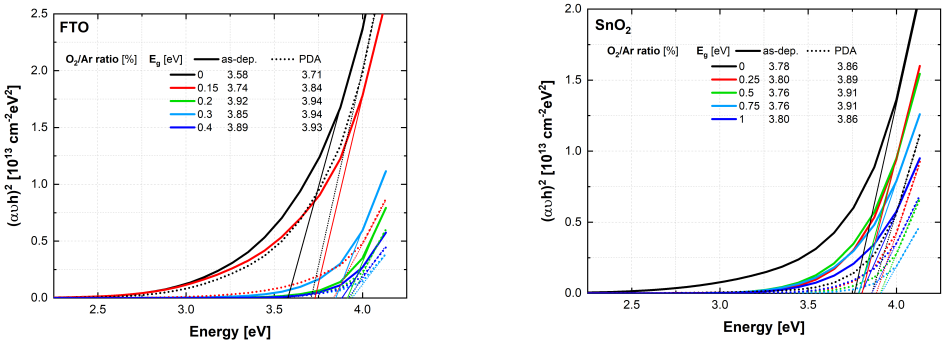

a) b)

Figure B.2: Tauc plots of (a) FTO and (b) SnO_2 thin films (~ 200 nm thick) deposited with varying O_2/Ar ratios, assuming direct bandgap transitions. Solid lines correspond to as-deposited (as-dep.) samples, and dashed lines represent post-deposition annealed (PDA) films.

B.2. Influence of hydrogen on optical properties

B.2.1. Extended reflectance and transmittance spectra

Figure B.4 presents the complete transmittance (T) and reflectance (R) spectra of FTO and SnO_2 films deposited under varying H_2/Ar ratios, with the oxygen content fixed at 1% O_2/Ar. The spectra correspond to hydrogen concentrations of 0%, 0.2%, 0.4%, and 0.6% H_2/Ar.

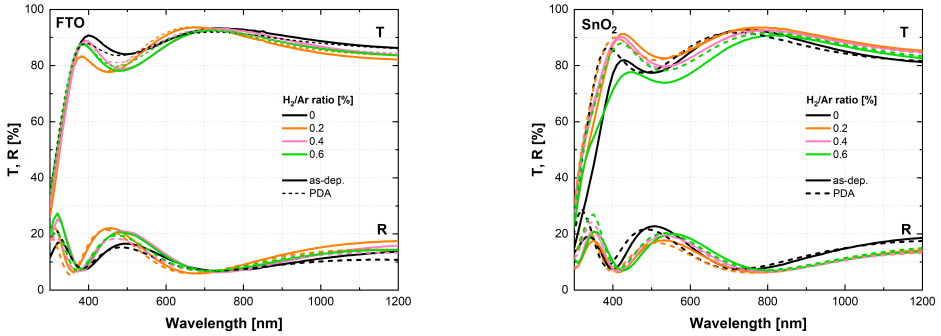

a) b)

Figure B.3: Transmittance (T) and reflectance (R) spectra of (a) FTO and (b) SnO_2 thin films (~ 200 nm thick) deposited at varying H_2/Ar ratios, with a fixed oxygen concentration of 1% O_2/Ar. Solid lines correspond to as-deposited (as-dep.) samples, and dashed lines represent post-deposition annealed (PDA) films.

B.2.2. Tauc plot analysis

Figure B.4 shows the complete Tauc plots for FTO and SnO_2 thin films deposited under varying H_2/Ar ratios, with the O_2/Ar ratio fixed at 1%. The absorption coefficient (α) is derived from transmittance and reflectance spectra, and $(\alpha h\nu)^2$ is plotted versus photon energy ($h\nu$) to estimate the optical bandgap (E_g), assuming a direct bandgap transition.

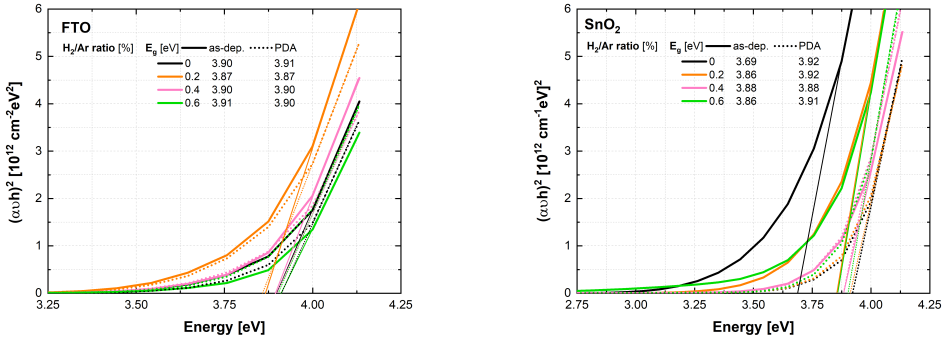

a) b)

Figure B.4: Tauc plots of (a) FTO and (b) SnO_2 thin films (~ 200 nm thick) deposited at different H_2/Ar ratios, assuming direct bandgap transitions. Solid lines correspond to as-deposited (as-dep.) samples, and dashed lines represent post-deposition annealed (PDA) films.

B.2.3. Urbach energy

Figure B.5 shows the Urbach energy (E_U) analysis for FTO films deposited with 0% and 0.4% H_2/Ar, with the oxygen content fixed at 1% O_2/Ar. The plots show the linear fit of ln(α) versus photon energy (hν), which are used to extract the Urbach energy values.

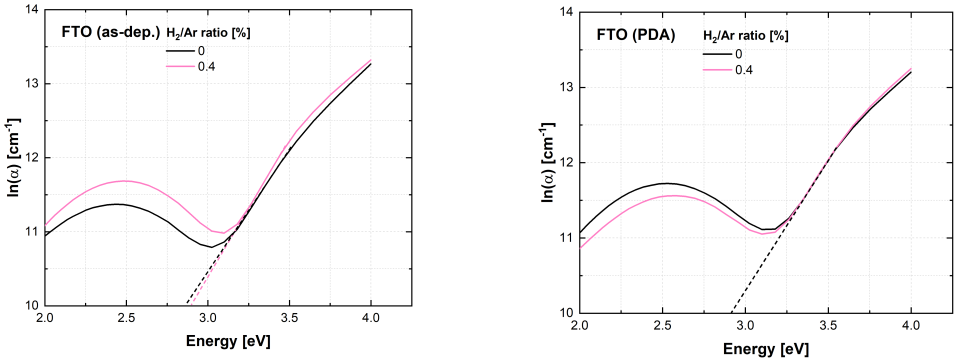

a) b)

Figure B.5: Linear fit on ln(α) vs photon energy (hν) for FTO films sputtered with 0% and 0.4% H_2/Ar: (a) as-deposited (as-dep.) and (b) post-deposition annealed (PDA) films.

Figure B.6 shows the Urbach energy (E_U) analysis for SnO_2 films deposited with 0% and 0.4% H_2/Ar, with the oxygen content fixed at 1% O_2/Ar. The plots show the linear fit of ln(α) versus photon energy (hν), which are used to extract the Urbach energy values.

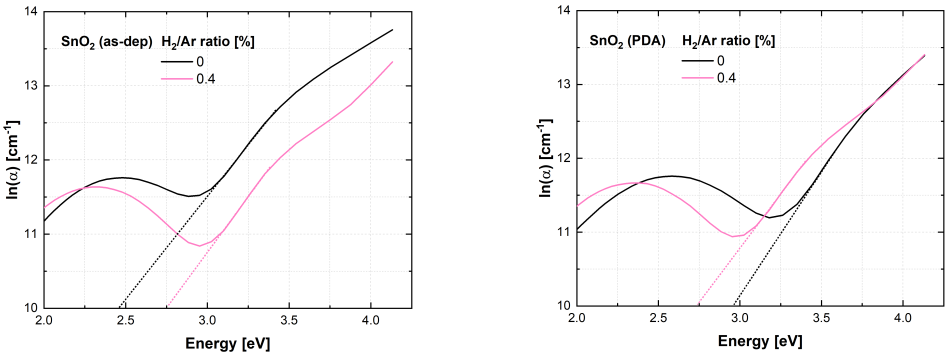

a) b)

Figure B.6: Linear fit on ln(α) vs photon energy (hν) for SnO_2 films sputtered with 0% and 0.4% H_2/Ar: (a) as-deposited (as-dep.) and (b) post-deposition annealed (PDA) films.

B.3. Carrier type and density

Table B.1 and Table B.2 summarize the measured carrier densities and conduction types for FTO and SnO_2 films deposited under different O_2/Ar and H_2/Ar gas ratios. In the as-deposited state, both n-type and p-type conductivity are detected. Following post-deposition annealing (PDA) in a pure nitrogen environment, all films consistently exhibit n-type behavior. The reported carrier density values represent the average of five Hall measurements performed on the same sample.

Table B.1: Carrier density (N) of FTO and SnO_2 films as a function of O_2/Ar sputtering gas ratios in the as-deposited and post-deposition annealed (PDA) states. Positive and negative signs indicate p-type and n-type conductivity, respectively, as determined by Hall effect measurements.

FTO	N [cm^{-3}]	
O_2/Ar [%]	as-deposited	PDA
0	$+4.45 \cdot 10^{21}$	$-2.84 \cdot 10^{20}$
0.15	$+4.22 \cdot 10^{21}$	$-1.64 \cdot 10^{21}$
0.2	$-2.34 \cdot 10^{20}$	$-2.23 \cdot 10^{20}$
0.3	$-2.15 \cdot 10^{20}$	$-2.30 \cdot 10^{20}$
0.4	$+2.25 \cdot 10^{19}$	$-3.86 \cdot 10^{20}$

SnO_2	N [cm^{-3}]	
O_2/Ar [%]	as-deposited	PDA
0	$+1.12 \cdot 10^{21}$	$-3.84 \cdot 10^{20}$
0.25	$-3.02 \cdot 10^{20}$	$-4.19 \cdot 10^{20}$
0.5	$-2.92 \cdot 10^{19}$	$-1.17 \cdot 10^{20}$
0.75	$+9.34 \cdot 10^{19}$	$-8.45 \cdot 10^{19}$
1	$-1.10 \cdot 10^{19}$	$-8.15 \cdot 10^{19}$

Table B.2: Carrier density (N) of FTO and SnO_2 films as a function of H_2/Ar sputtering gas ratios, with O_2/Ar ratio fixed at 1%, in both as-deposited and post-deposition annealed (PDA) states. Positive and negative values indicate p-type and n-type conductivity, respectively, based on Hall effect measurements.

FTO	N [cm^{-3}]	
H_2/Ar [%]	as-deposited	PDA
0	$+2.50 \cdot 10^{19}$	$-2.01 \cdot 10^{21}$
0.2	$+5.04 \cdot 10^{20}$	$-4.72 \cdot 10^{19}$
0.4	$+1.63 \cdot 10^{20}$	$-3.65 \cdot 10^{19}$
0.6	$+6.53 \cdot 10^{19}$	$-2.24 \cdot 10^{20}$

SnO_2	N [cm^{-3}]	
H_2/Ar [%]	as-deposited	PDA
0	$-1.10 \cdot 10^{19}$	$-8.15 \cdot 10^{19}$
0.2	$-2.00 \cdot 10^{21}$	$-3.22 \cdot 10^{19}$
0.4	$-4.62 \cdot 10^{19}$	$-3.39 \cdot 10^{19}$
0.6	$-4.15 \cdot 10^{20}$	$-3.30 \cdot 10^{19}$

B

B.4. EDX - atomic %

Table B.3 and Table B.4 present the elemental composition of FTO and SnO_2 films, respectively, obtained by energy-dispersive X-ray spectroscopy (EDX). The quantified elements include C, O, Si, Sn and F for the FTO samples, while C, O, Si, and Sn for the SnO_2 films. All values are reported with their corresponding measurement uncertainties. Quantification is carried out using the eZAF Smart Quant algorithm.

Table B.3: Elemental composition (at. %) of FTO films, including C, O, Si, Sn, and F, with measurement uncertainties (error %).

O_2/Ar [%]	C K at. %	C K error %	O K at. %	O K error %	F K at. %	F K error %	Si K at. %	Si K error %	Sn K at. %	Sn K error %
0	6.63	12.10	11.92	8.12	0.00	99.99	61.49	3.26	8.28	1.90
0.4	8.02	12.04	22.57	8.16	0.66	12.69	61.48	3.15	7.27	1.95
1	7.48	12.27	21.89	8.20	0.57	13.63	63.38	3.05	6.69	2.07
1 + 0.4% H_2/Ar	4.22	10.02	31.81	6.85	0.29	23.02	45.30	3.87	18.39	3.08

Table B.4: Elemental composition (at. %) of SnO_2 films, including C, O, Si, and Sn, with measurement uncertainties (error %).

O_2/Ar [%]	C K at. %	C K error %	O K at. %	O K error %	Si K at. %	Si K error %	Sn K at. %	Sn K error %
0	7.10	12.25	21.13	8.23	64.54	3.10	7.23	2.02
0.5	–	–	–	–	–	–	–	–
1	6.46	12.99	20.09	8.30	68.12	2.80	5.34	2.22
1 + 0.4% H_2/Ar	6.93	12.38	21.03	8.26	66.08	2.92	5.97	2.10

B.5. XPS analysis – extended data

Figure B.7 and Figure B.8 present the full X-ray photoelectron spectroscopy (XPS) survey spectra for FTO and SnO_2 films, respectively, in both as-deposited (as-dep.) and post-deposition annealing (PDA) states.

For FTO (Figure B.7), the detected core-level peaks include F 1s, O 1s, Sn 3d, and C 1s. A weak F 1s signal is consistently observed near 684.9 eV across all investigated conditions. The sputtering gas compositions are pure Ar (0% O_2/Ar), 0.4% O_2/Ar, 1% O_2/Ar, and 1% O_2/Ar + 0.4% H_2/Ar.

For SnO_2 (Figure B.8), the detected core-level peaks include O 1s, Sn 3d, and C 1s. The sputtering gas compositions are pure Ar (0% O_2/Ar), 0.5% O_2/Ar, 1% O_2/Ar, and 1% O_2/Ar + 0.4% H_2/Ar.

Figure B.9 shows the quantification of Sn^0, Sn^{2+}, and Sn^{4+} components derived from high resolution XPS data. The results are presented for FTO and SnO_2 films as a function of sputtering gas composition.

Table B.5 and Table B.6 list the atomic percentages of the core-level elements for FTO and SnO_2 films, respectively, in both as-deposited and PDA states.

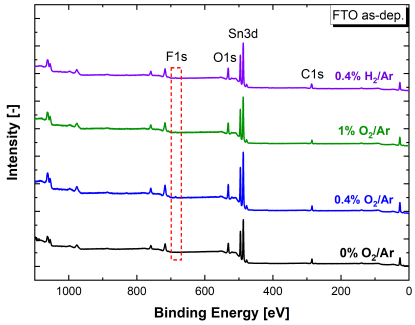

a)

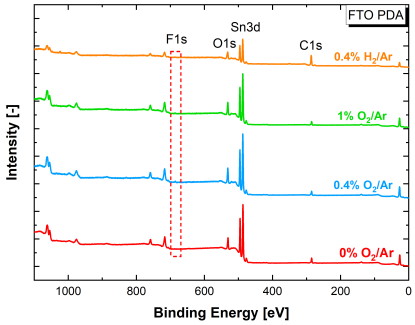

b)

Figure B.7: Full XPS survey spectra of FTO films under varying gas compositions in (a) as-deposited (as-dep.) and (b) post-deposition annealing (PDA) states. Detected core-level peaks include F 1s, O 1s, Sn 3d, and C 1s. A weak F 1s signal is visible near 684.9 eV for all gas compositions.

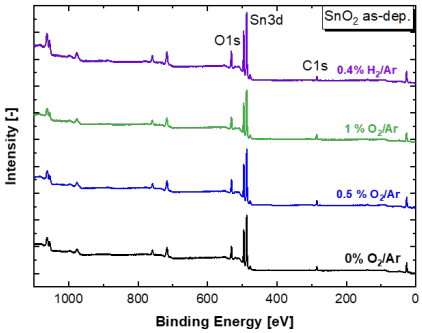

a)

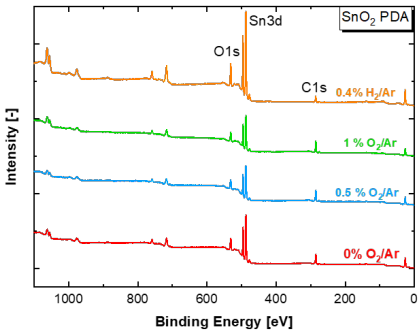

b)

Figure B.8: Full XPS survey spectra of SnO_2 films under varying gas compositions in (a) as-deposited (as-dep.) and (b) post-deposition annealing (PDA) states. Detected core-level peaks include O 1s, Sn 3d, and C 1s.

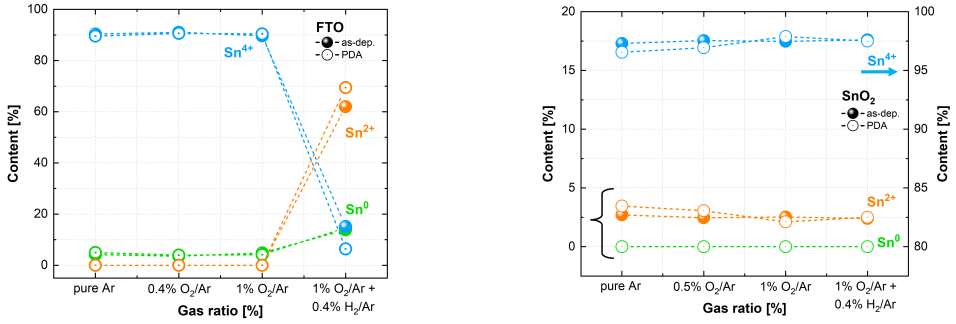

a) b)

Figure B.9: Quantification of Sn^0, Sn^{2+}, and Sn^{4+} components obtained from high resolution XPS measurements for (a) FTO and (b) SnO_2 films as a function of sputtering gas composition, shown for both as-deposited (as-dep.) and post-deposition annealed (PDA) states.

Table B.5: Atomic percentage of core-level elements (F, O, Sn, C) in FTO films, measured by XPS in as-deposited (as-dep.) and post-deposition annealed (PDA) states at different sputtering gas compositions.

O_2/Ar [%]	O1s at. % as-dep.	Sn3d5 % as-dep.	C1s at. % as-dep.	F1s % as-dep.	O1s at. % PDA	Sn3d5 % PDA	C1s at. % PDA	F1s % PDA
0	31.8	29.8	38.4	<1	29.2	37.2	33.6	<1
0.4	38.0	34.3	25.8	1.9	36.7	35.0	26.7	1.6
1	35.7	34.4	28.9	0.9	37.3	35.9	25.2	1.6
1 + 0.4% H_2/Ar	31.4	27.8	40.4	0.5	20.5	14.0	64.2	1.2

Table B.6: Atomic percentage of core-level elements (O, Sn, C) in SnO_2 films, measured by XPS in as-deposited (as-dep.) and post-deposition annealed (PDA) states at different sputtering gas compositions.

O_2/Ar [%]	O1s at. % as-dep.	Sn3d5 % as-dep.	C1s % as-dep.	O1s at. % PDA	Sn3d5 % PDA	C1s % PDA
0	37.0	33.8	29.2	49.4	27.1	23.5
0.5	35.3	34.3	30.5	57.2	25.5	17.3
1	36.8	33.6	29.7	57.3	23.1	19.6
1 + 0.4% H_2/Ar	38.4	38.3	23.3	37.7	35.2	27.1

B.6. XRD analysis of high temperature APCVD FTO

A representative FTO sample deposited by atmospheric pressure chemical vapor deposition (APCVD) is characterized using X-ray diffraction (XRD). The film is grown on an aluminum substrate under standard industrial processing conditions at 500 °C. The XRD pattern (Figure B.10) displays pronounced diffraction peaks corresponding to the (110) and (200) planes, indicating that these are the preferred crystallographic orientations

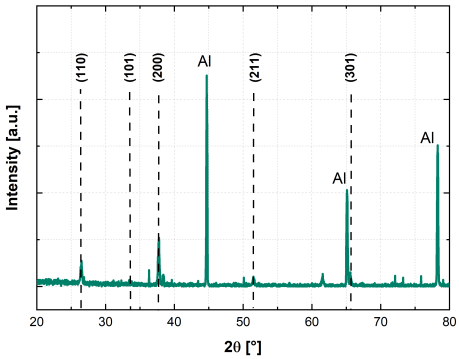

Figure B.10: XRD patterns of a representative FTO film deposited by atmospheric pressure chemical vapor deposition (APCVD) at 500 °C. The prominent peaks at (110) and (200) indicate preferred crystal orientations. The measurement is performed on 700 nm FTO film on aluminum substrate.

B.7. SEM analysis

A comparative scanning electron microscopy (SEM) analysis of representative FTO (Figure B.11) and SnO_2 (Figure B.12) films, deposited on (100)-oriented silicon wafers, reveals distinct differences in film thickness and surface morphology through high resolution cross-sectional and top-view imaging.

In the cross-sectional views (Figure B.11a and Figure B.12a), both films exhibit vertically aligned columnar structures, characteristic of directional growth during sputtering. A distinct seed layer is visible at the film–substrate interface, acting as a nucleation site for grain formation and influencing the orientation, density, and size of the columns. As deposition progresses, the columns widen, leading to grain coarsening and the formation of larger structural features near the surface.

Top-view SEM images highlight clear morphological differences. In the FTO film (Figure B.11b), the grains are not tightly packed together, and there are visible gaps, boundaries, or irregular spacing between them. The SnO_2 film (Figure B.12b) exhibits a denser, more uniform surface morphology, indicating more effective grain coalescence and compact growth.

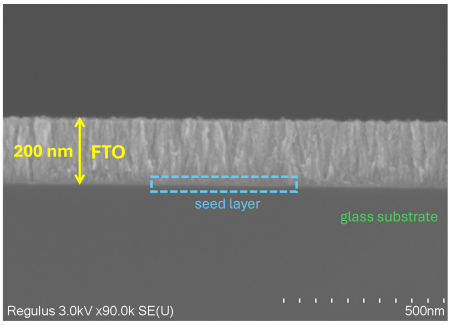

a)

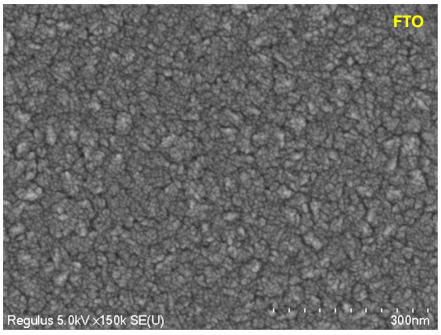

b)

Figure B.11: SEM images of a representative FTO film (200 nm thick) deposited on a (100)-oriented Si wafer: (a) cross-sectional view; (b) top-view.

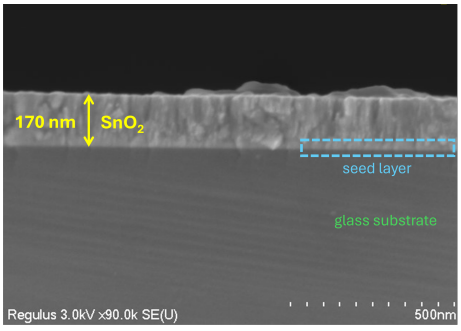

a)

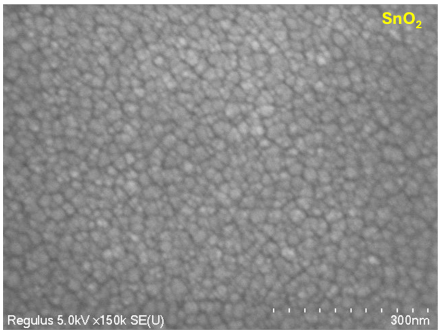

b)

Figure B.12: SEM images of a representative SnO_2 film (170 nm thick) deposited on a (100)-oriented Si wafer: (a) cross-sectional view; (b) top-view.

C

APPENDIX

C

C.1. GenPro4 scattering matrices

In GenPro4, each optical interface is described by angular scattering matrices that define how light is redistributed after interacting with the interface. For every incident angle, the matrices specify the probability that light exits the interface at a given outgoing angle. Four scattering channels are considered: forward transmission, forward reflection, backward transmission, and backward reflection.

For visualization, these channels are combined into a single 2×2 block matrix, as illustrated in Figure C.1. The horizontal axis represents the incident angle, θ_{in}, and the vertical axis the outgoing angle, θ_{out}. The left and right columns correspond to light incident from the air and substrate sides, respectively, while the upper and lower rows represent light exiting toward the substrate and air. Each quadrant therefore describes a specific scattering process.

Angles are defined with respect to the surface normal, ranging from normal incidence (0°) to grazing propagation (±90°). The color scale represents the normalized redistribution probability, indicating the fraction of incident light redirected from a given incident angle into a specific outgoing angle. The angular domain is discretized into finite intervals, with the resolution chosen to balance numerical accuracy and computational cost.

For each incident direction, energy conservation requires that the sum over all outgoing angles equals unity, while optical reciprocity imposes symmetry relations between forward and backward scattering processes.

For flat interfaces, the scattering matrices are fully determined by the Fresnel equations and Snell's law, resulting in purely specular reflection and refraction. Specular reflection appears as a diagonal feature because the incident and reflected angles coincide, whereas transmission generates curved features associated with refracted propagation that terminate at the critical angle for total internal reflection. These characteristic signatures are visible in the scattering matrix of the flat air/glass interface shown in Figure C.1.

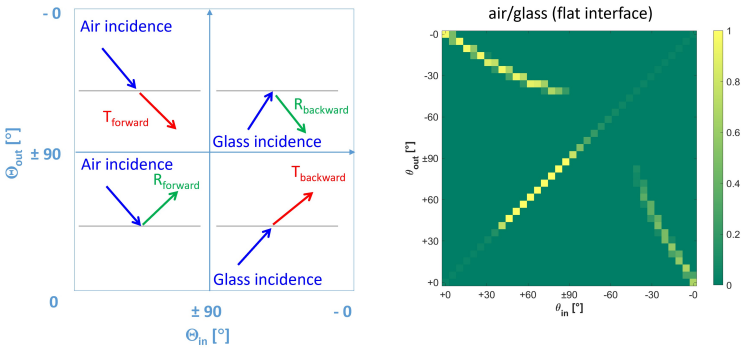

Figure C.1: Schematic illustration of the four scattering processes arranged in a two by two block matrix (left). Angular scattering matrix representation of a flat air/glass interface in a solar cell device.: light redistribution probability as a function of incident angle θ_{in} and outgoing angle θ_{out} (right).

C.2. Sensitivity analysis

A sensitivity analysis is performed prior to experimental validation to identify the defect-related electronic parameters that most strongly govern the performance of the reference a-Si:H and nc-Si:H single-junction devices. The analysis focuses on the Urbach energies (E_U) of the exponential band tails and the density of mid-gap dangling bonds (N_{DB}), which influence sub-gap absorption, Shockley–Read–Hall (SRH) recombination, and ultimately the attainable short-circuit current density (J_{sc}) and open-circuit voltage (V_{oc}). For both absorbers, a two-dimensional parameter sweep is conducted by varying E_U and N_{DB} over experimentally relevant ranges while keeping all remaining parameters fixed at their baseline values.

For the a-Si:H device, the acceptor-like Urbach energy is varied between 0.010–0.070 eV, the donor-like Urbach energy between 0.018–0.078 eV, and the dangling-bond density over the range typical of PECVD-deposited a-Si:H. The resulting contour maps (Figure C.2) show that J_{sc} is partially sensitive to variations in tail-state width or defect concentration, as tail states primarily broaden the absorption edge while contributing comparatively weakly to recombination under the calibrated capture cross-sections.

In contrast, V_{oc} exhibits a pronounced dependence on both E_U and N_{DB}. Larger E_U values increase the density of band-tail states extending into the bandgap, while higher N_{DB} concentrations introduce mid-gap defects that strongly enhance SRH recombination. Although the total tail-state density ($\sim 10^{20}$ cm^{-3} eV^{-1}) is several orders of magnitude higher than the dangling-bond density ($\sim 10^{16}$ cm^{-3}), the mid-gap energetic position of the dangling bonds makes them the dominant recombination centers contributing to voltage loss.

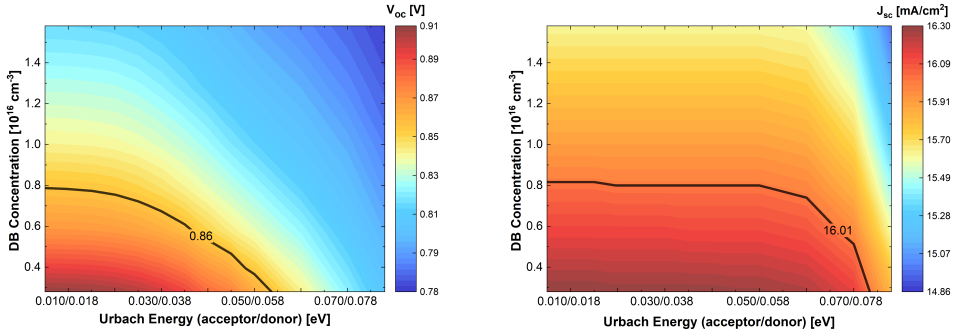

Figure C.2: Sensitivity of the calibrated a-Si:H single-junction solar cell to defect-related parameters: (a) contour map of the open-circuit voltage (V_{oc}) as a function of Urbach energy (E_U) and dangling-bond concentration (N_{DB}); (b) corresponding contour map of the short-circuit current density (J_{sc}) within the same parameter space. The black contour lines mark the combinations that reproduce the experimental performance (V_{oc} = 0.86 V, J_{sc} = 16.01 mA/cm^2).

A similar analysis is performed for the nc-Si:H single-junction device, which is represented using three depth-dependent sublayers to capture the evolution of crystalline fraction and defect density during film growth. The resulting contour maps (Figure C.3) reveal trends consistent with those observed in a-Si:H: J_{sc} remains relatively insensitive to E_U and N_{DB}, whereas V_{oc} depends strongly on both parameters due to enhanced mid-gap recombination.

Despite their lower absolute concentrations (10^{14}–10^{15} cm^{-3}), dangling-bond defects again dominate voltage loss because of their energetic position and high recombination activity. Tail states influence V_{oc} through their effect on quasi-Fermi-level splitting, but remain less critical than mid-gap defects.

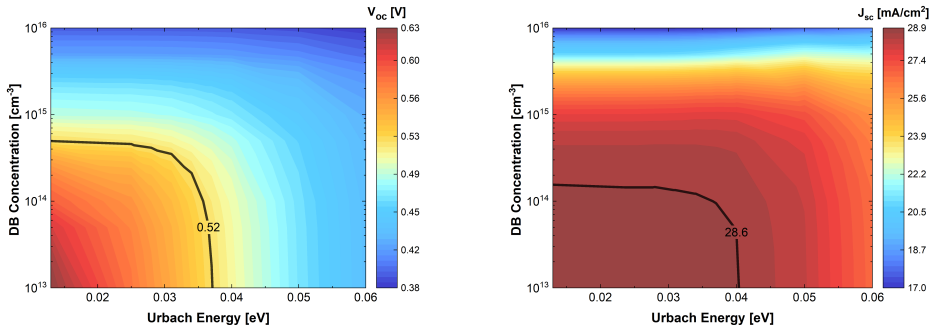

Figure C.3: Sensitivity of the calibrated nc-Si:H single-junction solar cell to defect-related parameters: (a) contour map of the open-circuit voltage (V_{oc}) as a function of Urbach energy (E_U) and dangling-bond concentration (N_{DB}); (b) corresponding contour map of the short-circuit current density (J_{sc}) for the same parameter space. The black contour lines mark the combinations that reproduce the experimental values (V_{oc} = 0.52 V, J_{sc} = 28.6 mA/cm^2).

Overall, the sensitivity analysis shows that J_{sc} in both a-Si:H and nc-Si:H absorbers is primarily governed by optical absorption and carrier collection, while V_{oc} is controlled by the density and energetic distribution of recombination-active defects. Minimizing mid-gap dangling-bond states while maintaining moderate Urbach energies therefore emerges as the most effective strategy for optimizing voltage and overall device performance in both TF-Si absorbers.

C.3. Sentaurus TCAD input parameters

Tables C.1–C.4 report the input parameters used in the Sentaurus TCAD device simulations. Further details regarding the non-local tunneling models implemented across all simulated solar cells, the optical absorptance profiles employed in the optoelectrical simulations, and additional insights into the material properties, device configurations, and physical models are provided in our previous work [271].

Table C.1: Material, defect and doping parameters for the p–i–n single junction a–Si:H solar cell.

Parameter	AZO	nc–SiO_x (p^+)	nc–SiO_x (p)	a–Si:H (i)	nc–SiO_x (n)
Extended states					
Bandgap, E_g [eV]	3.3	2.84	2.84	1.63	2.42
Electron affinity, χ [eV]	4.5	3.37	3.37	4.00	3.55
ϵ_r [–]	9.0	11.9	11.9	11.9	11.9
N_c [cm^{-3}]	1.0×10^{20}	1.0×10^{20}	1.0×10^{20}	1.0×10^{20}	1.0×10^{20}
N_v [cm^{-3}]	1.0×10^{20}	1.0×10^{20}	1.0×10^{20}	1.0×10^{20}	1.0×10^{20}
μ_n [cm^2/Vs]	20	10	10	10	10
μ_p [cm^2/Vs]	10	2	2	2	2
Doping concentration [cm^{-3}]	3.8×10^{20}	-1.0×10^{20}	-6.0×10^{19}	–	2.0×10^{19}
Valence band tails					
Urbach energy, E_u [eV]	–	0.05	0.05	0.03	0.094
$N_{v,tail}$ [cm^{-3}/eV]	–	1.0×10^{21}	1.0×10^{21}	2.0×10^{20}	1.0×10^{21}
σ_e [cm^2]	–	1.0×10^{-16}	1.0×10^{-16}	1.0×10^{-16}	1.0×10^{-16}
σ_h [cm^2]	–	1.0×10^{-16}	1.0×10^{-16}	1.0×10^{-16}	1.0×10^{-16}
Conduction band tails					
Urbach energy, E_u [eV]	–	0.08	0.08	0.022	0.068
$N_{c,tail}$ [cm^{-3}/eV]	–	1.0×10^{21}	1.0×10^{21}	2.0×10^{20}	1.0×10^{21}
σ_e [cm^2]	–	1.0×10^{-16}	1.0×10^{-16}	1.0×10^{-16}	1.0×10^{-16}
σ_h [cm^2]	–	1.0×10^{-16}	1.0×10^{-16}	1.0×10^{-16}	1.0×10^{-16}
Dangling bonds					
N_{DB} [cm^{-3}]	–	1.3×10^{18}	1.3×10^{18}	7.8×10^{15}	1.3×10^{18}
Peak width [eV]	–	0.21	0.21	0.14	0.21
Donor peak position [eV]	–	1.1	1.1	0.92	0.9
Acceptor peak position [eV]	–	1.4	1.4	1.02	1.2
Donor σ_e [cm^2]	–	3.0×10^{-14}	3.0×10^{-14}	3.0×10^{-14}	3.0×10^{-14}
Donor σ_h [cm^2]	–	3.0×10^{-15}	3.0×10^{-15}	3.0×10^{-15}	3.0×10^{-15}
Acceptor σ_e [cm^2]	–	3.0×10^{-15}	3.0×10^{-15}	3.0×10^{-15}	3.0×10^{-15}
Acceptor σ_h [cm^2]	–	3.0×10^{-14}	3.0×10^{-14}	3.0×10^{-14}	3.0×10^{-14}

Table C.2: Parameters used for the perovskite based single junction and tandem devices. The nc–SiO_x (p) parameters are adopted from the a–Si:H single junction solar cell (Table C.3).

Parameter	Perovskite (WBG)	Perovskite (Sn–Pb)	C60	BCP	NiO_x	PEDOT:PSS	PTAA	2PACz (SAM)	nc–SiO_x (p)
Bandgap, E_g [eV]	1.68	1.23	2.10	3.50	3.80	1.60	3.30	3.40	2.84
Electron affinity, χ [eV]	4.00	3.90	3.90	2.50	1.46	3.50	1.80	1.70	3.37
Permittivity, ϵ_r [–]	6.5	20	10	10	10.7	3	3	10	11.9
Doping concentration [cm^{-3}]	–	–	1.0×10^{19}	1.0×10^{20}	1.0×10^{19}	1.0×10^{19}	1.0×10^{19}	1.0×10^{20}	1.0×10^{20}
N_c [cm^{-3}]	1.0×10^{20}	1.0×10^{18}	2.0×10^{18}	2.0×10^{18}	2.0×10^{18}	2.2×10^{18}	2.2×10^{18}	2.0×10^{18}	1.0×10^{20}
N_v [cm^{-3}]	1.0×10^{19}	1.0×10^{18}	2.0×10^{19}	1.8×10^{19}	1.8×10^{19}	1.8×10^{19}	1.8×10^{19}	2.0×10^{19}	1.0×10^{20}
μ_n [cm^2/Vs]	35	20	8.9×10^{-4}	1.0×10^{-3}	1.0×10^{-2}	1.0×10^{-3}	4.0×10^{-5}	1.0×10^{-3}	10
μ_p [cm^2/Vs]	35	10	8.9×10^{-4}	5.0×10^{-2}	1.0×10^{-3}	1.9×10^{-2}	4.0×10^{-5}	1.0×10^{-3}	2
Bulk lifetime, τ [s]	1.0×10^{-6}	1.0×10^{-6}	–	–	1.0×10^{-7}	5.0×10^{-6}	1.0×10^{-5}	–	–
Surface recombination velocity [cm/s]	–	–	–	–	100	100	20	–	–

C

Table C.3: Material, defect and doping parameters for the p–i–n single junction nc–Si:H solar cell.

Parameter	IO:H	AZO	nc–SiO_x (p^+)	nc–SiO_x (p)	nc Si_1	nc–Si_2	nc–Si_3	nc–SiO_x (n)
Extended states								
Bandgap, E_g [eV]	3.3	3.4	2.84	2.84	1.25	1.20	1.15	2.42
Electron affinity, χ [eV]	4.5	4.4	3.33	3.33	4.05	4.05	4.05	3.39
ε_r [–]	9.0	9.0	11.9	11.9	11.9	11.9	11.9	11.9
N_c [cm^{-3}]	1.0×10^{20}	1.0×10^{20}	1.0×10^{20}	1.0×10^{20}	8.0×10^{19}	8.0×10^{19}	8.0×10^{19}	1.0×10^{20}
N_v [cm^{-3}]	1.0×10^{20}	1.0×10^{20}	1.0×10^{20}	1.0×10^{20}	6.0×10^{19}	6.0×10^{19}	6.0×10^{19}	1.0×10^{20}
μ_n [cm^2/Vs]	20	20	10	10	20	25	30	10
μ_p [cm^2/Vs]	10	10	2	2	3	5	6	2
Doping concentration [cm^{-3}]	3.8×10^{20}	1.0×10^{15}	-1.0×10^{20}	-6.0×10^{19}	–	–	–	2.0×10^{19}
Valence band tails								
Urbach energy, E_u [eV]	–	–	0.05	0.05	0.031	0.034	0.037	0.094
$N_{v,tail}$ [cm^{-3}/eV]	–	–	1.0×10^{21}	1.0×10^{21}	1.0×10^{19}	5.0×10^{19}	1.0×10^{20}	1.0×10^{21}
σ_e [cm^2]	–	–	1.0×10^{-16}	1.0×10^{-16}	1.0×10^{-16}	1.0×10^{-16}	1.0×10^{-16}	7.0×10^{-16}
σ_h [cm^2]	–	–	1.0×10^{-16}	1.0×10^{-16}	1.0×10^{-17}	1.0×10^{-17}	1.0×10^{-17}	7.0×10^{-16}
Conduction band tails								
Urbach energy, E_u [eV]	–	–	0.08	0.08	0.031	0.034	0.037	0.068
$N_{c,tail}$ [cm^{-3}/eV]	–	–	1.0×10^{21}	1.0×10^{21}	1.0×10^{19}	5.0×10^{19}	1.0×10^{20}	1.0×10^{21}
σ_e [cm^2]	–	–	1.0×10^{-16}	1.0×10^{-16}	1.0×10^{-17}	1.0×10^{-17}	1.0×10^{-17}	7.0×10^{-16}
σ_h [cm^2]	–	–	1.0×10^{-16}	1.0×10^{-16}	1.0×10^{-16}	1.0×10^{-16}	1.0×10^{-16}	7.0×10^{-16}
Dangling bonds								
N_{DB} [cm^{-3}]	–	–	1.3×10^{18}	1.3×10^{18}	1.5×10^{14}	1.5×10^{14}	1.5×10^{14}	1.3×10^{18}
Peak width [eV]	–	–	0.21	0.21	0.14	0.14	0.14	0.21
Donor peak position [eV]	–	–	0.9	0.9	0.7	0.7	0.7	1.1
Acceptor peak position [eV]	–	–	1.2	1.2	0.85	0.85	0.85	1.2
Donor σ_e [cm^2]	–	–	3.0×10^{-14}	3.0×10^{-14}	3.0×10^{-15}	3.0×10^{-15}	3.0×10^{-15}	3.0×10^{-14}
Donor σ_h [cm^2]	–	–	3.0×10^{-15}	3.0×10^{-15}	3.0×10^{-16}	3.0×10^{-16}	3.0×10^{-16}	3.0×10^{-15}
Acceptor σ_e [cm^2]	–	–	3.0×10^{-15}	3.0×10^{-15}	3.0×10^{-16}	3.0×10^{-16}	3.0×10^{-16}	3.0×10^{-15}
Acceptor σ_h [cm^2]	–	–	3.0×10^{-14}	3.0×10^{-14}	3.0×10^{-15}	3.0×10^{-15}	3.0×10^{-15}	3.0×10^{-14}

Table C.4: Material, defect and doping parameters for the p–i–n junctions of the tandem a–Si:H/nc–Si:H solar cell for rigid and flexible substrates.

	a–Si:H top subcell		nc–Si:H bottom subcell			
Parameter	nc–SiO_x (p)/a–SiO_x	a–Si:H (i)	nc–SiO_x (n)	nc–SiO_x (p^+)/(p)	nc–Si:H (i)	nc–SiO_x (n)
Extended states						
Bandgap, E_g [eV]	2.84	1.65	2.42	2.84	1.25	2.42
Electron affinity, χ [eV]	3.37	4.00	3.55	3.33	4.05	3.39
ε_r [–]	11.9	11.9	11.9	11.9	11.9	11.9
N_c [cm^{-3}]	1.0×10^{20}	1.0×10^{20}	1.0×10^{20}	1.0×10^{20}	6.0×10^{19}	1.0×10^{20}
N_v [cm^{-3}]	1.0×10^{20}	1.0×10^{20}	1.0×10^{20}	1.0×10^{20}	8.0×10^{19}	1.0×10^{20}
μ_n [cm^2/Vs]	10	10	10	10	30	10
μ_p [cm^2/Vs]	2	2	2	2	6	2
Doping concentration [cm^{-3}]	$1.0\times10^{20}/1.0\times10^{18}$	–	8.0×10^{19}	$2.0\times10^{20}/6.5\times10^{19}$	–	4.0×10^{19}
Valence band tails						
Urbach energy, E_u [eV]	0.05	0.03	0.094	0.05	0.036	0.094
$N_{v,tail}$ [cm^{-3}/eV]	1.0×10^{21}	2.0×10^{20}	1.0×10^{21}	1.0×10^{20}	4.8×10^{19}	1.0×10^{21}
σ_e [cm^2]	1.0×10^{-16}	1.0×10^{-16}	1.0×10^{-16}	1.0×10^{-16}	1.0×10^{-16}	1.0×10^{-16}
σ_h [cm^2]	1.0×10^{-16}	1.0×10^{-16}	1.0×10^{-16}	1.0×10^{-16}	1.0×10^{-17}	1.0×10^{-16}
Conduction band tails						
Urbach energy, E_u [eV]	0.08	0.022	0.068	0.08	0.036	0.068
$N_{c,tail}$ [cm^{-3}/eV]	1.0×10^{21}	2.0×10^{20}	1.0×10^{21}	1.0×10^{20}	9.6×10^{19}	1.0×10^{21}
σ_e [cm^2]	1.0×10^{-16}	1.0×10^{-16}	1.0×10^{-16}	1.0×10^{-16}	1.0×10^{-17}	1.0×10^{-16}
σ_h [cm^2]	1.0×10^{-16}	1.0×10^{-16}	1.0×10^{-16}	1.0×10^{-16}	1.0×10^{-16}	1.0×10^{-16}
Dangling bonds						
N_{DB} [cm^{-3}]	1.3×10^{18}	1.74×10^{16}	1.3×10^{18}	1.3×10^{18}	3.0×10^{15}	1.3×10^{18}
Peak width [eV]	0.21	0.14	0.21	0.21	0.14	0.21
Donor peak position [eV]	1.1	0.92	1.1	1.1	0.7	1.1
Acceptor peak position [eV]	1.2	1.02	1.2	1.4	0.85	1.2
Donor σ_e [cm^2]	3.0×10^{-14}	3.0×10^{-14}	1.0×10^{-14}	1.0×10^{-14}	3.0×10^{-15}	1.0×10^{-14}
Donor σ_h [cm^2]	3.0×10^{-15}	3.0×10^{-15}	1.0×10^{-15}	1.0×10^{-15}	3.0×10^{-16}	1.0×10^{-15}
Acceptor σ_e [cm^2]	3.0×10^{-15}	3.0×10^{-15}	1.0×10^{-15}	1.0×10^{-15}	3.0×10^{-16}	1.0×10^{-15}
Acceptor σ_h [cm^2]	3.0×10^{-14}	3.0×10^{-14}	1.0×10^{-14}	1.0×10^{-14}	3.0×10^{-15}	1.0×10^{-14}

C.4. Optical constants of absorber materials used in GenPro4

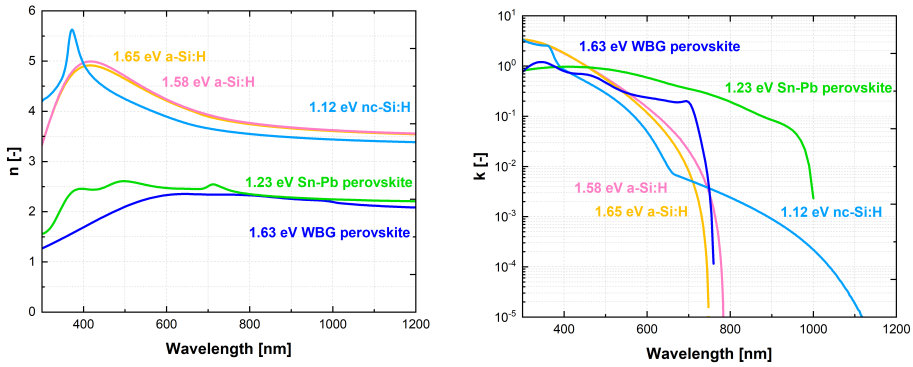

a) b)

Figure C.4: Refractive index (n) and extinction coefficient (k) of the absorber materials, including a-Si:H, nc-Si:H, and perovskite absorbers with different bandgaps.

REFERENCES

[1] F. T. Si, O. Isabella, and M. Zeman, *Too many junctions? A case study of multijunction thin-film silicon solar cells,* Advanced Sustainable Systems, 1, 1700077 (2017).

[2] S. Khosroabadi, R. Eghbali, and A. Shokouhmand, *Enhancing efficiency in a-Si:H/μc-Si micromorph tandem solar cells through advanced light-trapping techniques using ARC, TRJ, and DBR,* Journal of Materials Science: Materials in Engineering, 19, 28 (2024).

[3] G. Padmakumar, M. Criel, T. Kashyap, F. Saitta, P. Perez-Rodriguez, R. A. van Swaaij, and A. H. Smets, *Superimposed sacrificial texturing to enhance the optical performance in thin-film solar cells,* Progress in Photovoltaics: Research and Applications (2025).

[4] G. Padmakumar, A. Balaji, M. Criel, F. Saitta, G. Limodio, P. Perez-Rodriguez, R. A. van Swaaij, and A. H. Smets, *Engineering of hexagonal microtextures on glass,* ACS Applied Optical Materials, 3, 2360 (2025).

[5] S. Zhong, C. Qian, F. Yu, Z. Wu, Z. Huang, H. Yin, J. Zhang, H. Xu, R. Xu, and W. Shen, *Surface texturing for advanced light management in crystalline silicon solar cells: From submicron pyramid fabrication to outdoor validation,* Renewable Energy, 124546 (2025).

[6] K. Sreejith, A. K. Sharma, P. K. Basu, and A. Kottantharayil, *Etching methods for texturing industrial multi-crystalline silicon wafers: A comprehensive review,* Solar Energy Materials and Solar Cells, 238, 111531 (2022).

[7] J. Yoo, *Reactive ion etching (rie) technique for application in crystalline silicon solar cells,* Solar Energy, 84, 730 (2010).

[8] K. ElKhamisy, H. Abdelhamid, E.-S. M. El-Rabaie, and N. Abdel-Salam, *A comprehensive survey of silicon thin-film solar cell: challenges and novel trends,* Plasmonics, 19, 1 (2024).

[9] F. Meillaud, M. Boccard, G. Bugnon, M. Despeisse, S. Hänni, F.-J. Haug, J. Persoz, J.-W. Schüttauf, M. Stuckelberger, and C. Ballif, *Recent advances and remaining challenges in thin-film silicon photovoltaic technology,* Materials today, 18, 378 (2015).

[10] J. Ramanujam, D. M. Bishop, T. K. Todorov, O. Gunawan, J. Rath, R. Nekovei, E. Artegiani, and A. Romeo, *Flexible cigs, cdte and a-si:h based thin film solar cells: A review,* Progress in Materials Science, 110, 100619 (2020).

[11] Y. Li, X. Ru, M. Yang, Y. Zheng, S. Yin, C. Hong, F. Peng, M. Qu, C. Xue, J. Lu, *et al.*, *Flexible silicon solar cells with high power-to-weight ratios,* Nature, 626, 105 (2024).

[12] T. Tachibana, K. Shirasawa, and K. Tanahashi, *Development of lightweight and flexible crystalline silicon solar cell modules with pet film cover for high reliability in high temperature and humidity conditions,* Solar Energy Materials and Solar Cells, 262, 112541 (2023).

[13] M. Izu and T. Ellison, *Roll-to-roll manufacturing of amorphous silicon alloy solar cells with in situ cell performance diagnostics,* Solar Energy Materials and Solar Cells, 78, 613 (2003).

[14] S. K. Jha, A. S. Farooq, and A. Ghosh, *Thin-film solar cells for building-integrated photovoltaic (BIPV) systems,* Architecture, 5, 116 (2025).

[15] K. Jäger, J. Lenssen, P. Veltman, and E. Hamers, *Large-area production of highly efficient flexible light-weight thin-film silicon pv modules,* Proc. 28th European Photovoltaic Solar Energy Conf., Paris, France, 2164 (2013).

[16] A. Maalouf, T. Okoroafor, Z. Jehl, V. Babu, and S. Resalati, *A comprehensive review on life cycle assessment of commercial and emerging thin-film solar cell systems,* Renewable and Sustainable Energy Reviews, 186, 113652 (2023).

[17] R. Frischknecht, R. Itten, P. Sinha, M. de Wild-Scholten, J. Zhang, G. A. Heath, and C. Olson, *Life cycle inventories and life cycle assessments of photovoltaic systems*, Tech. Rep. (National Renewable Energy Laboratory (NREL), Golden, CO (United States), 2014).

[18] I. Ihoume, M. van Noord, and A. Augusto, *Toward a transparent life cycle assessment of photovoltaic systems: Addressing regulatory and methodological challenges,* Environmental impact assessment review, 118, 108290 (2026).

[19] F. C. Krebs, T. Tromholt, and M. Jørgensen, *Upscaling of polymer solar cell fabrication using full roll-to-roll processing,* Nanoscale, 2, 873 (2010).

[20] M. A. Green, E. D. Dunlop, M. Yoshita, N. Kopidakis, K. Bothe, G. Siefer, X. Hao, and J. Y. Jiang, *Solar cell efficiency tables (version 66),* Progress in Photovoltaics, 33 (2025).

[21] T. Matsui, A. Bidiville, K. Maejima, H. Sai, T. Koida, T. Suezaki, M. Matsumoto, K. Saito, I. Yoshida, and M. Kondo, *High-efficiency amorphous silicon solar cells: Impact of deposition rate on metastability,* Applied Physics Letters, 106 (2015).

[22] H. Sai, T. Matsui, H. Kumagai, and K. Matsubara, *Thin-film microcrystalline silicon solar cells: 11.9% efficiency and beyond,* Applied Physics Express, 11, 022301 (2018).

[23] G. Richhariya, A. Kumar, and Samsher, *Chapter 2 - solar cell technologies,* in *Photovoltaic Solar Energy Conversion*, edited by S. Gorjian and A. Shukla (Academic Press, 2020) pp. 27–50.

[24] H. Wen, B. Weng, B. Wang, W. Xiao, X. Liu, Y. Wang, M. Zhang, and H. Huang, *Advancements in transparent conductive oxides for photoelectrochemical applications,* Nanomaterials, 14, 591 (2024).

[25] D. Du, J. Liang, and W. Shen, *Optimized optical and electrical properties for silicon heterojunction solar cells with an indium tin oxide buffer layer,* Solar Energy Materials and Solar Cells, 286, 113595 (2025).

[26] T. Koida and J. Nomoto, *Sustainable transparent conducting oxides: Insights from amorphous SnO_x thin films via oxygen stoichiometry control,* Chemistry of Materials, 36, 6838 (2024).

[27] H. Cao and L. Liang, *Tin oxide-based thin-film transistors and their circuits,* in *Tin Oxide Materials* (Elsevier, 2020) pp. 441–476.

[28] Z. Xu, T. Xue, Q. Guo, J. Yao, G. Li, J. Du, E. Zhou, and Z. Tan, *Emerging flexible photovoltaic technology: From materials to devices,* Information & Functional Materials, 2, 1 (2025).

[29] G. Limodio, D. Bartesaghi, G. Padmakumar, D. Rajagopal, A. M. Shah, E. Hamers, and A. Smets, *Modulated surface texturing of temporary al foils substrates for high-efficiency thin-film, flexible solar cells,* 2021 IEEE 48th Photovoltaic Specialists Conference (PVSC), 1103 (2021).

[30] G. T. Chavan, Y. Kim, M. Q. Khokhar, S. Q. Hussain, E.-C. Cho, J. Yi, Z. Ahmad, P. Rosaiah, and C.-W. Jeon, *A brief review of transparent conducting oxides (TCO): the influence of different deposition techniques on the efficiency of solar cells,* Nanomaterials, 13, 1226 (2023).

[31] M. Musztyfaga-Staszuk, A. Czupryński, and R. Radev, *Review of the chosen methods of producing front contacts to transparent conductive oxides layers in photovoltaic structures,* Energies, 15, 9026 (2022).

[32] C. Habis, J. Zaraket, and M. Aillerie, *Transparent conductive oxides. Part II. Specific focus on ITO, ZnO-AZO, SnO2-FTO families for photovoltaics applications,* Defect and Diffusion Forum, 417, 257 (2022).

[33] A. Seyhan and E. Kartal, *Optical, electrical and structural properties of ITO/IZO and IZO/ITO multilayer transparent conductive oxide films deposited via radiofrequency magnetron sputtering,* Coatings, 13, 1719 (2023).

[34] X. Yu, T. J. Marks, and A. Facchetti, *Metal oxides for optoelectronic applications,* Nature materials, 15, 383 (2016).

[35] J. Patel, R. K. Sharme, M. A. Quijada, and M. M. Rana, *A review of transparent conducting films (TCFs): Prospective ITO and AZO deposition methods and applications,* Nanomaterials, 14, 2013 (2024).

[36] K. Chopra, S. Major, and D. Pandya, *Transparent conductors—a status review,* Thin solid films, 102, 1 (1983).
[37] R. Bel Hadj Tahar, T. Ban, Y. Ohya, and Y. Takahashi, *Tin doped indium oxide thin films: Electrical properties,* Journal of Applied Physics, 83, 2631 (1998).
[38] K. T. Selvi and S. Sagadevan, *Recent developments in optoelectronic and photonic applications of metal oxides,* Metal oxides for optoelectronics and optics-based medical applications, 33 (2022).
[39] N. Preissler, O. Bierwagen, A. T. Ramu, and J. S. Speck, *Electrical transport, electrothermal transport, and effective electron mass in single-crystalline In_2O_3 films,* Physical Review B—Condensed Matter and Materials Physics, 88, 085305 (2013).
[40] H. Heffner, M. Soldera, and A. F. Lasagni, *Optoelectronic performance of indium tin oxide thin films structured by sub-picosecond direct laser interference patterning,* Scientific Reports, 13, 9798 (2023).
[41] A. Korneluk, J. Szymczak, and T. Stefaniuk, *Annealing-free fabrication of high-quality indium tin oxide films for free-carrier-based hybrid metal–semiconductor nanophotonics,* Scientific Reports, 13, 18520 (2023).
[42] S. M. Rozati and S. A. M. Ziabari, *A review of various single layer, bilayer, and multilayer TCO materials and their applications,* Materials chemistry and physics, 292, 126789 (2022).
[43] Y.-S. Lee, L.-Y. Chuang, C.-J. Tang, Z.-Z. Yan, B.-S. Le, and C.-C. Jaing, *Investigation into the characteristics of double-layer transparent conductive oxide ITO/TNO anti-reflection coating for silicon solar cells,* Crystals, 13, 80 (2023).
[44] X. Yan, W. Li, A. G. Aberle, and S. Venkataraj, *Surface texturing studies of bilayer transparent conductive oxide (TCO) structures as front electrode for thin-film silicon solar cells,* Journal of Materials Science: Materials in Electronics, 26, 7049 (2015).
[45] D. K. Ghosh, S. Bose, G. Das, S. Mukhopadhyay, and A. Sengupta, *Realization of performance enhancement of thin film silicon solar cells by applying ITO/AZO bilayer TCO films as front electrode,* Journal of Materials Science: Materials in Electronics, 34, 2189 (2023).
[46] M. N. Rezaie, N. Manavizadeh, E. M. N. Abadi, E. Nadimi, and F. A. Boroumand, *Comparison study of transparent RF-sputtered ITO/AZO and ITO/ZnO bilayers for near UV-OLED applications,* Applied Surface Science, 392, 549 (2017).
[47] H. Tan, E. Moulin, F. T. Si, J.-W. Schüttauf, M. Stuckelberger, O. Isabella, F.-J. Haug, C. Ballif, M. Zeman, and A. H. Smets, *Highly transparent modulated surface textured front electrodes for high-efficiency multijunction thin-film silicon solar cells,* Progress in Photovoltaics: research and applications, 23, 949 (2015).
[48] Z. Du, X. Liu, Y. Zhang, J. Shuai, and H. Li, *Robust AZO/i-ZnO bilayer front contact for high-performance thin film solar cells,* RSC Advances, 6, 108067 (2016).
[49] H. Liu, V. Avrutin, N. Izyumskaya, Ü. Özgür, and H. Morkoç, *Transparent conducting oxides for electrode applications in light emitting and absorbing devices,* Superlattices and Microstructures, 48, 458 (2010).
[50] C. Battaglia, L. Erni, M. Boccard, L. Barraud, J. Escarré, K. Söderström, G. Bugnon, A. Billet, L. Ding, M. Despeisse, *et al., Micromorph thin-film silicon solar cells with transparent high-mobility hydrogenated indium oxide front electrodes,* Journal of Applied Physics, 109 (2011).
[51] L. Barraud, Z. Holman, N. Badel, P. Reiss, A. Descoeudres, C. Battaglia, S. De Wolf, and C. Ballif, *Hydrogen-doped indium oxide/indium tin oxide bilayers for high-efficiency silicon heterojunction solar cells,* Solar Energy Materials and Solar Cells, 115, 151 (2013).
[52] T. Minami, *New n-type transparent conducting oxides,* MRS bulletin, 25, 38 (2000).
[53] K. Saw, N. Aznan, F. Yam, S. Ng, and S. Pung, *New insights on the Burstein-Moss shift and band gap narrowing in indium-doped zinc oxide thin films,* PloS one, 10, e0141180 (2015).
[54] Z. Wang, C. Chen, K. Wu, H. Chong, and H. Ye, *Transparent conductive oxides and their applications in near infrared plasmonics,* physica status solidi (a), 216, 1700794 (2019).

[55] H. Knoops, B. W. van de Loo, S. Smit, M. V. Ponomarev, J.-W. Weber, K. Sharma, W. M. Kessels, and M. Creatore, *Optical modeling of plasma-deposited ZnO films: Electron scattering at different length scales,* Journal of Vacuum Science & Technology A, 33 (2015).

[56] J. R. D'Rozario, S. J. Polly, G. T. Nelson, D. Wilt, and S. M. Hubbard, *Modeling free-carrier absorption in ultrathin III-V solar cells with light management,* Optics Express, 30, 7096 (2022).

[57] H. Tan, E. Psomadaki, O. Isabella, M. Fischer, P. Babal, R. Vasudevan, M. Zeman, and A. H. Smets, *Micro-textures for efficient light trapping and improved electrical performance in thin-film nanocrystalline silicon solar cells,* Applied Physics Letters, 103 (2013).

[58] M. Boccard, N. Rodkey, and Z. C. Holman, *High-mobility hydrogenated indium oxide without introducing water during sputtering,* Energy Procedia, 92, 297 (2016).

[59] T. Kataoka, Y. Magari, H. Makino, and M. Furuta, *Nondegenerate polycrystalline hydrogen-doped indium oxide (InO_x:H) thin films formed by low-temperature solid-phase crystallization for thin film transistors,* Materials, 15, 187 (2021).

[60] L. Xu, J. Yang, K. Li, L. Yang, and J. Zhu, *Effect of post-deposition annealing on the structural evolution and optoelectronic properties of In_2O_3:H thin films,* Nanomaterials, 12, 3533 (2022).

[61] Y. Magari, T. Kataoka, W. Yeh, and M. Furuta, *High-mobility hydrogenated polycrystalline In_2O_3 (In_2O_3:H) thin-film transistors,* Nature communications, 13, 1078 (2022).

[62] D. Erfurt, M. D. Heinemann, S. Körner, B. Szyszka, R. Klenk, and R. Schlatmann, *Improved electrical properties of pulsed DC magnetron sputtered hydrogen doped indium oxide after annealing in air,* Materials Science in Semiconductor Processing, 89, 170 (2019).

[63] C. Han, G. Yang, A. Montes, P. Procel, L. Mazzarella, Y. Zhao, S. Eijt, H. Schut, X. Zhang, M. Zeman, *et al.*, *Realizing the potential of RF-sputtered hydrogenated fluorine-doped indium oxide as an electrode material for ultrathin SiO_x/poly-Si passivating contacts,* ACS Applied Energy Materials, 3, 8606 (2020).

[64] A. S. Hassanien and A. A. Akl, *Effect of Se addition on optical and electrical properties of chalcogenide CdSSe thin films,* Superlattices and Microstructures, 89, 153 (2016).

[65] S. Arooj, T. Xu, X. Hou, Y. Wang, J. Tong, R. Chu, and B. Liu, *Green emission of indium oxide via hydrogen treatment,* RSC advances, 8, 11828 (2018).

[66] G. A. Kumar, M. R. Reddy, and K. N. Reddy, *Structural and Optical properties of ZnO thin films grown on various substrates by RF magnetron sputtering,* in *IOP Conference Series: Materials Science and Engineering*, Vol. 73 (2015) p. 012133.

[67] A. Ismail and M. Abdullah, *The structural and optical properties of ZnO thin films prepared at different RF sputtering power,* Journal of King Saud University-Science, 25, 209 (2013).

[68] R. Krishna, V. Baranwal, Y. Katharria, D. Kabiraj, A. Tripathi, F. Singh, S. Khan, A. Pandey, and D. Kanjilal, *Nanostructure formation on zinc oxide film by ion bombardment,* Nuclear Instruments and Methods in Physics Research Section B: Beam Interactions with Materials and Atoms, 244, 78 (2006).

[69] H. Yu, J. Wang, Y. Yan, X. Wang, B. Gao, H. Liu, and Y. Du, *Zno thin films produced by the RF magnetron sputtering,* in *Proceedings of 2011 International Conference on Electronic & Mechanical Engineering and Information Technology*, Vol. 5 (IEEE, 2011) pp. 2486–2489.

[70] M. A. Cruz, O. Ceballos-Sanchez, E. Luévano-Hipólito, and L. Torres-Martínez, *Zno thin films deposited by rf magnetron sputtering: Effects of the annealing and atmosphere conditions on the photocatalytic hydrogen production,* International Journal of Hydrogen Energy, 43, 10301 (2018).

[71] Y. Ye, *Zinc-oxynitride TFTs: Toward a new high-mobility low-cost thin-film semiconductor,* Information Display, 29, 20 (2013).

[72] T. Pisarkiewicz, K. Zakrzewska, and E. Leja, *Scattering of charge carriers in transparent and conducting thin oxide films with a non-parabolic conduction band,* Thin Solid Films, 174, 217 (1989).

[73] D. Zhang and H. Ma, *Scattering mechanisms of charge carriers in transparent conducting oxide films,* Applied physics A, 62, 487 (1996).
[74] R. A. Afre, N. Sharma, M. Sharon, and M. Sharon, *Transparent conducting oxide films for various applications: A review,* Reviews on advanced materials science, 53, 79 (2018).
[75] G. K. Deyu, J. Hunka, H. Roussel, J. Brötz, D. Bellet, and A. Klein, *Electrical properties of low-temperature processed Sn-doped In_2O_3 thin films: The role of microstructure and oxygen content and the potential of defect modulation doping,* Materials, 12, 2232 (2019).
[76] K. Ellmer, *Resistivity of polycrystalline zinc oxide films: current status and physical limit,* Journal of Physics D: Applied Physics, 34, 3097 (2001).
[77] M. Chen, Z. Pei, X. Wang, Y. Yu, X. Liu, C. Sun, and L. Wen, *Intrinsic limit of electrical properties of transparent conductive oxide films,* Journal of Physics D: Applied Physics, 33, 2538 (2000).
[78] T. Minami, T. Miyata, and H. Tokunaga, *Electron scattering from disordered grain boundaries in degenerate polycrystalline Al-doped ZnO thin films,* physica status solidi (a), 216, 1700783 (2019).
[79] K. Ellmer and R. Mientus, *Carrier transport in polycrystalline ITO and ZnO: Al II: The influence of grain barriers and boundaries,* Thin Solid Films, 516, 5829 (2008).
[80] B. Mahapatra and S. Sarkar, *Understanding of mobility limiting factors in solution grown Al doped ZnO thin film and its low temperature remedy,* Heliyon, 8 (2022).
[81] J. Y. Seto, *The electrical properties of polycrystalline silicon films,* Journal of Applied Physics, 46, 5247 (1975).
[82] G. Baccarani, B. Ricco, and G. Spadini, *Transport properties of polycrystalline silicon films,* Journal of applied physics, 49, 5565 (1978).
[83] E. Płaczek-Popko, K. Paradowska, M. Pietrzyk, and A. Kozanecki, *Carrier transport mechanisms in the ZnO based heterojunctions grown by MBE,* Opto-Electronics Review, 25, 181 (2017).
[84] R. M. Hewlett and M. A. McLachlan, *Surface structure modification of ZnO and the impact on electronic properties,* Advanced materials, 28, 3893 (2016).
[85] S. Kang, R. Nandi, J.-K. Sim, J.-Y. Jo, U. Chatterjee, and C.-R. Lee, *Characteristics of an oxide/metal/oxide transparent conducting electrode fabricated with an intermediate Cu–Mo metal composite layer for application in efficient CIGS solar cell,* RSC advances, 7, 48113 (2017).
[86] R. Ramarajan, D. Paul Joseph, K. Thangaraju, and M. Kovendhan, *Indium-free alternative transparent conducting electrodes: An overview and recent developments,* Metal and Metal Oxides for Energy and Electronics, 149 (2020).
[87] S. Suh, Z. Zhang, W.-K. Chu, and D. M. Hoffman, *Atmospheric-pressure chemical vapor deposition of fluorine-doped tin oxide thin films,* Thin Solid Films, 345, 240 (1999).
[88] G. K. Dalapati, H. Sharma, A. Guchhait, N. Chakrabarty, P. Bamola, Q. Liu, G. Saianand, A. M. S. Krishna, S. Mukhopadhyay, A. Dey, *et al.*, *Tin oxide for optoelectronic, photovoltaic and energy storage devices: a review,* Journal of materials chemistry A, 9, 16621 (2021).
[89] C. Yu, Q. Zou, Q. Wang, Y. Zhao, X. Ran, G. Dong, C.-W. Peng, V. Allen, X. Cao, J. Zhou, *et al.*, *Silicon solar cell with undoped tin oxide transparent electrode,* Nature Energy, 8, 1119 (2023).
[90] A. Mussabekova, B. Ilyassov, A. imukhanov, A. Tussupbekova, A. Zeinidenov, D. Valiev, V. Paygin, V. Kudryashov, and A. Zhakanova, *Promising sno_x electron transport layer for polymer solar cells,* Physica B: Condensed Matter, 666, 415113 (2023).
[91] A. Muthukumar, G. Giusti, M. Jouvert, V. Consonni, and D. Bellet, *Fluorine-doped SnO_2 thin films deposited on polymer substrate for flexible transparent electrodes,* Thin Solid Films, 545, 302 (2013).

[92] H. Tao, Z. Ma, G. Yang, H. Wang, H. Long, H. Zhao, P. Qin, and G. Fang, *Room-temperature processed tin oxide thin film as effective hole blocking layer for planar perovskite solar cells,* Applied Surface Science, 434, 1336 (2018).

[93] L. Qiu, Z. Liu, L. K. Ono, Y. Jiang, D.-Y. Son, Z. Hawash, S. He, and Y. Qi, *Scalable fabrication of stable high efficiency perovskite solar cells and modules utilizing room temperature sputtered SnO_2 electron transport layer,* Advanced Functional Materials, 29, 1806779 (2019).

[94] A. F. Palmstrom, G. E. Eperon, T. Leijtens, R. Prasanna, S. N. Habisreutinger, W. Nemeth, E. A. Gaulding, S. P. Dunfield, M. Reese, S. Nanayakkara, *et al.*, *Enabling flexible all-perovskite tandem solar cells,* Joule, 3, 2193 (2019).

[95] T. Koida, T. Matsui, and H. Sai, *Amorphous SnO_2 as earth-abundant stable transparent conductive oxide and its application to Si heterojunction solar cells,* Solar Rrl, 7, 2300381 (2023).

[96] H. Sai, T. Koida, and T. Matsui, *Improved electrical contact properties in Indium-free silicon heterojunction solar cells with amorphous SnO_2 TCO layers,* Solar Energy Materials and Solar Cells, 278, 113191 (2024).

[97] F. Sahli, J. Werner, B. A. Kamino, M. Bräuninger, R. Monnard, B. Paviet-Salomon, L. Barraud, L. Ding, J. J. Diaz Leon, D. Sacchetto, *et al.*, *Fully textured monolithic perovskite/silicon tandem solar cells with 25.2% power conversion efficiency,* Nature materials, 17, 820 (2018).

[98] M. Zarrinkhameh, A. Zendehnam, S. Hosseini, N. Robatmili, and M. Arabzadegan, *Effect of oxidation and annealing temperature on optical and structural properties of SnO_2,* Bulletin of Materials Science, 37, 533 (2014).

[99] S. Baco, A. Chik, and F. M. Yassin, *Study on optical properties of tin oxide thin film at different annealing temperature,* Journal of Science and Technology, 4 (2012).

[100] Q.-Z. Chen, Z.-X. Zhang, W.-Q. Fu, J.-R. Duan, Y.-X. Yang, C.-N. Chen, and S.-Y. Lien, *Low resistivity and high carrier concentration in SnO_2 thin films: The impact of nitrogen–hydrogen annealing treatments,* Nanomaterials, 15, 986 (2025).

[101] H. M. Yates, P. Evans, D. W. Sheel, S. Nicolay, L. Ding, and C. Ballif, *The development of high performance SnO_2:F as TCOs for thin film silicon solar cells,* Surface and Coatings Technology, 213, 167 (2012).

[102] Y. Wang, Z. Ba, S. Dong, W. Xie, Z. Wu, and C. Ran, *Advancing SnO_2 electron transport layer for efficient perovskite photovoltaics: a critical review,* ACS Applied Materials & Interfaces, 17, 27651 (2025).

[103] A. Uddin and H. Yi, *Progress and challenges of SnO_2 electron transport layer for perovskite solar cells: A critical review,* Solar RRL, 6, 2100983 (2022).

[104] C. Hernández-Gutiérrez, O. Vigil Galán, S. Melo, E. Rodríguez, Y. Kudriavtsev, and D. Cardona, *The role of SnO_2 high resistivity transparent layer deposited onto commercial conducting glass as front contact in superstrate configuration thin films solar cells technology: influence of the deposition technique,* Revista mexicana de física, 65, 554 (2019).

[105] C. Guillén, *Determination of the band gap energy of SnO_2 and ZnO thin films with different crystalline qualities and doping levels,* Electronic Materials, 6, 3 (2025).

[106] G. G. Riungu, S. W. Mugo, J. M. Ngaruiya, G. M. John, and N. Mugambi, *Optical band energy, urbach energy and associated band tails of nano crystalline TiO_2 films at different annealing rates,* American Journal of Nanosciences, 7, 28 (2021).

[107] N. A. Bakr, S. A. Salman, and M. N. Ali, *Effect of fluorine doping on structural and optical properties of SnO_2 thin films prepared by chemical spray pyrolysis method,* Advances in Materials, 5, 23 (2016).

[108] S. J. Ikhmayies and R. N. Ahmad-Bitar, *An investigation of the bandgap and urbach tail of spray-deposited SnO_2:F thin films,* Physica Scripta, 84, 055801 (2011).

[109] R. Ponte, E. Rauwel, and P. Rauwel, *Tailoring SnO_2 defect states and structure: reviewing bottom-up approaches to control size, morphology, electronic and electrochemical properties for application in batteries,* Materials, 16, 4339 (2023).
[110] M. Batal, G. Nashed, and F. H. Jneed, *Conductivity and thermoelectric properties of nanostructure tin oxide thin films,* Journal of the Association of Arab Universities for Basic and Applied Sciences, 15, 15 (2014).
[111] S. Jain, P. Griffin, and J. Plummer, *Hall measurements of bilayer structures,* Journal of applied physics, 93, 1060 (2003).
[112] Q. Wali, M. Aamir, M. E. Khan, R. Jose, W. Fan, and S. Yang, *Tin oxide as an electron transport layer in perovskite solar cells: Advances and challenges,* Solar Energy, 270, 112382 (2024).
[113] L. Xiong, Y. Guo, J. Wen, H. Liu, G. Yang, P. Qin, and G. Fang, *Review on the application of SnO_2 in perovskite solar cells,* Advanced Functional Materials, 28, 1802757 (2018).
[114] H. Peelaers, E. Kioupakis, and C. G. Van de Walle, *Fundamental limits on optical transparency of transparent conducting oxides: Free-carrier absorption in SnO_2,* Applied Physics Letters, 100 (2012).
[115] I. Miccoli, F. Edler, H. Pfnür, and C. Tegenkamp, *The 100th anniversary of the four-point probe technique: the role of probe geometries in isotropic and anisotropic systems,* Journal of Physics: Condensed Matter, 27, 223201 (2015).
[116] J. Orton and M. Powell, *The hall effect in polycrystalline and powdered semiconductors,* Reports on Progress in Physics, 43, 1263 (1980).
[117] W. Zheng, Y. Zhang, and J. Tian, *Effect of fluorine doping concentration on semiconductive property of tin dioxide,* Chalcogenide Letters, 14, 275 (2017).
[118] Z. Y. Banyamin, P. J. Kelly, G. West, and J. Boardman, *Electrical and optical properties of fluorine doped tin oxide thin films prepared by magnetron sputtering,* Coatings, 4, 732 (2014).
[119] M. Kam, Q. Zhang, D. Zhang, and Z. Fan, *Room-temperature sputtered SnO_2 as robust electron transport layer for air-stable and efficient perovskite solar cells on rigid and flexible substrates,* Scientific reports, 9, 6963 (2019).
[120] M. Morán-Pedroso, J. Sánchez-Marcos, A. de Andrés, and C. Prieto, *Fluorinated tin oxide (FTO) deposited at room temperature: Influence of hydrogen and oxygen in the sputtering gas on the optical and electrical properties,* Applied Surface Science, 459, 349 (2018).
[121] I. Kim, J. Ko, D. Kim, K. Lee, T. Lee, J.-H. Jeong, B. Cheong, Y.-J. Baik, and W. Kim, *Scattering mechanism of transparent conducting tin oxide films prepared by magnetron sputtering,* Thin Solid Films, 515, 2475 (2006).
[122] F.-J. Haug and C. Ballif, *Light management in thin film silicon solar cells,* Energy & Environmental Science, 8, 824 (2015).
[123] B. Zhu, F. Liu, K. Li, K. Lv, J. Wu, Z. Gan, J. Liu, D. Zeng, and C. Xie, *Sputtering deposition of transparent conductive F-doped SnO_2 (FTO) thin films in hydrogen-containing atmosphere,* Ceramics International, 43, 10288 (2017).
[124] M. Moran-Pedroso, R. Gago, J. Julin, E. Salas-Colera, I. Jimenez, A. De Andrés, and C. Prieto, *Correlated effects of fluorine and hydrogen in fluorinated tin oxide (FTO) transparent electrodes deposited by sputtering at room temperature,* Applied Surface Science, 537, 147906 (2021).
[125] A. Rahal, S. Benramache, and B. Benhaoua, *The effect of the film thickness and doping content of SnO_2:F thin films prepared by the ultrasonic spray method,* Journal of Semiconductors, 34, 093003 (2013).
[126] A. Schleife, J. Varley, F. Fuchs, C. Rödl, F. Bechstedt, P. Rinke, A. Janotti, and C. Van de Walle, *Tin dioxide from first principles: Quasiparticle electronic states and optical properties,* Physical Review B—Condensed Matter and Materials Physics, 83, 035116 (2011).
[127] Z. Ni, Z. Yu, and J. Huang, *Unveiling the ambipolar carrier transport property of SnO_{2-x} for multiple-functional interlayers in perovskite solar cells,* Applied Physics Letters, 119 (2021).

[128] F. Herklotz, E. Lavrov, V. Melnikov, Z. Galazka, and V. Agekyan, *Comprehensive study of the interstitial hydrogen donor in SnO_2*, Physical Review B, 108, 205204 (2023).

[129] H. Luo, L. Y. Liang, H. T. Cao, Z. M. Liu, and F. Zhuge, *Structural, chemical, optical, and electrical evolution of SnO_x films deposited by reactive rf magnetron sputtering,* ACS applied materials & interfaces, 4, 5673 (2012).

[130] K. Henkel, J. Haeberle, K. Müller, C. Janowitz, and D. Schmeißer, *Preparation, properties and electronic structure of SnO_2*, in *Single Crystals of Electronic Materials* (Elsevier, 2019) pp. 547–572.

[131] S. Venkataraman, *Investigation of opto-electrical and structural properties of atmospheric pressure chemical vapor deposition of fluorine-doped tin oxide,* Master's thesis, Delft University of Technology, Delft, The Netherlands (2023).

[132] M. A. Gafur, M. S. Bashar, and M. M. Alam, *Comparative study of structural, optical and electrical properties of SnO_2 thin film growth via CBD, drop-cast and dip-coating methods,* Materials Sciences and Applications, 12, 578 (2021).

[133] E. Elangovan, M. Singh, and K. Ramamurthi, *Studies on structural and electrical properties of spray deposited SnO_2:F thin films as a function of film thickness,* Materials Science and Engineering: B, 113, 143 (2004).

[134] M. Batzill and U. Diebold, *The surface and materials science of tin oxide,* Progress in surface science, 79, 47 (2005).

[135] F. Ali, N. D. Pham, H. J. Bradford, N. Khoshsirat, K. Ostrikov, J. M. Bell, H. Wang, and T. Tesfamichael, *Tuning the amount of oxygen vacancies in sputter-deposited SnO_x films for enhancing the performance of perovskite solar cells,* ChemSusChem, 11, 3096 (2018).

[136] J. Szuber, G. Czempik, R. Larciprete, D. Koziej, and B. Adamowicz, *XPS study of the L-CVD deposited SnO_2 thin films exposed to oxygen and hydrogen,* Thin Solid Films, 391, 198 (2001).

[137] P.-C. Hsu, C.-J. Hsu, C.-H. Chang, S.-P. Tsai, W.-C. Chen, H.-H. Hsieh, and C.-C. Wu, *Sputtering deposition of p-type SnO films with SnO_2 target in hydrogen-containing atmosphere,* ACS applied materials & interfaces, 6, 13724 (2014).

[138] P.-C. Hsu, S.-P. Tsai, C.-H. Chang, C.-J. Hsu, W.-C. Chen, H.-H. Hsieh, and C.-C. Wu, *Preparation of p-type SnO thin films and transistors by sputtering with robust Sn/SnO_2 mixed target in hydrogen-containing atmosphere,* Thin Solid Films, 585, 50 (2015).

[139] T. Minami, *Transparent conducting oxide semiconductors for transparent electrodes,* Semiconductor science and technology, 20, S35 (2005).

[140] D. Flak, A. Braun, B. S. Mun, J. B. Park, M. Parlinska-Wojtan, T. Graule, and M. Rekas, *Spectroscopic assessment of the role of hydrogen in surface defects, in the electronic structure and transport properties of TiO_2, ZnO and SnO_2 nanoparticles,* Physical Chemistry Chemical Physics, 15, 1417 (2013).

[141] P. Borges, L. Scolfaro, and L. V. C. Assali, *Complex centers of hydrogen in tin dioxide,* Theoretical Chemistry Accounts, 134, 131 (2015).

[142] S. Abdullahi, F. Sani, S. Buda, A. Idris, M. Aliyu, and B. Abdullahi, *Structural and electrical properties of fluorine doped tin oxide (FTO) thin film deposited by spin coating technique,* International Journal of Science for Global Sustainability (IJSGS), 10 (2024).

[143] M. A. Martinez-Puente, J. Tirado, F. Jaramillo, R. Garza-Hernandez, P. Horley, L. G. Silva Vidaurri, F. S. Aguirre-Tostado, and E. Martinez-Guerra, *Unintentional hydrogen incorporation into the SnO_2 electron transport layer by ALD and its effect on the electronic band structure,* ACS Applied Energy Materials, 4, 10896 (2021).

[144] X. Wang, X. Wang, Q. Di, H. Zhao, B. Liang, and J. Yang, *Mutual effects of fluorine dopant and oxygen vacancies on structural and luminescence characteristics of F doped SnO_2 nanoparticles,* Materials, 10, 1398 (2017).

[145] A. Adjimi, M. L. Zeggar, N. Attaf, and M. S. Aida, *Fluorine-doped tin oxide thin films deposition by sol-gel technique,* Journal of Crystallization Process and Technology, 8, 89 (2018).

[146] B. S. Tosun, R. K. Feist, A. Gunawan, K. A. Mkhoyan, S. A. Campbell, and E. S. Aydil, *Sputter deposition of semicrystalline tin dioxide films,* Thin Solid Films, 520, 2554 (2012).
[147] Y. Yang, B. Maeng, D. G. Jung, J. Lee, Y. Kim, J. Kwon, H. K. An, and D. Jung, *Annealing effects on SnO_2 thin film for H_2 gas sensing,* Nanomaterials, 12, 3227 (2022).
[148] N. H. Kim, H. K. Kim, K. M. Lee, H. C. Sohn, J. S. Roh, and D. J. Choi, *Effects of Ag doping on the crystallization properties of Sb-rich GeSb thin films,* Thin Solid Films, 519, 5323 (2011).
[149] O. Elsherif, G. Muftah, O. Abubaker, and I. Dharmadasa, *Structural, optical and electrical properties of SnO_2:F thin films deposited by spray pyrolysis for application in thin film solar cells,* Journal of Materials Science: Materials in Electronics, 27, 12280 (2016).
[150] A. Shah, H. Schade, M. Vanecek, J. Meier, E. Vallat-Sauvain, N. Wyrsch, U. Kroll, C. Droz, and J. Bailat, *Thin-film silicon solar cell technology,* Progress in photovoltaics: Research and applications, 12, 113 (2004).
[151] J. Yang, B. Yan, and S. Guha, *Amorphous and nanocrystalline silicon-based multi-junction solar cells,* Thin Solid Films, 487, 162 (2005).
[152] S. Kim, J.-W. Chung, H. Lee, J. Park, Y. Heo, and H.-M. Lee, *Remarkable progress in thin-film silicon solar cells using high-efficiency triple-junction technology,* Solar Energy Materials and Solar Cells, 119, 26 (2013).
[153] S. Guha, J. Yang, and B. Yan, *High efficiency multi-junction thin film silicon cells incorporating nanocrystalline silicon,* Solar Energy Materials and Solar Cells, 119, 1 (2013).
[154] T. de Vrijer, M. Wiering, D. van Nijen, G. Padmakumar, S. Sambamurthy, G. Limodio, and A. H. Smets, *The optical performance of random and periodic textured mono crystalline silicon surfaces for photovoltaic applications,* EPJ Photovoltaics, 13, 23 (2022).
[155] S. Schicho, D. Hrunski, R. Van Aubel, and A. Gordijn, *High potential of thin (< 1 μm) a-Si:H/μc-Si:H tandem solar cells,* Progress in Photovoltaics: Research and Applications, 18, 83 (2010).
[156] M. Zeman, O. Isabella, S. Solntsev, and K. Jäger, *Modelling of thin-film silicon solar cells,* Solar Energy Materials and Solar Cells, 119, 94 (2013).
[157] H. Sai, T. Matsui, K. Matsubara, M. Kondo, and I. Yoshida, *11.0%-efficient thin-film microcrystalline silicon solar cells with honeycomb textured substrates,* IEEE Journal of Photovoltaics, 4, 1349 (2014).
[158] H. Sai, T. Matsui, T. Koida, K. Matsubara, M. Kondo, S. Sugiyama, H. Katayama, Y. Takeuchi, and I. Yoshida, *Triple-junction thin-film silicon solar cell fabricated on periodically textured substrate with a stabilized efficiency of 13.6%,* Applied Physics Letters, 106 (2015).
[159] L. Salgado-Conrado, C. Álvarez-Macías, and B. Reyes-Durán, *A review of simulation tools for thin-film solar cells,* Materials, 17, 5213 (2024).
[160] K. Jäger, D. N. Linssen, O. Isabella, and M. Zeman, *Optimized nano-textured interfaces for thin-film silicon solar cells: identifying the limit of randomly textured interfaces,* in *Photonics for Solar Energy Systems V*, Vol. 9140 (SPIE, 2014) pp. 112–120.
[161] M. Zeman and J. Krc, *Optical and electrical modeling of thin-film silicon solar cells,* Journal of materials research, 23, 889 (2008).
[162] K. Ding, T. Kirchartz, B. E. Pieters, C. Ulbrich, A. M. Ermes, S. Schicho, A. Lambertz, R. Carius, and U. Rau, *Characterization and simulation of a-Si:H/μc-Si:H tandem solar cells,* Solar Energy Materials and Solar Cells, 95, 3318 (2011).
[163] M. Topič, M. Sever, B. Lipovšek, A. Čampa, and J. Krč, *Approaches and challenges in optical modelling and simulation of thin-film solar cells,* Solar Energy Materials and Solar Cells, 135, 57 (2015).
[164] K. W. Robertson, R. R. LaPierre, and J. J. Krich, *Efficient wave optics modeling of nanowire solar cells using rigorous coupled-wave analysis,* Optics express, 27, A133 (2019).
[165] D. Thorp and S. R. Wenham, *Ray-tracing of arbitrary surface textures for light-trapping in thin silicon solar cells,* Solar Energy Materials and Solar Cells, 48, 295 (1997).

[166] S. Y. Myong, S. W. Kwon, *et al., Superstrate type flexible thin-film Si solar cells using flexible glass substrates,* Thin Solid Films, 550, 705 (2014).

[167] M. Pisarenco and I. Setija, *On the complexity of aperiodic Fourier modal methods for finite periodic structures,* Journal of Computational Physics, 261, 130 (2014).

[168] K. Jäger, D. Linssen, O. Isabella, and M. Zeman, *Designing nanotextures using perlin noise, the scalar scattering theory and the finite elements method,* in *Optical Nanostructures and Advanced Materials for Photovoltaics* (Optica Publishing Group, 2014) pp. PW4C–2.

[169] J. Springer, A. Poruba, A. Feifar, M. Vanecek, N. Wyrsch, L. Feitknecht, J. Meier, and A. Shah, *Nanotextured thin film silicon solar cells: optical model,* in *16th EC Photovoltaic Solar Energy Conference* (2000) pp. 434–437.

[170] R. Santbergen, T. Meguro, T. Suezaki, G. Koizumi, K. Yamamoto, and M. Zeman, *GenPro4 optical model for solar cell simulation and its application to multijunction solar cells,* IEEE journal of photovoltaics, 7, 919 (2017).

[171] R. Santbergen, A. H. Smets, and M. Zeman, *Optical model for multilayer structures with coherent, partly coherent and incoherent layers,* Optics express, 21, A262 (2013).

[172] K. Jäger, D. N. Linssen, O. Isabella, and M. Zeman, *Ambiguities in optical simulations of nanotextured thin-film solar cells using the finite-element method,* Optics Express, 23, A1060 (2015).

[173] K. Jäger, M. Fischer, R. Van Swaaij, and M. Zeman, *A scattering model for nano-textured interfaces and its application in opto-electrical simulations of thin-film silicon solar cells,* Journal of Applied Physics, 111 (2012).

[174] J. Zhang, B.-M. Hodge, A. Florita, S. Lu, H. F. Hamann, and V. Banunarayanan, *Metrics for evaluating the accuracy of solar power forecasting,* Tech. Rep. (National Renewable Energy Laboratory (NREL), Golden, CO., 2013).

[175] Y. Liu, J. Rath, and R. Schropp, *Development of micromorph tandem solar cells on foil deposited by VHF-PECVD,* Surface and Coatings Technology, 201, 9330 (2007).

[176] T. Matsui, H. Sai, A. Bidiville, H.-J. Hsu, and K. Matsubara, *Progress and limitations of thin-film silicon solar cells,* Solar Energy, 170, 486 (2018).

[177] M. Lluscà, J. D. Santos, S. Fernández, J. P. González, J. J. Gandía, J. Cárabe, A. Antony, J. M. Asensi, J. Bertomeu, *et al., Textured glass substrates for thin film silicon solar cells,* in *28th Eur. Photovolt. Sol. Energy Conf. Exhib* (2012) pp. 2170–2174.

[178] D. Y. Kim, E. Guijt, F. T. Si, R. Santbergen, J. Holovskỳ, O. Isabella, R. A. van Swaaij, and M. Zeman, *Fabrication of double-and triple-junction solar cells with hydrogenated amorphous silicon oxide (a-SiO_x:H) top cell,* Solar Energy Materials and Solar Cells, 141, 148 (2015).

[179] D. Y. Kim, E. Guijt, R. A. van Swaaij, and M. Zeman, *Development of a-SiO_x:H solar cells with very high V_{oc}×FF product,* Progress in Photovoltaics: research and applications, 23, 671 (2015).

[180] G. Bugnon, G. Parascandolo, S. Hänni, M. Stuckelberger, M. Charrière, M. Despeisse, F. Meillaud, and C. Ballif, *Silicon oxide buffer layer at the p–i interface in amorphous and microcrystalline silicon solar cells,* Solar Energy Materials and Solar Cells, 120, 143 (2014).

[181] H. M. Yates, J. M. Gaskell, M. E. Thomson, D. W. Sheel, B. Delaup, and M. Morales-Masis, *APCVD of dual layer transparent conductive oxides for photovoltaic applications,* Thin Solid Films, 590, 260 (2015).

[182] J. Sap, O. Isabella, K. Jäger, and M. Zeman, *Extraction of optical properties of flat and surface-textured transparent conductive oxide films in a broad wavelength range,* Thin Solid Films, 520, 1096 (2011).

[183] G. Chen, C. Han, L. Yan, Y. Li, Y. Zhao, and X. Zhang, *Simulation and application of external quantum efficiency of solar cells based on spectroscopy,* Journal of Semiconductors, 40, 122701 (2019).

[184] C. Herzinger, B. Johs, W. McGahan, J. A. Woollam, and W. Paulson, *Ellipsometric determination of optical constants for silicon and thermally grown silicon dioxide via a multi-sample, multi-wavelength, multi-angle investigation,* Journal of Applied Physics, 83, 3323 (1998).

[185] A. Kasikov and L. Aarik, *Calculating the absorption edge of thin films,* Bulgarian Journal of Physics, 51 (2024).

[186] K. Ellmer, *Past achievements and future challenges in the development of optically transparent electrodes,* Nature Photonics, 6, 809 (2012).

[187] P. B. Johnson and R.-W. Christy, *Optical constants of the noble metals,* Physical review B, 6, 4370 (1972).

[188] C. V. Cushman, B. I. Johnson, A. Martin, B. M. Lunt, N. J. Smith, and M. R. Linford, *Eagle XG® glass: Optical constants from 196 to 1688 nm (0.735–6.33 eV) by spectroscopic ellipsometry,* Surface Science Spectra, 24 (2017).

[189] Y. Pan, Y. Fan, and J. Niu, *Optical properties of ultra-thin silver films deposited by thermal evaporation and its application in optical filters,* Infrared Physics & Technology, 104, 103123 (2020).

[190] M. Fischer, H. Tan, J. Melskens, R. Vasudevan, M. Zeman, and A. H. Smets, *High pressure processing of hydrogenated amorphous silicon solar cells: Relation between nanostructure and high open-circuit voltage,* Applied Physics Letters, 106 (2015).

[191] J. Jang, T. G. Kim, S. C. Kim, J. M. Jun, and K. C. Park, *Stable amorphous silicon double stacked solar cell using low band gap amorphous silicon bottom i layer,* Applied physics letters, 60, 2880 (1992).

[192] B. Liang, X. Chen, H. Yuan, X. Wang, G. Hou, Y. Zhao, and X. Zhang, *Enhancing optical and electrical performances via nanocrystalline Si-Based thin films for Si heterojunction solar cells,* ACS omega, 9, 49935 (2024).

[193] Y. Abdulraheem, I. Gordon, T. Bearda, H. Meddeb, and J. Poortmans, *Optical bandgap of ultra-thin amorphous silicon films deposited on crystalline silicon by PECVD,* AIP Advances, 4 (2014).

[194] R. Treharne, A. Seymour-Pierce, K. Durose, K. Hutchings, S. Roncallo, and D. Lane, *Optical design and fabrication of fully sputtered CdTe/CdS solar cells,* in *Journal of Physics: Conference Series,* Vol. 286 (2011) p. 012038.

[195] L. Mazzarella, S. Kolb, S. Kirner, S. Calnan, L. Korte, B. Stannowski, B. Rech, and R. Schlatmann, *Optimization of PECVD process for ultra-thin tunnel SiO_x film as passivation layer for silicon heterojunction solar cells,* in *2016 IEEE 43rd Photovoltaic Specialists Conference (PVSC)* (IEEE, 2016) pp. 2955–2959.

[196] A. J. Olivares, J. P. Seif, P.-A. Repecaud, C. Longeaud, M. Morales-Masis, M. Bivour, and P. R. i Cabarrocas, *Highly conductive p-type nc-SiO_x:H thin films deposited at 130°C via efficient incorporation of plasma synthesized silicon nanocrystals and their application in SHJ solar cells,* Solar Energy Materials and Solar Cells, 266, 112675 (2024).

[197] E. Agocs, P. Petrik, S. Milita, L. Vanzetti, S. Gardelis, A. Nassiopoulou, G. Pucker, R. Balboni, and M. Fried, *Optical characterization of nanocrystals in silicon rich oxide superlattices and porous silicon,* Thin Solid Films, 519, 3002 (2011).

[198] J. Sancho-Parramon, D. Gracin, M. Modreanu, and A. Gajović, *Optical spectroscopy study of nc-Si-based p–i–n solar cells,* Solar Energy Materials and Solar Cells, 93, 1768 (2009).

[199] M. Khardani, M. Bouaïcha, and B. Bessaïs, *Bruggeman effective medium approach for modelling optical properties of porous silicon: comparison with experiment,* physica status solidi c, 4, 1986 (2007).

[200] W. Y. Cho and K. S. Lim, *A simple optical properties modeling of microcrystalline silicon for the energy conversion application by the effective medium approximation method,* Japanese Journal of Aapplied Physics, 36, 1094 (1997).

[201] P. Petrik, M. Fried, E. Vazsonyi, P. Basa, T. Lohner, P. Kozma, and Z. Makkai, *Nanocrystal characterization by ellipsometry in porous silicon using model dielectric function,* Journal of Applied Physics, 105 (2009).

[202] S. Adachi and H. Mori, *Optical properties of fully amorphous silicon,* Physical Review B, 62, 10158 (2000).

[203] A. Smets, T. Matsui, and M. Kondo, *High-rate deposition of microcrystalline silicon pin solar cells in the high pressure depletion regime,* Journal of Applied Physics, 104 (2008).

[204] M. V. Shuba, M. Faryad, M. E. Solano, P. B. Monk, and A. Lakhtakia, *Adequacy of the rigorous coupled-wave approach for thin-film silicon solar cells with periodically corrugated metallic backreflectors: spectral analysis,* Journal of the Optical Society of America A, 32, 1222 (2015).

[205] B. J. Civiletti, A. Lakhtakia, and P. B. Monk, *Analysis of the rigorous coupled wave approach for p-polarized light in gratings,* Journal of Computational and Applied Mathematics, 386, 113235 (2021).

[206] T. D. Raju, V. Murugadoss, K. A. Nirmal, T. D. Dongale, A. V. Kesavan, and T. G. Kim, *Advancements in perovskites for solar cell commercialization: A review,* Advanced Powder Materials, 4, 100275 (2025).

[207] Z. Liu, Y. Wang, D. Luo, Z. Xie, Z. Liu, Q. Peng, S. Liu, and Y. Duan, *A comprehensive review of recent advances in flexible perovskite solar cells: Materials, fabrication, and applications,* Advanced Optical Materials, 14, e01157 (2026).

[208] J. Chung, S. S. Shin, K. Hwang, G. Kim, K. W. Kim, D. S. Lee, W. Kim, B. S. Ma, Y.-K. Kim, T.-S. Kim, *et al.*, *Record-efficiency flexible perovskite solar cell and module enabled by a porous-planar structure as an electron transport layer,* Energy & Environmental Science, 13, 4854 (2020).

[209] Renshine Solar, *Renshine's 30 × 40 cm perovskite module achieves 20.84% efficiency,* (2025), `https://www.perovskite-info.com`.

[210] H. Nikbakht, P. Mariani, L. Vesce, F. D. Giacomo, E. Leonardi, G. Viskadouros, E. Spiliarotis, K. Rogdakis, S. Pescetelli, A. Agresti, *et al.*, *Upscaling perovskite photovoltaics: from 156 cm^2 modules to 0.73 m^2 panels,* Advanced Science, 12, 2416316 (2025).

[211] Y. Gao, K. Huang, C. Long, Y. Ding, J. Chang, D. Zhang, L. Etgar, M. Liu, J. Zhang, and J. Yang, *Flexible perovskite solar cells: From materials and device architectures to applications,* ACS energy letters, 7, 1412 (2022).

[212] D. I. Kutsarov, E. Rezaee, J. Lambert, W. T. Stroud, A. Panagiotopoulos, and S. R. P. Silva, *Progress in flexible perovskite solar cells: paving the way for scalable manufacturing,* Advanced materials technologies, 10, 2401834 (2025).

[213] A. Chandrakar and A. Khare, *A comprehensive review of flexible perovskite solar cells: materials, mechanisms, properties, applications, and commercialization status,* Solar Energy, 298, 113649 (2025).

[214] A. Ranka, M. Layek, S. Kochiyama, C. López-Pernia, A. M. Chandler, C. A. Kocoj, E. Magliano, A. Di Carlo, F. Brunetti, P. Guo, *et al.*, *Cracking in polymer substrates for flexible electronic devices and its mitigation,* npj Flexible Electronics, 9, 92 (2025).

[215] M. Stolterfoht, P. Caprioglio, C. M. Wolff, J. A. Márquez, J. Nordmann, S. Zhang, D. Rothhardt, U. Hörmann, Y. Amir, A. Redinger, *et al.*, *The impact of energy alignment and interfacial recombination on the internal and external open-circuit voltage of perovskite solar cells,* Energy & environmental science, 12, 2778 (2019).

[216] B. G. Krishna, D. S. Ghosh, and S. Tiwari, *Hole and electron transport materials: A review on recent progress in organic charge transport materials for efficient, stable, and scalable perovskite solar cells,* Chemistry of Inorganic Materials, 1, 100026 (2023).

[217] M. Zhang, Z. Li, Z. Gong, Z. Li, and C. Zhang, *Perspectives on the mechanical robustness of flexible perovskite solar cells,* Energy Advances, 2, 355 (2023).

[218] T.-Y. Yang, Y. Y. Kim, and J. Seo, *Roll-to-roll manufacturing toward lab-to-fab-translation of perovskite solar cells,* APL Materials, 9 (2021).
[219] E. Parvazian and T. Watson, *The roll-to-roll revolution to tackle the industrial leap for perovskite solar cells,* nature communications, 15, 3983 (2024).
[220] M. Van den Donker, A. Gordijn, H. Stiebig, F. Finger, B. Rech, B. Stannowski, R. Bartl, E. Hamers, R. Schlatmann, and G. Jongerden, *Flexible amorphous and microcrystalline silicon tandem solar modules in the temporary superstrate concept,* Solar Energy Materials and Solar Sells, 91, 572 (2007).
[221] Y. Xu, Z. Lin, W. Wei, Y. Hao, S. Liu, J. Ouyang, and J. Chang, *Recent progress of electrode materials for flexible perovskite solar cells,* Nano-Micro Letters, 14, 117 (2022).
[222] P. Holzhey, M. Prettl, S. Collavini, C. Mortan, and M. Saliba, *Understanding the impact of surface roughness: changing from FTO to ITO to PEN/ITO for flexible perovskite solar cells,* Scientific Reports, 13, 6375 (2023).
[223] G. Tang and F. Yan, *Recent progress of flexible perovskite solar cells,* Nano Today, 39, 101155 (2021).
[224] Synopsys, *Sentaurus device user guide,* Synopsys Inc. (2010).
[225] P.-C. Huang, T.-J. Yang, C.-J. Lin, M.-Y. Wang, and W.-C. Lin, *Unraveling the heat-and UV-induced degradation of mixed halide perovskite thin films via surface analysis techniques,* Langmuir, 40, 11873 (2024).
[226] J. Zhou, Z. Liu, P. Yu, G. Tong, R. Chen, L. K. Ono, R. Chen, H. Wang, F. Ren, S. Liu, *et al.*, *Modulation of perovskite degradation with multiple-barrier for light-heat stable perovskite solar cells,* Nature Communications, 14, 6120 (2023).
[227] F. Saitta, G. Padmakumar, P. Perez Rodriguez, P. Procel Moya, R. Santbergen, and A. H. Smets, *Time-efficient, accurate, and experimentally grounded optical modeling of multiscale-textured thin-film solar cells,* Global Challenges, 10, e00448 (2026).
[228] J. Prentice, *Optical generation rate of electron-hole pairs in multilayer thin-film photovoltaic cells,* Journal of Physics D: Applied Physics, 32, 2146 (1999).
[229] P. Procel-Moya, Y. Zhao, and O. Isabella, *Unlocking the potential of carrier-selective contacts: Key insights for designing c-Si solar cells with efficiency beyond 28%,* Solar Energy Materials and Solar Cells, 285, 113504 (2025).
[230] C. M. Wolff, S. A. Bourelle, L. Q. Phuong, J. Kurpiers, S. Feldmann, P. Caprioglio, J. A. Marquez, J. Wolansky, T. Unold, M. Stolterfoht, *et al.*, *Orders of recombination in complete perovskite solar cells–linking time-resolved and steady-state measurements,* Advanced Energy Materials, 11, 2101823 (2021).
[231] J. Bisquert, *Interpretation of the recombination lifetime in halide perovskite devices by correlated techniques,* The Journal of Physical Chemistry Letters, 13, 7320 (2022).
[232] A. Shah, *Thin-film silicon solar cells* (EPFL press, 2010).
[233] W. Xu, L. J. Hart, B. Moss, P. Caprioglio, T. J. Macdonald, F. Furlan, J. Panidi, R. D. Oliver, R. A. Pacalaj, M. Heeney, *et al.*, *Impact of interface energetic alignment and mobile ions on charge carrier accumulation and extraction in p-i-n perovskite solar cells,* Advanced Energy Materials, 13, 2301102 (2023).
[234] A. Richter, V. Smirnov, A. Lambertz, K. Nomoto, K. Welter, and K. Ding, *Versatility of doped nanocrystalline silicon oxide for applications in silicon thin-film and heterojunction solar cells,* Solar Energy Materials and Solar Cells, 174, 196 (2018).
[235] W. H. Kouider and A. Belfar, *Comparison of using p-nc-SiO_X:H and p-nc-Si:H as window layer in amorphous silicon based solar cells,* Optik, 222, 165444 (2020).
[236] T. de Vrijer, F. T. Si, H. Tan, and A. H. M. Smets, *Chemical stability and performance of doped silicon oxide layers for use in thin-film silicon solar cells,* IEEE Journal of Photovoltaics, 9, 3 (2018).

[237] A. Bouhdjar, M. Adaika, A. Meftah, R. Boumaraf, A. Meftah, and N. Sengouga, *Performance study of the micromorph silicon tandem solar cell using silvaco TCAD simulator,* Transactions on Electrical and Electronic Materials, 20, 494 (2019).

[238] P. Otero, J. Rodriguez, M. Vetter, J. Andreu, E. Comesaña, and A. Garcia-Loureiro, *Simulation of the temperature dependence of a-Si:H solar cell current-voltage characteristics,* in *Proceedings of the 8th Spanish Conference on Electron Devices, CDE'2011* (IEEE, 2011) pp. 1–4.

[239] D. Qiu, A. Lambertz, W. Duan, L. Mazzarella, P. Wagner, A. B. Morales-Vilches, G. Yang, P. Procel, O. Isabella, B. Stannowski, *et al.*, *A review: application of doped hydrogenated nanocrystalline silicon oxide in high efficiency solar cell devices,* Advanced science, 11, 2403728 (2024).

[240] K. Morigaki and H. Hikita, *Modeling of light-induced defect creation in hydrogenated amorphous silicon,* Physical Review B—Condensed Matter and Materials Physics, 76, 085201 (2007).

[241] M. N. Islam and H. R. Ghosh, *Performance enhancement of an a-Si:H/μc-Si:H heterojunction pin solar cell by tuning the device parameters,* Dhaka University Journal of Science, 69, 88 (2021).

[242] J. Wang, H. Gao, J. Zhang, F. Meng, and Q. Ye, *Investigation of an a-Si/c-Si interface on a c-Si (P) substrate by simulation,* Journal of Semiconductors, 33, 033001 (2012).

[243] Y. Zhao, L. Mazzarella, P. Procel, C. Han, G. Yang, A. Weeber, M. Zeman, and O. Isabella, *Doped hydrogenated nanocrystalline silicon oxide layers for high-efficiency c-Si heterojunction solar cells,* Progress in Photovoltaics: research and applications, 28, 425 (2020).

[244] E. Kessels, *Remote plasma deposition of hydrogenated amorphous silicon,* Plasma Processes, Film Growth and Material Properties. Eindhoven University of Technology, 1 (2000).

[245] J. A. Peck *et al.*, *High deposition rate nanocrystalline and amorphous silicon thin film production,* Surface and Coatings Technology, 325, 370 (2017).

[246] T. Söderström, F.-J. Haug, X. Niquille, V. Terrazzoni, and C. Ballif, *Asymmetric intermediate reflector for tandem micromorph thin film silicon solar cells,* Applied Physics Letters, 94 (2009).

[247] V. M. Le Corre, M. Stolterfoht, L. Perdigon Toro, M. Feuerstein, C. Wolff, L. Gil-Escrig, H. J. Bolink, D. Neher, and L. J. A. Koster, *Charge transport layers limiting the efficiency of perovskite solar cells: how to optimize conductivity, doping, and thickness,* ACS Applied Energy Materials, 2, 6280 (2019).

[248] C.-H. Kuan, X. Jiang, Q. Zhou, X. Wen, S.-F. Hung, H.-L. Chen, Y.-S. Shih, S. Narra, M. Ma, J.-W. Chiou, *et al.*, *Overcoming the stability issue for hydrophobic hole transporting layers utilized in Tin-Lead perovskite and tandem solar cells,* Advanced Functional Materials, 36, e22134 (2026).

[249] J. Cameron and P. J. Skabara, *The damaging effects of the acidity in PEDOT:PSS on semiconductor device performance and solutions based on non-acidic alternatives,* Materials Horizons, 7, 1759 (2020).

[250] Y. Wang, L. Duan, M. Zhang, Z. Hameiri, X. Liu, Y. Bai, and X. Hao, *PTAA as efficient hole transport materials in perovskite solar cells: a review,* Solar Rrl, 6, 2200234 (2022).

[251] Z. Li, X. Sun, X. Zheng, B. Li, D. Gao, S. Zhang, X. Wu, S. Li, J. Gong, J. M. Luther, *et al.*, *Stabilized hole-selective layer for high-performance inverted pin perovskite solar cells,* Science, 382, 284 (2023).

[252] X. Yin, Y. Guo, H. Xie, W. Que, and L. B. Kong, *Nickel oxide as efficient hole transport materials for perovskite solar cells,* Solar Rrl, 3, 1900001 (2019).

[253] W. Peng, K. Mao, F. Cai, H. Meng, Z. Zhu, T. Li, S. Yuan, Z. Xu, X. Feng, J. Xu, *et al.*, *Reducing nonradiative recombination in perovskite solar cells with a porous insulator contact,* Science, 379, 683 (2023).

[254] D. S. Mann, S. Thakur, S. S. Sangale, K.-U. Jeong, S.-N. Kwon, and S.-I. Na, *Interfacial engineering of nickel oxide-perovskite interface with amino acid complexed NiO to improve perovskite solar cell performance,* Small, 20, 2405953 (2024).
[255] Y. Yang, F. Li, R. Chen, and H. Wang, *Interface engineering of inverted wide-bandgap perovskite solar cells for tandem photovoltaics,* Energy Mater. Devices, 2, 9370031 (2024).
[256] C. Peike, I. Hädrich, K.-A. Weiß, I. Dürr, and F. Ise, *Overview of PV module encapsulation materials,* Photovolt. Int, 19, 85 (2013).
[257] K. Sreejith, V. Venkatesh, G. Padmakumar, and A. H. Smets, *Comprehensive glare hazard analysis of Ethylene Tetrafluoroethylene (ETFE) based frontsheet for flexible photovoltaic applications,* IEEE Journal of Photovoltaics, 14, 930 (2024).
[258] P. Procel, J. Knobbe, N. Rezaei, V. Zardetto, N. Phung, M. Ma, M. Simor, M. Creatore, S. Veenstra, R. Santbergen, *et al.*, *Opto-electrical modelling and roadmap for 2T monolithic Perovskite/CIGS tandem solar cells,* Solar Energy Materials and Solar Cells, 274, 112975 (2024).
[259] K. Jiang, F. Wu, G. Zhang, P. C. Chow, C. Ma, S. Li, K. S. Wong, L. Zhu, and H. Yan, *Inverted planar perovskite solar cells based on CsI-doped PEDOT:PSS with efficiency beyond 20% and small energy loss,* Journal of Materials Chemistry A, 7, 21662 (2019).
[260] X. Wu, D. Wu, G. Cui, Z. Jiang, C. Zhao, X. Tang, X. Dong, N. Liu, Z. Zuo, L. Kong, *et al.*, *Exceeding 20% efficiency for highly efficient and stable inverted perovskite solar cells via sodium borohydride induced interface engineering,* Solar RRL, 7, 2200833 (2023).
[261] A. Kumar, S. Singh, and A. Yadav, *Recent progress in inverted perovskite solar cells employing nickel oxide (NiO_x) as a hole transport materials,* Materials Today: Proceedings, 46, 5827 (2021).
[262] L. Li, X. Zhang, H. Zeng, X. Zheng, Y. Zhao, L. Luo, F. Liu, and X. Li, *Thermally-stable and highly-efficient bi-layered NiOx-based inverted planar perovskite solar cells by employing a p-type organic semiconductor,* Chemical Engineering Journal, 443, 136405 (2022).
[263] J. Z. Mbese, *Advancements in inorganic hole-transport materials for perovskite solar cells: a comparative review,* Energies, 18, 2374 (2025).
[264] J. Zeng, J. Wang, J. Wang, J. Li, J. Chen, F. Wei, J. Zhang, W. Song, and X. Fan, *Flexible narrow bandgap Sn–Pb perovskite solar cells with 21% efficiency using N, $N^{'}$-Carbonyldiimidazole treatments,* ACS nano, 18, 31390 (2024).
[265] J. Jin, J. Shang, Z. Zhu, T. Guo, Y. Wang, L. Chen, Y. Ming, J. Li, G. Tang, and Q. Tai, *Highly conductive and homogeneous NiO_x nanoparticles for stable and efficient flexible perovskite solar cells,* Chemical Communications, 61, 3844 (2025).
[266] G. Padmakumar, F. Saitta, K. Sreejith, P. Perez-Rodriguez, R. A. van Swaaij, and A. H. Smets, *Mitigating the optical cavities in superstrate thin film silicon multijunction solar cells,* Solar Energy, 311, 114537 (2026).
[267] L. Li, Y. Wang, X. Wang, R. Lin, X. Luo, Z. Liu, K. Zhou, S. Xiong, Q. Bao, G. Chen, *et al.*, *Flexible all-perovskite tandem solar cells approaching 25% efficiency with molecule-bridged hole-selective contact,* Nature Energy, 7, 708 (2022).
[268] M. Li, H. Gao, L. Li, E. Wang, Z. Liu, I. T. Cheong, P. Wu, Y. Zhang, Y. Wang, X. Zheng, *et al.*, *In situ coating strategy for flexible all-perovskite tandem modules,* Nature Photonics, 19, 1255 (2025).
[269] Z. Liu, R. Lin, M. Wei, M. Yin, P. Wu, M. Li, L. Li, Y. Wang, G. Chen, V. Carnevali, *et al.*, *All-perovskite tandem solar cells achieving > 29% efficiency with improved (100) orientation in wide-bandgap perovskites,* Nature Materials, 24, 252 (2025).
[270] R. Lin, H. Gao, J. Lou, J. Xu, M. Yin, P. Wu, C. Liu, Y. Guo, E. Wang, S. Yang, *et al.*, *All-perovskite tandem solar cells with dipolar passivation,* Nature, 648, 600 (2025).
[271] B. Huijskes, *Designing Flexible Thin-Film Architectures: A Numerical Opto-Electrical Simulation Study,* Master thesis, Delft University of Technology (2025).

ACKNOWLEDGMENTS

A mia madre. A mio padre. A Giorgia.
Alle donne della mia vita. E a tutti gli altri membri della mia famiglia.

Il vostro amore, inesauribile e potente, è la mia più grande fonte di ispirazione e accompagna ogni mio passo. Grazie per avermi sostenuta, spronata e amata incondizionatamente lungo questo percorso. La vostra protezione è una luce che non abbaglia, ma orienta: quella di chi è accanto a me ogni giorno e quella di chi continua a vegliare su di me da lassù.

To my professor. Thank you. I still remember that email in July 2021. I was immersed in my MSc thesis when you asked me to come to your office. For a moment, I feared I had taken a wrong turn. But I hadn't. You wanted to speak with me about a PhD opportunity.
My instinctive reaction was, "Me?". I asked whether you truly believed I could rise to the challenge of a PhD, and you told me that I had all the qualities needed to pursue this path. And here I am, five years later.
I am deeply grateful to have had a mentor who sees people before roles, and potential before results. You saw something in me that I am still learning to see myself.

To fox, sloth, and bunny. And to bear and elephant. Being supervised by you has been an honor. You gave me constant support and taught me that I do not always need to be harsh with myself or with my mistakes, and that slow, steady work can lead to meaningful results. You showed me that the world is indeed under my feet (though I will return to *you* later in this flow of gratitude).
When my compass stopped pointing North and I felt lost, I found a bear and an elephant ready to guide me. A bear, with strength and protective patience, creating a safe space where I could find my balance again. And an elephant, with wisdom and a calm, grounding presence, reminding me that even small steps move you forward when taken with intention.

To my PhD fellow, it feels like yesterday when we started greeting each other with four fingers raised. You are an exceptional person, and I am grateful that our paths crossed.
And to all the office mates, colleagues, technicians, and friends from the PVMD group: there is no need to name you one by one. Thank you for the thoughtful and professional conversations that broadened my perspective, for the constant help during moments of struggle in the labs (which, admittedly, often lasted much longer than a moment), and for the countless smiles and bursts of laughter that brightened even the most demanding days. Each of you has contributed to this journey in ways I will carry with me well beyond this PhD.

To all the students I had the privilege of working with. This journey would not have been the same without you. Guiding you through your MSc thesis projects or internships has been a truly rewarding experience, and I learned from each of you more than I could have expected. Thank you for your trust, and for reminding me that teaching and learning always go hand in hand.

To Jas and Myrto, on my side as paranymphs for the PhD defense, and on my side in every aspect of life. Our friendship is something I will always protect with care and affection.
And together with you, to all the friends I have met in the Netherlands: I love you all. You transformed this place from somewhere I simply moved to into a place that truly feels like home.

Se fossimo un libro, Andre, saremmo uno dai capitoli infiniti, sempre pronti a scriverne di nuovi, a reinventarci, a volerci bene. Oggi sai cosa voglio fare. Fare come quando piove e io mi scordo l'ombrello. Là fuori com'è? Come me e te. Non sempre bello eppure.
And to all my friends in Milan and scattered around the world. You know how deeply I value what we share, and how much richer you have made my life. I owe you a heartfelt thank you.

Finally, to *you*. You stand by my side in countless ways and became part of my life in a way I could never have imagined. You support me and push me beyond the limits I convince myself I have, limits you continue to prove are not truly there. You are the shoulder that welcomes my tears, the playful bunny who brings lightness to my days, and the companion who dares to dream forward into a future we imagine together. I do not know where this journey will lead us. The effort, however, is something we share. And whatever the future may hold, you will remain a part of my world... altijd.

LIST OF PUBLICATIONS

First-authored peer-reviewed journal articles:

1. **Saitta, F.**, Kalpoe, P., Ahluwalia, V., Padmakumar, G., Perez-Rodriguez, P., Limodio, G., Santbergen, R., & Smets, A. H. M. *De-coupling of Optical and Electrical Properties in Front TCO Using the Bilayer Concept for Thin Film Solar Cells.* Solar Energy Materials and Solar Cells, 290, 113723 (2025).

2. **Saitta, F.**, Padmakumar, G., Perez-Rodriguez, P., Wilson, A., Gonugunta, P., Anusuyadevi, P. R., Santbergen, R., & Smets, A. H. M. *Room-Temperature Sputtered SnO_2-Based Thin Films as Earth-Abundant Transparent Conductive Oxides for Photovoltaic Applications.* ACS Applied Electronic Materials, 7(20), 9489-9504 (2025).

3. **Saitta, F.**, Padmakumar, G., Perez-Rodriguez, P., Procel Moya, P., Santbergen, R., & Smets, A. H. M. *Time-Efficient, Accurate, and Experimentally Grounded Optical Modeling of Multiscale Textured Thin-Film Solar Cells.* Global Challenges, e00448 (2025).

4. **Saitta, F.**, Huijskes, B., van Silfhout, N., Padmakumar, G., Perez-Rodriguez, P., Procel Moya, P., Santbergen, R., & Smets, A. H. M. *Bridging Flexible Perovskite Photovoltaics with Thin-Film Silicon Manufacturing through High Temperature Superstrate Foils.* EES Solar (under review, 2026).

Co-authored peer-reviewed journal articles:

1. Padmakumar, G., Criel, M., Kashyap, T., **Saitta, F.**, Perez-Rodriguez, P., van Swaaij, R. A., & Smets, A. H. M. *Superimposed Sacrificial Texturing to Enhance the Optical Performance in Thin-Film Solar Cells.* Progress in Photovoltaics: Research and Applications (2025).

2. Padmakumar, G., Balaji, A., Criel, M., **Saitta, F.**, Limodio, G., Perez-Rodriguez, P., van Swaaij, R. A., & Smets, A. H. M. *Engineering of Hexagonal Microtextures on Glass.* ACS Applied Optical Materials, 3(10), 2360-2372 (2025).

3. Padmakumar, G., Balaji, A., **Saitta, F.**, Perez-Rodriguez, P., van Swaaij, R. A., & Smets, A. H. M. *Hexagonal Microtextured Glass to Achieve High Optical Performance in Thin-film Silicon Solar Cells.* Solar Energy, 306, 114292 (2026).

4. Padmakumar, G., **Saitta, F.**, Sreejith, K.P., Perez-Rodriguez, P., van Swaaij, R. A., & Smets, A. H. M. *Mitigating the interference effects induced by optical cavities in superstrate thin-film silicon multi-junction solar cells.* Solar Energy, 311, 114537 (2026).

5. de Vrijer, T., Bouazzata, B., Ravichandran, A., van Dingen, J. E. C., Roelandschap, P. J., Roodenburg, K., Roerink, S. J., **Saitta, F.**, Blackstone, T., & Smets, A. H. M. *Opto-Electrical Properties of Group IV Alloys: The Inherent Challenges of Processing Hydrogenated Germanium.* Advanced Science, 9(18), 2200814 (2022).

6. de Vrijer, T., Roodenburg, K.,**Saitta, F.**, Blackstone, T., Limodio, G., & Smets, A. H. M. *PECVD Processing of low bandgap-energy amorphous hydrogenated germanium-tin (a-GeSn: H) films for opto-electronic applications.* Applied Materials Today, 27, 101450 (2022).

Conference contributions:

1. **Saitta, F.**, Smink, I., Limodio, G., Santbergen, R., Isabella, O., & Smets, A. H. M. *Optical Model with Combined Ray and Wave Optics for Optimization of Textures of Thin-Film Solar Cells.* In Optical Devices and Materials for Solar Energy and Solid-state Lighting (pp. PvW2H-3). Optica Publishing Group, Maastricht, the Netherlands (2022). [oral]

2. **Saitta, F.**, Smink, I., Limodio, G., Santbergen, R., Isabella, O., & Smets, A. H. M. *Optical Modeling for Optimization of Sub-Micron Textures for Multi-Junction Solar Cells.* In 33rd International Photovoltaic Science and Engineering Conference, Nagoya, Japan (2022). [oral]

3. **Saitta, F.**, Kalpoe, P., Padmakumar, G., Perez-Rodriguez, P., Limodio, G., Santbergen, R., & Smets, A. H. *Transparent Conductive Oxide Bi-Layer as Front Contact for Multijunction Thin-Film Silicon Solar Cells.* In 2023 IEEE 50th Photovoltaic Specialists Conference (PVSC) (pp. 1-3). IEEE, San Juan, Puerto Rico (2023). [poster]*

4. **Saitta, F.**, Kalpoe, P., Ahluwalia, V., Padmakumar, G., Perez-Rodriguez, P., Limodio, G., Santbergen, R., & Smets, A. H. M. *Transparent Conductive Oxide Bi-layer as Front Contact Architecture for Multijunction Thin-film Silicon Solar Cells.* In 40th European Photovoltaic Solar Energy Conference & Exhibition, Lisbon, Portugal (2023). [poster]

5. **Saitta, F.**, *Optical Modelling of Flexible Multijunction Solar Cells: From Thin-Film Silicon Towards Perovskites.* In 4th European Workshop on Optics for Solar Energy at Helmholtz-Zentrum Berlin (HZB), Berlin, Germany (2023). [invited talk]

6. **Saitta, F.**, Kessels, L., Santbergen, R., Perez-Rodriguez, P., Janssen, R. & Smets, A. H. M. *Optical Modeling and Performance Assessment of Thin-Film Silicon/Perovskite Tandem Solar Cells.* In Photonics for Solar Energy Systems X (p. PC1301403). SPIE (2024). [oral]

7. **Saitta, F.**, Balaji, A., Ahluwalia, V., Padmakumar, G., Perez-Rodriguez, P., Santbergen, R., & Smets, A. H. M. *Novel Transparent Conductive Oxide Bilayer Designs for Thin-Film Silicon Solar Cells.* In 2024 IEEE 52nd Photovoltaic Specialist Conference (PVSC) (pp. 0766-0768). IEEE, Strasbourg, France (2024). [oral]

8. **Saitta, F.**, Kessels, L., Santbergen, R., Perez-Rodriguez, P., Janssen, R. & Smets, A. H. M. *Optical Modeling of Flexible Thin-Film Tandem Solar Cells: Enhancing Efficiency with Amorphous Silicon and Tin-Lead Perovskite Absorber Layers.* In TandemPV Workshop, Amsterdam, the Netherlands (2024). [poster]†

*It has won the Best Poster Award in Silicon Photovoltaic Materials and Devices area
†This work was presented by Rudi Santbergen

9. **Saitta, F.**, Padmakumar, G., Perez-Rodriguez, P., Wilson, A., Santbergen, R., & Smets, A. H. M. *SnO_2-based Thin Films as Earth-Abundant Transparent Conductive Oxides for Next-Generation Photovoltaics.* In 36th International Photovoltaic Science and Engineering Conference, Bangkok, Thailand (2025). [oral]

10. **Saitta, F.**, Padmakumar, G., Perez-Rodriguez, P., Procel Moya, P., Santbergen, R., & Smets, A. H. M. *Advanced Optical Modeling for Thin-Film Solar Cells on Multiscale Textures.* In 36th International Photovoltaic Science and Engineering Conference, Bangkok, Thailand(2025). [oral]

ABOUT THE AUTHOR

Federica Saitta was born on 26 July 1997 in Milan, Italy. She obtained her Bachelor of Science degree in Electrical Engineering from the Politecnico di Milano. She later earned her Master of Science in Sustainable Energy Technology at Delft University of Technology, the Netherlands.

During her MSc, she carried out an internship at the Ricerca sul Sistema Energetico (RSE) institute in Milan. She implemented and tested control algorithms for modular multilevel converters (MMC) with integrated battery energy storage systems (BESS) for power-grid connected applications.

She then joined the Photovoltaic Materials and Devices (PVMD) group for her MSc thesis project, where she worked on the optical design and modeling of triple-junction solar cells for thin-film silicon photovoltaic applications.

In 2022, she continued within the same research group to undertake her doctoral research. Her PhD focused on the development of flexible, lightweight, and ultra-thin photovoltaic devices. The project was carried out in collaboration with the Dutch company LiftPV (former HyET Solar), and addressed materials and solar devices optimization, and scalable roll-to-roll manufacturing strategies for the advancement of thin-film photovoltaic technologies.


TUDelft